U.PORTO
FEUP FACULDADE DE ENGENHARIA
UNIVERSIDADE DO PORTO

Chemical Engineering Department

Transport Phenomena Research Center

Two-phase flow in PEM fuel cells: 1D + 3D model development and numerical simulations

Rui Carlos Barata Ferreira

Thesis presented for the **Doctor of Philosophy** degree in Chemical and Biological Engineering from the Faculty of Engineering of University of Porto

Supervisors

Alexandra Maria Pinheiro da Silva Ferreira Rodrigues Pinto

Daniela Sofia de Castro Falcão

Vânia Sofia Brochado de Oliveira

Porto, May 2017

STATEMENT OF ORIGINALITY

I certify that this work does not contain any material that has been used, or will be used, for the award of any other degree or diploma in my name or anyone, in any university or institution. Moreover, I certify that, to the best of my knowledge, this work does not contain any material previously published or written by another person, except where due reference has been made in the text.

(Rui Carlos Barata Ferreira)

STATEMENT

In order to fulfil the Rules of Ethics of the Doctoral Program of Chemical and Biological Engineering (PDEQB), we hereby declare that all the contents of the thesis presented by Rui Carlos Barata Ferreira, entitled “Two-phase flow in PEM fuel cells: 1D + 3D model development and numerical simulations”, are exclusively from the author. Accordingly, all the results here shown were obtained by the author of the thesis.

____

(Rui Carlos Barata Ferreira)

____

(Alexandra Maria Pinheiro da Silva Ferreira Rodrigues Pinto)

____

(Daniela Sofia de Castro Falcão)

____

(Vânia Sofia Brochado de Oliveira)

ABSTRACT

Proton exchange membrane (PEM) fuel cells are a viable, clean and efficient power generation technology for the future. Water management, *i.e.*, the balance between membrane drying and liquid water flooding, is a major technical issue in the operation of these devices. Water flooding, in particular, results into a gas-liquid two-phase flow that affects their performance, durability and cost. Mathematical models play and important role for a deeper understanding of the two-phase flow phenomenon occurring in a PEM fuel cell.

The main goal of this work was to move one step ahead on PEM fuel cells modeling and simulation. A numerical model that couples the volume of fluid (VOF) method to simulate the air-water two-phase flow in the cathode gas channels (GCs) with the electrochemical reactions taking place in the catalyst layer (CL) and the water transport in the membrane was developed. The multi-fluid saturation method was also implemented to describe the water transport in the gas diffusion layer (GDL). A 3D domain was considered for the cathode GDL and CGs, whereas the remaining components of the cell were simplified to 1D.

The model was validated against the electrochemical performance of an experimental fuel cell, considering polarization curves and individual voltage losses. A transparent fuel cell was also employed to visualize the water distribution in the cathode in order to validate the model two-phase flow predictions.

The water dynamics in a single-serpentine channel of a fuel cell with an active area of 25 cm^2 was numerically investigated. When decreasing the operating voltage, droplets grew larger and suffered more deformation, and the amount of water accumulated in the channel was higher. Accordingly, the two-phase flow pressure drop was higher at lower voltages. Furthermore, it was found that more water accumulated in the elbows, and at the top and side walls of the channel. Current density and liquid water generation distributions were displayed and correlated with the water emergence profile through the GDL into the serpentine channel. It was also demonstrated that the model can compute the effects of flooding in the cell electrochemical output.

An experimental study on the membrane electrode assembly (MEA) design was also conducted. The effects of the microporous layer (MPL), membrane thickness and GDL hydrophobic treatment were investigated. The MPL was found to improve the cell performance at low to medium current densities. However, at high currents, it reduced the cell electrical output. Decreasing the membrane thickness and applying a hydrophobic treatment to the GDL resulted into significantly better performances.

Further numerical simulations were conducted employing a 2.4 cm^2 cell with single and multi-serpentine channels, in which the influence of the channel walls wettability on the two-phase flow was studied. Water was transported as films attached to the channel upper corners when the walls were set hydrophilic, whereas when the walls were considered hydrophobic it moved along the channel mostly in the form of droplets. Higher pressure drops were obtained when considering hydrophobic walls. Increasing the air stoichiometry decreased the influence of the channel walls wettability and increased the pressure drop. Setting a different wettability to the elbows of the serpentine did not provide more beneficial flow patterns. However, setting the top wall hydrophilic while considering the side walls hydrophobic appeared to be a better option than having all the walls hydrophilic or hydrophobic. Similar two-phase flow patterns were obtained using single and multi-serpentine channels, with the same effects of the channel walls wettability. However, the pressure drop in the multi-serpentine configuration was significantly lower.

In the model developed in this work, important issues on PEM fuel cells modelling and simulation were addressed, especially those concerning coupling the VOF technique with the electrochemical reactions and the proper experimental validation of the results. Both the model and the results of numerical simulations contribute to a better understanding of the two-phase flow phenomenon that occurs in PEM fuel cells. Such knowledge is essential to find suitable strategies to mitigate its negative effects, further contributing for the development and optimization of this technology.

Keywords: PEM fuel cells, Water management, Two-phase flow, Numerical modelling and simulation, Volume of fluid method

Resumo

As células de combustível com membrana de permuta protónica (*proton exchange membrane (PEM) fuel cells*) surgem como uma tecnologia viável, limpa e eficiente para a geração de energia no futuro. A gestão de água, ou seja, o balanço entre como evitar a secagem da membrana e o encharcamento da célula, é um aspeto muito importante na operação destes dispositivos. O encharcamento da célula leva ao aparecimento de um escoamento bifásico (gás-líquido) que afeta o seu desempenho, durabilidade e custo. Os modelos matemáticos desempenham um papel relevante na aquisição de um conhecimento aprofundado acerca dos fenómenos relacionados com o escoamento bifásico que ocorre numa célula de combustível do tipo PEM.

O principal objetivo deste trabalho foi avançar na área da modelação e simulação de células de combustível do tipo PEM. Desenvolveu-se um modelo matemático acoplando o método *Volume of Fluid* (VOF), que simula o escoamento bifásico ar-água nos canais do cátodo, com as reações eletroquímicas que ocorrem na camada catalítica e com o transporte de água na membrana. O método *Multi-Fluid* foi também implementado para descrever o transporte de água na camada difusora. Considerou-se um domínio 3D para os canais e para a camada difusora do cátodo, e para os restantes componentes da célula considerou-se um domínio simplificado em 1D. Esta estratégia permitiu a diminuição do tempo de cálculo numérico.

O modelo foi validado através dos valores experimentais do desempenho eletroquímico de uma célula de combustível do tipo PEM, considerando curvas de polarização e os valores individuais dos vários tipos de perdas de tensão. Foi também usada uma célula de combustível transparente de modo a visualizar a distribuição de água no cátodo e validar as previsões do modelo relativamente ao escoamento bifásico.

Analisou-se numericamente a formação e escoamento da água num canal em forma de serpentina de uma célula de combustível com uma área ativa de 25 cm^2. Para valores decrescentes da tensão de operação, as gotas de água aumentaram de tamanho, sofreram uma maior deformação e a quantidade de água acumulada no canal aumentou. Consequentemente, a queda de pressão no escoamento bifásico aumentou também para menores valores de tensão. Verificou-se igualmente a ocorrência de uma maior acumulação de água nos "cotovelos" do canal, nas suas paredes laterais e no topo. Correlacionou-se a distribuição espacial da corrente especifica e da geração de água líquida com o perfil de aparecimento de água no canal, através da camada difusora. Foi

também demonstrado que o modelo desenvolvido é capaz de prever o efeito do encharcamento da célula no seu desempenho eletroquímico.

Realizou-se igualmente um estudo experimental sobre o *design* do conjunto membrana-elétrodos (*membrane electrode assembly* (MEA)), onde foram analisados os efeitos da camada microporosa (*microporous layer* (MPL)), da espessura da membrana e do tratamento hidrofóbico da camada difusora no desempenho da célula. Verificou-se que a MPL melhorou o desempenho da célula quando esta operou a correntes específicas baixas e médias. No entanto, a MPL levou a uma redução do desempenho da célula aquando do funcionamento a correntes elevadas. Verificou-se ainda que, quer uma diminuição da espessura da membrana, quer a aplicação de um tratamento hidrofóbico à camada difusora, melhorou significativamente o desempenho da célula.

Efetuou-se um conjunto adicional de simulações numéricas considerando uma célula com 2.4 cm^2 de área ativa e placa distribuidora de fluxo com um único canal em serpentina e com vários canais também com uma geometria em serpentina. Nestes estudos, analisou-se a influência da molhabilidade no escoamento bifásico. Para paredes do canal hidrofílicas, formaram-se filmes de água que se acumularam nos cantos superiores do canal, enquanto que quando as paredes foram consideradas hidrofóbicas, a água movimentou-se ao longo do canal principalmente sob a forma de gotas. Obtiveram-se maiores quedas de pressão com paredes hidrofóbicas. Aumentando o excesso de ar, diminuiu a influência da molhabilidade das paredes do canal e aumentou a queda de pressão. A aplicação de uma diferente molhabilidade nos “cotovelos” da serpentina não gerou padrões de escoamento mais favoráveis. No entanto, considerar a parede do topo do canal como hidrofílica e as paredes laterais hidrofóbicas revelou-se uma melhor opção do que ter todas as paredes hidrofílicas ou hidrofóbicas. Obtiveram-se padrões de escoamento bifásico semelhantes em canais com serpentina única e com múltiplas serpentinas, com os mesmos efeitos da molhabilidade das paredes dos canais. No entanto, a queda de pressão na configuração em multi-serpentina foi significativamente menor.

No modelo desenvolvido neste trabalho foram abordados aspetos importantes na modelação e simulação de células de combustível do tipo PEM, especialmente os relativos ao acoplamento da técnica VOF com as reações eletroquímicas e a uma validação adequada do mesmo com resultados experimentais. Quer o modelo, quer os resultados das simulações numéricas contribuem para uma melhor compreensão do escoamento bifásico que ocorre neste tipo de células. Tal conhecimento é essencial na

conceção de estratégias adequadas para mitigar os seus efeitos negativos, contribuindo assim para o desenvolvimento e otimização desta tecnologia.

Palavras-chave: Células de combustível com membrana de permuta protónica, Gestão de água, Escoamento bifásico, Modelação e simulação numérica, Método *Volume of Fluid*

Acknowledgments

I would like to thank my supervisors, professor Alexandra, Vânia and Daniela, for giving me the opportunity and conditions to perform the present work and for their constant guidance.

I thank to my colleagues from CEFT for valuable tips and discussions. Thanks to all colleagues from chemical engineering department who also contribute to this work.

Thanks to my family, friends and girlfriend for their unconditional support.

I acknowledge my doctoral scholarship SFRH/BD/89572/2012 financed by the Portuguese "Fundação para a Ciência e Tecnologia" (FCT), POPH/QREN and European Social Fund (ESF). I also appreciate the financial support from the Transport Phenomena Research Center (*Centro de Estudos de Fenómenos de Transporte* – CEFT) (supported by POCI (FEDER)).

List of Publications

Rui B. Ferreira, D.S. Falcão, V.B. Oliveira, A.M.F.R. Pinto. A one-dimensional and two-phase flow model of a proton exchange membrane fuel cell. J Chem Technol Biotechnol 2015; 90(9):1547-1551.

Rui B. Ferreira, D.S. Falcão, V.B. Oliveira, A.M.F.R. Pinto. Numerical simulations of two-phase flow in proton exchange membrane fuel cells using the volume of fluid method - A review. J Power Sources 2015; 277:329-342.

Rui B. Ferreira, D.S. Falcão, V.B. Oliveira, A.M.F.R. Pinto. Numerical simulations of two-phase flow in an anode gas channel of a proton exchange membrane fuel cell. Energy 2015; 82(0):619-628.

Rui B. Ferreira, D.S. Falcão, V.B. Oliveira, A.M.F.R. Pinto. Experimental study on the membrane electrode assembly of a proton exchange membrane fuel cell: effects of microporous layer, membrane thickness and gas diffusion layer hydrophobic treatment. Electrochim Acta 2017; 224:337-45.

Rui B. Ferreira, D.S. Falcão, V.B. Oliveira, A.M.F.R. Pinto. 1D + 3D two-phase flow numerical model of a proton exchange membrane fuel cell. Submitted.

Rui B. Ferreira, D.S. Falcão, V.B. Oliveira, A.M.F.R. Pinto. Numerical study on the gas channels walls wettability of a proton exchange membrane fuel cell. To be submitted.

List of Figures

List of Tables

Nomenclature

a	water activity (Equations **(5.43)** and **(5.44)**); Tafel equation y-axis intercept (V) (Equations **(3.1)** and **(3.2)**)
b	Tafel slope (V)
A	area (m^{2})
C	molar concentration (mol m^{-3})
C^{ref}	reference molar concentration (mol m^{-3})
D	effective diffusion coefficient (m^{2} s^{-1})
D^{0}	binary diffusion coefficient (m^{2} s^{-1})
D_{cap}	capillary diffusion coefficient (kg m^{-3} s^{-1})
E	energy (J)
f	volume fraction
F	Faraday's constant (C mol^{-1})
$\vec{F}$	momentum source term (N m^{-3})
g	gravitational acceleration (N m^{-3})
H	height of a gas channel (m)
iR	cell internal electrical resistance (Ω cm^{2})
I	current density (A cm^{-2})
I_0	exchange current density (A cm^{-2})
I_L	limiting current density (A cm^{-2})
I^{ref}	reference current density (A cm^{-2})
I_0^{ref}	reference exchange current density (A cm^{-2})
J	Leverett J-function
K	permeability (m^{2})
k_{eff}	effective thermal conductivity (W m^{-1}K^{-1})
$\dot{m}$	mass flow per volume (kg m^{-3}s^{-1})
M	molecular weight (kg mol^{-1})
n	number of electrons (Equations **(1.4)**, **(1.7)** and **(1.8)**); total number of computational cells (Equation **(5.33)**); total number of fluids (Equations **(2.1)**, **(2.2)**, **(2.6)**) surface normal (Equations **(2.10)**, **(2.11)**, **(5.8)** and **(5.24)**)

n_{drag}^{sat}	electro-osmotic drag coefficient in a fully hydrated membrane
$\hat{n}$	unit normal
N	molar flux (mol m^{-2})
OCV	open circuit voltage (V)
P	pressure (Pa)
P_{cap}	capillary pressure (Pa)
P_{sat}	saturation pressure (bar)
Q	volumetric gas flow rate (m^3 s^{-1})
r	height of roughness elements (m)
R	ideal gas constant (J mol^{-1} K^{-1})
R_T	total resistance (Ω cm^2)
R_{act}	activation resistance (Ω cm^2)
R_{ohm}	ohmic resistance (Ω cm^2)
R_{mt}	mass transfer resistance (Ω cm^2)
RH	relative humidity
s	liquid water saturation
S	source term
t	time (s)
$\hat{t}$	surface tangent
T	temperature (°C)
U	unit tensor
v	velocity (m s^{-1})
V	operating voltage (V)
V_0	theoretical voltage at standard temperature and pressure (V)
$V_{T,P}$	theoretical voltage at temperature T and pressure P (V)
w	water
x	Cartesian coordinate (direction of the 1D domain)
X	multiplicative factor for liquid water velocity
Y	mass fraction
Y^*	mass fraction at the cell adjacent to a wall
Z	real part of impedance (Ω cm^2)
Z'	imaginary part of impedance (Ω cm^2)

Greek symbols

α	transfer coefficient in Tafel equation (Equations **(1.5)**,**(3.2)**,**(3.3)** and **(5.35)**); water transport coefficient in the membrane (Equations **(5.29)** and **(5.41)**);
δ	diffusion distance (m) (Equation **(1.7)**); thickness (m) (Equations **(5.37)**, **(5.39)**, **(5.45)** and **(5.46)**)
ε	porosity
η_{act}	activation losses (V)
η_{ohm}	ohmic losses (V)
η_{mt}	mass transfer losses (V)
η_{c}	cathode overpotential (V)
θ	contact angle (°)
κ	curvature of the interface (m^{-1})
λ	reactant stoichiometry (Equation **(5.16)**); membrane water content (Equations **(5.40)-(5.43)**)
μ	dynamic viscosity (Pa s)
ρ	density (kg m^{-3})
σ	proton conductivity (S m^{-1})
τ	surface tension (N m)

Superscripts

CL	catalyst layer
GC	gas channel
GDL	gas diffusion layer
m	exponent for effective porosity
n	exponent for effective saturation
PEM	proton exchange membrane
ref	reference value
sat	saturation value

Subscripts

a	anode
B	indication of bulk concentration
c	cathode
cap	capillary
h	heat
i	arbitrary phase/fluid (Equations **(2.3)** and **(2.4)**); specie (Equations **(5.10)**, **(5.11)** and **(5.24)**); counter for the number of computational cells (Equation **(5.33)**)
j	arbitrary phase/fluid
PEM	proton exchange membrane
p	arbitrary phase/fluid
q	arbitrary phase/fluid
sat	saturation value
w	liquid water
$wall$	wall of a gas channel

List of Abbreviations

AC	Alternating Current
AFC	Alkaline Fuel Cell
CFD	Computational Fluid Dynamics
CL	Catalyst Layer
CPE	Constant Phase Element
CSF	Continuum Surface Force
CSS	Continuum Surface Stress
CSTR	Continuously Stirred Tank Reactor
CV	Cyclic Voltammetry
DAQ	Data Acquisition
ECSA	Electrochemical Surface Area
EIS	Electrochemical Impedance Spectroscopy
FEP	Fluorinated Ethylene Propylene
GC	Gas Channel
GDL	Gas Diffusion Layer
HFR	High Frequency Resistance
HOR	Hydrogen Oxidation Reaction
LB	Lattice Boltzmann
LSV	Linear Sweep Voltammetry
MAC	Marker-And-Cell
MCFC	Molten Carbonate Fuel Cell
MEA	Membrane Electrode Assembly
MPL	Microporous Layer
MRI	Magnetic Resonance Imaging
NASA	National Aeronautics and Space Administration
OCV	Open Circuit Voltage
ORR	Oxygen Reduction Reaction
PAFC	Phosphoric Acid Fuel Cell
PEM	Proton Exchange Membrane
PET	Polyethylene Terephthalate
PFSA	Perfluorocarbon Sulfonic Acid

PLIC	Piecewise-Linear Interface Calculation
PN	Pore-Network
PRESTO!	Pressure Staggering Option scheme
PTFE	Polytetrafluoroethylene
RH	Relative Humidity
SEM	Scanning Electron Microscope
SIMPLE	Semi-Implicit Method for Pressure Linked Equations
SLIC	Simple Line Interface Calculation
SOFC	Solid Oxide Fuel Cell
UDF	User Defined Function
UDS	User Defined Scalar
VOF	Volume of Fluid

Table of Contents

1. INTRODUCTION

1.1. Background

Global energy supply system and associated problems

Fossil fuels, including coal, oil and natural gas, meet about 80 % of the world total primary energy supply [1]. However, they are finite and eventually are going to be depleted. Moreover, their use releases greenhouse gases that are leading to the global warming of the planet [2]. Climate changes have had widespread impacts on human and natural systems [2]. The atmosphere and ocean have warmed, the quantity of snow and ice have decreased, and the sea level has increased [2]. Continued emission of such gases will cause further warming and long-lasting changes in the climate system, increasing the probability of severe, pervasive and irreversible impacts for people and ecosystems [2]. A large and sustained reduction of fossil fuels burning is urgently required to limit climate change and its consequences. The current global energy supply system needs therefore to suffer major transformations in order to be based on renewable energy sources with minimal environmental impact.

1.2. Fuel cells technology

Fuel cells and how they can be an alternative for energy generation / Hydrogen energy economy / Types of fuel cells / Applications

A fuel cell, first demonstrated by Sir Willian Grove in 1839 [3], is an electrochemical energy conversion device that directly transforms the chemical energy of a fuel into electricity. A brief history of fuel cells development, since their discovery to the present days, can be found in Ref. [4, 5].

Fuel cells are a central part to the so called hydrogen energy economy, where hydrogen, the lightest, most efficient and cleanest fuel, is used as the primary energy vector [6, 7]. Most of the hydrogen produced today still derives from fossil raw materials. However, it can also be obtained through water electrolysis using electricity generated from renewable resources, such as solar or wind. In a fuel cell, hydrogen can be converted into electricity very efficiently and with virtually no harmful greenhouse gases emissions. Fuel cells thus appear as a sustainable alternative technology to generate power for the future.

There are several types of fuel cells. They are generally classified based on the electrolyte employed. Accordingly to such classification, there are 5 major groups of fuel cells: alkaline fuel cells (AFCs); proton exchange membrane (PEM) fuel cells; phosphoric acid fuel cells (PAFCs); molten carbonate fuel cells (MCFCs); and solid oxide fuel cells (SOFCs). These fuel cells differ from each other according to their operating temperature, efficiency, applications and cost. A comparative study of design, working principle, applications, advantages and disadvantages of the various fuel cell technologies can be found elsewhere [8]. These technologies are already being commercialized or are near commercialization. After the installation of its first unit on Google's main campus in 2008, Bloom Energy have provided SOFCs systems for many companies, including Walmart, Bank of America, Apple, Honda, The Coca Cola Company, NASA, etc. ACFs have been used in the Unites States space program since 1960 [4]. PAFCs systems are being commercialized by Doosen Corporation (former UTC Power) for several years. In 2013, FuelCell Energy Solutions delivered its first MCFCs power plant to the German federal ministry of education and research office complex, located in Berlin. Examples of applications of PEM fuel cells systems, those with the broadest range of applicability, are presented in a separate section.

1.3. PEM fuel cells

PEM fuel cells in particular have highly desirable features. They operate at low temperature, rendering them easier to handle, reducing thermal losses and allowing a rapid startup. They are also generally the smallest and lightest fuel cells. Such characteristics makes them suitable for almost every application. That is why most of the fuel cell research and development activities involve PEM fuel cells, as is the case of the present thesis. This section is dedicated to a brief overview of PEM fuel cells technology.

1.3.1. Basic principle of operation

Reactions / Theoretical efficiency and voltage / Nernst equation / Comparison with heat engines efficiency

In a PEM fuel cell, hydrogen is fed on the anode side (negative electrode) where it is split into its primary constituents: protons (H^+) and electrons (e^-). This reaction is designated as hydrogen oxidation reaction (HOR) (Equation **(1.1)**). Protons travel through the electrolyte towards the cathode, whereas the electrons are forced to travel through an external electrical circuit, where they perform useful work. At the cathode side (positive electrode), protons and electrons coming from the anode react with oxygen (generally from air) that is introduced on this side. From the oxygen reduction reaction (ORR), water is produced and heat is released (Equation **(1.2)**). The operating principle of a PEM fuel cell is schematized in **Figure 1.1**.

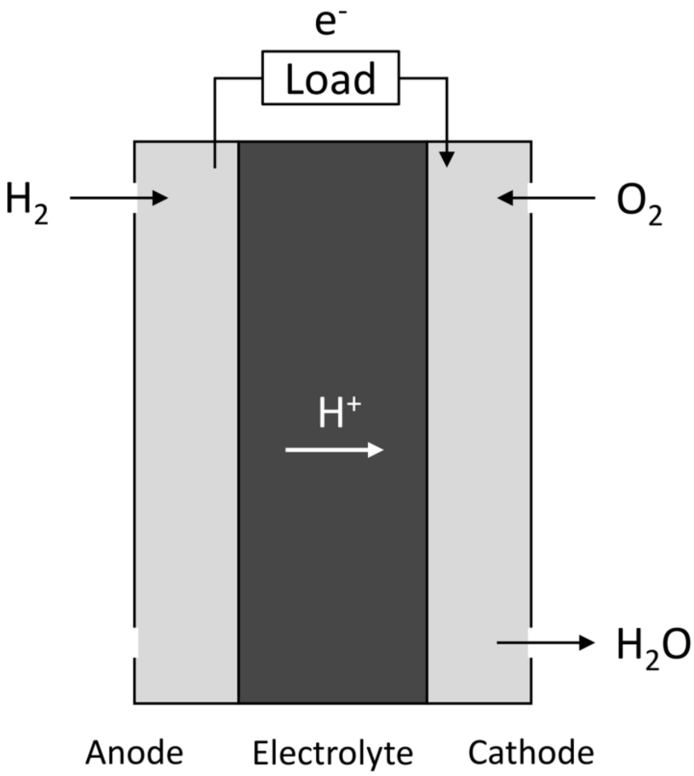

Figure 1.1. Operating principle of a PEM fuel cell.

PEM fuel cell reactions include, at the anode:

$$H_2\ (g) \rightarrow 2H^+\ (aq) + 2e^- \tag{1.1}$$

and at the cathode:

$$\frac{1}{2}O_2\ (g) + 2H^+\ (aq) + 2e^- \rightarrow H_2O\ (l) + Heat \tag{1.2}$$

The overall reaction can be written as follows:

$$H_2\ (g) + \frac{1}{2} O_2\ (g) \rightarrow H_2O\ (l)\ +\ Electricity +\ Heat \qquad (1.3)$$

The theoretical efficiency of this reaction, considering hydrogen's higher heating value, is about 83 %, at standard temperature and pressure (25 °C and 1 atm). The corresponding potential, V_0, is close to 1.23 V, and represents the theoretical maximum voltage that can be delivered by the fuel cell at such conditions. The theoretical voltage at different temperature and pressure, $V_{T,P}$, can be obtained through the Nernst equation:

$$V_{T,P} = V_0 + \frac{RT}{nF} \ln\left(P_{H_2} P_{O_2}^{0.5}\right) \qquad (1.4)$$

where R is the universal ideal gas constant, T is the temperature, n = 2 is the number of electrons per H_2 molecule, F is the Faraday's constant, and P is the partial pressure of each specie. Equation **(1.4)** considers that the water produced is in the liquid state (therefore, P_{H_2O} = 1).

The fuel cell efficiency at low temperatures is significantly higher than that of heat engines such as the internal combustion motors, which are limited by Carnot efficiency. For example, a PEM fuel cell operated at 80 °C, and releasing heat into the environmental at 25 °C, has a maximum theoretical efficiency of about 80 %, whereas at the same conditions a heat engine presents an efficiency of around 16 %.

1.3.2. Components and materials

Fuel cell main components - functions and materials / Polymeric membrane / Catalyst layers / Gas diffusion layers / Microporous layers / Bipolar plates

A scheme of a PEM fuel cell showing its main constituents is depicted in **Figure 1.2**. The heart of a PEM fuel cell is its electrolyte, a polymeric membrane. It is often designated as proton exchange membrane or polymer electrolyte membrane, and it gives the name to this type of fuel cell. The catalyst layers (CLs), where the electrochemical reactions occur, are placed at both sides of the membrane. Next to each CL, are the gas diffusion layers (GDLs), which uniformly distribute the reactants over the CL surface. The multilayer structure that comprises these components is commonly referred as membrane electrode assembly (MEA). A microporous layer (MPL) is also usually applied between the CL and the GDL to improve water management. The MEA is sandwiched between two bipolar plates, where gas channels (GCs) are machined to provide pathways for reactants flow. They also physically connect the cathode of one cell to the anode of an adjacent unit, and vice-versa, in the case of multi-cell configuration, called stack.

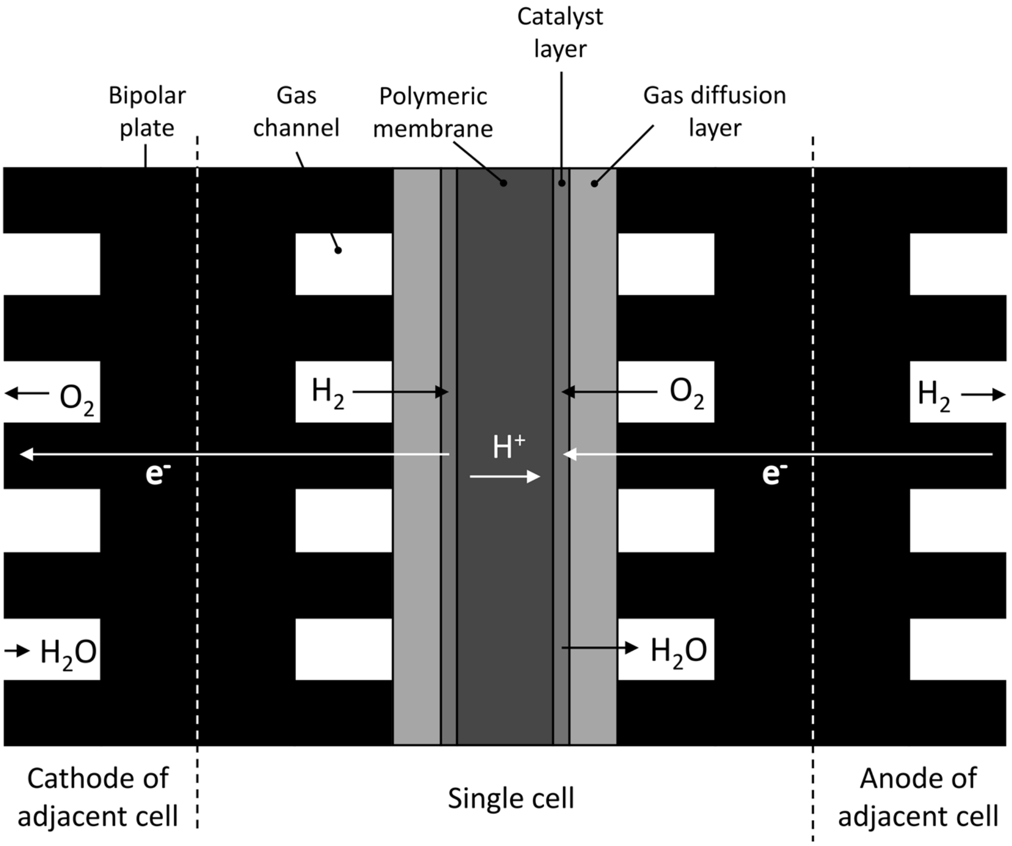

Figure 1.2. Scheme of a single PEM fuel cell within a stack and identification of its components.

1.3.2.1. Polymeric membrane

The membrane must present high proton conductivity, needs to be impermeable to gas, and must be chemically and mechanically stable in the fuel cell operating conditions. They are typically made of perfluorocarbon sulfonic acid (PFSA) ionomer. Nafion is at the present days the best known membrane material. The most recent Nafion membranes being commercialized for this type of fuel cells are the NR211 and NR212 [9], with thickness of 25.4 µm and 50.8 µm, respectively. The proton conductivity of Nafion membranes depends heavily on their water content. Such feature creates a water management issue, which is described in detail in Section **1.3.6**, that influences PEM fuel cells performance and durability. Therefore, finding better alternatives for PEM fuel cells membranes is an active field of research. Reviews addressing the main challenges and developments on PEM fuel cells electrolytes can be found in Ref. [10-13].

1.3.2.2. Catalyst layers (CLs)

The CL is a very complex structure. The electrochemical reactions occurring in this layer involve three different kinds of species (reactant gases, electrons and protons), so it has to provide pathways for all of them. Electrons travel through the catalyst and its support. The most common catalyst applied in both PEM fuel cell electrodes (anode and cathode) is platinum (Pt). Pt loading range is typically 0.3-0.6 mg cm $^{-2}$. Its particles have small size (less than 4 nm [4]) in order to maximize the surface area. Carbon powers are generally used to support the catalyst. Protons move through the ionomer. To allow the passage of reactants gases to the reaction sites, the CL is also porous. Generally, the CL is not a free-standing layer: it is either deposited into the GDL surface or directly into the polymeric membrane.

1.3.2.3. Gas diffusion layers (GDLs)

GDLs generally consist on carbon fiber-based porous materials, such as papers (**Figure 1.3** A) and cloths (**Figure 1.3** B). Typical average pore size of a GDL ranges from 20 to 100 μm. Its thickness varies from 100 to 400 μm, depending on the material used. In order to facilitate water removal, GDLs are usually subjected to a hydrophobic treatment, using agents such as polytetrafluoroethylene (PTFE or Teflon) [14-17] or fluorinated ethylene propylene (FEP) [18]. Typical PTFE loadings range from 5 % to 30 % [4]. Important functions of a GDL include: to distribute the reactant gases uniformly along the CL surface; to provide a pathway for products (water and heat) from the CLs to the GCs; to electrically and thermally connect the CLs to the bipolar plates; and to give mechanical support to the MEA [4]. Reviews dedicated to the GDLs can be found in Ref. [19-22].

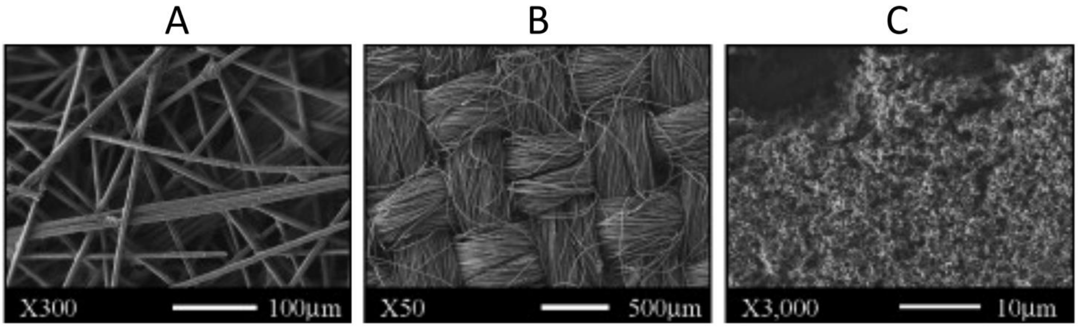

Figure 1.3. Scanning electron microscope (SEM) image of (A) carbon paper, (B) carbon cloth and (C) MPL (adapted from Ref. [23]).

1.3.2.4. Microporous layers (MPLs)

The MPL (**Figure 1.3** C) is a powdery mixture of carbon black and a hydrophobic agent, which is often applied to the side of the GDL facing the CL. As the name suggests, it has a smaller mean pore size than the GDL, typically not higher than 10 µm [19]. Its thickness is also lower, usually below 100 µm [22]. The addition of MPL is generally known to be beneficial for the cell performance, but the reasons for such improvement are still not completely understood [24, 25]. It has been shown that the MPL seems to create a capillary pressure barrier between the CL and the GDL, forcing water to move from the cathode to the anode, thus improving the overall hydration state of the membrane [14, 23, 26]. Moreover, the MPL seems to modify the liquid water arrangement inside the cell into a more favorable one for reactants transport [25, 27]. MPL is also referred to improve electrical contacts and to prevent GDL fibers intrusion into the CL [28].

1.3.2.5. Bipolar plates

The bipolar plates house the GCs for reactants distribution along the GDLs. Different flow field designs can be machined into these plates. Some of the most adopted configurations include the single or multi-serpentine designs, the parallel design and the interdigitated design (**Figure 1.4**). More on these designs, and on other alternative options, can be found in Ref. [29, 30]. In a stack, bipolar plates acquired additional and essential functions, namely to connect electrically different cells and to separate the gases between adjacent cells [4]. Bipolar plates are commonly made of graphite (or graphite composites) because of its corrosion resistance and good conductivity [29]. Due to the high cost of these plates and the challenges of their mass production, coated metallic plates have also been applied [29].

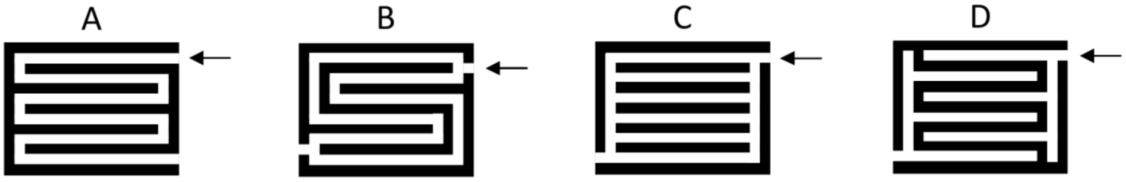

Figure 1.4. Schematic representation of (A) single-serpentine, (B) multi-serpentine, (C) parallel and (D) interdigitated flow field designs.

1.3.3. Performance evaluation and diagnostics

Polarization curve / Activation losses / Ohmic losses / Concentration losses / Electrochemical Impedance Spectroscopy / Other electrochemical and physical/chemical diagnostic tools

The standard method for evaluating the performance of a fuel cell is the polarization curve (also called I-V curve), which relates the cell voltage with the operating current density. A typical PEM fuel cell polarization curve is depicted in **Figure 1.5**. When a PEM fuel cell is supplied with its reactants and no electrical energy is drawn, the cell potential is expected to be close to the theoretical voltage for the corresponding operating conditions, given by Nernst equation (Equation **(1.4)**). However, in practice, this voltage (designated as open circuit voltage (OCV)) is significantly lower than the theoretical one, usually less than 1 V [4]. Such decrease is mainly caused by species crossover from one side of the cell to the other (mainly H_2 from the anode to the cathode) and internal electrical shortcuts. When electrical current is being extracted, the voltage drops even further due to three loss mechanisms: activation losses, ohmic losses and mass transfer losses. The terms polarization and overpotential can also be used when referring to voltage losses.

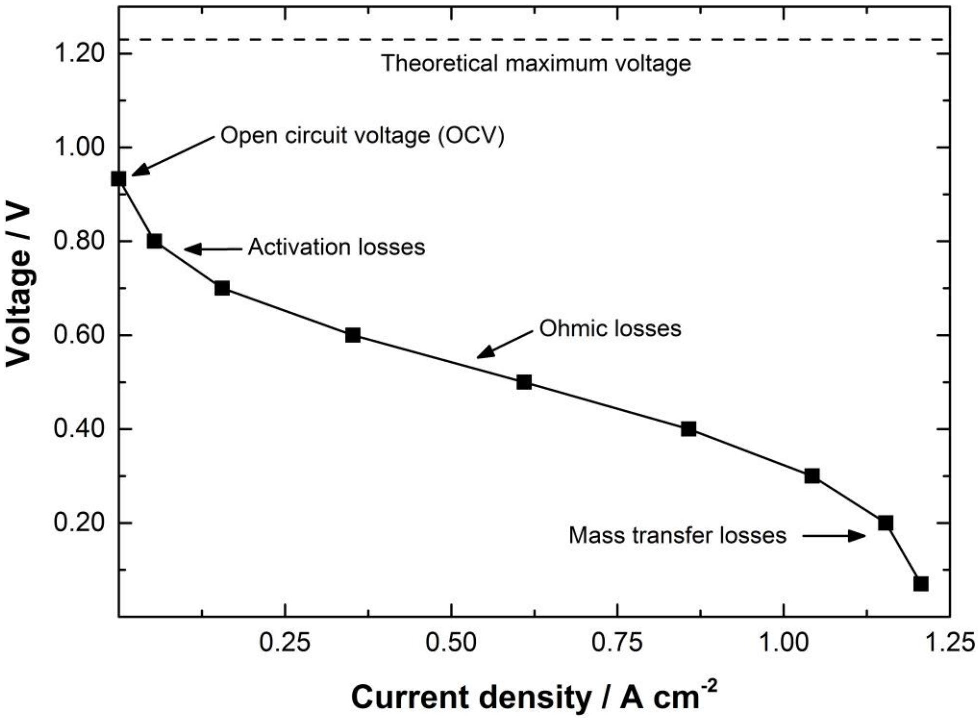

Figure 1.5. Typical PEM fuel cell polarization curve and associated voltage losses.

Activation losses are associated with the energy barrier that needs to be overcome in order to initiate the electrochemical reactions [5]. As pointed in **Figure 1.5**, this type of polarization dominates losses at low current densities and measures the catalyst effectiveness at a given temperature [5]. Activation polarization, η_{act}, is given by Butler-Volmer equation. However, in practice, it is generally approximated by the Tafel equation [4]:

$$\eta_{act} = \frac{RT}{\alpha F} \ln\left(\frac{I}{I_0}\right) \tag{1.5}$$

where α is the transfer coefficient, I is the current density and I_0 is the exchange current density. Activation overpotential is the major contributor to the cell voltage drop at any given current density, as shown in **Figure 1.6**. Although activation losses occur at both electrodes, the kinetics of the ORR in the cathode is significantly slower than that of the HOR in the anode, so the latter is often neglected.

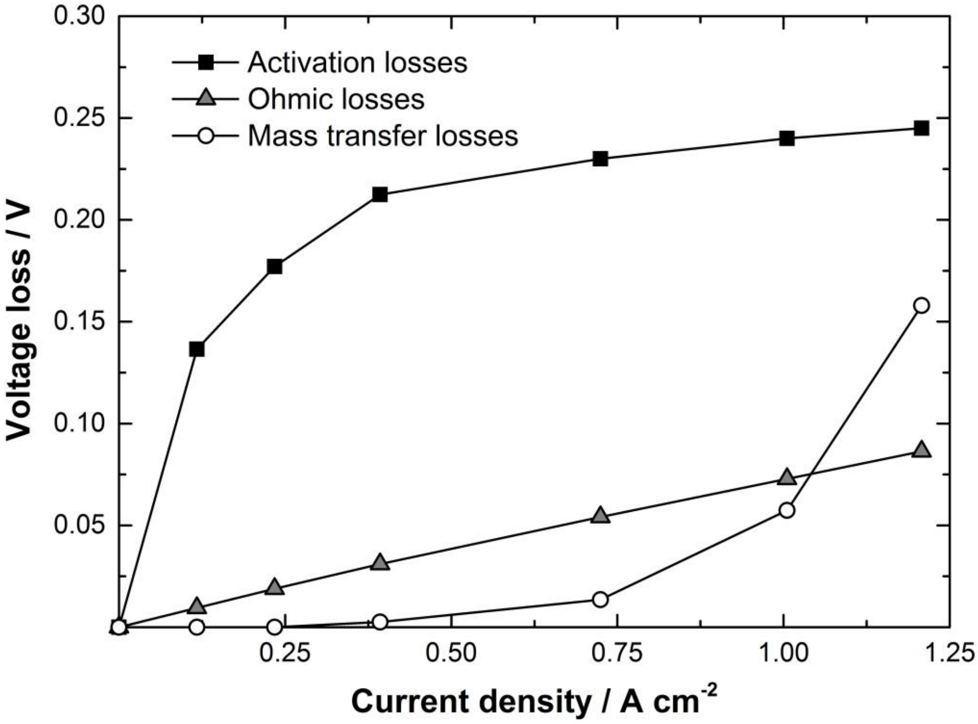

Figure 1.6. Typical profile of voltage losses in a PEM fuel cell.

Ohmic losses are caused by the resistance to the flow of charges in fuel cell components. Ohmic overpotential, η_{Ohm}, is described by Ohm's law [4]:

$$\eta_{Ohm} = IR_T \tag{1.6}$$

where R_T is the total cell resistance, which includes ionic, electronic and contact resistances. Electronic bulk resistance is generally negligible, because all the cell materials are good conductors. Therefore, ohmic polarization is mainly caused by proton transport resistance and electrical contact resistances. Ohmic losses vary linearly with current density, as seen in **Figure 1.6**, and are responsible for the linear voltage decrease at intermediate current densities, as depicted in **Figure 1.5**.

Mass transfer losses, or concentration losses, occur when the amount of reactants reaching the CL reactive sites is insufficient, thereby altering their concentration at its surface. When reactants are consumed at the same rate as they are reaching the catalyst surface, their concentration approaches zero. The current density at which this occurs is designated as limiting current density, I_L, and is given by [4]:

$$I_L = \frac{nFDC_B}{\delta} \tag{1.7}$$

where D is the effective diffusion coefficient, C_B is the reactant bulk concentration, and δ is the diffusion distance. Mass transfer losses, η_{mt}, can then be obtained by [4]:

$$\eta_{mt} = \frac{RT}{nF} ln\left(\frac{I_L}{I_L - I}\right) \tag{1.8}$$

When the limiting current density is reached, the fuel cell cannot produce more energy, mass transfer losses increase rapidly (**Figure 1.6**) and a sharp drop of the cell potential is verified (**Figure 1.5**). Because exchange current density in Equation **(1.5)** also depends on reactants concentration [4], activation losses are also affected by the reduced reactants concentration. Hydrogen is lighter and has considerably higher molecular diffusivity than oxygen, so its mass transport overpotential is, in most cases, neglected.

Although polarization curves give useful indicators of the overall performance of a PEM fuel cell, they fail to isolate the different phenomena occurring during the cell operation. For more specific information on the cell electrochemical behavior, other techniques/measurements are required. Current interruption method can be employed to measure ohmic losses [31-33]. Cyclic voltammetry (CV) is commonly used to characterize the catalyst activity by measuring the electrochemical surface area (ECSA) [34-36]. The rate of reactants gases crossover through the membrane can be obtained by linear sweep voltammetry (LSV) [37, 38]. This technique also allows to check for electrical shorts. Electrochemical Impedance Spectroscopy (EIS) in particular is a very powerful technique. During EIS, a small AC signal (voltage or current) is applied to the fuel cell, and changes on its amplitude and phase are measured at different frequencies [4]. EIS can be used to separate the contribution of each voltage loss, proving results such as those depicted in **Figure 1.6**, thus giving detailed information on the fuel cell operation. Moreover, it allows to obtain important kinetic parameters, such as α and i_0 in Equation **(1.5)**, which are essential input parameters for mathematical models. More about the EIS fundamentals and applications in PEM fuel cells research can be found in Ref. [39-42]. High frequency resistance (HFR) is a subset of the EIS method that allows to determine the cell ohmic resistance with minimal disturbance. It consists on applying a single frequency, instead of the broad range of frequencies applied in EIS, at which the cell is behaving in a purely resistive manner [43]. Typical frequencies of HFR measurements range from 1 kHz to 10 kHz [43].

Apart from the electrochemical techniques referred above, several other physical and chemical methods have been applied to get more information on PEM fuel cells operation [44]. Pressure drop is an important design parameter for the flow field of bipolar plates [29, 30, 45], and a reliable indicator of liquid water flooding [46]. Neutron imaging [47-51], magnetic resonance imaging (MRI) [52, 53], X-Ray imaging [54-56], and optical imaging through transparent fuel cells [23, 57-62] have been employed to locate liquid water inside different components of a fuel cell. Temperature distribution along the cell active area has been measured employing infrared transparent cells [63-65] and embedded sensors [66, 67]. Segmented fuel cells have also been developed in order to track the current density distribution [68, 69].

1.3.4. Operating conditions

Temperature / Pressure / Flow rate and humidity of reactants gases / Their influence on cell performance and typical values employed

PEM fuel cells most relevant operating conditions include temperature, pressure, and reactants flow rate and humidity. Their effects on the cell performance are briefly discussed below. Typical values applied are also provided.

1.3.4.1. Temperature

A PEM fuel cell can operate at freezing conditions, although not at full power. It is one of the features that makes it suitable for automobiles. The upper limit of temperature is imposed by the membrane. Because polymeric membranes such as Nafion need to be hydrated to conduct protons, their temperature needs to be below 100 °C. Typical operating temperatures of a PEM fuel cell are between 50 °C and 80 °C [4]. Increasing temperature has several benefits. The proton conductivity of the Nafion membrane increases, as well as the exchange current density. Moreover, gas transport properties are improved when temperature is increased, and liquid water flooding is reduced. However, the maximum theoretical potential decreases with temperature (Equation **(1.4)**), and activation losses increase (Equation **(1.5)**). Generally, there is an optimal operating temperature for each cell design at a specific operating condition.

1.3.4.2. Pressure

PEM fuel cells can be operated at atmospheric pressure or they can be pressurized. Increasing pressure generally improves cell performance. The theoretical voltage (Equation **(1.4)**) and exchange current density [4] are higher when the pressure is raised. However, for cells fed with air, it needs to be pressurized and that requires a compressor that adds complexity to the system and consumes energy. In such cases, the operating pressure does not go higher than 3 bar [4]. For H_2/O_2 fuel cells, operating pressure can be up to 10-12 bar [4].

1.3.4.3. Reactants flow rate

In general, higher flow rates result in better performances, in particular when reactants gases are not pure, such as when air is used in the cathode. In such situation, increasing the air flow rate facilitates liquid water removal and allows to keep the oxygen mass fraction high. However, air flow rate is controlled by a blower or a compressor whose energy consumption increases with the flow rate applied. Reactants flow rate is usually evaluated by the stoichiometry ratio (the flow rate employed divided by the reactant theoretical consumption rate). Hydrogen stoichiometry is generally from 1 to 1.2 whereas for oxygen it is usually between 1.2 and 1.5 [4]. Air stoichiometry often ranges from 2 to 2.5 [4].

1.3.4.4. Reactants humidity

The humidification level of reactant gases is generally expressed by their relative humidity (RH), which is the ratio between water vapor partial pressure and saturation pressure. The latter represents the maximum amount of water vapor that can be present in a gas for a given temperature. Because the membrane needs to have a high water content to properly conduct protons, reactants gases are often humidified. Most commonly, both are required to be saturated, *i. e.*, with RH of 100 % [4].

1.3.5. Applications

Stationary / Portable / Transportation

Due to their attractive properties, PEM fuel cells are already being commercialized and/or have been demonstrated in a large number of different applications, including stationary, portable and transportation. Examples of such applications are provided below. Some of them are shown in **Figure 1.7**.

1.3.5.1. Stationary

After providing fuel cell modules for the first 1 MW PEM fuel cell power plant installed at the SolVin plant in Belgium in 2009, Nedstack recently announced to have participated in the delivery of the world’s largest PEM fuel cell power plant to Ynnovate in China, capable of generating 2 MW of electricity. Panasonic and Tokyo Gas have been installing thousands of PEM fuel cells residential units in Japan. After staring sales in 2008, Panasonic announced to have reached a cumulative production of 50,000 units in November 2014.

1.3.5.2. Portable

Horizon and myFC currently offer solutions for charging electronic mobile devices such as smartphones and tables. Protonex commercializes PEM fuel cells portable units, especially for the military sector.

1.3.5.3. Transportation

PEM fuel cells have been demonstrated for nearly all means of transportation. Fuel cell vehicles are currently made available by Toyota, Hyundai and Honda (Toyota Mirai, Hyundai ix35 Fuel Cell and Honda Clarity Fuel Cell, respectively). In fact, almost every automobile manufacturer has already presented at least one prototype car [4]. Alstom recently presented its PEM fuel cell-powered train that is expected to start operation in Germany by the end of 2017. Ballard has also announced agreements for applying their fuel cell modules to power trams and buses to be deploy in China. PEM fuel cells systems have also been demonstrated in motorcycles (Honda Fuel Cell Motorcycle, Suzuki Burgman Fuel Cell Scooter), forklifts (HyLIFT-EUROPE project), golf cars (UKM Hydrogen Fuel Cell Car), spaceships (Project Gemini from NASA), boats (Duffy-Herreshoff DH30 watertaxi), airplanes (Boing Fuel Cell Demonstrator Airplane) and submarines (German Type 212 submarine).

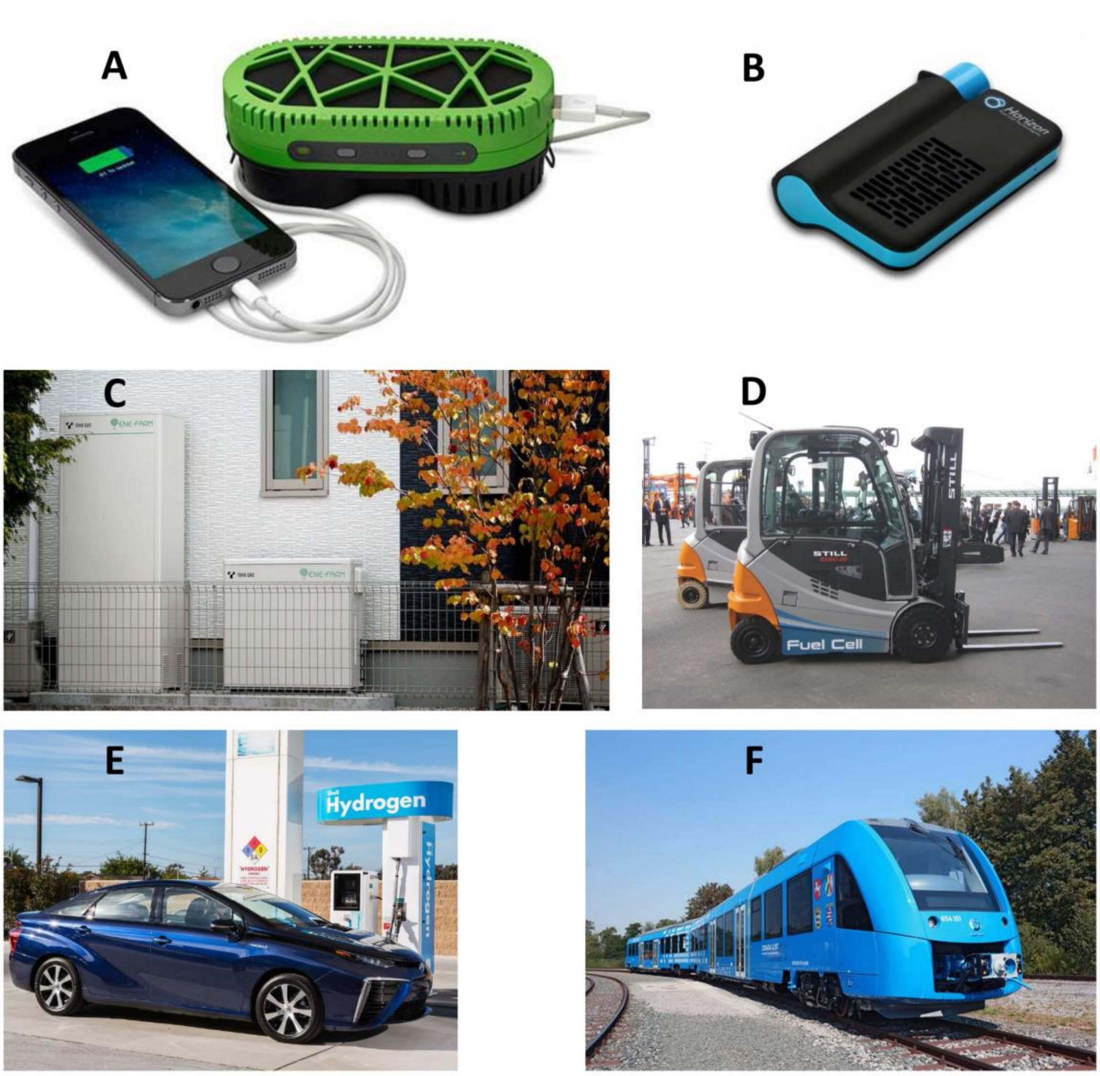

Figure 1.7. Examples of PEM fuel cells applications. A – myFC PowerTrekk [70]; B – Horizon MiniPak [71]; C – *Ene-Farm* residential fuel cell unit from Tokyo Gas [72]; D – Forklift from the HyLIFT-EUROPE project [73]; E – Toyota Mirai [74]; F – Alstom train [75].

1.3.6. Water management

Membrane drying vs. liquid water flooding / Two-phase flow and its implications

PEM fuel cells pose many important advantages, namely high efficiency and power density, zero emissions, quick startup, low size and weight, and easy scale-up. However, some drawbacks still hamper their widespread commercialization. The most critical are the high cost, especially due to the use of Pt as catalyst, and the lack of a hydrogen infrastructure. Water management is another important technical issue in the operation of these devices that influences their performance, durability and cost [76-80].

The protonic conductivity of a polymeric membrane such as Nafion strongly depends on its water content. To achieve proper humidification of the membrane, the reactant gases are generally humidified. This usually involves the use of external humidifiers that increase the system complexity and cost. To keep the membrane hydrated, along with its chemical and mechanical stability, the cell operating temperature is kept low, usually not higher than 80 ºC. This makes the appearance of liquid water unavoidable. Water floods the different components of the cell, the GCs of the bipolar plates and the pores of the GDLs and CLs, blocking the reactants passage, increasing mass transfer resistance and decreasing the cell performance. This gas-liquid two-phase flow also increases pressure drop along the GCs, creating parasitic energy losses that decrease the overall system efficiency. A delicate balance between membrane drying and liquid water flooding needs therefore to be maintained during PEM fuel cells operation, in order to guarantee high performance and durability.

1.3.7. Modeling and simulation

Importance and categorization / Brief historical overview / Two-phase flow modeling approaches / The VOF method and major challenges

Modeling and simulation play a significant role in PEM fuel cells design and development. Mathematical models help to further down-select designs to fabricate and test, reducing optimization time and costs [5]. Moreover, they can be used for diagnostic purposes, identifying faults and their causes, as well as defining and improving suited control strategies [81]. Models can be categorized according to different key features, such as: the approach (analytical, empirical/semi-empirical, or mechanistic); the state (steady or transient); the system boundary (single cell component, complete fuel cell, or entire stacks with auxiliary equipment); and the spatial dimension (zero-dimensional (0D), 1D, 2D and 3D). More about models characterization can be found in Ref. [82-84]. Recent reviews addressing the main progresses and current challenges of PEM fuel cells modeling and simulation are available elsewhere [81, 85-88]. Here, a brief historical overview on PEM fuel cells modeling is presented, with focus on the incorporation of two-phase flow phenomenon, the topic addressed in this thesis.

PEM fuel cells modeling can be traced back to the early nineties when pioneers 1D studies where published by Springer *et al.* [89] and Bernardi and Verbrugge [90, 91]. The modeling strategy to account for water transport in the membrane presented by Springer *et al.* [89], together with related empirical equations based on measurements made with Nafion 117, became popular and remains the classical approach to compute the membrane water balance. Gurau *et al.* [92] were the first to consider a 2D domain for all the main components of a fuel cell. Um *et al.* [93] reported the first model based on computational fluid dynamics (CFD). The above-mentioned works introduced fundamental understanding on the transport phenomena in PEM fuel cells and laid the foundation for modeling these devices. However, they generally assumed that water only exists as vapor. Since 2000, attempts to incorporate liquid water transport began to be reported, employing mostly two different two-phase flow approaches: the multiphase mixture (M^2) [94-97] and the multi-fluid (or two-fluid) [98-102] models. The theory applied in such studies to account for liquid water transport in the porous media of a PEM fuel cell was clarified and systematized in the works of Nam and Kaviany [103] and Pasaogullari and Wang [104]. In this theory, gas pressure is assumed to be uniform and gravity effect is neglected, resulting in liquid water transport driven by capillary pressure which is described by Darcy’s law. This approach became popular and has been largely used [105-114]. It was also implemented in a 1D model developed during the execution of the present work [115]. Moreover, it is adopted in the widely used Fuel Cell and Electrolysis add-on module [116] available with the commercial CFD package ANSYS Fluent.

In the M^2 and multi-fluid schemes, the inclusion of capillary flow allows to reasonably predict liquid water distribution inside the porous media, as liquid water saturation, and to compute its effects on the cell performance. However, such models have several limitations. Because the GDL is an inherently heterogeneous structure, liquid water is not uniformly distributed and preferential flow paths are formed. As macroscopic continuum models, the porous media microstructure cannot be properly incorporated in the M^2 and multi-fluid approaches, so this phenomenon cannot be captured. For these reasons, pore-scale models, mainly Lattice Boltzmann (LB) [117-121] and pore-network (PN) [122-129] approaches, have been applied in order to better describe and understand liquid water transport in the porous media. Another limitation of models that apply the M^2 or multi-fluid approaches is that, in the GCs, liquid water velocity is assumed to be equal to the gas velocity (fine mist). Such assumption makes it impossible to identify the presence of water droplets and films that accumulate in the GCs. Therefore, the two-phase flow in the GCs cannot be properly described. To better address this, interface tracking algorithms are essential. In this respect, the volume of fluid (VOF) method has become largely popular. This technique is able to simulate immiscible fluids by solving a single set of momentum equations and to track the volume fraction of each fluid throughout the domain. Moreover, it is capable of considering surface tension and wall adhesion effects.

A detailed review on numerical simulations employing the VOF method to simulate the two-phase flow in PEM fuel cells was published under the executing of the present work [130], and an up-to-date version of it is included in Chapter **2**. From such review it was found that one of the major challenges of applying the VOF method is to couple this technique with the electrochemical reactions that occur in a PEM fuel cell, due to the different length and time scales between those phenomena. Although some important advancements have been reported in this area [131-133], there are still relevant aspects that need to be properly addressed. Those include: to adequately correlate liquid water generation rate in the VOF method with the electrical current being produced by the cell; to validate the cell electrochemical performance predicted by VOF-based models against experimental I-V curves; and to include water transport in the membrane, so the effects of strategies dealing with two-phase flow issues on the membrane hydration can be accounted for. Moreover, because the VOF method is a very computational intensive numerical tool, efforts should be made to develop models that, at the same time, consider computational domains large enough to be representative of a real PEM fuel cell and have reasonable simulation times.

1.4. Objectives

1D + 3D model development / Experimental validation / Numerical simulations

The goal of the present work is to move one step forward on PEM fuel cells modeling and simulation, more specifically on coupling the VOF method to track the two-phase flow with the electrochemical reactions occurring in the cell. A numerical model is presented that simulates the air-water flow in the cathode side together with the electrical current being produced and the water transport in the membrane. Moreover, a hybrid 1D + 3D computational domain is implemented that allows to capture the relevant physical details of a complete fuel cell with acceptable simulation times.

A PEM fuel cell test station is developed, and the electrochemical performance calculated by the model is validated against an experimental polarization curve. Furthermore, a transparent fuel cell is employed to visualize liquid water distribution inside the cathode GCs, in order to validate the model two-phase flow predictions.

Numerical simulations are then conducted with the aim of gather a better understanding on the two-phase flow and its implications. The effects of operating conditions, GCs walls wettability and flow field design are investigated.

1.5. Thesis structure

This thesis has six main chapters. The subjects addressed in each chapter are summarized below.

Chapter **1** contains an introduction to the present work. The main issues of the current energy supply system and the reasons why fuel cells, in particular PEM fuel cells, can be an alternative for power generation are initially presented. A brief overview of PEM fuel cells is then provided, addressing their operating principle, components and materials, performance evaluation and diagnostics, operating conditions and applications. The water management issue is also described, and the main challenges of two-phase flow modeling and simulation are identified. Finally, the objectives and structure of the present thesis are presented.

Chapter **2** encloses a literature review related with numerical simulations of the two-phase flow in PEM fuel cells employing the VOF method.

In Chapter **3**, the test station and the fuel cells used are described, along with the experimental procedures adopted.

Chapter **4** presents the experimental results obtained, namely on the effects of MEA design and on liquid water distribution inside a transparent fuel cell.

In Chapter **5**, the 1D + 3D model is described and experimentally validated. Moreover, its main outputs are analyzed.

Chapter **6** shows the results of numerical simulations employing the model presented and validated in Chapter **5**, with focus on the two-phase flow phenomenon in the cathode GCs. The effects of the walls wettability, operating conditions, and flow field design are investigated.

The major conclusions drawn from the present research are included in Chapter **7**. Moreover, recommendations for future works are presented.

2. REVIEW ON NUMERICAL STUDIES EMPLOYING THE VOF METHOD

In the present chapter, the numerical studies on PEM fuel cells two-phase flow applying the VOF approach are reviewed. A first version of this review was already published [130], covering the papers published until the end of 2014. Here, such reviewed is updated by including the research articles reported in the last two years, 2015 and 2016. A short presentation of the VOF method is first provided, addressing its history, typical applications and general mathematical formulation. Then, the literature review itself is conducted, where the focus, the numerical details and the main results of each research work are discussed. Finally, the main conclusions are drawn and the major challenges are identified.

2.1. The VOF method

2.1.1. History and applications

The historical development of the VOF formulation can be presented considering the numerical methods for capturing the interface between fluids. The VOF method is based on earlier Marker-And-Cell (MAC) methods [134]. First reports of what is now referred as the VOF method were given by Noh and Woodward [135], who presented the simple line interface calculation (SLIC) algorithm. However, the first publication of the VOF method in a scientific journal was made by Hirt and Nichols [136], and to whom the authorship of the method is often given. In these two early approaches, the interface was represented by a piecewise-constant line in each two-fluid cell, either vertically or horizontally [137]. However, the first implementations of the VOF method using this methodology showed some imperfections in the interface description. This was overcome by Youngs [138] who introduced the piecewise-linear interface calculation (PLIC) scheme. The method of Youngs [138] was shown to be very robust and efficient, and the use of the VOF method with PLIC scheme is currently widely applied.

Early applications of the VOF method include those from Torrey *et al.* [139, 140], who performed simulations for NASA. Nowadays, typical applications of the VOF method include the prediction of a jet breakup, the motion of bubbles in a liquid, the movement of a liquid after a dam break, and the steady or transient tracking of any liquid-gas interface [141].

2.1.2. Mathematical formulation

In this section, the general mathematical formulation of the VOF method is presented. Most of the information here provided is taken from the ANSYS Fluent theory guide [141].

The VOF formulation assumes that two or more phases (fluids) are not interpenetrating. For each additional phase that is added, a variable is introduced: the volume fraction of that phase in the computational domain. In each control volume, the sum of the volume fractions of all phases is equal to one. The fields for all the variables and properties are shared by the phases and represent volume-averaged values, as long as the volume fraction of each phase is known at each location. Thus, the variables and properties in any given cell are either purely representative of one of the phases, or representative of a mixture of the phases, depending upon the volume fraction values. This means that, if the volume fraction of the fluid q in the cell is f_q, the three following situations are possible:

- $f_q = 0$, the cell is empty of the fluid q;
- $f_q = 1$, the cell is full with the fluid q;
- $0 < f_q < 1$, the cell contains the fluid q and one or more other fluids.

Based on the local value of f_q, the properties and variables are assigned to each control volume within the domain.

In order to track the interface(s) between the phases, a continuity equation for the volume fraction of one (or more) of the phases is solved. For the phase q, the continuity equation is given by:

$$\frac{1}{\rho_q}\left[\frac{\partial}{\partial t}\left(f_q\rho_q\right) + \nabla\cdot\left(f_q\rho_q\vec{v}_q\right) = S_{f_q} + \sum_{p=1}^{n}\left(\dot{m}_{pq} - \dot{m}_{qp}\right)\right] \tag{2.1}$$

where ρ_q is the density of the phase q, $\vec{v}_q$ is the velocity of the phase q, S_{f_q} is the mass source term for phase q, $\dot{m}_{pq}$is the mass transferred from phase p to phase q, and $\dot{m}_{qp}$ is the mass transferred from phase q to phase p.

The properties present in the transport equations are determined by the presence of the component phases in each control volume. For example, for an n-phase system, the volume-fraction-averaged density is given by:

$$\rho = \sum_{q=1}^{n} f_q \rho_q \tag{2.2}$$

All other properties (*e.g.*, viscosity (μ)) are calculated in the same way. In the specific case of a two-phase system (case of PEM fuel cells), for example, if the phases are represented by the subscripts i and j, and if the volume fraction of the phase j is being tracked, the density and viscosity in each cell are calculated by:

$$\rho = f_j \rho_j + \left(1 - f_j\right) \rho_i \tag{2.3}$$

$$\mu = f_j \mu_j + \left(1 - f_j\right) \mu_i \tag{2.4}$$

A single momentum equation is solved throughout the domain, and the resulting velocity field is shared among the phases. The momentum equation is dependent on the volume fractions of all phases through the properties ρ and μ:

$$\frac{\partial}{\partial t}(\rho \vec{v}) + \nabla \cdot (\rho \vec{v} \vec{v}) = -\nabla P + \nabla \cdot [\mu(\nabla \vec{v} + \nabla \vec{v}^T)] + \rho \vec{g} + \vec{F} \tag{2.5}$$

where $\vec{g}$ corresponds to the gravitational acceleration and $\vec{F}$ is a source term which accounts for surface tension effects. The calculation of the term $\vec{F}$ is explained further ahead in this section.

The energy equation, which is also shared among the phases, is given by:

$$\frac{\partial}{\partial t}(\rho E) + \nabla \cdot \left(\vec{v}(\rho E + P)\right) = \nabla \cdot \left(k_{eff} \nabla T\right) + S_h \tag{2.6}$$

where the energy, E, and temperature, T, are treated as mass-averaged variables:

$$E = \frac{\sum_{q=1}^{n} f_q \rho_q E_q}{\sum_{q=1}^{n} f_q \rho_q} \tag{2.7}$$

where E_q for each phase is based on the specific heat of that phase and the shared temperature. The properties ρ and k_{eff} (effective thermal conductivity) are shared by the phases. The source term in Equation **(2.6)**, S_h, contains contributions from radiation as well as any other volumetric heat sources.

A key feature of the VOF method is the ability to capture the effects of surface tension, which is an important and sometimes the dominant force in microflows. Two main surface tension models are used in the VOF method: the continuum surface force (CSF) model and the continuum surface stress (CSS) model.

The CSF model, proposed by Brackbill *et al.* [142], includes the surface tension effects in the VOF calculation by adding a source term in the momentum equation (term $\vec{F}$ in Equation **(2.5)**). Surface tension can be written in terms of pressure jump across the surface. The force at the surface can be expressed as a volume force using the divergence theorem, and it is given by:

$$\vec{F}(CSF) = \sum_{pairs\, ij, i<j} \tau_{ij} \frac{f_i \rho_i \kappa_j \nabla f_j + f_j \rho_j \kappa_i \nabla f_i}{\frac{1}{2}(\rho_i + \rho_j)} \tag{2.8}$$

where τ_{ij} stands for the surface tension between phases i and j, and κ is the curvature define in terms of divergence of unit normal, $\hat{n}$:

$$\kappa = \nabla \cdot \hat{n} \tag{2.9}$$

where

$$\hat{n} = \frac{n}{|n|} \tag{2.10}$$

and n corresponds to the surface normal, defined as the gradient of the volume fraction of the phase q:

$$n = \nabla f_q \tag{2.11}$$

Equation **(2.8)** allows for a smooth superposition of forces near cells where more than two-phases are present. If only two phases are present in a cell, then $\kappa_i = -\kappa_j$ and $\nabla f_i = -\nabla f_j$, and Equation **(2.8)** takes the following form:

$$\vec{F}(CSF) = \tau_{ij} \frac{\rho \kappa_i \nabla f_i}{\frac{1}{2}\left(\rho_i + \rho_j\right)} \tag{2.12}$$

The CSS method models surface tension in a conservative manner, contrarily to the non-conservative formulation of the CSF model. CSS avoids the explicit calculation of curvature, and could be represented as an anisotropic variant of modeling capillary forces based on surface stresses. In this scheme, the surface tension force is represented as:

$$F(CSS) = \nabla \cdot \left[\tau \left(|\nabla f| U - \frac{\nabla f \otimes \nabla f}{|\nabla f|}\right)\right] \tag{2.13}$$

where U is the unit tensor and $\otimes$ is the tensor product of two vectors (the original normal and the transformed normal).

The CSS method has few added advantages over the CSF method, especially for cases involving variable solution surface tension. For variable surface tension, the CSF model requires modeling an additional term in the tangential direction to the interface based on the surface tension gradient whereas the CSS model does not require any additional term due to its conservative formulation. Moreover, the CSS method does not require any explicit calculation for the curvature. Therefore, it performs physically in under-resolved regions, such as sharp corners.

Wall adhesion effects are also taken into account in the VOF method. This is accomplished by using the contact angle that the fluid is assumed to make with the wall to adjust the surface normal in cells near the wall. This so-called dynamic boundary condition results in the adjustment of the curvature of the surface near the wall. Considering θ_{wall} as the contact angle at the wall, then the surface normal at the cell next to the wall can be obtained by:

$$\hat{n} = \hat{n}_{wall} \cos \theta_{wall} + \hat{t}_{wall} \sin \theta_{wall} \tag{2.14}$$

where $\hat{n}_{wall}$ and $\hat{t}_{wall}$ are the unit vectors normal and tangential to the wall, respectively.

2.2. Literature review

Table 2.1 presents the numerical studies in which the VOF method was employed to investigate the two-phase flow in PEM fuel cells, sorted by publication date. It summarizes the main focus and the numerical details (computational domain, software, surface tension model and spatial dimension) of each research work. Each study is discussed in detail below in this section.

Table 2.1. Numerical studies on two-phase flow in PEM fuel cells using the VOF method.

Reference and published year	**Research objective**	**Numerical simulation details**			
		Computational domain	**Software**	**Surface tension model**	**Dimension**
Quan *et al.* [143] (2005)	Investigate the two-phase flow along part of a serpentine GC	40 mm long U-shaped GC with round corner and cross-section of 1 mm × 1 mm	Fluent	CSF	3D
Golpaygan and Ashgriz [144] (2005)	Investigate the deformation and detachment of a water droplet adhering to the GDL surface	Fraction of a GC	-	CSS	2D
Cai *et al.* [145] (2006)	Study the effects of the GC walls wettability on liquid water removal	20 mm long straight GC with rectangular cross-section of 1 mm × 1 mm	Fluent	CSF	3D
Jiao *et al.* [146] (2006)	Investigate the two-phase flow in a PEM fuel cell stack with parallel serpentine GCs	Three 10 mm long parallel serpentine GCs with round corners and cross-sections of 1 mm × 1 mm, connected by 12 mm long manifolds with cross-sections of 2 mm × 2 mm	Fluent	CSF	3D
Jiao *et al.* [147] (2006)	Investigate the two-phase flow in a PEM fuel cell stack with straight parallel GCs	Five 10 mm long straight parallel GCs with cross-sections of 1 mm × 1 mm, connected by 20 mm long manifolds with cross-sections of 5 mm × 5 mm	Fluent	CSF	3D
Theodorakakos *et al.* [148] (2006)	Study the detachment of liquid water droplets from the GDL surface	Small fraction of a GC with a water inlet pore with diameter of 0.05 mm, 0.100 mm or 0.50 mm	GFS	CSF	3D
Zhan *et al.* [149] (2006)	Study the motion of liquid water in straight and serpentine GCs considering the hydrophilicity of the graphite plate and the hydrophobicity of the GDL	11.5 mm long straight GC with cross-section of 1 mm × 1 mm; 23 mm long U-shaped GC with round corner and cross-section of 1 mm × 1 mm	Fluent	CSF	3D

Jiao and Zhou [150] (2007)	Test the effectiveness of three proposed innovative GDLs in solving liquid water flooding	30 mm long U-shaped GC with round corner and cross-section of 1 mm × 1 mm. The proposed GDLs consisted of: 0.1 mm × 0.1 mm × 0.1 mm cubic holes; and trapeziform holes with 0.1 mm height and minimum area of 0.1 mm × 0.1 mm facing the GCs or the CL	Fluent	CSF	3D
Quan and Lai [151] (2007)	Study the effects of GCs walls surface hydrophilicity, GCs geometry, and air inlet velocity on the two-phase flow	23 mm long U-shaped GC with round or rectangular corners and cross section of 1 mm × 0.5 mm, attached to a uniform GDL of 0.2 mm thickness	Fluent	CSF	3D
Zhu *et al.* [152] (2007)	Analyze the effects of the static contact angle, pore size, and air and water inlet velocities on liquid water dynamics	1 mm × 0.25 mm straight GC with a pore of diameter of 0.05 mm on the bottom surface	Fluent	CSF	2D
Zhu *et al.* [153] (2007)	Investigate the effects of GCs and pore sizes and coalescence of droplets on liquid water dynamics	1.00 mm × 0.25 mm straight GC with a pore of diameter of 0.05 mm on the bottom surface	Fluent	CSF	2D
Jiao and Zhou [154] (2008)	Study how liquid water flows through the GDL into the GC	30 mm long U-shaped GC with round corner and cross-section of 0.9 mm × 1.0 mm, attached to a 0.1 mm thick GDL represented by small paths of cross-section of 0.2 mm × 0.2 mm, and a uniform 0.1 mm thick CL	Fluent	CSF	3D
Bazylak *et al.* [155] (2008)	Better understand the changing of the preferential water breakthrough locations from the GDL over time	0.025 mm × 0.1 mm channel linked to a 0.050 mm× 0.1 mm channel by a 0.050 mm× 0.1 mm horizontal channel, both connected to a 0.375 m × 0.1 mm GC	Fluent	CSF	2D
Fang *et al.* [156] (2008)	Study the contact angle hysteresis effects on the two-phase flow	Rectangular parallelepiped cavity of 10 mm × 10 mm × 10 mm (for studying the droplet flow); and a 5 mm long straight GC with cross-section of 0.5 mm × 45 mm (for studying the slug flow)	-	CSF	3D

Golpaygan and Ashgriz [157] (2008)	Investigate the deformation and detachment of a water droplet adhering to the GDL surface	Fraction of a GC	-	CSS	2D
Jiao and Zhou [158] (2008)	Study the effects of the wettability of the best innovative GDL proposed in Ref. [150]	30 mm long U-shaped GC with round corner and cross-section of 1 mm × 1 mm, and a GDL having trapeziform holes with 0.1 mm height and the 0.1 mm × 0.1 mm minimum area facing the GCs	Fluent	CSF	3D
Le and Zhou [133] (2008)	Study the behavior of liquid water in the GCs and its effects on PEM fuel cell performance	Unit PEM fuel cell (membrane, CLs, GDLs, GCs and current collectors) with a single-serpentine GC	Fluent	CSF	3D
Shirani and Masoomi [159] (2008)	Investigate the effects of surrounding fluid properties (velocity, density and viscosity) on a droplet behavior	Fraction of a GC	-	CSS	2D
Zhu *et al.* [160] (2008)	Study the dynamic behavior of an emerging water droplet as a function of operating and material parameters	0.1 mm long straight GC with rectangular cross-section of 0.25 mm × 0.25 mm having a pore of diameter of 0.05 m on the bottom surface	Fluent	CSF	3D
Le and Zhou [161] (2009)	Study the behavior of liquid water in the GCs and its effects on PEM fuel cell performance	Unit PEM fuel cell (membrane, CLs, GDLs, GCs and current collectors) with multi-serpentine GCs	Fluent	CSF	3D
Le and Zhou [162] (2009)	Study the behavior of liquid water in the GCs and its effects on PEM fuel cell performance	Unit PEM fuel cell (membrane, CLs, GDLs, GCs and current collectors) with interdigitated GCs	Fluent	CSF	3D
Le and Zhou [163] (2010)	Investigate how single-cell flooding affects the stack performance	Three-cells PEM fuel cell stack with a single-serpentine GC	Fluent	CSF	3D

Ding *et al.* [164] (2010)	Investigate the influence of the GDL surface microstructure	1.2 mm long straight GC with rectangular cross-section of 0.25 mm × 0.25 mm having a uniform inlet, 1-pore inlet, 4-pore inlet, 16-pore inlet, or 64-pore inlet as the GDL microstructure, all with the same open area and liquid flow rate	Fluent	CSF	3D
Quan and Lai [165] (2010)	Study the effects of surface wettability and operating pressure drop in the transport of liquid water in interdigitated GC	12 mm long portion of two GCs from a interdigitated configuration with cross section of 0.5 mm × 0.5 mm, attached to a 0.2 mm thick uniform GDL	Fluent	CSF	3D
Du *et al.* [166] (2010)	Analyze the effects of water introduction configurations, walls wettability and air flow rate on the two-phase flow characteristics	300 mm × 1.6 mm straight GC	Fluent	CSF	2D
He *et al.* [167] (2010)	Study the effects of the GC walls roughness on the water behavior	1.05 mm × 1 mm straight GC. The roughness of the bottom wall was represented by rectangles ribs with height from 0 to 0.05 mm and width from 0.0025 to 0.1 mm. The distance between two adjacent rectangles center was varied from 0.05 to 20 mm	Fluent	CSF	2D
Suresh and Jayanti [168]	Investigated the effects of the air cross-flow on liquid water transport through the GDL	0.196 mm × 0.03 mm straight GC section connected to a 0.096 mm thick GDL assumed as a layered structure with perfect circular fibers of diameter 0.008 mm	Fluent	CSF	2D
Park *et al.* [169] (2010)	Investigate liquid water behavior in the GDL	Cubical numerical domain with length of 0.15 mm plus a 0.15 mm long buffer zone for gas flow. The GDL was reconstructed using impermeable cylinders with diameter of 0.02-0.05 mm	Fluent	CSF	2D

Le *et al.* [170] (2010)	Qualitative and quantitative validate the VOF method	180 mm long serpentine GC with rectangular corners and cross section of 1.7 mm × 2 mm	Fluent	CSF	3D
Kim *et al.* [171] (2010)	Study the effects of GCs geometry and surface properties on liquid water exhaust capability	U-shaped GC with round or rectangular corners, having a cross section width varying from 1 to 2 mm and height fixed to 1 mm	Fluent	CSF	3D
Zhu *et al.* [172] (2010)	Investigate the effects of GC cross-section geometry on the dynamic behavior of an emerging water droplet	1 mm long straight GC having a pore of diameter of 0.05 mm on the bottom surface. Ten different cross-section geometries were tested: rectangles of aspect ratio (height (H)/width (W)) of 0.1, 0.25, 0.5, 1 and 2; rectangles of H/W = 1 with a curved bottom wall; trapezoid of H/W = 1; upside down trapezoid of H/W = 1; triangle of H/W = 1; and semicircle of H/W = 1	Fluent	CSF	3D
Ding *et al.* [173] (2011)	Investigate the two-phase flow patterns	100 mm long straight GC with rectangular cross-section of 1 mm × 1 mm having 320 pores of diameter of 0.4 mm on the bottom surface (2 pores along the GC width direction)	Fluent	CSF	3D
Kang *et al.* [174] (2011)	Analyze liquid water transport in a PEM fuel cell cathode with interdigitated GCs	4 inlet and 3 outlet parallel GCs (cross section of 1.7 mm × 2 mm with 1 mm distance between adjacent GCs) attached to a 0.3 mm GDL with 2.4 mm × 2.4 mm area	Fluent	CSF	3D
Wang and Zhou [175] (2011)	Analyze liquid water transport in a PEM fuel cell cathode with straight parallel GCs	7 parallel GCs (cross section of 1.7 mm × 2 mm with 1 mm distance between adjacent GCs) attached to a 0.3 mm GDL 2.4 mm × 2.4 mm area	Fluent	CSF	3D
Mondal *et al.* [176] (2011)	Investigate the effects of the GDL hydrophilicity level and air velocities on the two-phase flow	8 mm long straight GC with cross-section of 1 mm × 1 mm	Fluent	CSF	3D

Raman *et al.* [177] (2011)	Investigate the effects of the GDL hydrophobicity level and air velocities on the two-phase flow	8 mm long straight GC with cross-section of 1 mm × 1 mm	Fluent	CSF	3D
Golpaygan *et al.* [178] (2011)	Investigate the deformation and detachment of a water droplet adhering to the GDL surface	Fraction of a GC	-	CSF	3D
Zhu *et al.* [179] (2011)	Investigated the effects of pore location on the water droplet dynamics	1 mm long straight GC with rectangular cross-section of 0.25 mm × 0.25 mm having a pore of diameter of 0.05 mm on the bottom surface. Three pore distances from the side walls were employed: 0, 1/4 and 1/2 of the pore width.	Fluent	CSF	3D
Cai *et al.* [180] (2012)	Investigate the two-phase flow along part of a serpentine GC	4 mm long U-shaped GC with round or rectangular corners and cross section of 1 mm × 1.0 mm, having 5 pores of diameter of 0.2 mm on the bottom surface	Fluent	CSF	3D
Carton *et al.* [181] (2012)	Investigate the coalescence of droplets and movement of slugs	Two 20 mm long U-shaped GCs with a round corner and rectangular cross-section of 1 mm × 1 mm	Fluent	-	3D
Chen *et al.* [132] (2012)	Investigate the effects of liquid water distribution on pressure drop, reactant transport and current density	2.4 mm long straight GC with cross-section of 0.34 mm × 0.28 mm, connected to a 0.2 mm thick two-layer GDL composed by a homogeneous first layer and a second layer with solid cubes (cross section of 0.04 mm × 0.04 mm and height of 0.02 mm) dispersed in void spaces for representing the GDL microstructure. Water was injected by a larger pore with cross-section of 0.06 mm × 0.06 mm	Fluent	CSF	3D

Chen *et al.* [182] (2012)	Study the effects of GDL roughness on liquid water transport	1 mm long straight GC with cross section of 0.3 mm × 0.3 mm having one square pore (0.06 mm width) for water injection on the GDL surface. The roughness of GDL surface was represented by an array of square holes (0.04 mm depth and 0.02 mm width) distributed on the GDL surface. Different roughness were considered by varying the gap between the holes	Fluent	CSF	3D
Cho *et al.* [183] (2012)	Validate analytical solutions for water droplet deformation and detachment from the GDL surface	40.0 mm long straight GC with cross-section of 1.0 mm × 1.6 mm	Fluent	CSF	2D and 3D
Qin *et al.* [184] (2012)	Explore the competition between film and droplet flows	1 mm straight GC with cross section of 0.20 mm × 0.45 mm. Water was injected through 3 cylindrical pipes (diameters of 0.04 or 0.05 mm), and the CL was simplified as a water reservoir which provided water for the pipes	Fluent	CSF	3D
Ahmad *et al.* [185] (2013)	Study the effects of GDL PTFE loading on capillary pressure and droplet detachment velocity	0.400 mm × 0.304 mm straight GC connected to a 0.096 mm GDL assumed as a layered structure with perfect circular fibers of diameter 0.008 mm	Fluent	CSF	2D
Chen *et al.* [186] (2013)	Investigate the effects of the GDL surface microstructures on the dynamic behavior of a water droplet	1.2 mm long straight GC with cross-section of 0.34 mm × 0.30 µm. The carbon fibers of the GDL were represented by rectangles with square cross-section and three different distributions of theses rectangles were considered to represent GDL microstructures: crisscross distribution (rectangles evenly crisscross generating uniformly distributed square cavities); parallel distribution (rectangles only distributed parallel to the flow direction); and orthogonal distribution (rectangles aligned perpendicular to the flow direction)	Fluent	CSF	3D

Ding *et al.* [187] (2013)	Investigate two-phase flow distribution in inter-connected parallel GCs	Two parallel GCs, each 100 mm long with cross-section of 1 mm × 1 mm, connected by several (from 1 to 20) communication channels (with depth and length of 1 mm and widths from 0.25 to 2 mm). Water was injected from two pores at the entrance of each branch on the GDL surface (bottom surface)	Fluent	CSF	3D
Ding *et al.* [188] (2013)	Investigate the effects of two-phase flow patterns on PEM fuel cell performance	100 mm long straight GC with rectangular cross-section of 1 mm × 1 mm, having equally spaced 20 pores of diameter of 0.25 mm on the GDL surface	Fluent	CSF	3D
Ding *et al.* [189] (2013)	Investigate the effects of two-phase flow maldistribution on PEM fuel cell performance	Two parallel GCs, each 50 mm long with cross-section 1.0 mm × 1.0 mm, having equally spaced 20 pores of diameter of 0.25 mm on the GDL surface	Fluent	CSF	3D
Fontana *et al.* [190] (2013)	Study the two-phase flow inside a tapered GC	50 mm long tapered GC with 1 mm height at air inlet, inclination of 0.75°, and approximately 100 pores with diameter of 0.05 mm for water injection	Fluent	CSF	2D
Mancusi *et al.* [191] (2013)	Study the two-phase flow inside a tapered GC	Last 10 mm of a 50 mm long tapered GC with 1 mm height at air inlet, inclination of 0° to 0.75°, and 20 pores with diameter of 0.05 mm for water injection	Fluent	CSF	2D
Hossain *et al.* [192] (2013)	Find an optimum water pore arrangement that would provide minimum water coverage on the GDL surface	1 mm long straight GC with rectangular cross-section of 0.25 mm × 0.25 mm. The water inlet pores diameters tested were 0.05 mm and 0.02 mm, and the distance among the pores employed was: 0.20 mm, 0.15 mm, 0.10 mm or 0.75 mm	Fluent	CSF	3D
Kim *et al.* [193] (2013)	Investigate the inter-droplet interactions	4 mm long straight GC with cross-section of 1 mm × 0.25 mm, having two rectangular pores (cross-section of 0.05 mm × 0.05 mm) for water injection	Fluent	CSF	3D

Qin *et al.* [194] (2013)	Test the effectiveness of a novel GC with a hydrophilic needle in the middle of the GC and to investigate the effects of the needle dimensions	50 mm long straight GC with cross-section of 1 mm × 1 mm, having a small cylindrical needle placed in the middle of the GC with diameter varied from 0.01 mm to 0.1 mm and length from 0.40 mm to 1 mm	Fluent	CSF	3D
Qin *et al.* [195] (2013)	Investigate the effects of the GDL surface and the inserted needle wettability on the novel GC proposed in [194]	50 mm long straight GC with cross-section of 1 mm × 1 mm, having a small cylindrical needle placed in the middle of the GC with diameter of 0.1 mm and length of 0.7 mm	Fluent	CSF	3D
Qin *et al.* [196] (2014)	Test the effectiveness of a novel GC with a hydrophilic plate in the middle of the GC and to investigate the effects of the plate dimensions and wettability	50 mm long straight GC with cross-section of 1 mm × 1 mm, having a hydrophilic plate placed in the middle of the GC with height varied from 0.6 mm to 0.8 mm and length from 0.5 mm to 2 mm	Fluent	CSF	3D
Bao *et al.* [197] (2014)	Study the influence of the GDL deformation on liquid water transport	10 mm long straight GC with cross-section of 1 mm × 0.5 mm, having one pore of 0.5 mm diameter for water injection	Fluent	CSF	3D
Song *et al.* [198] (2014)	Analyze the effects of hydrophilic/hydrophobic properties of a serpentine GC on liquid water transport	13.1 mm long U-shaped GC with round corner and cross-section of 1.1 mm × 0.6 mm, having four rectangular pores (0.05 mm × 0.05 mm) for water injection	Fluent	CSF	3D
Ashrafi and Shams [199] (2015)	Investigate the effects of the GDL surface roughness on droplet transport in the GCs	1.00 mm × 0.25 mm straight GC	Fluent	CSF	2D
Ferreira *et al.* [200] (2015)	Study the effects of hydrogen velocity, operating temperature and walls wettability on water dynamics in an anode GC	5 mm long straight GC with cross-section of 1 mm × 1 mm	Fluent	CSF	3D

Guelli Ulson de Souza *et al.* [201] (2015)	Study the two-phase flow inside a tapered GC	10 mm long tapered GC with 1 mm height at air inlet, inclination of 0 and 0.75°, and several pores with diameter of 50 µm for water injection	Fluent	CSF	2D
Jo and Kim [202] (2015)	Investigate liquid water behavior inside a right angle GC	20 mm long GC with cross-section of 0.25 mm × 0.25 mm having a right angle bent in the middle, and a pore with diameter of 0.05 mm placed close to the air inlet for water emergence	Fluent	CSF	3D
Lorenzini-Gutierrez *et al.* [203] (2015)	Understand liquid water removal from the GCs in the form of films and slugs, and test the effectiveness of suggested GC cross-section geometries	15 and 30 mm long GC with rectangular cross-section of 0.7 mm × 0.4 mm; 30 long GCs with trapezoidal (with open angles of 40 °, 50 ° or 60 °) and circular cross-section with fixed height of 0.4 mm and area of 0.28 mm^2	Fluent	CSF	3D
Niu *et al.* [204] (2015)	Study the turbulent two-phase flow that might occur in the GCs of a PEM fuel cell	6.2 mm long straight GC with cross-section of 1 mm × 1 mm	Open FOAM	CSF	3D
Ashrafi *et al.* [205] (2016)	Analyze droplets dynamics in simple and tapered straight GCs and in simple and filleted serpentine GCs	1 mm long straight GC with inlet height of 0.250 mm and outlet height (tapered GC) of 0.125 mm; 25 mm long (approx.) serpentine GC with main height of 1.5 mm	Fluent	CSF	2D
Cai *et al.* [206] (2016)	Investigate the influence of GCs orientation and walls wettability on water droplet emergence and movement	1 mm long straight GC with rectangular cross-section of 1 mm × 1mm, having a pore of diameter of 0.2 mm on the bottom surface.	Fluent	CSF	3D
Hou *et al.* [207] (2016)	Explore the differences of water removal between the anode and cathode GCs	10 mm long straight GC with cross-section of 1 mm × 1 mm; 20 mm long (approx.) U-shaped GC cross-section of 1 mm × 1 mm, having round rectangular corners	Fluent	CSF	3D

2.2.1. First studies – water initially placed in the GCs or emerging uniformly from the GDL

The first study in which the VOF method was used to simulate the two-phase flow in a PEM fuel cell was published by Quan *et al.* [143]. The computational domain was a U-shaped channel in order to represent a key component of a serpentine GC: the bend area. Different PEM fuel cell operating conditions were simulated by placing, in the beginning of each simulation, a certain amount of water (from a single droplet to a water film) in a certain location of the channel. The results showed that a secondary flow was induced by the interaction of liquid water and air flow in the bend area, which strongly affected water behavior in the bend and in the area after the bend. It not only drove water to the surrounding surfaces, but also affected water distribution in the air flow inside the channel. For the cases with the largest amounts of water, simulations showed that water distribution after the bend might block the reactant supply to the reaction sites (by covering the GDL surface) and also the reactant transport inside the GC, which would decrease the fuel cell performance. With the aim of identifying design guidelines for the GCs, Kim *et al.* [171] employed a similar numerical setup to study the effects of the GC geometry and surface properties. The results showed that hydrophobic surfaces, round corner, and smaller channels width lead to a faster exhaust of liquid water with a smaller stagnant volume.

Jiao *et al.* [146, 147] numerically investigated the air-water flow in the cathode side of PEM fuel cells stacks with parallel serpentine [146] and straight parallel [147] GCs. For both channels designs, the air flow could be severely blocked even if there was only a small amount of water in the channels, thus causing the air flow to be unevenly distributed. The serpentine design, however, could provide a powerful water removal characteristic caused by the U-turns, which the authors called “collecting and separating water effect”. In the “collecting and separating water effect”, water was collected and then separated into different parts. Thus, since the water films were separated into small droplets, it was easier to remove them.

Cai *et al.* [145] simulate the two-phase flow in a straight channel of a PEM fuel cell in order to study the effects of the hydrophilic/hydrophobic properties of the channel walls on liquid water removal. A volume fraction of liquid water was introduced in the beginning of the simulations to capture the interface motion. It was found that the wettability of the channel walls had a great influence on water transport in the channel, in both water distribution along the channel and the time for water to be discharged out of the channel. A hydrophobic GDL surface and hydrophilic channel walls showed to be the best combination, being beneficial to water removal as well as to gas transportation from the channel to the GDL. The motion of liquid water under different air velocities was studied by Zhan *et al.* [149] in straight and serpentine channels considering the hydrophilicity of the graphite plate and the hydrophobicity of the GDL, which form the typical walls of a PEM fuel cell GC. The results showed that the more hydrophobic the surfaces of the channel were, the more easily the water was discharged. Moreover, liquid water was easier to be removed under high air velocity than under lower air velocity, and in a straight channel than in a serpentine channel.

The effects of channel surface hydrophilicity, channel geometry, and air inlet velocity on water behavior, water content inside the channel, and two-phase pressure drop were numerically investigated by Quan and Lai [151]. A U-shaped air flow channel (analyzing both sharp and round corners) attached to the GDL (modeled as a homogenous porous) with constant liquid water mass flux was used as the computational domain. It was found that a hydrophilic channel surface provided an effective water management strategy inside the GC but with a significant increase in pressure drop. A sharp corner channel design, with negligible increase in pressure drop, was found to be the best design, leading to water accumulation in the upper surfaces of the channel, thus leaving more GDL surface area for reactant transport. It was also observed that the pressure drop in the channels increased almost linearly with the air inlet velocity. In a later study [165], the authors applied the same approach for an interdigitated configuration. The results showed that liquid water only accumulated in the oulet channel. Moreover, the mechanisms of water removal were strongly dependent on the operating pressure drop. With increasing operating pressure drop, the flow regime shifted from a mixture of corner and slug flow, to corner flow only, and finally to a regime of shear flow with fast water movement along the GC.

2.2.2. Droplets behavior – emergence, deformation, detachment and movement

In the first studies on two-phase flow in PEM fuel cells discussed in the above subsection, liquid water was placed in the GCs in the beginning of each simulation or it was considered to enter in the GCs as a constant liquid water mass flux throughout a uniform GDL surface. However, as experimental studies have shown [60, 62, 208], water emerges from the GDL surface through specific pores with the formation of droplets. The droplet behavior, including emergence, deformation, detachment and movement in the GC, including the interaction with other droplets and formation of films, is thus a very important aspect that has to be studied in order to fully understand the two-phase flow in the GCs.

Theodorakakos *et al.* [148] focused their work on the detachment of droplets from GDLs used in PEM fuel cells under the influence of a cross-flowing air. The simulation results were compared with those obtained experimentally, and a good agreement was found. Parametric studies investigating the effects of various parameters showed that: a droplet was more easily swept away by an uniform air velocity rather than by a developing flow; decreasing surface tension values (which simulated an increase in temperature) resulted into smaller adhesion forces and easier droplet deformation and thus faster removal from the GDL surface; the effect of gravity was negligible; and the droplets were removed at lower velocities when in contact with the side or top surfaces of the channel.

Bazylak [155] employed a combination of fluorescence and liquid pressure drop measurements to investigate the dynamic liquid water transport behavior in a simulated GC of a PEM fuel cell. It was observed that water droplets emerge from the surface of the GDL in preferential locations corresponding to the path of least resistance and that these preferential water breakthrough locations changed over time. To help to explain this phenomena, the VOF method was used to simulate the filling behavior of liquid water within two competing pathways of a GDL. These 2D simulations showed that once a new preferential pathway was found, less preferable pathways receded (**Figure 2.1**), which was in accordance with the experimental observations of receding droplets.

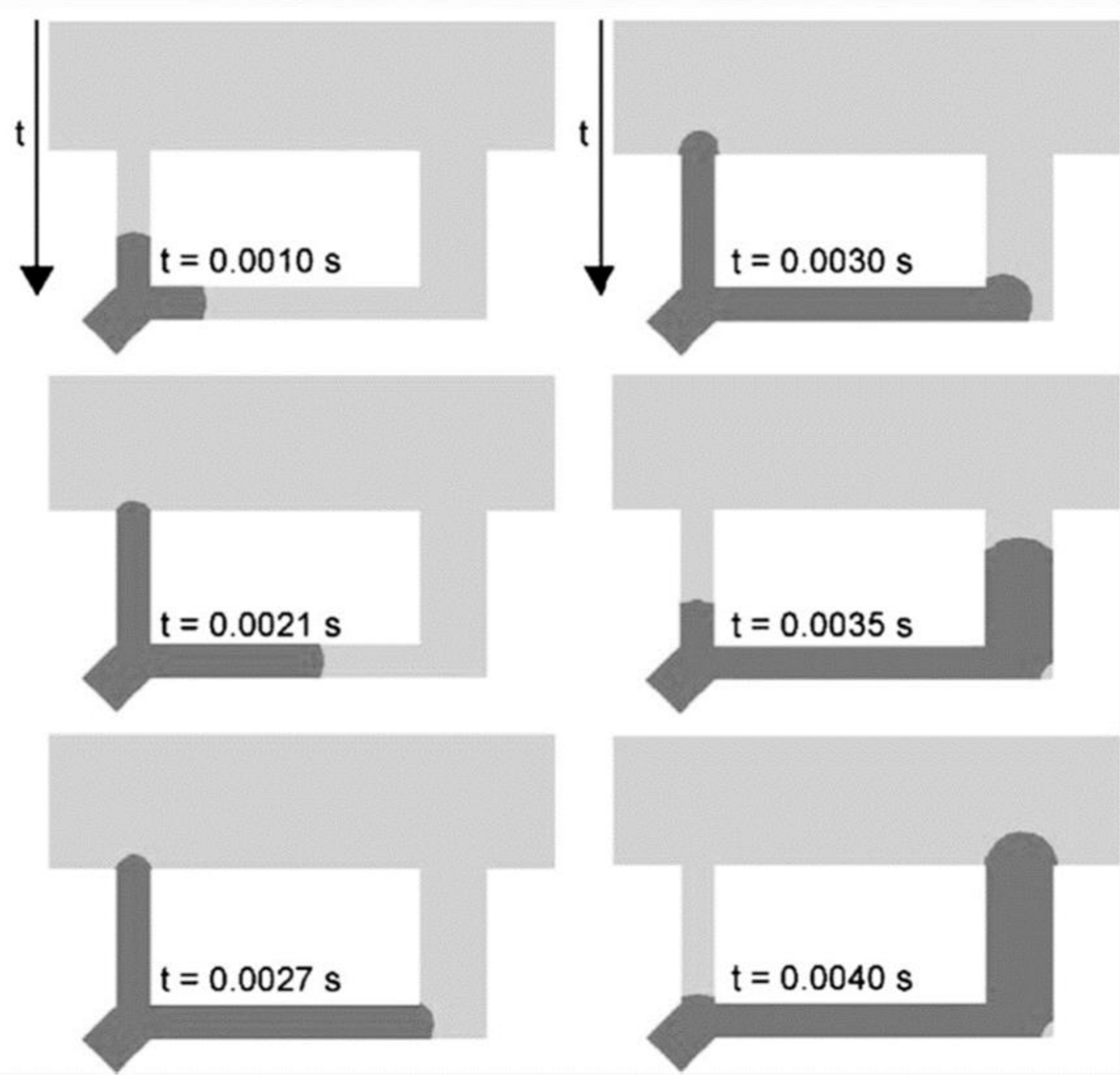

Figure 2.1. Temporal sequence of VOF simulations showing the primary filling of the smaller channel (0.0010-0.0030 s), followed by the secondary filling of the larger channel with liquid water receding in the smaller channel (0.0035-0.0040 s) (dark gray represents liquid water, and light gray represents air) (adapted from Ref. [155]).

A contact angle hysteresis model based on the VOF method was presented by Fang *et al.* [156] to analyze the influence of the contact angle hysteresis on microchannel flows. The model was qualitatively validated against experimental data from droplet and slug dynamics, and good agreement was achieved for a wide range of flow conditions. The results revealed that the contact angle hysteresis was responsible for droplet elongation and post-detachment instability. Moreover, the authors stated that the model presented could be used to estimate the surface properties for cases where an *in-situ* measurement is difficult to conduct.

Deformation and detachment conditions for a water droplet adhering to the cathode GDL surface of a PEM fuel cell GC were numerically investigated by Golpaygan and Ashgriz [144, 157]. Through 2D simulations, the effects of droplet and gas properties, channel geometry and flow velocity on the mechanism of separation and break-up of the droplet were studied, and surface tension was found to be the most relevant parameter determining the mobility of the droplet. Later, the same group extended their work to 3D analysis [178] which further confirmed the determining effect of surface tension forces on the droplet dynamics.

The effects of the surrounding fluid properties (velocity, density and viscosity) on a droplet in a microchannel, as well as the flow structures inside and outside the droplet, were studied by Shirani and Masoomi [159]. VOF simulations showed that increasing the density, velocity and viscosity of the surrounding fluid forced the droplet to deform more rapidly and that surface tension prevented the droplet deformation.

Zhu *et al.* [152] presented 2D VOF numerical analysis of the two-phase flow in PEM fuel cells GCs that consider the pore through which water emerges. The complete droplet emergence and formation process as well as the subsequent detachment and/or film formation were tracked. The effects of the static contact angle, pore size, and air and water inlet velocities on the water droplet dynamics were investigated, and the critical air velocity at which droplet detachment occurred was predicted. It was observed that a hydrophobic GDL surface resulted in breaking away of the water droplet whereas a hydrophilic GDL surface resulted in spreading of the water droplet on the bottom wall and the onset of film flow. High air inlet velocity induced the water droplet to collapse and to adhere to the GDL earlier leading to the formation of film flow prior breaking away. Moreover, the critical air velocity was found to decrease with increasing hydrophobicity of the surface and with increasing initial dimension of the droplet. In a later study, Zhu *et al.* [153] focused on the emergence of water onto the hydrophobic PTFE treated GDL typically employed in PEM fuel cells, and investigated the effects of channel and pore sizes and coalescence of droplets on liquid water dynamics in the GC. The results showed that the downstream deformation of water droplets slowed down in larger channels (higher height) and that the coalescence of two water droplets accelerated liquid water motion. In addition, the critical air velocity decreased with decreasing the pore diameter. In order to obtain a complete representation of the dynamic processes occurring in the GCs of PEM fuel cells, Zhu *et al.* [160] extended their previous 2D works to three-dimensions and analyzed the growth, deformation, detachment, motion, coalescence and film formation, and the associated water coverage and friction factors as a function of several parameters (both operational and material). The results showed that the emergence of droplets into the GC was a highly dynamic and almost a periodic process with cyclic formation, growth, deformation, detachment, and removal of water droplets. Moreover, the frequency of this periodic process increased with decreasing the wettability of the GDL surface and increasing air inlet velocity The authors also investigated the effects of pore location on the droplet dynamics [179]. Results revealed that the behavior of the droplet only depended on the wettability of the GDL when it emerges from the centerline. When the emergence location was closer to the one of the lateral walls, these walls wettability significantly affected the dynamics of the droplet.

The water droplet motion in a PEM fuel cell straight GC with a wide range of hydrophilicity levels and inlet air velocities was investigated by Mondal *et al.* [176]. It was found that droplet motion was slow for a channel wall with low contact angles (more hydrophilic channel) and that a high air velocity forced water to move faster, especially for large contact angles. Within the same research group, similar work was performed by Raman *et al.* [177], but focusing on hydrophobic channel walls. The results showed that a super hydrophobic channel surface was required to decrease the droplet removal time.

Le *et al.* [170] performed optical visualization of liquid water in a simulated PEM fuel cell air channel with serpentine configuration. A number of droplets were injected into the channel entrance via hypodermic needles. The aim was to compare the results with those obtained by numerical simulations in order to validate the VOF method. The shapes and locations of a droplet at a given time in the numerical model and in the experiments were in good agreement and provided a qualitative validation. A quantitative validation was achieved by comparing pressure drop in the channel and the pressure rise due to liquid water in both cases. Later on, a similar numerical setup was employed to investigate the liquid water flooding process in GCs with interdigitated [174] and parallel [175] flow fields. Simulation results were able to demonstrate the avalanche phenomena created by the interdigitated design when gas blockage by liquid water occurred, as well as the maldistribution of the gas flow caused by the parallel channel design.

The VOF method was used to simulate water droplet movement and slug formation in a section of a PEM fuel cell double serpentine GC by Carton *et al.* [181]. In addition, optical visualization of water droplets and slugs was conducted in ex-situ GCs to obtain experimental model validation. From the results it was observed that the excess water in the channels from the collision and coalescence of droplets could form liquid water slugs.

Moreover, one channel of the double serpentine flow field design became blocked due to the redistribution of air flow and pressure caused by slug formation.

U-shaped GCs with round or sharp corners having five pores designed at the GDL bottom wall for water droplets emergence were considered by Cai *et al.* [180], and parametric studies varying air and water inlet velocities and walls wettability were conducted. It was observed that water was more easily transported in the round corner channel. Moreover, increasing the hydrophobicity of the channel walls reduced water content in the GC, but increased the portion of the bottom wall (corresponding to the GDL) covered by water. Furthermore, as air velocity was increased, the influence of walls wettability and air and water velocities was diminished. Recently, the authors simulated the emergence and movement of one droplet from a straight GC with various orientations [206], and found that, as previously reported by Theodorakakos *et al.* [148], gravity plays a minor role in water motion.

Cho *et al.* [209] derived an analytical expression to describe the droplet shape change in a PEM fuel cell GC by examining the forces over the droplet at various conditions and different locations. In a sequel paper [183], the authors compared the analytical solutions of the droplet deformation and removal with experimental data and VOF predictions. Experimental data were obtained through optical visualization in a simulated PEM fuel cell GC. A high pressure near the stagnation point and low pressure at the site where the flow acelerated were observed through the numerical analysis. Furthermore, quantitative comparisons between the developed analytical solution and experimental/numerical results showed reasonably agreement.

Kim *et al.* [193] analyzed the inter-droplet interactions of water droplets emerging from two pores into the air flow stream of a PEM fuel cell cathode channel. The effects of the distance between the pores, distance from the GC side walls, contact angle of the side walls and air flow rate on liquid water removal from the GC were investigated. The results revealed that the coalescence of two droplets enhanced the water removal in comparison with two separate droplets, the droplet near the hydrophilic wall improved reactant transport, and clogging was more likely to occur for a hydrophobic channel wall surface and low air velocity. In a more recent publication [198], the authors focused on the effects of hydrophilic/hydrophobic properties of a serpentine GC. A set of 3D VOF simulations was conducted for a hybrid case consisting of hydrophilic channel walls at the straight part but hydrophobic walls at the turning part of the serpentine. The numerical results showed that this hybrid case enhances water removal compared with two other cases in which the channel wall is homogeneously hydrophilic or hydrophobic.

To ensure proper contact between layers and also to seal a PEM fuel cell, the different layers are compressed during the assembling process. The flexible, porous microstructure of the GDL deforms considerably when subjected to compressive loadings. A recent study conducted by Bao *et al.* [197] investigates how GDL deformation influences the droplet dynamics in a GC of a PEM fuel cell. The results suggested that a more significantly deformed GDL increases the contact area between the water droplet and the GDL/channel surfaces, thus leading to a slower water removal.

In typical operating conditions of a PEM fuel cell, the flow in GCs is generally laminar. However, when large reactions areas (300 cm^2) and high load operation (3 A cm^{-2}) are considered, turbulent flow may occur. Niu *et al.* [204] used a modified VOF approach to capture water droplet transport in a straight GC at a very high air velocity, corresponding to turbulent regime. Significantly different two-phase flow patterns were observed when comparing to with those obtained under laminar conditions. For turbulent flow, the droplet deformed asymmetrically and most of it became a water film spreading in the GDL surface. When considering laminar regime, the droplet deformed symmetrically and less water was accumulated in the GDL.

Jo and Kim [202] focused on water behavior in a right angle GC. The aim was to study how water droplets interact with the bent sections of typical PEM fuel cells GCs. Pores for water emergence were designed not only in the middle of the bottom GDL surface (equally distanced from each side wall), as usually considered in VOF simulations, but also closer to each side wall. When increasing the GDL surface hydrophobicity, droplets emerging from pores located closer to the side walls tended to move along these walls or along the lower edges, whereas droplets emerging from the center pore showed more complicated flow patterns. Moreover, as the contact angle of the side and top walls increased, the GDL surface water coverage ratio also increased (negative outcome), whereas the water volume fraction decreased (positive outcome). Based on such results, the authors emphasized that the performance of a PEM fuel cell may be determined by the balance between water volume fraction in the GCs and GDL surface water coverage.

2.2.3. GDL microstructure – pore arrangement and roughness

In the literature discussed so far, the focus was mainly on the dynamics of a single droplet or a few droplets emerging from pore(s) of a uniform and smooth GDL surface. However, in a PEM fuel cell, many droplets emerge at multiple sites from a GDL that is porous and rough. To simulate these features of the GDL, detailed consideration of its microstructure is needed. To the present date, just a few studies employed the VOF method to investigate the liquid water transport in the GDL with detailed representation of its fibrous structure. Suresh and Jayanti [168] considered the GDL microstruture in a 2D computational domain as a layered structure with circular fibers, and investigated the effect of the air flow on liquid water transport. The results showed the beneficial effects of air cross-flow in removing liquid water from the GDL which is typically observed when serpentine and interdigitated flow fields are employed. Ahmad *et al.* [185] used a similar computational domain to study the effects of GDL PTFE loading on liquid water removal from a PEM fuel cell. The PTFE content in the GDL was varied by changing the surface tension and the contact angle. VOF simulations showed that increasing the PTFE content in the GDL decreased the detachment velocity and, thus, facilitated liquid water removal. However, higher PTFE loading also raised the required capillary pressure for liquid water to penetrate the GDL. Park *et al.* [169] reconstruted the GDL structure by 3D solid cylinders randomly distributed in the in-plane directions, and also found that the amount of pressure gradient caused by the cross-flow is sufficient and effective to get rid of the liquid water accumulated in the GDL.

The VOF pore-scale simulations above discussed have associated an extremely large computational time, therefore, they can only be employed efficiently for very small length scales. For this reason, researchers have been trying to develop more practical strategies in order to consider the effects of the GDL microstructure while performing simulations at larger scales. Two main features of the GDL microstructure are especially important: (1) the pore arrangement for liquid water emergence and (2) the roughness of the GDL surface. The pore arrangement is important in order to adequately describe water emergence processes in the GCs, whereas the GDL roughness affects flow resistance and cannot be neglected in microflows.

In the study conducted by Jiao and Zhou [154], the porous holes on the GDL were represented by small paths with square cross sections connected to a U-shaped channel. The aim of the study was to investigate how liquid water flows through the GDL into the

GC. Simulations were conducted in an accelerated mode in which the theoretical water velocity from the GDL to the GC was increased 1000 times in order to shorten the computational time. Since the velocity of water is too small compared to that of air, its increase only affects the time of water transport but does not change the basic physical nature of water transport across the GDL. The results revealed that the serpentine design of the GCs can help water drainage because it facilitated breaking up of water films.

Ding *et al.* [164] focused their work on the effects of the GDL microstructure on the two-phase flow patterns in the GCs of PEM fuel cells. The microstructure of the GDL was simplified by creating a number of representative pores on its surface and droplet formation and movement were simulated using the VOF technique. Five representations of the GDL microstructure (**Table 2.1**), with the same open area and liquid water flow rate, were selected for simulations. The 4-pore case was found to be the minimum number of pores to represent the microstructure of the GDL surface since the two-phase flow patterns with 4-pores and 64-pores were very similar (**Figure 2.2**). It was thus concluded that, in the channel width direction, at least 2 pores are required to represent the microstructure of the GDL surface. Based on that, Ding *et al.* [173] extended the previous work by implementing the 2 pores in the channel width direction GDL microstructure to a larger channel with dimensions comparable to those used in real PEM fuel cells. Three stages of two-phase flow patterns in the GC were identified, namely emergence and merging of liquid water in the GDL surface, accumulation on the side walls and detachment from the top wall (**Figure 2.2**). Parametric studies were also conducted and it was observed that a more hydrophobic GDL surface and/or more hydrophilic channel walls would be beneficial to liquid water removal. However, a more hydrophobic GDL surface increased the pressure drop and more hydrophilic channel walls increased the GDL water coverage ratio as well as the water residence time. Moreover, with increasing liquid water injection rate, the flow pattern evolved from corner droplet flow to top wall film flow, annular flow, and finally slug flow. These flow patterns agree reasonably well with those observed in visualization experiments [60], as shown in **Figure 2.3**. The same research group then focused on the two-phase flow distribution in inter-connected parallel flow channels [187]. The aim was to represent and study the communication between parallel channels that naturally occurs in a PEM fuel cell through the porous GDL via in-plane diffusion (**Figure 2.4**). The results showed that the communication channels caused flow maldistribution and increased liquid water residence time, especially for wide channels. Furthermore, numerical results were compared with experimental data from two designs of communicating channels and a qualitative validation was obtained.

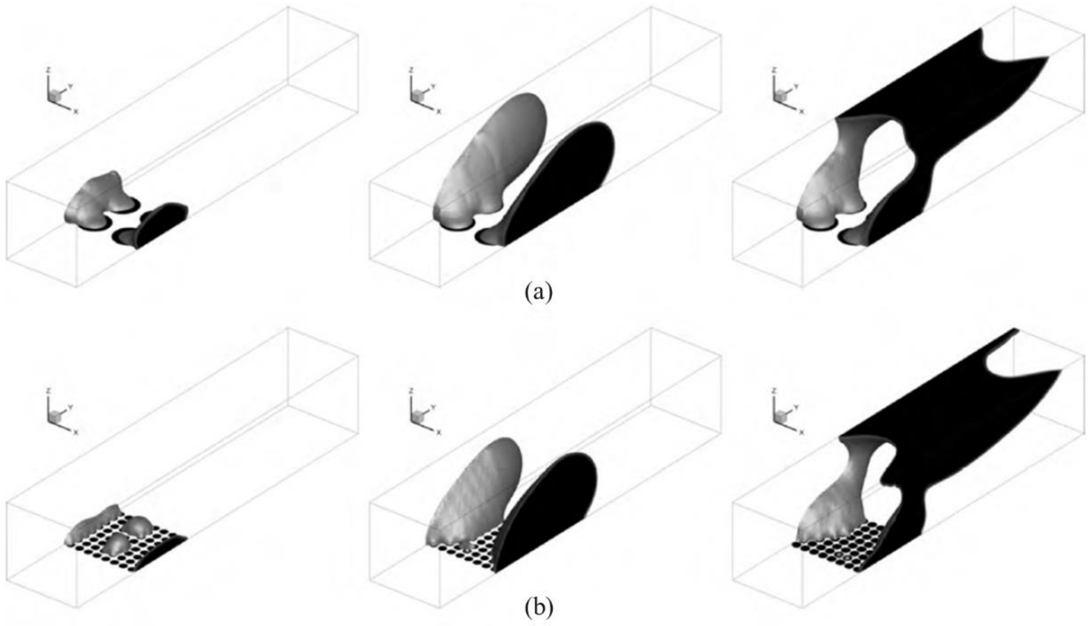

Figure 2.2. Effects of the GDL microstructure on the two-phase flow pattern in the GCs: (a) 4-pore, and (b) 64-pore (adapted from Ref. [164]). Three stages of two-phase flow patterns can be observed, namely emergence and merging of liquid water in the GDL surface (left), accumulation (center) and detachment (right).

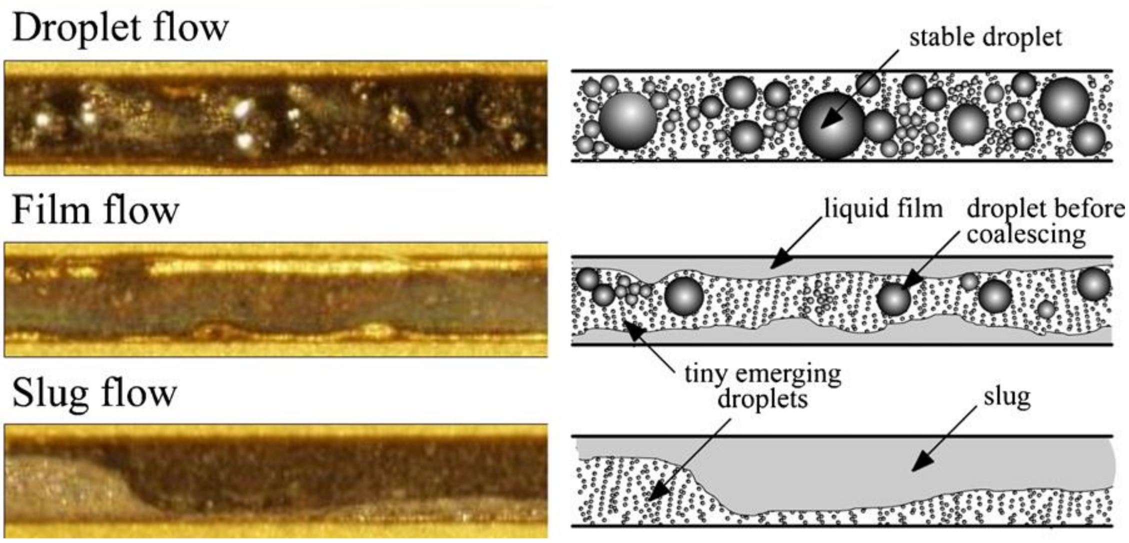

Figure 2.3. Typical two-phase flow patterns in PEM fuel cell GCs (adapted from Ref. [60]).

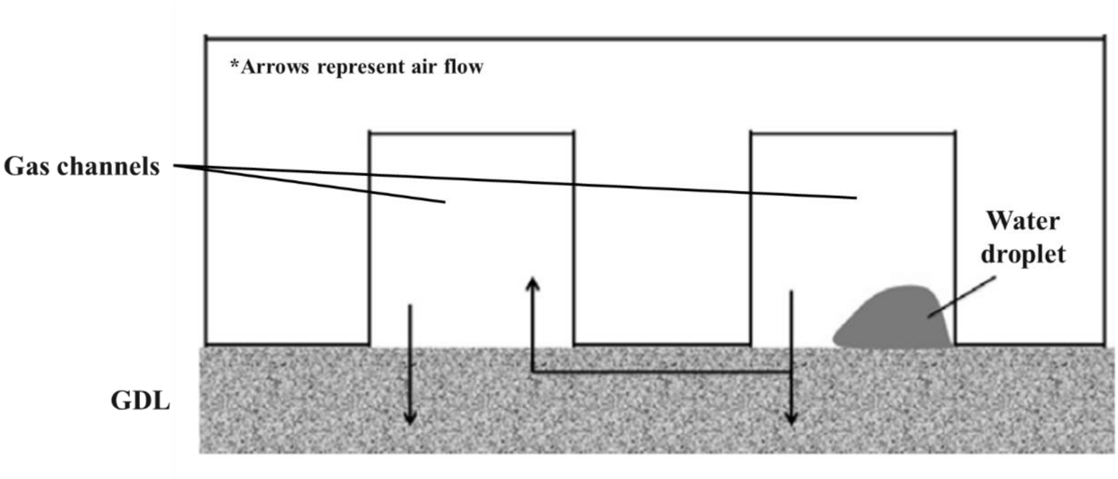

Figure 2.4. Illustration of the communication between adjacent parallel channels created by the porous GDL via in-plane diffusion (adapted from Ref. [187])

Du *et al.* [166] analyzed the effects of the water injection methods on the two-phase flow characteristics in PEM fuel cells GCs. Side liquid water introduction, continuous liquid introduction along the channel bottom wall with uniform and non-uniform flow rates, and liquid water introduction from the inlet together with the gas phase were the methods considered. VOF simulations showed that when water was introduced from side walls along the channel, water accumulation increased compared to the case with water injected from the channel inlet. Less possibility for slug formation in the channel was observed when water was introduced non-uniformly along the channel and more near the outlet. For water feed from the bottom wall, water emerged and accumulated, forming slugs which lead to high pressure drops. Through parametric studies, it was found that the gas flow rate and walls wettability had significant effects on water behavior and a change in their values could lead to the transition between flow patterns. Moreover, increasing the surface tension led to a small increase of the slug length and a small decrease in slug frequency.

A novel geometrical setup to conduct a series of direct simulations of the liquid water dynamics in a PEM fuel cell GC was proposed by Qin *et al.* [184]. The conducting pathways in the GDL were simplified by three cylindrical pipes connected to a liquid water reservoir representing the CL. In this study, the competition between film and droplet flow was investigated. Simulations showed that increasing the gas flow rate could mitigate the film flooding but with an increase in pressure drop along the GC. Moreover, it was found that a proper contact angle of the channel side walls should be selected to balance two requirements: (1) increase the film removal ability (less hydrophilicity) and (2) fast removal of the water clogging (higher hydrophilicity).

In order to obtain complete information of water dynamics in a PEM fuel cell, Hossain *et al.* [192] implemented two different modeling approaches: (1) the Eulerian two-phase mixture, which provided overall information of species distribution inside the whole cell and (2) the VOF method, which showed the emergence of water droplets from the GDL into the cathode channel and the subsequent water removal from the channel. The main goal of the study was to find an optimum water pore arrangement that would provide the minimum water coverage on the GDL surface. The results showed that the surface coverage of the GDL by liquid water could be reduced by reducing the pore diameter, by placing water inlets near the channel walls and by increasing the inter-pore distance. According to the results obtained, the authors suggested a GDL layer made of a column of hydrophilic fibrer arranged inside the randomly distributed hydrophobic fibre matrix that could lead to the precise control of water path through the GDL into the channel and, thus, to a better water management in the GC.

He *et al.* [167] investigated the effects of wall roughness on the water behavior related to the PEM fuel cell GCs by two-phase flow VOF simulations. The wettability of the wall surface, the relative roughness height (ratio between the height of the roughness elements and height of the channel (r/H)), the roughness element density, and roughness element type were considered. The results showed that the roughness of the wall surface affected the water behavior differently depending on the wettability of the channel wall. The water behavior was considerably altered when considering a hydrophilic wall even for a low r/H value (0.2 %) and increasing r/H showed to be positive for water removal. In contrast, considering a hydrophobic wall, there was nearly no effect for r/H = 0.2 % and increasing r/H was disadvantageous for liquid water removal. For both cases, however, the average pressure drop increased with increasing roughness. Moreover, increasing the roughness element could help water removal for a hydrophilic surface and the triangle roughness element was better than the rectangle element with the same height. Liquid water transport in a PEM fuel cell GC with a rough GDL surface was numerically investigated by Chen *et al.* [182]. The GDL roughness was described by placing an array of cubic holes on its surface. The results showed that the GDL roughness acelerated the removal of a droplet and reduced the water coverage ratio, because the GDL roughness led to lower retention forces and higher detachment forces acting on the water droplet.

However, it was also observed that higher GDL roughness led to higher pressure drop in the GC.

The effects of the GDL roughness on the dynamic behavior of a water droplet in a PEM fuel cell was also numerically studied by Chen *et al.* [186]. Three GDL microstructures were analyzed by representing the carbon fibers as rectangles with different orientations (see **Table 2.1**). The results showed that the parallel distribution of the carbon fibers had the best capacity of detaching adhered droplets and reducing flooding in the channels. In the same paper, the authors also presented an analytical force balance model which accounted for the GDL microstructures and surface tension, and it could be used to predict the droplet detachment size.

In a recent 2D simulation work conducted by Ashrafi and Shams [199], a random function was used to generate the GDL surface with various roughness. The GDL roughness considerably affected water dynamics. Among other findings, it was observed that the formation of liquid water films attached to the GDL surface, an undesirable flow pattern during PEM fuel cells operation, was facilitated when increasing the GDL roughness.

2.2.4. Impact of the two-phase flow in the fuel cell performance

The numerical investigations using the VOF method presented in the previous subsections only focus on the behaviors of liquid water from a perspective of fluid dynamics while the reactant transfer and the electrochemical reactions were not considered. However, as discussed in Chapter **1** (section **1.3.6**), the two-phase flow has a significant effect on a PEM fuel cell performance, which is important to be quantified.

Le and Zhou [133] published one of the most complete models for a PEM fuel cell. The model was 3D, unsteady, multi-phase and multicomponent with VOF interface tracking technique. Moreover, it considered all the necessary components of a PEM fuel cell (membrane, CLs, GDLs, GCs and current collectors) and coupled the fluid flow (momentum transport), species transport, energy transport, electron and proton transport, with electrochemical reactions. The two-phase flow patterns were analyzed and the effects of liquid water on velocity field, pressure distribution, reactants concentration, current density and temperature distribution were investigated. In following articles, the authors applied this general model to study the liquid water flow in serpentine-parallel channels [161] and in interdigitated channels [162]. The results showed that liquid water caused high pressure drop, increased mass transfer resistance of reactants and decreased the local cell temperature. However, it was also observed that the presence of liquid water increased the ionic conductivity of the CLs and the membrane. In addition, the liquid water could be easier removed from the serpentine-parallel channels, compared with a single-serpentine channel. Regarding the results with the interdigitated design, it was found that the reactants transport could be enhanced by the forced convection created by this kind of flow field. However, the water vapor inside the porous media could also be taken away which reduced its ionic conductivity. Posteriorly, Zhou and co-workers applied their general model to a three-cells PEM fuel cell stack [163]. Simulations revealed that the distribution of reactant gases in a flooded cell is lower than that in the other cells containing no liquid water. This not only resulted in a decrease in the overall current density of the flooded cell but also affected the performance of the stack. Despite the complexity and the new insights given by the model developed by Le and Zhou [133], one important drawback is that simulations were performed by initially locating liquid water droplets on the cathode GCs instead of water being continuously emerging from the GDL, as it occurs in real fuel cells. This feature limits the applicability of the model.

Chen *et al.* [132] numerically analyzed the effects of liquid water distribution in a GC on pressure drop, reactant transport and current density under different inlet air velocities, wall wettability and water inlet positions. Electrochemical reactions were considered in the VOF formulation through user defined functions (UDFs) for the effective diffusivity of oxygen in the GDL and boundary conditions of oxygen mass fraction on the GDL bottom surface. Moreover, a hybrid structural model was adopted to consider the GDL surface microstructure (see **Table 2.1**). Simulation results revealed that the presence of liquid water in the GC increased pressure drop, caused local peak region of current density and led to high non-uniformity of current density distribution. Furthermore, it was observed that having larger pores within the GDL near the side wall of the GC rather than at the center of the channel were helpful to form the desirable flow pattern of liquid water, which was found to be the flow of water as a film on the top wall of the GC. Ding *et al.* [188] coupled a 3D air channel VOF model with a 1D model for the membrane electrode assembly (MEA) to investigate the effects of the two-phase flow patterns on the PEM fuel cell performance. By comparing the cell performance predicted by single-phase and two-phase simulations, it was found that the presence of slug flow decreased the cell voltage output in the mass transport region (high current densities). Moreover, increasing the gas flow rate as well as the MEA contact angle improved cell performance. However, a too high gas flow rate and a very hydrophobic MEA surface also increased the pressure drop. In a follow work, Ding *et al.* [189] applied the same 1D + 3D two-phase flow model to a PEM fuel cell consisting of two parallel flow channels in order to investigate the effects of flow maldistribution on the fuel cell performance. The results showed that flow maldistribution led to slug flow patterns which significantly increased the GDL water coverage ratio and consequently decreased the cell voltage. The studies published by Chen *et al.* [132] and Ding *et al.* [131] provide some new insights on how to consider electrochemical reactions when applying the VOF technique, without the need for the complexity present in models such as that developed by Le and Zhou [133], which often limits their practicability due to the large computational times involved. However, some issues can still be addressed in order to obtain a more comprehensive model with a larger range of applicability. In relation to Chen *et al.* [132], the velocity of liquid water entering into the GCs was set manually to an arbitrary value, instead of being calculated as function of the current density produced. Moreover, water balance in the membrane was not considered. Ding *et al.* [131] added the feature of water velocity in each pore being related with water generation rate nearby. However, although ohmic losses were considered to better predict the current density, the membrane was considered to be fully humidified. In both studies, the model applicability is limited in the sense that they cannot predict the influence of strategies dealing with two-phase flow issues that might have negative effects on the hydration state of the membrane (*e.g.* increasing gas flow rate or cell temperature). Another aspect that is missing in the studies where electrochemical reactions are considered along with the VOF methodology is the validation of the cell performance predicted by the models against experimental polarization curves.

2.2.5. Novel GDL or GC designs

The focus of the numerical simulations addressed along the previous sections was on understanding the two-phase flow in the GCs and its implications on cell performance considering the materials and designs normally employed in PEM fuel cells. Some researchers, however, used VOF simulations in order to test the effectiveness of novel GDL and GC designs.

Jiao and Zhou [150] proposed three innovative GDLs containing different geometries of their pores (see **Table 2.1**) in order to mitigate liquid water flooding in PEM fuel cells. The effectiveness of each GDL was studied through numerical investigations of air-water flow across each GDL together with a U-shaped channel using the VOF method. The results showed that the trapeziform porous holes with the minimum area facing the GCs was the best option for water removal due to its ability to enhance the air flow inside the CL. The worst condition was achieved when the trapeziform porous holes with the minimum area facing the CL were employed. In a later paper [158], the authors studied the wettability of the best GDL by assigning different static contact angles to the electrode. It was found that a hydrophilic GDL was not beneficial for liquid water removal, because it retained water formed in the CL and also attracted water from the GC. Moreover, the results showed that the hydrophobicity of the GDL should be carefully selected, and the CL should have higher or equal hydrophobic level by comparing to the GDL, in order to expel liquid water in the right direction (from the CL to the GDL and finally to the GC).

Fontana *et al.* [190] employed the VOF formulation to investigate the two-phase transport inside a tapered GC. From 2D simulations it was found that, although causing an increase in pressure drop, the slug flow acted as the most effective mechanism of water removal, capturing the growing droplets as they moved toward the channel outlet, thus reducing the liquid water content inside the channel. The tapered channel revealed to favor the slug formation, thus helping the water management inside the GC. In following studies [191, 201], the same research group employed a multi-fluid 3D model to describe the performance of a PEM fuel cell and to calculate the amount of water produced with different taper angles. The amount of water calculated was then used to obtain liquid water velocity in 2D VOF simulations. From the 3D model simulations, it was found that, for temperatures greater than or equal to 333 K, the channel tapering played a beneficial role in terms of decreasing the liquid water saturation and increasing the limit current density value. Regarding the 2D VOF simulations, it was observed that increasing the taper angle led to the formation of liquid water films and thus faster water removal from the channel. However, an increase in channel tapering also produced a significant increase in the pressure drop and an increase in the GDL surface water coverage. Therefore, it was concluded that an optimum taper angle has to be found allowing a fast liquid water removal while causing minimal increase in pressure drop and GDL surface water coverage. The effect of the GDL hydrophobicity was also analyzed and it was found that the formation of films increased as the contact angle decreased. Ashrafi *et al.* [205] also simulate water dynamics in a tapered GC. Moreover, the authors suggested a serpentine flow field with filleted corners. Results from 2D calculations showed that both designs help to create desirable flow patterns, in which less water accumulates in the GDL surface. Additionally, the filleted serpentine channels reduced pressure drop.

Qin *et al.* [194] proposed a novel PEM fuel cell GC design to improve water management and removal in the channel. The novel channel consisted of a conventional GC which was modified by inserting a hydrophilic needle (small cylinder) in the middle of the channel. The effectiveness of the proposed channel was evaluated through numerical simulations using the VOF method and the effects of the needle diameter and length were studied. The results showed that the needle reduced the water coverage in the GDL, but also induced an extra pressure drop in the channel. Regarding the needle dimensions, it was found that the optimal diameter and length of the needle should balance the need for water removal from the GDL surface (bigger needle) and the lower values of the pressure drop (smaller needle). In a later study, Qin *et al.* [195] analyzed the effects of the surface wettability of the GDL and the inserted needle on the water removal processes. Simulations revealed that GDLs having a larger contact angle and needles with a smaller surface contact angle enhanced liquid water removal from the GDL surface. A drawback of the modified channel with a needle proposed by Qin *et al.* [194] was that the water droplet was suspended in the air for a long period after being removed from the GDL surface, which resulted in an increased pressure drop in the channel. To overcome this disadvantage, Qin *et al.* [196] substituted the needle by a thin hydrophilic plate. It was demonstrated that a water droplet could be removed more effectively from the GDL surface for the channel with a plate, and was transported along the hydrophilic plate surface until reaching channel surface, avoiding droplet suspension in the air and, thus, lowering the resultant pressure drop. Moreover, the contact angle of the inserted plate should be larger than that of the bottom surface and smaller than that of the GDL surface for an effective water removal from the channel.

The GC cross-section geometry is another design parameter that has deserved the attention from researches. Using the same 3D setup as that of their other studies [160, 179], Zhu *et al.* [172] systematically investigated the effects of the channel cross-section geometry on the dynamic behavior of an emerging water droplet, analyzing its effects on pressure drop, water saturation and water coverage ratio. From 10 channel geometries analyzed (**Table 2.1**), the rectangular channel with an aspect ratio (height/width) of 0.5 was recommended. Lorenzini-Gutierrez *et al.* [203] also studied the effect of cross-section geometry, but focused on film and slugs flows. A straight GC was considered where a liquid water slug was placed in the beginning of each simulation. After analyzing the effects of air velocity and walls wettability in slug removal from the typically employed rectangular GCs, the authors turned their attention to alternative cross-sections with trapezoidal and semicircular geometries (**Table 2.1)**. It was found that the trapezoidal shapes with open angles of 50 ° or 60 ° represent attractive options. These designs promoted the formation of top walls films (decreasing water coverage of the bottom GDL surface), reduced two-phase flow pressure drop fluctuation and accelerated water removal.

2.2.6. Two-phase flow in the anode GCs

All the VOF numerical studies on the two-phase flow in PEM fuel cell reviewed so far focused exclusively on the cathode side. This is reasonable since the cathode is the water-generating electrode and thus where flooding is more prone to occur. However, visualization experiments [58, 59, 61] have shown that, for certain operating conditions, flooding can also occur in the anode GCs, and it can be even more significant than that on the cathode side. The process of liquid water appearance in the anode GC is also different from that observed in the cathode side. Liquid water in the anode results mostly from water vapor condensation in the GCs top walls (that opposite to the GDL surface), instead of being continuously emerging from the GDL surface as it occurs in the cathode. Moreover, gas flow rate, density and viscosity of hydrogen in the anode are different from those of air in the cathode. This suggests that liquid water behavior might be very different for the two electrodes, which might lead to distinct water management strategies.

At the time that this review was first published, there were no numerical studies on the anode GCs two-phase flow, and that was one of the recommendations for future work made back then. The first study on this issue was published under the execution of the present research work [200]. A water droplet was placed in the top wall of a straight GC representing water formed by condensation as observed in visualization experiments [58, 61]. The droplet movement was then analyzed for different hydrogen velocities, operating temperatures and GC walls wettability. It was found that, for hydrophilic walls, the droplet spread into the top wall and remained there in the form of films. For hydrophobic walls, water moved as a droplet, attached to the top wall or freely suspended in the channel. Moreover, increasing the hydrogen velocity, the operating temperature and the GC walls wettability led to a faster water removal. However, when the hydrogen velocity was raised, pressure drop also increased considerably. A recent study conducted by Hou *et al.* [207] also addressed the two-phase flow in the anode side. The authors first explored the differences of the water removal process between the anode and cathode straight GCs, founding that it was more difficult to remove a water droplet from the anode side than from the cathode, when typical operating conditions of a PEM fuel cell were considered. The water behavior was then studied in a U-shaped anode GCs having sharp or round corners. In the GC with sharp corners, water was found to be stuck in the GC corners, and that was only avoided when extremely hydrophilic or hydrophobic walls were employed. When a GC with round corners was applied, water could be removed from the channel without the need of changing the walls wettability.

2.3. Summary and major challenges

A literature survey on the numerical studies on two-phase flow in PEM fuel cells using the VOF method was here conducted. It was found that several research groups have made VOF simulations for a great variety of purposes, namely: to analyze the liquid water flow from the perspective of fluid dynamics identifying flow patterns; to study the coupled process of liquid water transport and reactant transfer, including the effects of the liquid water on the cell performance; to investigate the effects of operating conditions, material properties and components design; to help to explain experimental results; to validate analytical solutions; and to test the effectiveness of novel proposed GDLs and GC designs.

VOF simulations can be categorized based on different classification manners. For the initial water distribution, some researchers started their simulations with liquid water placed in specific regions, and others considered liquid water gradually emerging from the GDL or the CL. For the representation of the GDL surface, some considered it as a smooth surface while others took into account its microstructure. For the computational domain, some focused only on the GCs or on the GDL, some further considered the GDL together with GCs or a complete electrode, and some more thoroughly took an entire cell into account. For the dimension, some performed 2D simulations while others considered the three dimensions. Furthermore, the majority of the VOF simulations were performed using the ANSYS Fluent software and the CSF surface tension model.

The results of VOF simulations have been essential to complement experimental results by giving more details and quantitative information about the two-phase flow in PEM fuel cells and its effects. The large majority of the numerical studies reported focus on the cathode two-phase flow. Gathering information from both numerical and experimental results obtained to date, the two-phase flow processes in the cathode side of a PEM fuel cell can be summarized as follows: liquid water, formed in the CL, travels through CL and GDL pores by capillary transport; it emerges into the GCs in preferential areas rather than uniformly along the GDL surface, and forms liquid water droplets; these liquid water droplets grow until they detach from the GDL surface; after detachment, droplets can move downstream in form of single-droplets or they can coalesce with each other to form films or slugs. These processes of emergence, detachment and motion of liquid are affected by the operating conditions, the design of the GDL and GCs, and their material properties. In general, results revealed that increasing the temperature and the gas flow rate is beneficial for water removal. Regarding the material characteristics, hydrophobic GDL and hydrophilic GCs surfaces, as well as a rectangular cross-section geometry for the GCs, have shown to be adequate. Regarding the effects of the two-phase flow on the cell output, results show that liquid water increases pressure drop in the GCs and the transport resistance of reactants to the active sites, which consequently decrease the cell performance. Although less frequent than that in the cathode side, water flooding can also occur in the anode. Experimental data have shown that liquid water appears in the anode side at the top walls of the GCs due to water vapor condensation. Numerical simulations have shown that, for hydrophilic GCs walls wettability, water stays in top and/or side walls of the GCs and it is removed in the form of films, whereas for hydrophobic GCs walls it moves along the channel as droplets. Moreover, liquid water removal from the anode GCs is much slower than that on the cathode side.

Great contributions for understanding the two-phase flow in PEM fuel cell and its effects on cell performance have been given by VOF simulations. However, there are still challenges ahead. One issue of with using the VOF method is related with the several length scales (from few micrometers to meters) present in a PEM fuel cell. Although the VOF method can be applicable at these scales, fully considering the electrodes microstructure is unfeasible due to the high computational times involved. For this reason, researchers have used the homogeneous porous media formulation or have handled the GDL microstructure in a simplified way. Coupling VOF two-phase models with electrochemical reactions and heat transport is another great challenge due to the different length and time scales between simulations. One promising strategy to deal with this issue is to simplify the MEA, and to couple a simpler model describing the heat, mass and electrochemical phenomena occurring in the MEA with a VOF model describing the two-phase flow in the GCs. This scheme was already attempted, but still with a very narrow range of applicability, allowing only to study specific phenomena. A more complete model, but still practical, able to account for water transport from its formation on the CL to accumulation in the GDL and the subsequent removal from the GCs is needed to provide a greater understanding of PEM fuel cells two-phase flow and its implications.

3. TEST STATION, FUEL CELLS AND EXPERIMENTAL PROCEDURES

A PEM fuel cell test station was developed during the present research. A fuel cell with a hardware close to that of an industrial fuel cell was designed, and a transparent fuel cell was employed. The main goal was to obtain experimental data to validate the 1D + 3D model developed in this work (Chapter **5**), including representative polarization curves and the distribution of liquid water inside the cathode side of the transparent fuel cell. The EIS technique was also used to get information about the kinetics of the electrochemical reactions, extracting essential input parameters for the model. Additionally, an experimental study on the MEA design was performed. In this chapter, the features of the test station, fuel cells and MEAs employed are presented. Furthermore, the experimental procedures adopted are described, regarding MEAs conditioning, polarization curves recording, EIS measurements, electrical equivalent fitting, kinetic parameters determination and liquid water visualization inside the transparent fuel cell.

3.1. Test station

A scheme of the PEM fuel cell test facility employed in the present work is shown in **Figure 3.1**. Pictures are displayed in **Figure 3.2**. Hydrogen and air flow rates were regulated by rotameters (Omega FLDH3301C and FLDA3213ST, respectively). Both reactant gases were humidified by bubbling them through heated water. The RH of each gas was monitored by humidity probes (Vaisala HMT337). Stainless steel tubing and glass vessels from water humidification to the fuel cell inlets, as well as the fuel cell, were surrounded by flexible heaters (50 W m^{-1}) and covered with glass wool for temperature control. At the vessels for RH reading and at the fuel cell, temperature was adjusted using readings from the corresponding type-K thermocouples and switching on/off the flexible heaters, both connected to a data acquisition (DAQ) system controlled through the LabVIEW software (National Instruments (NI)). Temperature at the other points of the setup was controlled by stand-alone temperature controllers (Osaka Ok31). Electrochemical measurements were performed using a Zahner Zennium electrochemical workstation coupled with an EL300 electronic load.

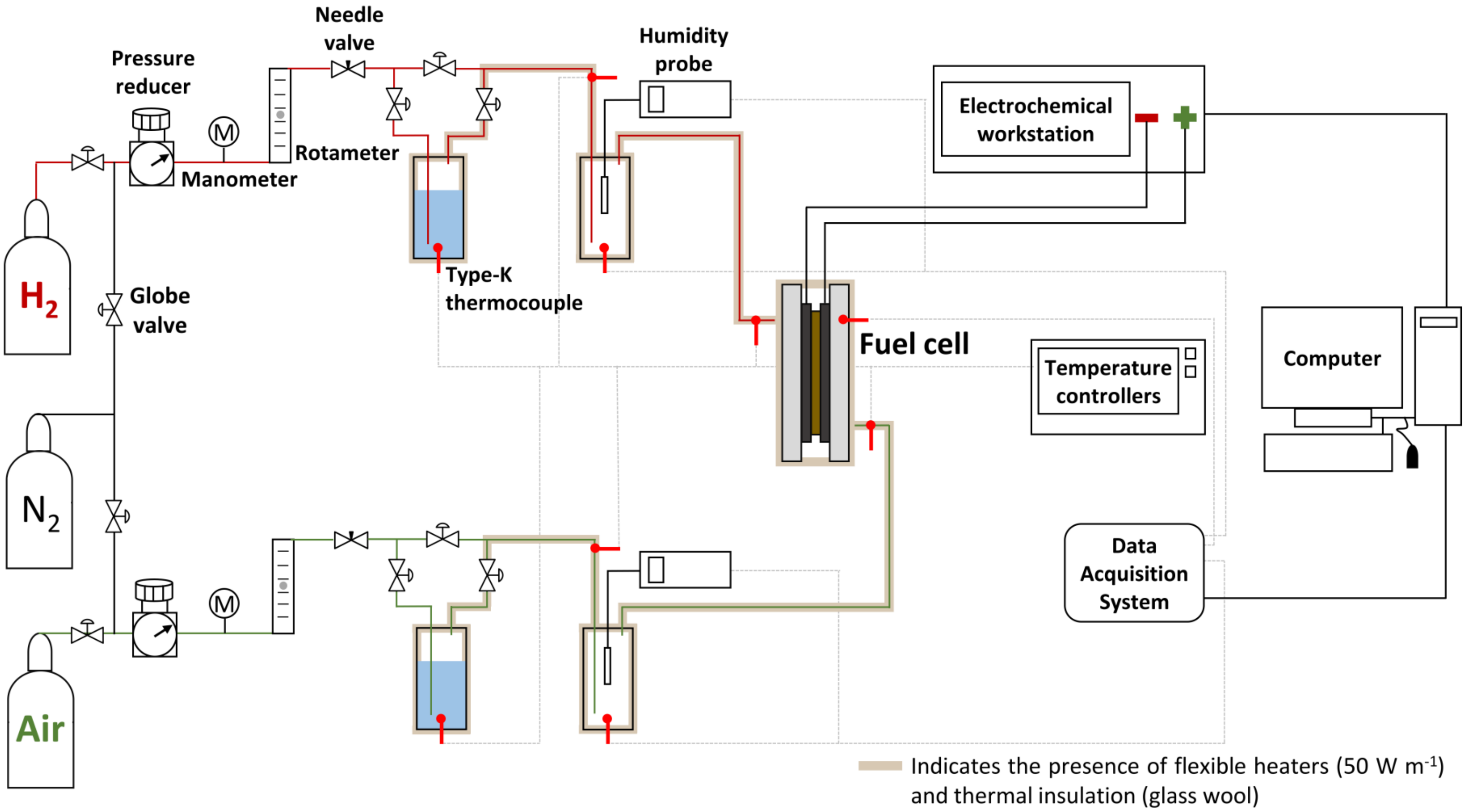

Figure 3.1. Scheme of the PEM fuel cell test facility used in the present work.

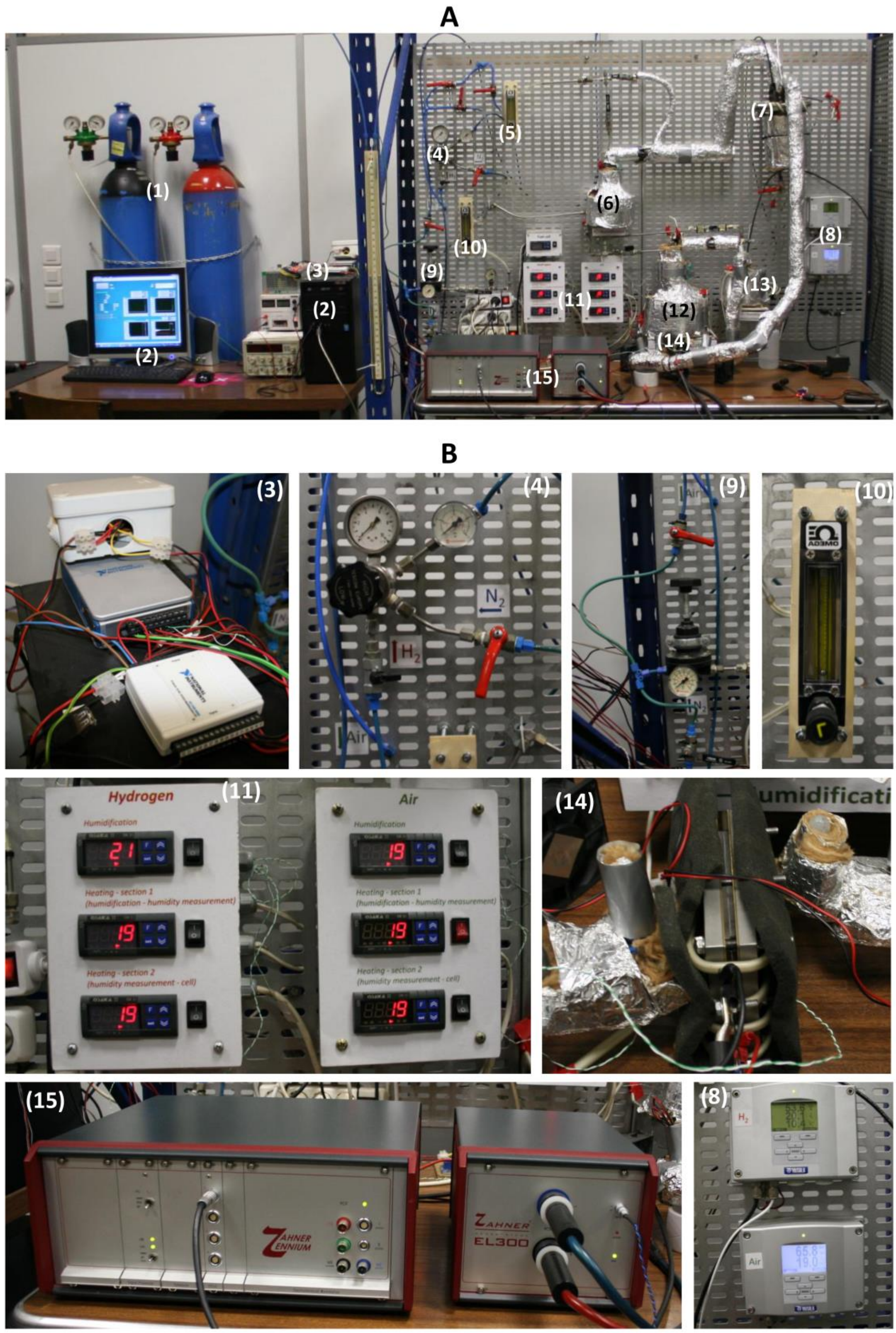

Figure 3.2. Photos showing the (A) entire test station and (B) some of its components. (1) Nitrogen and hydrogen pressurized tanks; (2) Computer; (3) DAQ; (4) Hydrogen pressure reducer and manometers; (5) Hydrogen rotameter; (6) Hydrogen humidification; (7) Hydrogen RH reading; (8) Graphical display of the RH sensors; (9) Air pressure reducer and manometer; (10)

Air rotameter; (11) Temperature controllers; (12) Air humidification; (13) Air RH reading; (14) Fuel cell; (15) Zahner workstation (left) and EL300 electronic load (right).

3.2. Fuel cells and MEAs

3.2.1. Non-transparent fuel cell

A cell with an active area of 25 cm^2 (5 cm × 5 cm) was used. The design and materials applied are close to those of industrial PEM fuel cells. End-plates consisting on 10.0 mm thick stainless steel plates were employed. Gold-copper plates with thickness of 0.5 mm were used as current collectors. Single-serpentine flow fields were machined into 3.5 mm thick graphite bipolar plates, having GCs with cross-section height and width of 1.0 mm and 1.4 mm, respectively. **Figure 3.3** displays photos of the non-transparent fuel cell and its components.

Four different MEAs from QuinTech were tested, all containing a catalyst loading of 0.3 and 0.6 mg Pt cm^{-2} in the anode and cathode sides, respectively. **Table 3.1** displays the features of the MEAs used, concerning the membrane and GDLs employed. Considering MEA 1 as the base case design, it can be seen that MEA 2 is equal to MEA 1 but the latter has a MPL in both electrodes. MEA 3 only differs from MEA 1 regarding the thickness of the Nafion membrane. Apart from a slight deviation in the GDLs thickness, the only difference between MEA 4 and MEA 1 is the PTFE treatment applied to the GDLs of the latter one. **Table 3.1** also displays the water-air static contact angle in one of the GDL surfaces of each MEA, measured with an OCA 15 plus optical contact angle system from Data Physics Instruments. The contact angle in a graphite plate was also measured, obtaining the value of 89.3º ± 0.9º. Measurements were conducted with distilled water at room temperature and pressure. **Figure 3.4** A and **Figure 3.4** B display pictures of water droplets in a graphite plate (hydrophilic) and in a GDL of MEA 2 (hydrophobic) during contact angle measurements, respectively. The MEAs described above were assembled in the non-transparent fuel cell, applying 3.0 N m in each of the 8 screws of the cell with a torque wrench (RS stock. 469-6481) (**Figure 3.3** B (7)).

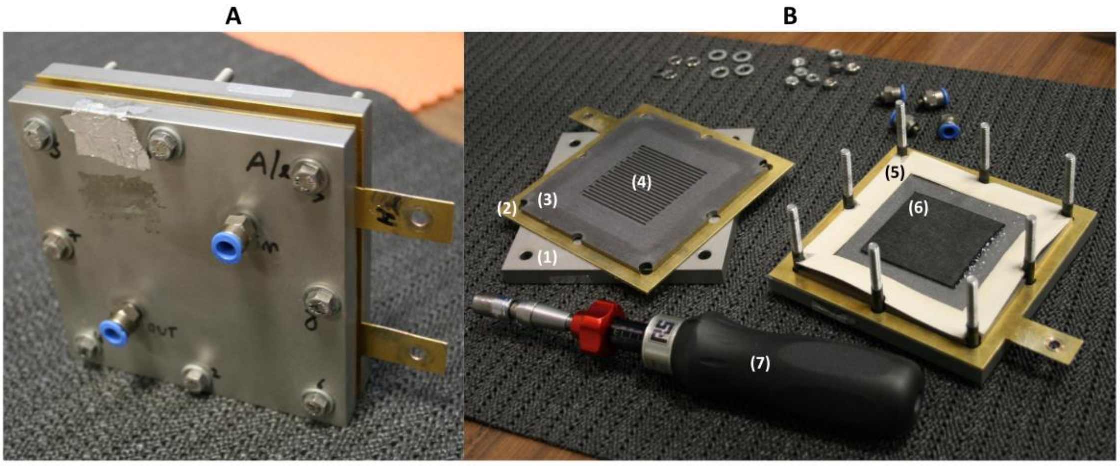

Figure 3.3. Photos of the non-transparent fuel cell and its components, as well as the torque wrench. A – Assembled cell; B – Disassembled cell. (1) Stainless steel end-plate; (2) Gold-coated copper plate; (3) Graphite plate; (4) Single-serpentine flow field; (5) Gasket; (6) MEA; (7) Torque wrench.

Table 3.1. Features of the MEAs tested in the non-transparent fuel cell, related with the membrane and GDLs employed.

	Membrane		**GDL[a] (Freudenberg carbon paper)**			
	Material	**Thickness**	**Thickness[b]**	**Hydrophobic treatment[c]**	**Contact angle[d]**	**MPL**
MEA 1	Nafion 212	50.8 µm	250 µm	Yes	136.6º ± 1.4º	Yes
MEA 2	Nafion 212	50.8 µm	230 µm	Yes	138.3º ± 9.1º	**No**
MEA 3	Nafion 211	**25.4 µm**	250 µm	Yes	140.9º ± 6.7º	Yes
MEA 4	Nafion 212	50.8 µm	255 µm	**No**	**120.1º ± 2.0º**	Yes

[a] Same at the anode and the cathode sides.

[b] Internal thickness at 0.025 MPa. Information provided by the MEAs supplier.

[c] Hydrophobicity conferred with 20-30 wt. % PTFE. Information provided by the MEAs supplier.

[d] Average between measurements made at 3 different locations on the GDL surface, followed by the standard deviation.

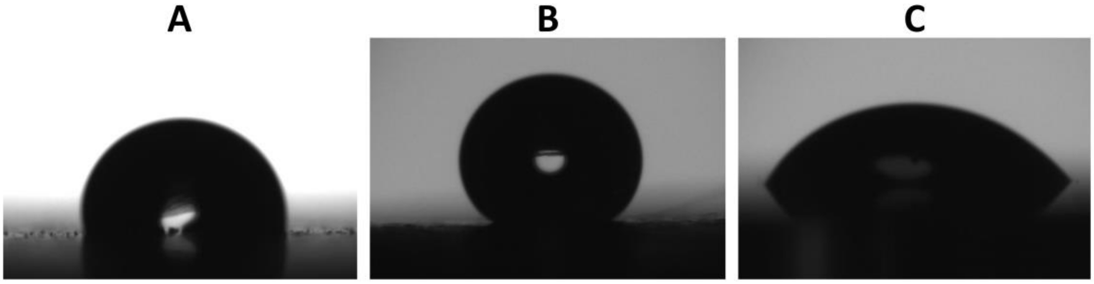

Figure 3.4. Water droplets placed on (A) graphite bipolar plate of the non-transparent fuel cell, (B) GDL surface of MEA 2 and (C) polycarbonate plate of the transparent fuel cell during contact angle measurements.

3.2.2. Transparent fuel cell

A ClearPak fuel cell from Pragma Industries, also with 25 cm^2 of active area, was employed to visualize liquid water behavior inside the cathode side. Two 20.0 mm thick end-plates made of transparent polycarbonate allowed the optical access to the GCs. A single-serpentine flow field, also having GCs with 1.0 mm height and 1.4 mm width, was engraved in both polycarbonate plates. A metallic mesh was employed between the GDLs and the end-plates to collect the current produced. Pictures of the transparent fuel cell and its components are displayed in **Figure 3.5**.

The MEA used in the ClearPak, also provided by Pragma Industries, had a catalyst loading of 0.3 and 0.6 mg Pt cm^{-2} in the anode and cathode, respectively, carbon paper as GDLs, and Nafion XL (thickness of 25.4 µm) as the electrolyte. A 100 µm thick polyethylene terephthalate (PET) sub-gasket was applied on both sides of the Nafion membrane to avoid the contact with the metallic mesh. The contact angle in the GDL and polycarbonate plate surfaces was measured to be $134.0 \pm 3.5^{\circ}$ and $50.3 \pm 0.2^{\circ}$, respectively. A picture of a water droplet in a polycarbonate plate of the transparent fuel cell during contact angle measurement is shown in **Figure 3.4** C. Before being assembled in the ClearPak (applying a torque of 1.5 N m in each of the 8 screws), the MEA was conditioned employing the non-transparent fuel cell described above, and the conditioning procedure provided below.

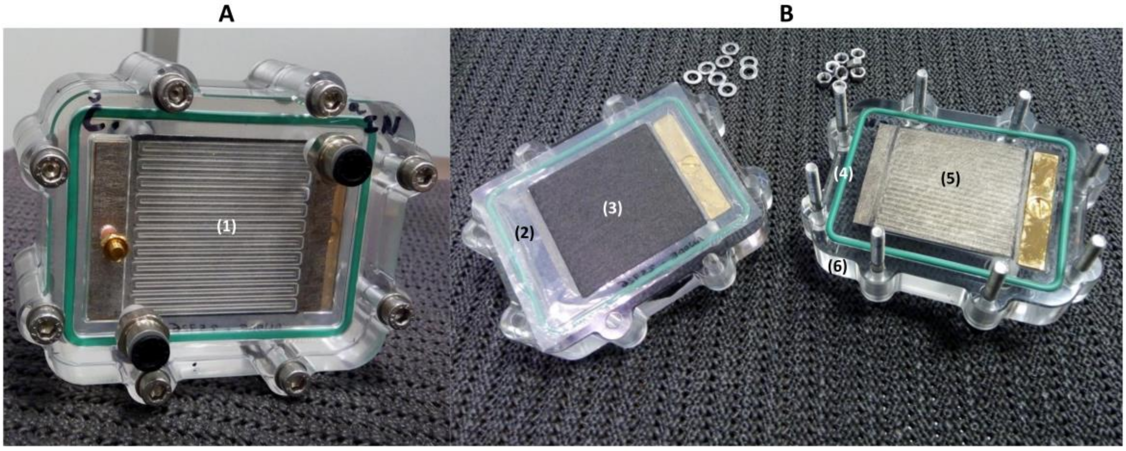

Figure 3.5. Photos of the transparent fuel cell and its components. A – Assembled cell; B – Disassembled cell. (1) Single-serpentine flow field; (2) PET sub-gasket; (3) MEA; (4) Gasket; (5) Metallic mesh; (6) Polycarbonate end-plate.

3.3. Procedures

3.3.1. MEA conditioning

Prior experiments, all MEAs were conditioned. This procedure, also designated as activation or break-in, is required to stabilize the MEA and ensure its best performance before subsequent testing [210]. The conditioning protocol applied in this research is close to the one reported in Ref. [211]. First, the voltage was adjusted to 0.6 V for 30 minutes, then cycles of 0.7 V and 0.5 V (20 minutes at each voltage) were performed. After each cycle, a polarization curve was recorded. The conditioning procedure was finished when no improvement in the cell performance was observed and the average difference (relative error) between subsequent curves was less than 10 %. Conditioning was conducted at a fuel cell temperature of 40 ºC (measured by placing a thermocouple in contact with the MEA at the cathode outlet), atmospheric pressure (considered to be 1 atm), hydrogen stoichiometry (λ_{H_2}) of 1.1 (fixed for a reference current density of 1.0 A cm^{-2}), hydrogen RH (RH_{H_2}) of 50 % (referenced for the cell temperature), air stoichiometry (λ_{air}) of 2.2, and air RH (RH_{air}) of 90 %. Both reactants gases were fed to the cell at 45 ºC.

3.3.2. Polarization curves

Polarizations curves were performed in potentiostatic mode, starting at the OCV and decreasing the voltage, waiting 3 minutes at each voltage. I-V curves were repeated until a stabilized performance was achieved, typically when the average difference between subsequent curves was less than 10 %. Between each curve, the cell voltage was set to 0.5 V for 10 minutes.

I-V graphs, as well as EIS spectra, were recorded for all MEAs employed in the non-transparent fuel cell (**Table 3.1**). Tests were conducted at 40 ºC cell initial temperature and atmospheric pressure. λ_{H_2} of 1.1 and RH_{H_2} of 50 % were used. λ_{air} of 1.4, 2.2, 3.2, 4.4 and 6.6 were tested for RH_{air} of 50 % and 90 %. Reactant gases were fed to the cell at 45 ºC.

3.3.3. EIS, electric equivalent fitting and kinetic parameters determination

EIS measurements were conducted right after polarization curves. Spectra were obtained at 0.80 V, 0.75 V, 0.70 V, 0.60 V, 0.50 V and 0.40 V by superimposing a 5 mV AC signal over a frequency range from 0.1 mHz to 100 kHz. At each voltage, before spectrum recording, a stabilization time of 3 minutes was applied.

Impedance spectra were fitted to an electric equivalent circuit by the complex non-linear regression least squares fitting using the Thales software from Zahner. The electric analogue employed in this work, depicted in **Figure 3.6**, considers a system with two time constants. It includes two resistance (R)-constant phase element (CPE) circuits, connected in series with a resistance and an inductance element (L). R_{act}, R_{ohm}, and R_{mt} are the resistances associated with activation losses in the cathode (kinetic losses in the anode were neglected), ohmic losses and mass transfer losses, respectively. The phenomena behind such losses are described in Chapter **1** (Section **1.3.3**). The CPEs account for the storage of charges at electrode-electrolyte interface taking into account the porous nature of the PEM fuel cell electrodes, and L considers possible interferences due to wires or other sources of disturbance.

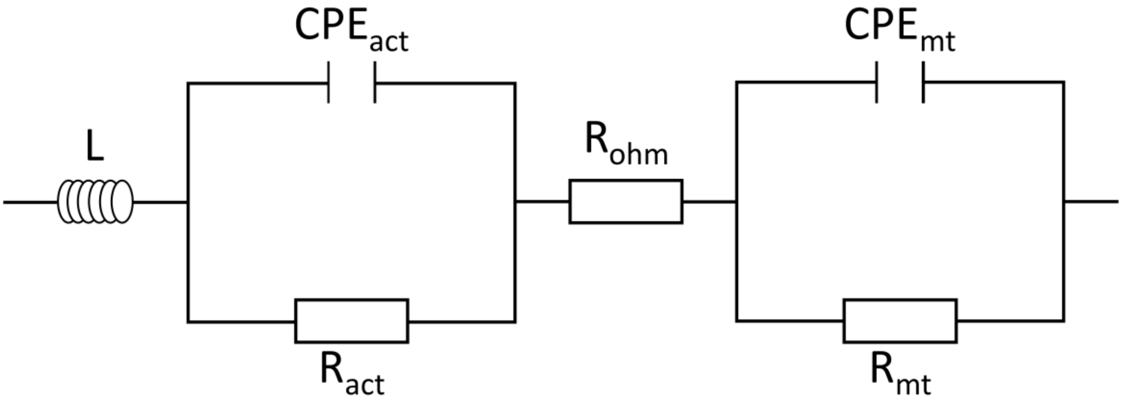

Figure 3.6. Electric equivalent circuit used to fit the EIS results.

In order to determine the electrochemical kinetic parameters, α and I_0, the Tafel equation (Equation **(1.5)**) was first considered in the following form:

$$\eta_{act} = a + b\ln(I) \tag{3.1}$$

where a and b are given by:

$$a = -\frac{RT}{\alpha F}\ln(I_0) \tag{3.2}$$

$$b = \frac{RT}{\alpha F} \tag{3.3}$$

Plotting η_{act} against $\ln(I)$ allows to determine a (y-axis intercept) and b (Tafel slope). Equations **(3.2)** and **(3.3)** were then used to obtain the values of I_0 and α, respectively. η_{act} in Equation **(3.1)** was calculated by:

$$\eta_{act} = OCV - V - R_{ohm}I - R_{mt}I \tag{3.4}$$

where V is the cell operating voltage and R_{ohm} and R_{mt} are obtained through EIS measurements.

3.3.4. Visualization of liquid water distribution inside a transparent fuel cell

For the visualization experiments both gases were fed into the cell at 40 ºC with RH of 50 % and 90 % for hydrogen and air, respectively. In this case, RH was referenced to the reactants inlet temperature. Hydrogen stoichiometry was set to 1.1. Air stoichiometries of 1.4, 2.2 and 3.2 were tested. Before measurements, the cell was left at the OCV for 20 minutes, then the current density was set to 0.10 A cm^{-2} or 0.16 A cm^{-2} for 5 minutes, and pictures of the cathode side were recorded each 2 seconds using a digital camera (Canon EOS 30D). The cell voltage, operating temperature and HFR were monitored during the visualization period. HFR was recorded at 3 kHz. Such frequency was selected based on preliminary EIS measurements with the same MEA employed in the non-transparent fuel cell. It corresponds to the value obtained when the imaginary component of the impedance was close to zero at the high frequency region, and thus the cell is expected to behave in a purely resistive manner [43].

4. EXPERIMENTAL RESULTS

In this chapter, the experimental results obtained in this work are presented. In the first part, published in Ref. [212], the results obtained when investigating the influence of the MEA design on cell performance are shown. The MEAs described in the previous chapter were used in the non-transparent fuel cell, and I-V and EIS measurements were conducted under various air stoichiometries and humidities. The EIS results are first interpreted and the quality of the electric analogue fitting is shown. Then, the effects of the MPL, membrane thickness and GDL hydrophobic treatment are discussed. In the second part, the results obtained when employing the transparent fuel cell are addressed. Its performance is first compared with the one obtained with the non-transparent fuel cell, and then liquid water distribution inside the cathode is analyzed under different current densities and air stoichiometries.

4.1. MEA design

4.1.1. EIS fitting

Figure 4.1 depicts a Nyquist plot (real (Z) versus imaginary (Z') part of the impedance) of EIS spectra for MEA 2, measured at an air stoichiometry of 1.4 and RH of 90 %. It may be seen that at high voltages (0.80 V and 0.75 V), the spectrum consists of a single semicircle, with high frequency intercept R_{ohm} and diameter R_{act}. With decreasing voltage, R_{act} first decreased quite rapidly from 0.80 V to 0.60 V, it remained almost constant at 0.50 V and then increased at 0.40 V. The increase of R_{act} at low voltages occurs when the time scale of the activation processes is close to that of the diffusion processes, so R_{act} may not reflect a pure kinetic control over the low potential range, and it might contain some contributions from other processes such as slow reactants transport [213]. Impedance plots from medium to low voltages (0.70 V to 0.40 V) contained a second loop at the low frequency region, which diameter (R_{mt}) increased when the voltage was decrease. Since water production rate increases with a decrease of voltage, the appearance of R_{mt} and its relation with the cell voltage is associated with liquid water flooding. From **Figure 4.1** it can also be observed a good agreement between the fittings using the equivalent circuit model described in Chapter **3** (Section **3.3.3**) and the experimental results. Impedance spectra with the same general patterns were obtained for the other operating conditions and MEAs employed, with the same level of similarity for the electric analogue fitting.

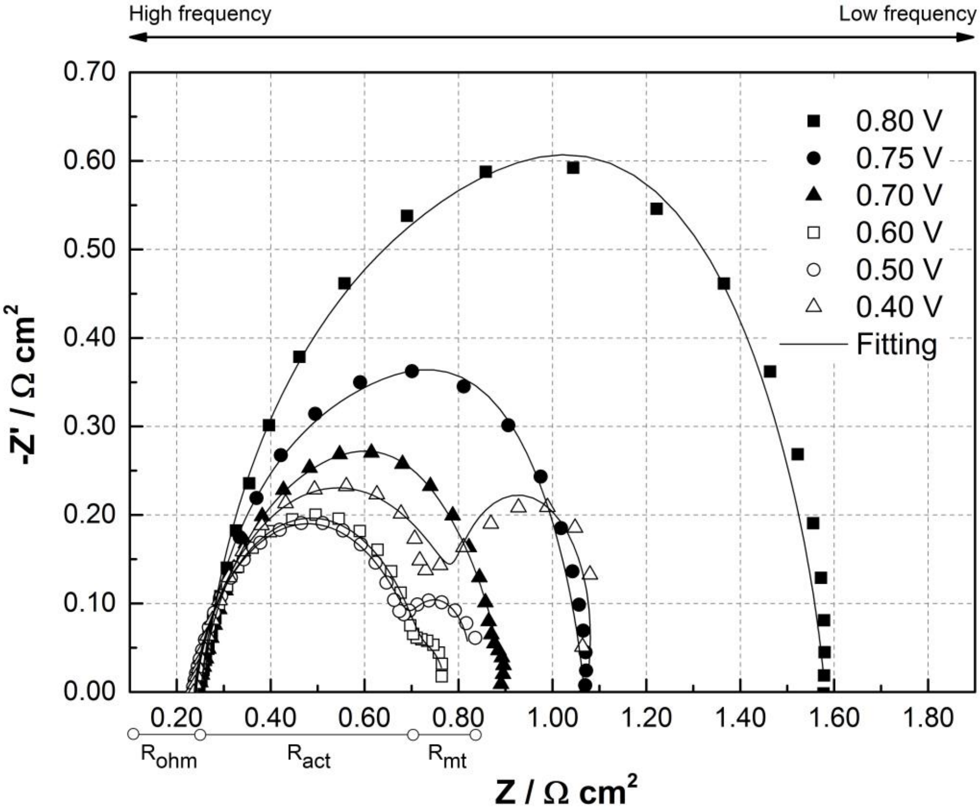

Figure 4.1. Nyquist plot of EIS spectra obtained at various voltages for MEA 2 (Nafion 212 membrane, treated GDL, without MPL).

4.1.2. Effect of MPL

Results obtained for the study of the effect of the MPL are shown in **Figure 4.2**. It includes the cell performance in terms of polarization and power density curves as well as activation, ohmic and mass transfer losses, for a MEA with MPL (MEA 1) and without it (MEA 2). Although five air stoichiometries were tested (1.4, 2.2, 3.2, 4.4 and 6.6), only the results for three of them (1.4, 3.2 and 6.6) are here presented. Since the general trend of the effects of air stoichiometry is kept, this does not affect the discussion of the results and facilitates their graphical interpretation.

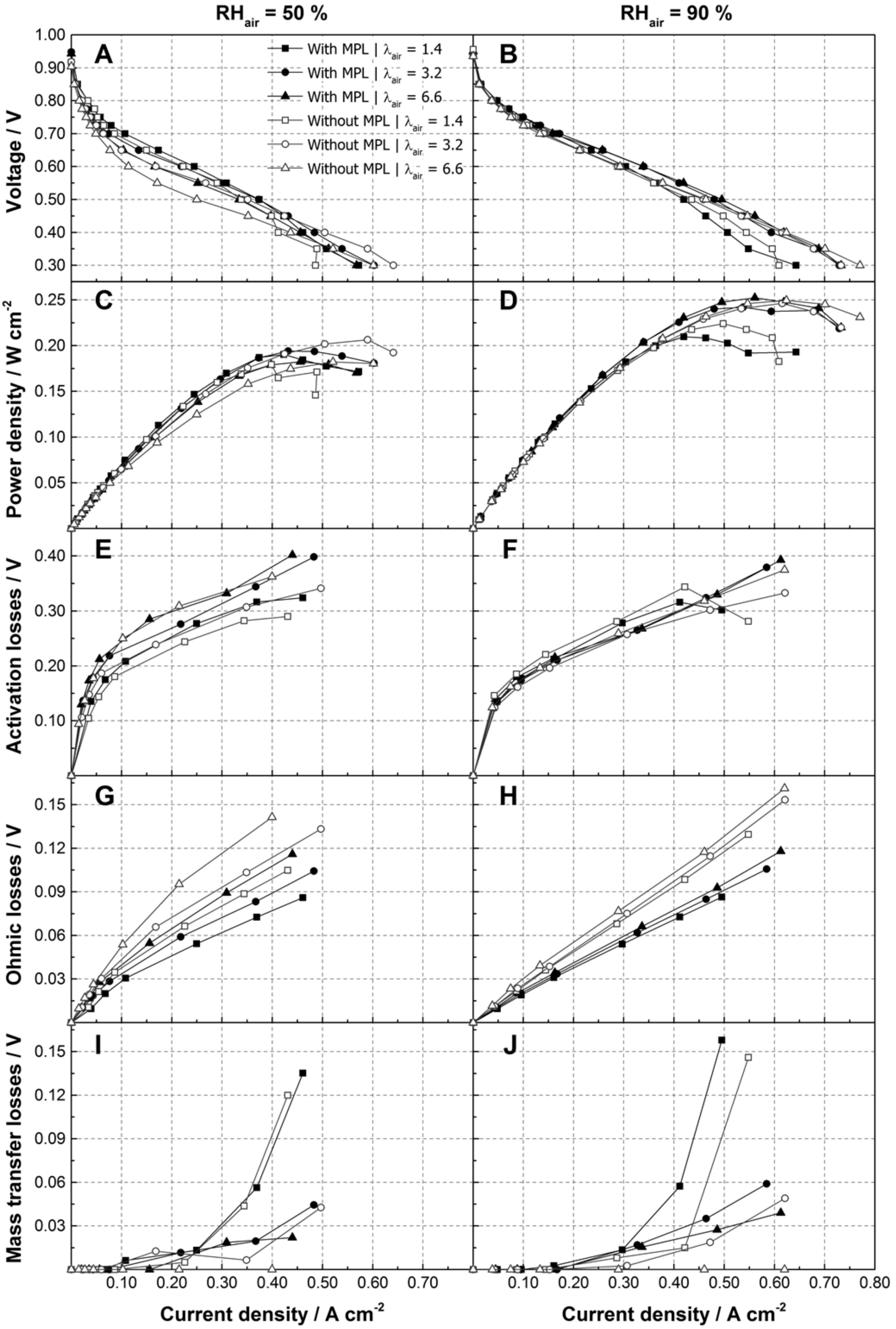

Figure 4.2. Results obtained when investigating the effect of the MPL on the cell performance, including polarization (A and B) and power density (C and D) curves as well as activation (E and F), ohmic (G and H) and mass transfer (I and J) losses, at various air stoichiometries (λ_{air}) and relative humidities (RH_{air}).

Before analyzing the effects of the MPL, the influence of operating conditions is first discussed. Starting by the effects of the air RH, one can observe that the cell performance was improved when the air RH was increased, independently of the air stoichiometry and MEA employed (**Figure 4.2** A-D). Contributing to such results was a better hydration state of the membrane at higher air RH, as shown by the lower ohmic losses obtained at an air RH of 90 % (**Figure 4.2** H) in comparison to those observed for an air RH of 50 % (**Figure 4.2** G), especially at high air stoichiometries. Moreover, activation losses increased when air RH decreased (**Figure 4.2** E and F), due to the dehydration of the CL ionomer that reduces proton activity. The effects of air stoichiometry, on the other hand, were dependent on air RH. For an air RH of 90 %, cell performance tended to increase with increasing air stoichiometry, especially for high current densities and when air stoichiometry was increased from 1.4 to 3.2 (**Figure 4.2** B and D). This was verified for both MEAs, and can be explained through the analysis of the mass transfer losses, which decreased significantly when air stoichiometry was increased (**Figure 4.2** J). Higher air stoichiometries lead to higher air velocities in the cathode side, facilitating water removal and the access of oxygen to the reaction sites of the CL. Moreover, because ohmic losses at an air RH of 90 % just slightly increased with increasing air stoichiometry (**Figure 4.2** H), the membrane was kept reasonably humidified even when the highest air stoichiometry was applied. Different results were observed when the RH of air was set to 50 %, where the best performance was obtained for the middle value of the air stoichiometry (**Figure 4.2** A and C). Under this less humidified condition, ohmic losses (**Figure 4.2** G) were more sensitive to air stoichiometry, and at an air stoichiometry of 6.6 membrane drying was observed. This caused a decrease of the cell performance, particularly for middle values of current density where such losses dominate. Moreover, contrarily to that observed at an air RH of 90 % (**Figure 4.2** F), activation losses at an air RH of 50 % (**Figure 4.2** E) showed significant variation with air stoichiometry. As explained above, this was caused by a decrease in proton activity in the CL due to dehydration of the ionomer, which in this case was intensified by an increase in the air stoichiometry.

Investigating the effect of the MPL, it can be observed that, for lower to medium current densities, the cell performance increased when the MPL was employed (**Figure 4.2** A-D). However, for high currents, better performances were generally obtained for a MEA without MPL. Ohmic losses were found to be lower for the cell having MPL (**Figure 4.2** G and H), which justifies the better performances at low to medium current densities, where this type of voltage loss is dominant. Such improvement was expected taking into account previous studies [14, 23, 26] reporting that, by creating a pressure barrier for the water produced at the cathode CL, the MPL pushes water across the membrane from the cathode to the anode side, hence increasing its water content and proton conductivity. Lower performances at high current densities for the MEA with MPL, however, were somehow unexpected. Because the MPL causes water to move to the anode side, less water would remain in the cathode porous media, hence liquid water flooding should be reduced. Moreover, according to several investigations [25, 27], the MPL should have facilitated liquid water removal from the cathode. The results obtained in the present study do not seem to support such fact, because a decrease in mass transfer losses for the MEA with MPL was not observed. In fact, mass transfer losses tended to increase when adding the MPL (**Figure 4.2** I and J). To explain such results, it should be considered the possibility of liquid water flooding at the anode side of the cell, caused or intensified by the presence of the MPL. Such possible explanation comes from the results obtained by Spernjak *et al.* [23], who visualized liquid water accumulation in the anode GCs only when adding a MPL to the cathode GDL. Although less frequent than that on the cathode, flooding at the anode side can occur under certain operating conditions [23, 58, 59, 61, 214], being in some situations [58, 59] even more severe than that on the cathode. In the present study, it was not possible to distinguish between anode and cathode flooding through the EIS measurements. However, during experiments it was possible to visualize liquid water being flushed out not only at the cathode outlet, but also at the anode outlet for low voltage values, clearly indicating that anode flooding occurred. This was observed for all the MEAs tested. The low hydrogen flow rate and cell operating temperature employed in this study are likely to have contributed to such outcome. The inclusion of a MPL would have intensified anode flooding by bringing more water from the cathode, causing the observed increase in the total mass transfer losses and the decrease in cell performance at high current densities. The results from the present study are relevant because they show what was previously anticipated by Spernjak *et al.* [23], *i.e*, under certain operating conditions, the presence of a MPL may lead to a reduction of the cell performance due to an extended blockage of the anode GCs. Therefore, the application of a MPL should be careful evaluated, and operating conditions and/or cell designs that would potentiate water accumulation in the anode should be avoided.

4.1.3. Effect of PEM thickness

Figure 4.3 contains the results obtained when analyzing the influence of the membrane thickness. It is clearly observed that the performance of the MEA having a thinner Nafion 211 membrane (MEA 3) was considerably higher than that of the MEA containing a thicker Nafion 212 membrane (MEA 1) (**Figure 4.3** A-D). Of the four MEA designs considered in the present study (**Table 3.1**), MEA 3 was the one that provided the highest maximum power density (0.32 W cm^{-2}). Analyzing the voltage losses for each case (**Figure 4.3** E-J), it can be seen that the results obtained were mainly caused by significantly lower ohmic losses observed when applying the thinner membrane (**Figure 6.** G and H). Since Nafion 211 has half of Nafion 212 thickness (**Table 3.1**), it imposes less resistance for proton transport, *i.e.*, protons have to travel a shorter distance to reach the cathode. Moreover, Nafion 211 gets humidified more easily, because the water produced in the cathode reaches the anode side faster due to its lower thickness. This effect can be observed when analyzing the rapid recovery from dehydration for the MEA with Nafion 211 membrane during polarization curves obtained at an air RH of 50 % (**Figure 4.3** A). At low to medium current densities (up to 0.30 A cm^{-2}), a decrease in performance for both MEAs was observed when increasing the air stoichiometry. At such low current operation, little water was produced at the cathode, which was not enough to counteract the large amounts of water being extracted from the membrane by the air stream with increasing velocity. Thus, the membrane tended to dehydrate. However, when current density was about 0.40 A cm^{-2} and higher, the relation of the cell voltage output with the air stoichiometry was inverted for the MEA with Nafion 211, *i.e*, higher performances were achieved when increasing the air stoichiometry. At higher current densities more water was produced at the cathode that was rapidly transported to the anode side of the thin Nafion 211 membrane, providing it with proper humidification. Because membrane drying was no longer observed at high currents, the performance of the cell became dominated by mass transfer losses, which were reduced when increasing air stoichiometry due to a faster liquid water removal from the porous media (**Figure 4.3** I).

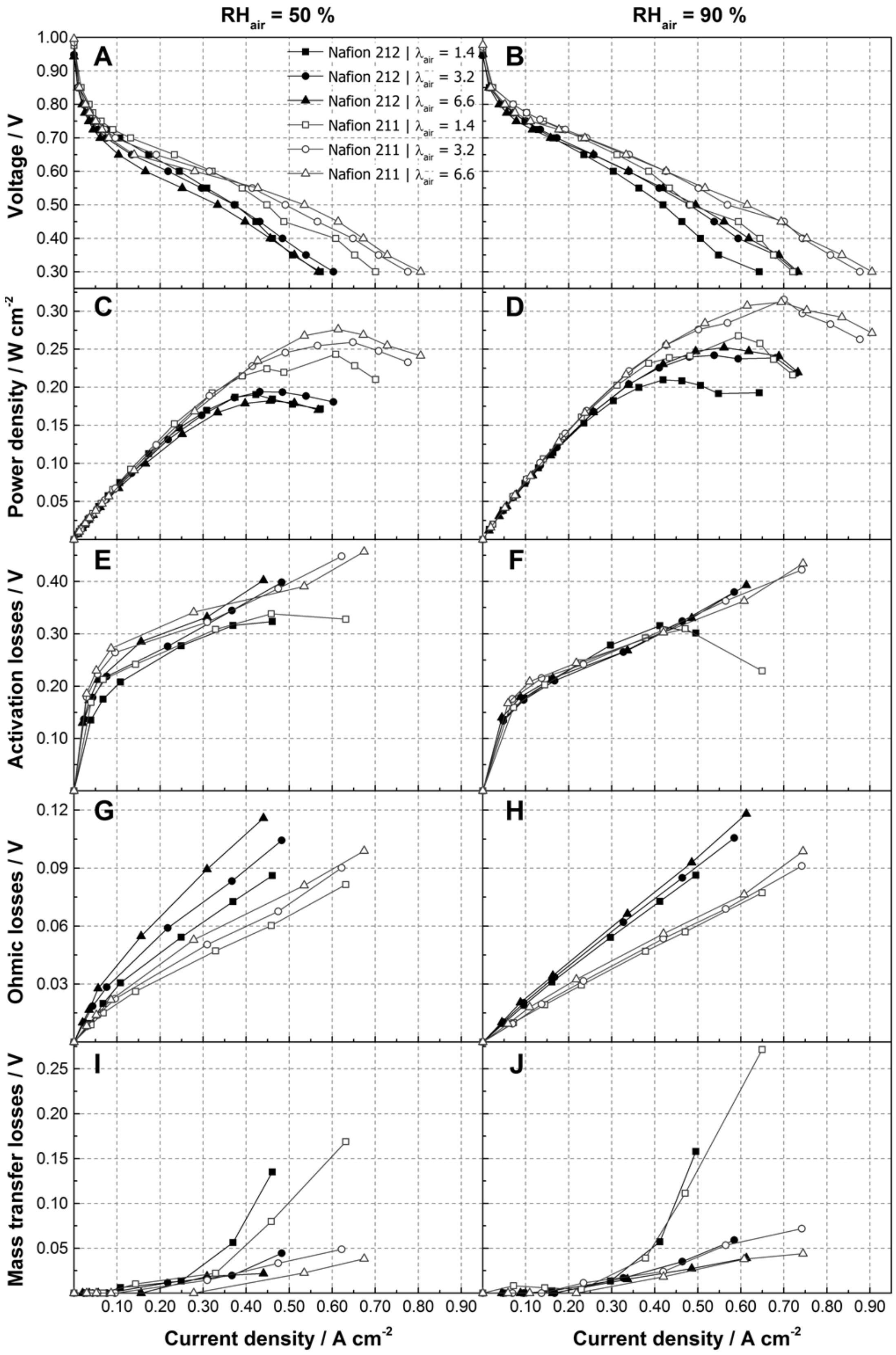

Figure 4.3. Results obtained when investigating the effect of the Nafion membrane thickness on the cell performance, including polarization (A and B) and power density (C and D) curves as well as activation (E and F), ohmic (G and H) and mass transfer (I and J) losses at various air stoichiometries (*λ_{air}*) and relative humidities (*RH_{air}*).

4.1.4. Effect of GDL hydrophobic treatment

The results obtained when investigating the effect of the GDL hydrophobic treatment in the cell performance are presented in **Figure 4.4**. It can be seen that, for all operating conditions tested, the MEA with treated GDLs (MEA 1) had higher performance than that obtained with the MEA containing untreated GDLs (MEA 4) (**Figure 4.4** A-D). From literature, it has been generally observed that adding an optimum dosage of a hydrophobic agent like PTFE or FEP into the GDL lead to an increase of the cell performance because it facilitates water removal, thus decreasing mass transport limitations [14, 16-18]. Although in this study a decrease in mass transfer losses can generally be observed when treated GDLs were employed (except for the higher air stoichiometry tested where mass transfer losses are less relevant) (**Figure 4.4** I and J), this was neither the unique nor the most relevant effect of applying GDL hydrophobic treatment. EIS measurements showed that activation losses increased significantly when untreated GDLs were employed (**Figure 4.4** E and F). Since both MEAs used had equal CLs and were provided by the same manufacturer, such results were not likely to be caused by differences in electrochemical kinetics, but probably by a decrease in proton activity due to ionomer drying. Because untreated GDLs are very inefficient in transporting liquid water, they might have acted as water-traps. Therefore, apart from difficulting oxygen transport to the CLs, an untreated GDL may also keep water out of the membrane and the CLs, contributing to their dehydration. Further analyzing the results at different air RHs seems to support such hypothesis. At an air RH of 90 %, ohmic losses were not affected by the GDL hydrophobic treatment (**Figure 4.4** H). At this condition the air stream had a humidity level close to saturation, so it could remove some water from the ionomer of the cathode CL but it could not take much water from the membrane, therefore the latter was kept properly humidified even when untreated GDLs were employed. However, when the air RH was set to 50 %, adding to a more significant CL ionomer drying (**Figure 4.4** E), ohmic losses increased when untreated GDLs were employed (**Figure 4.4** G). In this case, the less humidified air was capable of removing significant amounts of water from the membrane. Since the untreated GDL trapped significant amounts of liquid water (at high air stoichiometries (3.2 and 6.6) mass transport losses were kept high when untreated GDLs were applied (**Figure 4.4** I)) that otherwise would help to humidify the cell, it intensified membrane drying. Although in a lesser extent than that observed in the present work, Mathias *et al.* [215] also observed poorer membrane hydration (measured by HFR) at low current densities and reactants humidity when untreated GDL were employed.

The relevance of applying EIS is clearly shown here. By allowing to separate the different polarization losses, it revealed that applying a GDL hydrophobic treatment not only resulted into a better drainage of liquid water from the GDL, as shown in previous studies [14, 16, 18], but also had an important role on the overall water management inside a PEM fuel cell, avoiding water to be trapped inside the GDL thus allowing a proper CL ionomer and membrane humidification.

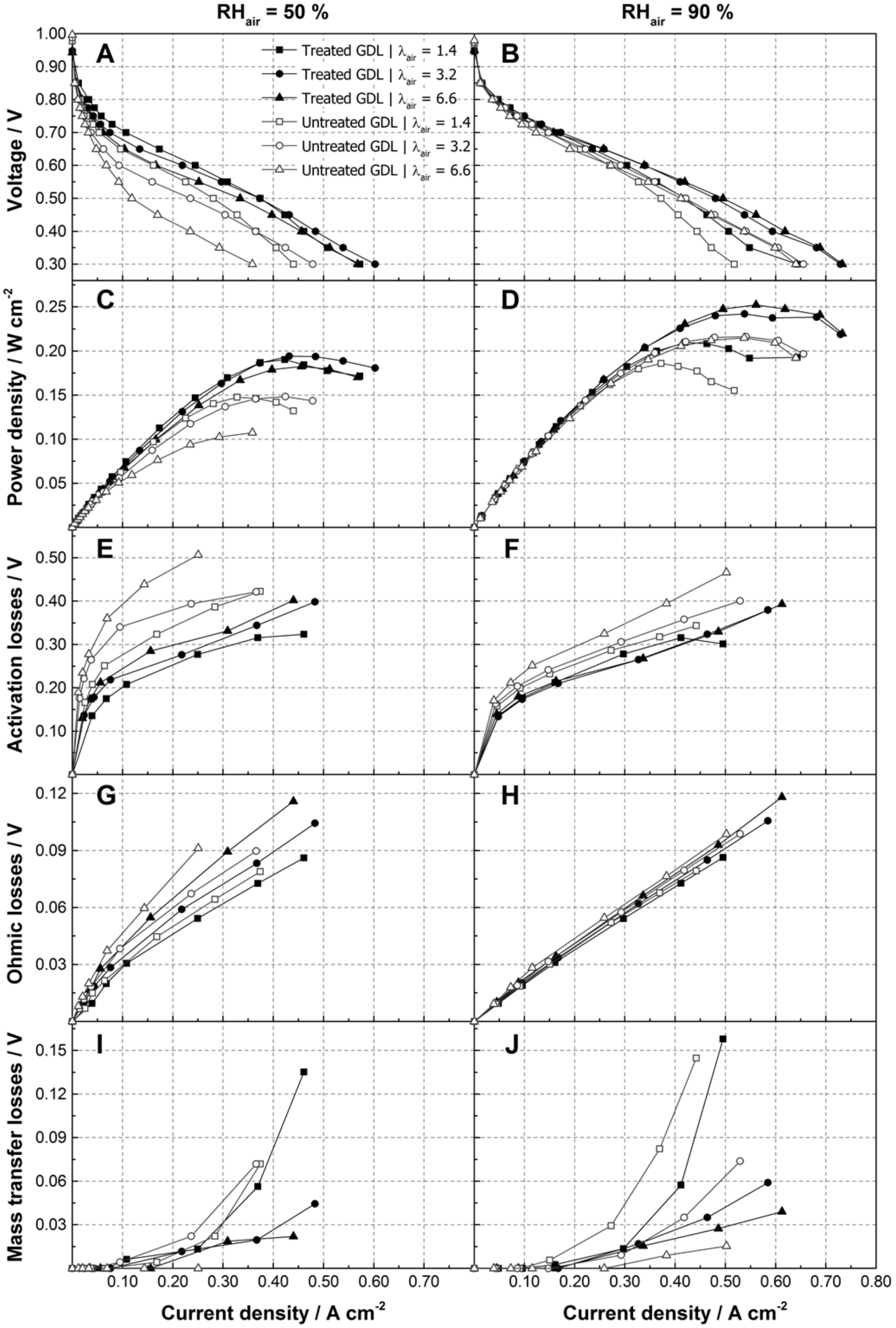

Figure 4.4. Results obtained when investigating the effect of the GDL hydrophobic treatment on the cell performance, including polarization (A and B) and power density (C and D) curves as well as activation (E and F), ohmic (G and H) and mass transfer (I and J) losses at various air stoichiometries (λ_{air}) and relative humidities (RH_{air}).

4.1.5. Summary

In this section, results of a study on the MEA design of a PEM fuel cell were presented. The effects of MPL, Nafion membrane thickness and GDL hydrophobic treatment were analyzed under various air stoichiometries and humidities.

The MPL improved the cell performance for low to medium current densities. However, for high currents, adding a MPL generally decreased the cell performance. By creating a capillary pressure barrier at the CL/GDL interface that pushes water from the cathode to the anode side, the MPL improved the hydration state of the membrane and decreased ohmic losses, which are dominant at low to medium current densities. The same phenomenon at high current densities, however, appeared to have intensified anode GCs flooding, elevating mass transfer losses that control polarization at such conditions. Thus, operating conditions and/or cell designs that would indicate significant water accumulation in the anode should be avoided when planning to apply a MPL.

The performance of a cell with a thinner membrane (Nafion 211) was considerably higher than that having a thicker one (Nafion 212). Such results were found to be caused by lower ohmic losses imposed by the thinner membrane. Moreover, during polarization curves at low air RH, the cell with Nafion 211 membrane showed a rapid recovery from dehydration for all the air stoichiometries employed.

GDL hydrophobic treatment significantly improved the cell performance. EIS measurements showed that it not only facilitated liquid water removal from the GDL, but also provided a better overall water management inside the cell. Untreated GDLs seem to have functioned as water-traps that kept most water inside the GDLs. This not only increased mass transfer limitations but also impeded the proper humidification of the CL ionomer and the membrane.

From all the MEAs analyzed in this study, the best performance, in terms of maximum power density, was obtained when using the one with MPL, Nafion 211 membrane and GDLs with hydrophobic treatment.

4.2. Liquid water visualization inside a transparent fuel cell

4.2.1. Transparent fuel cell performance

Figure 4.5 displays the performance of the transparent and the non-transparent fuel cells. It can be seen that the transparent cell performed considerably worse than the non-transparent one. At low current densities (less than 0.05 A cm^{-2}), when activation losses dominate, the performance of both cells was comparable. However, for higher currents, when the cell performance becomes dominated by ohmic losses, the performance of the transparent fuel cell dropped rapidly. Such results were probably caused by the different materials employed in the transparent cell. The polycarbonate end-plates of the transparent fuel cell have very low thermal conductivity, so the heat produced by the cell was hardly removed. **Figure 4.6** shows the temperature variation of the transparent fuel cell during polarization curve recording. It can be seen that the cell temperature increased significantly, even applying a waiting time at each voltage of just about 1 minute, instead of the 3 minutes applied with the non-transparent fuel cell. Such rapid increase of the cell temperature is likely to have cause the membrane to dehydrate, decreasing proton conductivity and increasing ohmic losses. Another factor that may have contributed to the results obtained was the use of a metallic mesh to extract the electrical current produced by the transparent cell. This mesh is hardly as effective in collecting the current as the bulk graphite plate applied in the non-transparent fuel cell, resulting into higher electrical resistance that also raises ohmic losses. Furthermore, this leads to more heat being released within the cell (Joule heating), intensifying the cell temperature increase and membrane drying.

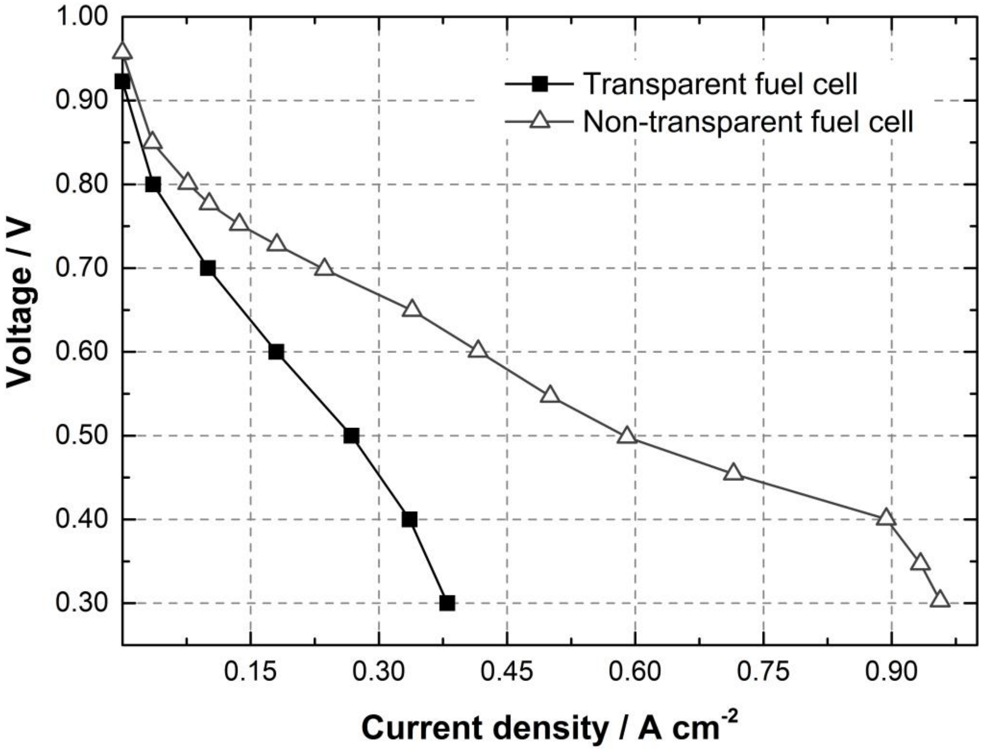

Figure 4.5. Performance of the transparent and the non-transparent fuel cells.

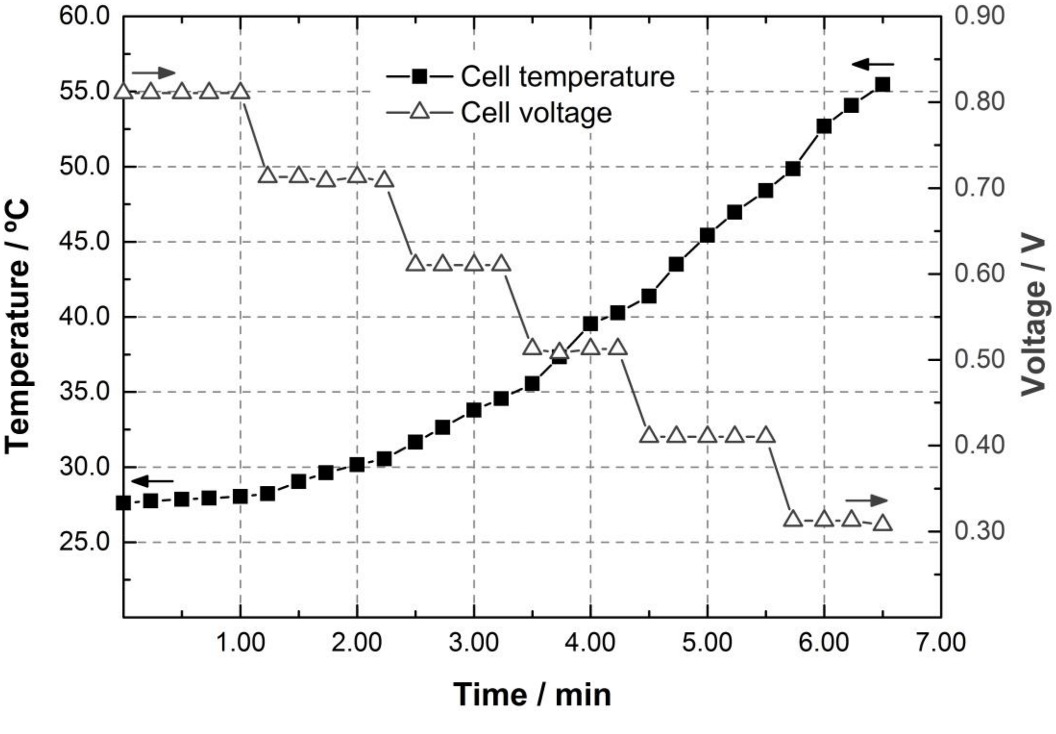

Figure 4.6. Temperature (left vertical axis) and voltage (right vertical axis) of the transparent fuel cell during polarization curve recording.

4.2.2. Water distribution in the cathode

The results presented above clearly show the importance of the materials choice to the performance of a PEM fuel cell. Moreover, they reveal the limitations of the transparent fuel cell and help to explain the experimental procedure adopted in the visualization experiments (Section **3.3.4**), which results are presented below. Low current densities (0.10 A cm^{-2} and 0.16 A cm^{-2}) were applied in order to prevent the excessive heating of the cell, which would rapidly evaporate all the liquid water. Because such low currents resulted into very low liquid water production rates, the cell was kept at the OCV during 20 minutes before each measurement, while feeding almost-saturated air (RH = 90 %) and at a higher temperature (40 °C) than that of the cell (about 30 °C). This allowed liquid water accumulation in the cell by condensation of water vapor from the air stream, and then its dynamics could be visualized.

Figure 4.7 and **Figure 4.8** display images of liquid water distribution inside the cathode side of the transparent fuel cell, at 0.10 A cm^{-2} and 0.16 A cm^{-2}, respectively, and for various air stoichiometries. **Figure 4.9**, **Figure 4.10** and **Figure 4.11** show the cell voltage, temperature and ohmic losses (obtained through HFR), respectively, during the 5 minutes visualization period. First, the effects of operating conditions are discussed by looking to the overall amount of water present in the cathode in each case. Then, the focus is on the main two-phase flow patterns visualized during the experiments.

At 0.10 A cm^{-2} (**Figure 4.7**), it can be observed that liquid water remained in the cell during the entire visualization period for all the air stoichiometries employed. Moreover, differences in the water content between tests with different air stoichiometries are slight and only clearly visible after 5 minutes. At this instant, it can be seen that the water content seems to decrease as air stoichiometry increases. This occurs because at higher air stoichiometries the increased air velocity facilitates liquid water removal. At this current density, the cell temperature (**Figure 4.10**) remained lower than the reactants inlet temperature (40 °C). This helped to keep the hydration state of the membrane, as shown by ohmic losses (**Figure 4.11**) that remained constant during the visualization period. The cell voltage (**Figure 4.9**) was also stable during the experiments and almost did not change when varying the air stoichiometry. At 0.16 A cm^{-2}, when air stoichiometry was adjusted to 1.4, there was no substantial difference between the water distribution observed (**Figure 4.8** A) and that obtained at 0.10 A cm^{-2} (**Figure 4.7** A). Although the highest cell temperature was obtained at 0.16 A cm^{-2} and air stoichiometry of 1.4

(**Figure 4.10**), this did not cause the membrane to dehydrate (as shown by the stable ohmic losses obtained at this condition (**Figure 4.11**)) and the cell voltage to decrease (**Figure 4.9**). The slow air flow is less effective in removing heat from the cell, and that is why temperature was higher is this case. However, such air steam also removes less water from the cell, and this explains why the membrane remained hydrated and the cell performance did not decrease. At an air stoichiometry of 2.2 and 0.16 A cm^{-2}, although the cell voltage was not affected (**Figure 4.9**), it can be seen that ohmic losses slightly increased over time (**Figure 4.11**). After 5 minutes of operation, the water content in the cathode (**Figure 4.8** B) was lower than that observed at 0.10 A cm^{-2} (**Figure 4.7** B), showing some signs of membrane dehydration. When the air stoichiometry was set to 3.2, membrane drying was clearly observed, as shown by the considerable increase of ohmic losses (**Figure 4.11**) with respect to time and the corresponding decrease of the cell voltage (**Figure 4.9**). At this condition, there was almost no liquid water in the cathode after 2 minutes of operation (**Figure 4.8** C).

Several two-phase flow patterns could be observed during the visualization experiments. Water droplets (**Figure 4.7** (1) and **Figure 4.8** (1)), formed by water condensation, were visible under the various conditions tested, being more abundant for the lower air stoichiometry applied. At higher stoichiometries, the shear force of the air flow removed the droplets more easily and/or caused them to coalesce into films and/or slugs. Long water films attached to the side walls of the channel could also be visualized (**Figure 4.7** (2) and **Figure 4.8** (2)), due to the hydrophilic nature of these surfaces. Moreover, a trend for water to accumulate at the elbows of the serpentine channel was observed (**Figure 4.7** (3) and **Figure 4.8** (3)). This was caused by the lower air velocity that is generally verified in these regions. In addition, the occurrence of water slugs occupying most (**Figure 4.7** (4)) or the entire (**Figure 4.7** (5)) cross-sectional area of the serpentine channel was captured. The flow patterns observed during the visualization experiments of the present work generally agree with those from other studies [23, 60, 208, 216, 217] (also schematized in **Figure 2.3**). How such two-phase flow patterns appear and develop over time is addressed in more detail in the next chapters, when analyzing the results of numerical simulations.

Figure 4.7. Liquid water distribution in the cathode of the transparent fuel cell over time, at 0.10 A cm^{-2} and various air stoichiometries (λ_{air}) (1) Droplets; (2) Films; (3) Accumulation at the elbows; (4) Slugs filling most of the cross-section; (5) Slug filling the entire cross-section.

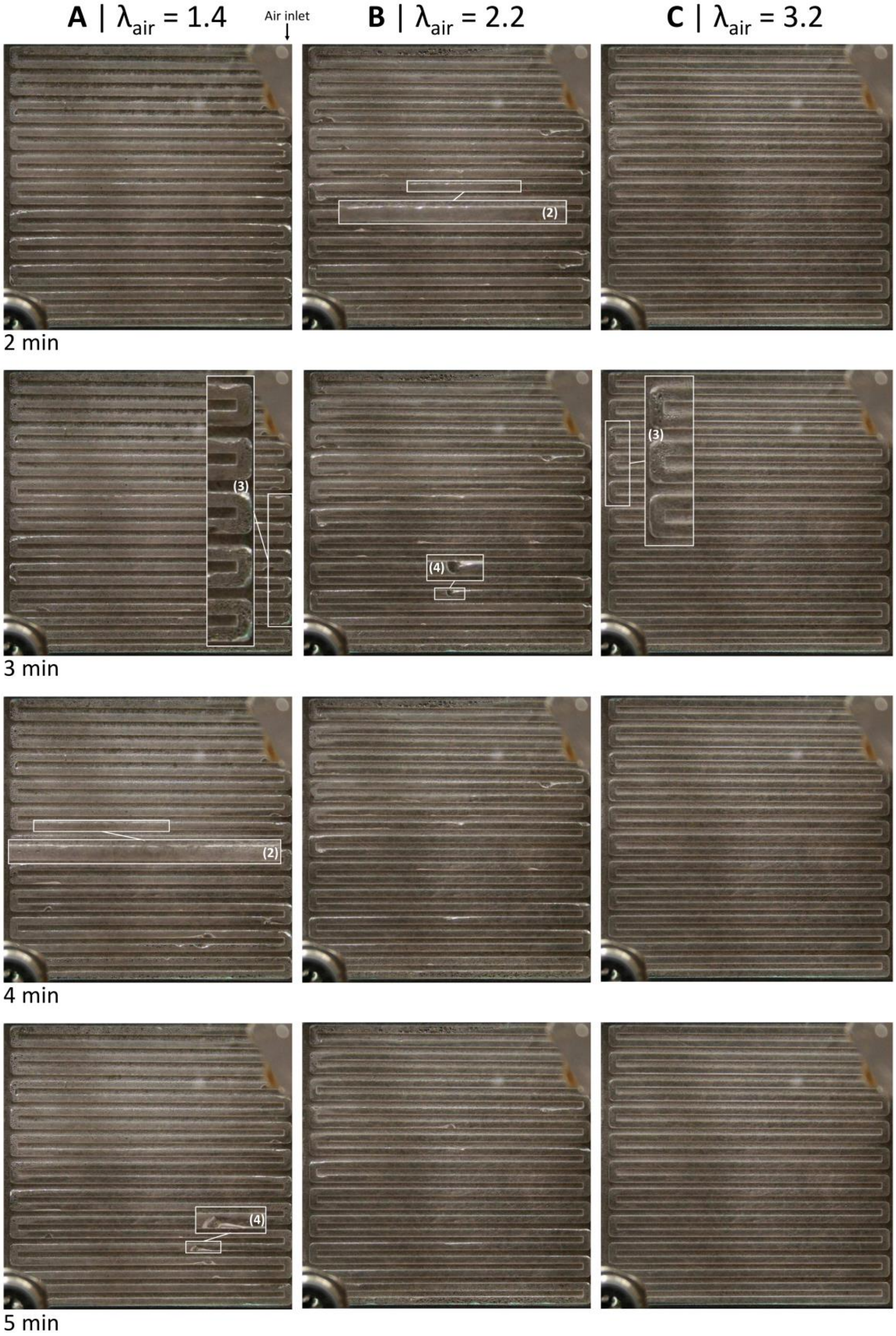

Figure 4.8. Liquid water distribution in the cathode of the transparent fuel cell over time, at 0.16 A cm^{-2} and various air stoichiometries (λ_{air}). (1) Droplets; (2) Films; (3) Accumulation at the elbows; (4) Slugs filling most of the cross-section; (5) Slug filling the entire cross-section.

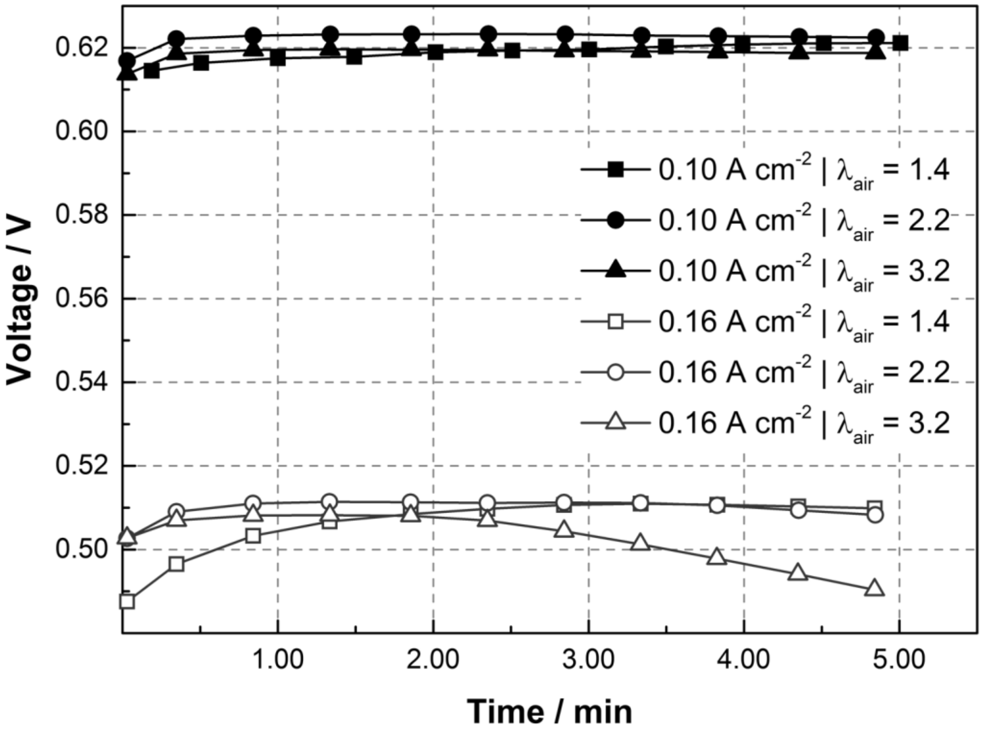

Figure 4.9. Voltage of the transparent fuel cell during the visualization experiments.

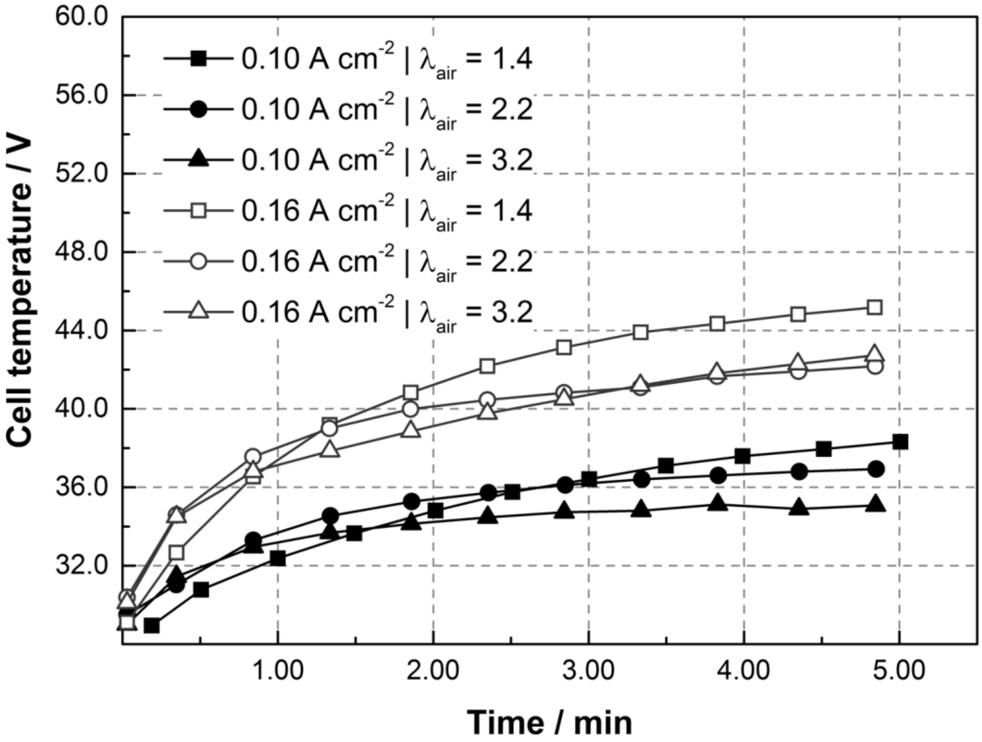

Figure 4.10. Temperature of the transparent fuel cell during the visualization experiments.

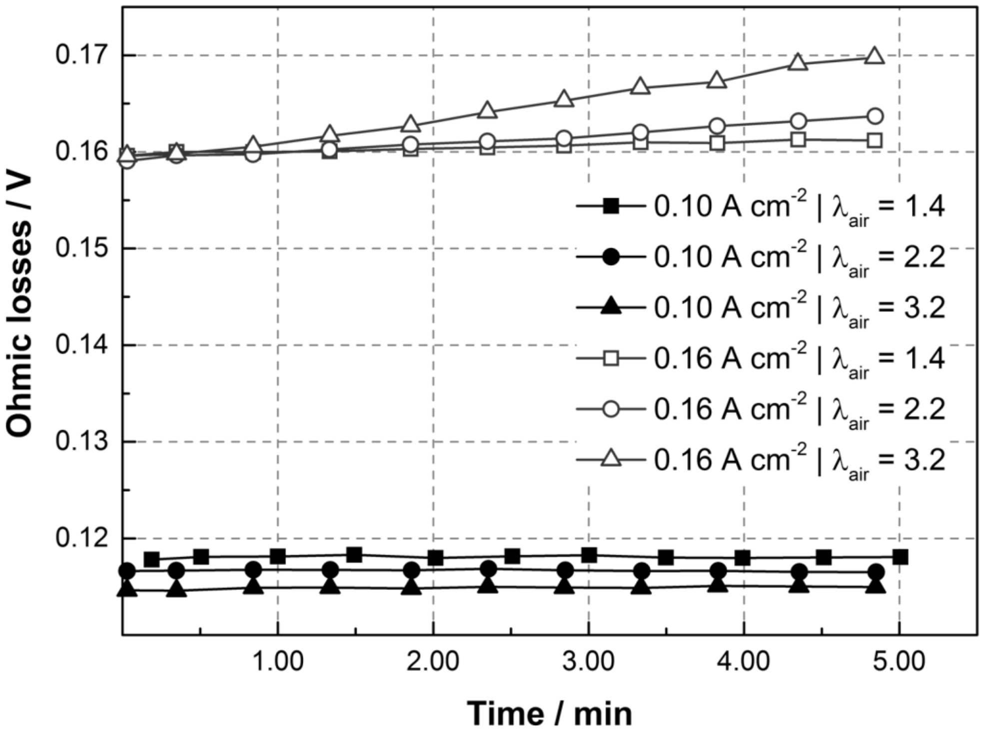

Figure 4.11. Ohmic losses of the transparent fuel cell during the visualization experiments.

5. 1D + 3D MODEL

The present chapter is devoted to the 1D + 3D model developed during this work. The model is first described in detail, addressing its computational domain, geometry and mesh, general assumptions, mathematical formulation, numerical implementation and calculation procedure. Results of its validation are then shown, where the model predictions are compared with an experimental polarization curve, individual voltage losses and liquid water distribution inside the transparent fuel cell. Finally, the main outputs of the model are analyzed, including water dynamics in a serpentine channel, current density and liquid water spatial distributions, two-phase flow pressure drop and the effects of flooding in the cell performance.

5.1. Description

5.1.1. Computational domain

In a PEM fuel cell, the most important performance losses are mainly related with the cathode operation. One reason is the slower kinetics of the ORR in the cathode in comparison with that of the HOR occurring in the anode. The cathode is also the electrode where water is generated and, therefore, where flooding is generally more significant. Moreover, the flow rate, viscosity and density of air in the cathode are considerably higher than those of hydrogen in the anode, which also makes this electrode the most influential for the hydration state of the membrane. For these reasons, the model developed in this work considers a 3D computational domain for the cathode GDL and GCs, being the cathode CL, the membrane and the anode side simplified to a 1D computational domain, as schematized in **Figure 5.1**. This computational domain, inspired in previous works [131, 218], allows to considerably decrease the grid requirements and to achieve acceptable computational times, without missing relevant physical details that influence the performance of a PEM fuel cell.

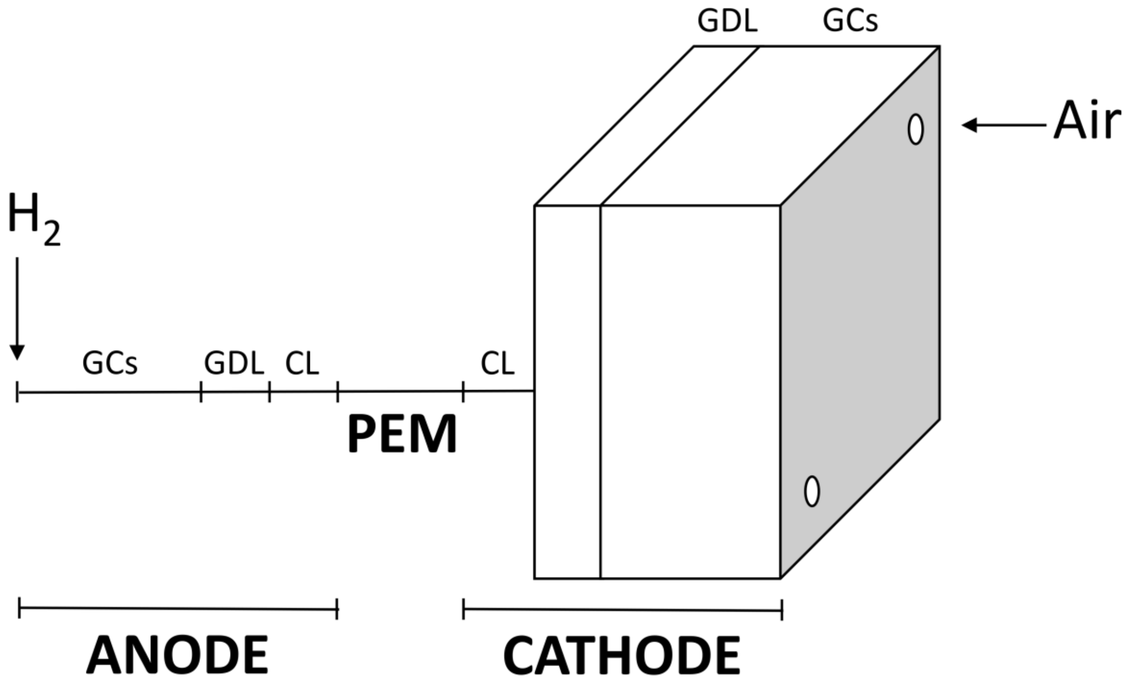

Figure 5.1. Schematic representation of the computational domain used.

5.1.2. Strategy for simulating liquid water dynamics in the cathode

At the end of Chapter **2**, based on findings from experimental and numerical studies, the water dynamics in the cathode and anode sides of a PEM fuel cells was described. Here, the general process of water transport in the cathode is briefly recalled as it helps to understand the methodology applied in the present model. A scheme is also provided in **Figure 5.2** to better illustrate liquid water transport. In the cathode, most liquid water first appears in the CL. When it reaches the GDL, liquid water moves by capillary flow through preferential pathways, those with the greatest cross-sections and therefore with less capillary pressure resistance. In the GCs, water emerges as droplets at the GDL surface. These droplets grow until they reach a critical size and detach from the GDL. After detachment, they can move downstream as single-droplets, or they can interact with other droplets leading to the formation of films and/or slugs. With a constant water production rate (*i.e.*, constant current operation), this process tends to repeat itself.

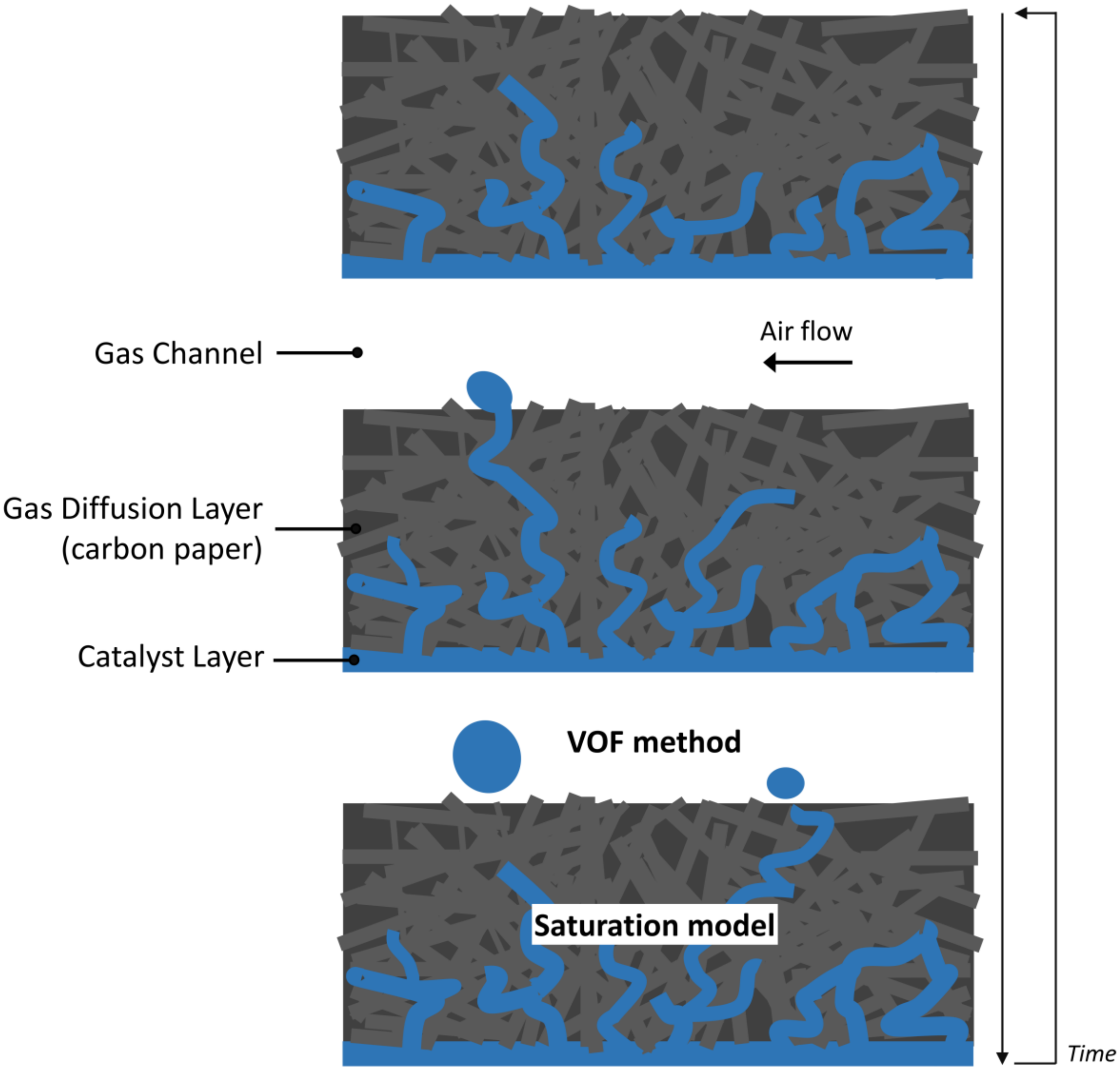

Figure 5.2. Scheme of water dynamics in the cathode of a PEM fuel cell, and indication of the domains where the VOF and saturation models are used for simulating liquid water transport.

The numerical simulation of all these processes is a significant challenge. Early two-phase flow modeling approaches, the multiphase-mixture and multi-fluid model, already presented in Chapter **1**, allow to reasonably describe the liquid flow inside the highly-resistant porous media, when appropriate effective transport properties are considered. However, as also pointed in Chapter **1**, liquid water velocity in the GCs is assumed to be equivalent to the gas velocity, making these models incapable of identifying the presence of droplets, films or slugs that accumulate in GCs. That is why interface tracking algorithms, particularly the VOF method, have been used. Although theoretically the VOF technique can also be applied to the scales of PEM fuel cells porous media, their complex microstructure needs be included in the domain, and that makes the resulting mesh untreatable with the current computational capacity. Another option is to use the homogeneous porous media formulation to consider liquid water transport in the GDL along with the VOF method. However, this would result in an uniform liquid water transport through the porous media and water emergence in the GCs without the formation of droplets [151]. As discussed and illustrated above, this is different from what is observed in operating PEM fuel cells.

In an attempt to adequately describe liquid water transport in the cathode of a PEM fuel cell, the present model considers two different two-phase flow approaches. In the GDL, liquid water transport is accounted for using the multi-fluid saturation model. This approach allows to obtain the distribution of water in the GDL as liquid water saturation, and to compute its effects on the cell performance. In the GCs, several pores are designed at the GDL surface to represent the main pathways for liquid water emergence, and the VOF interface tracking technique is used to capture the dynamics of liquid water. Water velocity in each pore is obtained based on the water generation rate nearby. This approach combines advantages of the two modeling techniques, and allows to simulate the main two-phase flow processes in the cathode in practical manner and to achieve a wide range of applicability. The domain where each two-phase flow model is applied is also indicated in **Figure 5.2**.

5.1.3. General assumptions

The present model relies on the following main assumptions:

- Gases are considered as ideal;
- The flow is considered laminar and under isothermal conditions;
- All materials are assumed to be isotropic;
- Gravity effect is neglected.

The flow is assumed laminar due to the lower Reynolds number (Re) verified. Re did not exceed 1000 in the simulations conducted of this work. Gravity is neglected taking into account the low values of the Bond number (Bo), which were not higher than 0.14. Other more specific assumptions and simplifications are considered for decreasing mathematical efforts and achieving more numerical stability. For a better comprehension, such simplifications are presented below along with the model description.

5.1.4. Mathematical formulation

5.1.4.1. 3D domain

VOF method for tracking the interface

The general formulation of the VOF technique is described in Chapter **2** (Section **2.1.2**). Here, equations are re-written showing their form when applying the VOF method to simulate the two-phase flow occurring in the cathode side of a PEM fuel cell. In this electrode there are two phases, liquid water and air, so their volume fractions (f_{air} and f_w, respectively) are related by:

$$f_{air} + f_w = 1 \tag{5.1}$$

Tracking the interface can then be achieved by solving the equation below in each computational cell:

$$\frac{\partial f_w}{\partial t} + \nabla \cdot (f_w \vec{v}_w) = 0 \tag{5.2}$$

The governing continuity and momentum equations take the following form:

$$\frac{\partial \rho}{\partial t} + \nabla \cdot (\rho \vec{v}) = 0 \tag{5.3}$$

$$\frac{\partial}{\partial t}(\rho \vec{v}) + \nabla \cdot (\rho \vec{v} \vec{v}) = -\nabla P + \nabla \cdot [\mu(\nabla \vec{v} + \nabla \vec{v}^T)] + \vec{F} \tag{5.4}$$

where ρ and μ are calculated as:

$$\rho = f_{air}\rho_{air} + f_w \rho_w \tag{5.5}$$

$$\mu = f_{air}\mu_{air} + f_w \mu_w \tag{5.6}$$

In the GCs, $\vec{F}$ is obtained by adopting the CSF model [142], here given by:

$$\vec{F} = \tau \frac{\rho \kappa_w \nabla f_w}{\frac{(\rho_{air} + \rho_w)}{2}} \tag{5.7}$$

κ_w is defined in terms of $\hat{n}$, and are calculated using Equations **(2.9)** and **(2.10)**, respectively. Equation **(2.11)** here becomes:

$$n = \nabla f_w \tag{5.8}$$

For the porous GDL, the Darcy drag force term is added into the momentum source term, so $\vec{F}$ is obtained by:

$$\vec{F} = \tau \frac{\rho k_w \nabla f_w}{\frac{(\rho_{air} + \rho_w)}{2}} - \frac{\mu}{K} \vec{v} \tag{5.9}$$

where K represents the intrinsic GDL permeability. An important procedure applied in the present model should be mentioned here. In PEM fuel cells, liquid water enters the GCs in the form of droplets which diameter grows to values considerably larger than that of the GDL pores. Therefore, the GDL acts as a wall when liquid water from the GCs touches its surface. Because GDLs are usually treated with a hydrophobic agent in order to facilitate water removal, such surface acquires a hydrophobic nature. For this reason, most VOF numerical studies focusing on the two-phase flow in the GCs specify the GDL surface as a hydrophobic wall. However, in this work, setting the cathode GDL/GCs interface as a hydrophobic wall would numerically inhibit the air flow through the GDL. This issue is overcome by specifying a lower value of K for the liquid phase. For air, K is set to 10^{-12} m^2, a typical value for GDL materials used in PEM fuel cells [4, 165, 167, 219]. For liquid water, a value of 10^{-15} m^2 is used. This decreases liquid water accumulation in the GDL, allowing to simulate the hydrophobic nature of its surface. Preliminary simulations were conducted in which the results obtained employing the present approach were compared with those where the GDL surface was set as an actual hydrophobic wall, and good agreement was achieved (**Appendix A**). It should be noted that, in the GDL, where liquid water transport is accounted for by the saturation model, the appropriate value of liquid water permeability is considered (**Table 5.1**).

Species transport

Since the gas-phase, air, is composed of several species, the conservation equation for each specie needs to be solved. It is given by:

$$\frac{\partial}{\partial t}(\varepsilon \rho_{air} Y_i) + \nabla \cdot (\rho_{air} Y_i \vec{v}) = -\nabla \cdot (\rho_{air} D_i \nabla Y_i) \tag{5.10}$$

where ε stands for porosity, and Y_i and D_i are the mass fraction and the effective diffusivity of specie i (O_2, H_2O or N_2), respectively. D_i is calculated by:

$$D_i = D_i^0 \varepsilon^m (1-s)^n \tag{5.11}$$

where s is the liquid water saturation. D_i^0 is the binary diffusion coefficient obtained using Fuller, Schettler and Giddings correlation [220]. In Equation **(5.11)**, Bruggeman correlation with exponents m and n equal to 1.5 has been largely applied. However, it has been argued that employing such values considerably overestimates D_i. Here, m and n are both set equal to 3.5, taking into account recent studies addressing this issue [221, 222].

Within the gas-phase and inside the GDL, the conservation equation for liquid water saturation (multi-fluid saturation model) is also solved, and it has the following form:

$$\frac{\partial}{\partial t}(\varepsilon \rho_w s) + \nabla \cdot \left[D_{cap} \nabla s\right] = 0 \tag{5.12}$$

where D_{cap} corresponds to the capillary diffusion coefficient, given by:

$$D_{cap} = \rho_w \frac{K s^3}{\mu_w} \frac{dP_{cap}}{ds} \tag{5.13}$$

and P_{cap} is the capillary pressure, related with s by the Leverett J-function, defined as:

$$P_{cap} = \frac{\tau \, cos(\theta^{GDL})}{(K/\varepsilon)^{1/2}} J(s) \tag{5.14}$$

with $J(s)$ described by:

$$J(s) = \begin{cases} 1.417(1-s) - 2.120(1-s)^2 + 1.263(1-s)^3, & for\ \theta < 90° \\ 1.417s - 2.120s^2 + 1.263s^3, & for\ \theta > 90° \end{cases} \tag{5.15}$$

The Leverett J-function was derived based on experimental data from homogeneous soil or a sand bed with constant wettability [223, 224]. However, in the GDLs of PEM fuel cells, the size of the pores is not uniform, and their wettability is affected by both the hydrophilic carbon substrate and the hydrophobic agent. It has thus been reported that this function is not accurate enough to describe precisely liquid water saturation in GDLs [225-227]. Although in several studies [219, 228-231] experimental P_{cap} data for various GDL usually applied in PEM fuel cells have been obtained, there is no universal correlation similar to Leverett J-function for all GDL materials. Therefore, Leverett J-function is still applied in the present model, as it has been shown that it is capable of qualitatively describe the effects of water flooding in the PEM fuel cell operation [225].

Boundary conditions

At the cathode GCs inlet, the air velocity, v, and species mass fractions are specified as:

$$v = \frac{\lambda_{air}}{0.21}\frac{I^{ref}A_{active}}{4F}\frac{RT}{P}\frac{1}{A_{GC_c\,inlet}} \tag{5.16}$$

$$Y_{H_2O} = \frac{RH_{air}P_{sat}}{P} \tag{5.17}$$

$$Y_{O_2} = 0.21(1 - Y_{H_2O}) \tag{5.18}$$

$$Y_{N_2} = 0.79(1 - Y_{H_2O}) \tag{5.19}$$

where A_{active} is the cell active area and $A_{GC_c\,inlet}$ is the cross-section area of the cathode GCs inlet. v is calculated for a fixed reference current density, I^{ref}, of 1.0 A cm^{-2}. P_{sat} is the saturation pressure, obtained by (adapted from [89]):

$$P_{sat} = 100000 \times 10^{-2.1794+0.02953T-9.1387\times10^{-5}T^2+1.4454\times10^{-7}T^3}, \quad T\ in\ °C \tag{5.20}$$

It is also specified that no liquid water enters in the cathode GCs inlet by:

$$f_w = 0 \tag{5.21}$$

$$s = 0 \tag{5.22}$$

At the cathode GCs outlet, pressure outlet boundary condition is used and gauge pressure is set.

At the solid walls, non-slip and zero diffusive flux for velocity and species boundary conditions, respectively, are prescribed:

$$v = 0 \tag{5.23}$$

$$\frac{\partial Y_i}{\partial n} = 0 \tag{5.24}$$

The only exception is the GDL bottom wall, where oxygen, Y_{O_2}, and water vapor, Y_{H_2O} mass fractions and liquid water saturation, s, are specified:

$$Y_{O_2} = Y_{O_2}^{*} + \frac{M_{O_2} N_{O_2} \Delta x}{D_{O_2} \rho_{air}} \tag{5.25}$$

$$Y_{H_2O} = Y_{H_2O}^{*} + \frac{M_{H_2O} N_{H_2O}(v) \Delta x}{D_{H_2O} \rho_{air}} \tag{5.26}$$

$$s = s^{*} + \frac{M_{H_2O} N_{H_2O}(l) \Delta x}{D_{cap}} \tag{5.27}$$

where Y^* and s^*refer to the corresponding values in the cells adjacent to the wall, and Δx is the distance between those cells center and the center of the corresponding face at the wall. M corresponds to the molecular weight and N_{O_2} is the oxygen molar flux, given by:

$$N_{O_2} = -\frac{I}{4F} \tag{5.28}$$

The values of the water vapor molar flux, $N_{H_2O}(v)$, and liquid water molar flux, $N_{H_2O}(l)$, are obtained first considering the total water molar flux, N_{H_2O}, given by:

$$N_{H_2O} = (1+\alpha)\frac{I}{2F} \tag{5.29}$$

where α corresponds to the membrane water transport coefficient, and comparing it with the corresponding value that would saturate the gas-phase with water vapor, $N_{H_2O}^{sat}$:

$$N_{H_2O}^{sat} = \frac{(Y_{H_2O}^{Sat} - Y_{H_2O}^{*})D_{H_2O}\rho_{air}}{M_{H_2O}\Delta x} \tag{5.30}$$

where $Y_{H_2O}^{Sat}$ is the saturation mass fraction obtained based of saturation pressure. $N_{H_2O}(v)$ and $N_{H_2O}(l)$ are then calculated by:

$$\left.\begin{aligned} N_{H_2O}(v) &= N_{H_2O} \\ N_{H_2O}(l) &= 0 \end{aligned}\right\} \; if\; N_{H_2O} \leq N_{H_2O}^{sat} \tag{5.31}$$

$$\left.\begin{aligned} N_{H_2O}(v) &= N_{H_2O}^{sat} \\ N_{H_2O}(l) &= N_{H_2O} - N_{H_2O}^{sat} \end{aligned}\right\} \; if\; N_{H_2O} > N_{H_2O}^{sat} \tag{5.32}$$

Such computation considers that, after being produced in the CL, water first saturates the gas-phase, and the remaining amount condenses instantaneously into liquid water. This approximation eliminates the need to add source terms for water condensation in the GDL, simplifying the model and increasing its numerical stability. Preliminary simulations were conducted using such source terms and the results obtained were reasonably close of the present approach (**Appendix B**). It is in the GDL bottom wall boundary condition that the 1D domain is incorporated into the 3D domain, providing the values of I and α needed in Equations **(5.28)** and **(5.29)**. How such values are computed in the 1D domain is explained in the next section.

At the pores placed in the bottom wall of the GCs (GDL surface), corresponding to the liquid water inlets, the velocity in each pore is obtained by considering the liquid water produced in the area closest to it. First, the GDL bottom wall is divided into the same number of areas as the number of pores, then the velocity of water in each pore is calculated by:

$$v = \frac{\frac{M_{H_2O}}{\rho_w} \sum_{i=1}^{i=n} N_{H_2O(l)_i} A_i}{A_{pore}} X \tag{5.33}$$

where i is the cell number and n is the total number of computational cells in the area closest to the pore. A_i corresponds to the area of the computational cell i, A_{pore} to the cross-section area of the pore and X is a multiplicative factor for the liquid water velocity. Since water generation rate is very slow under the typical working conditions of a PEM fuel cell, theoretical values need to be amplified a few orders of magnitude to shorten the time for water accumulation in the GCs. Such modification does not alter significantly the nature of the flow due to the large flow ratio between air and liquid water, and it is a current practice in PEM fuel cell numerical simulation when applying the VOF method [151, 154, 164]. In the simulations conducted in this chapter, X is set to 400, a value within the range applied in the mentioned studies. In this boundary condition, it is also specified that only liquid water enters through the pores by setting:

$$f_w = 1 \tag{5.34}$$

5.1.4.2. 1D domain

As mentioned above, it is in the 1D domain that the current density, I, being produced by the cell at a specified voltage is computed. Tafel equation is employed for this purpose, here considered in the following form:

$$I = (1 - s) I_0^{ref} \frac{C_{O_2}^{CL_c}}{C_{O_2}^{ref}} e^{\left(\frac{\alpha_c \eta_c F}{RT}\right)} \tag{5.35}$$

where I_0^{ref} and $C_{O_2}^{ref}$ correspond to the reference values of exchange current density and oxygen molar concentration, respectively. $C_{O_2}^{CL_c}$ is the oxygen molar concentration at the middle of cathode CL, and α_c is the cathode transfer coefficient. η_c corresponds to the cathode overpotential and is computed as:

$$\eta_c = OCV - V - R_{ohm} I \tag{5.36}$$

In Equation **(5.35)**, s is directly provided by the 3D domain (s^*). Therefore, the transport of liquid water in the CL water is here neglected, as it would increase considerably the mathematical complexity. Since the CL is very thin, this would not significantly affect the model predictions. The value $C_{O_2}^{CL_c}$ can be obtained taking the oxygen molar concentration at the cathode GDL/CL interface, $C_{O_2}^{GDL_c/CL_c}$, and subtracting the oxygen transfer resistance (based on Fick's law) in the CL:

$$C_{O_2}^{CL_c} = C_{O_2}^{GDL_c/CL_c} - \frac{I}{4F} \frac{\delta^{CL_c}/2}{D_{O_2}^{CL_c}} \tag{5.37}$$

where δ^{CL_c} refers to the cathode CL thickness, and $C_{O_2}^{GDL_c/CL_c}$ is obtained by:

$$C_{O_2}^{GDL_c/CL_c} = \frac{Y_{O_2}^{GDL_c/CL_c} \rho_{air}}{M_{O_2}} \tag{5.38}$$

where $Y_{O_2}^{GDL_c/CL_c}$ corresponds to the value of $Y_{O_2}^*$ provided by the 3D domain.

The electrical bulk resistance is generally negligible. In well-designed fuel cells, electrical contact resistances are also minimal. Proton resistance in the CL is also usually much smaller than that in the membrane. Therefore, R_{ohm} in Equation **(5.36)** is here approximated by the proton resistance in the membrane. This resistance is obtained by integrating the inverse of membrane proton conductivity, σ_{PEM}, over its thickness, δ^{PEM}. For simplicity, in the present model, R_{ohm} is approximated by:

$$R_{ohm} = \frac{\delta^{PEM}}{\sigma_{PEM}} \tag{5.39}$$

being σ_{PEM} given by [89]:

$$\sigma_{PEM} = 10^{-2}(0.005139\lambda - 0.00326)e^{\left[1268\left(\frac{1}{303}-\frac{1}{273+T}\right)\right]} \tag{5.40}$$

where λ corresponds to the water content in the membrane. The value of λ used in Equation **(5.40)** is computed as the average between the anode and cathode values.

In order to obtain λ, one needs to account for the water balance in the membrane. In this model, the water molar flux in the membrane, $N_{H_2O}^{PEM}$, is computed by considering electro-osmotic drag and back diffusion [89]:

$$N_{H_2O}^{PEM} = \alpha\frac{I}{2F} = 2n_{drag}^{sat}\frac{I}{2F}\frac{\lambda}{22} - \frac{\rho_{PEM}}{M_{PEM}}D_{PEM}\frac{d\lambda}{dx} \tag{5.41}$$

where n_{drag}^{sat} corresponds to the electro-osmotic drag coefficient in a fully hydrated membrane, ρ_{PEM} to the dry membrane density, M_{PEM} to the membrane molecular weight, and x to direction of water transport in the membrane. D_{PEM} is the water diffusion coefficient in the membrane, obtained by [89]:

$$D_{PEM} = 10^{-10}(2.563 - 0.33\lambda + 0.0264 - 0.000671\lambda^2)e^{\left[2416\left(\frac{1}{303}-\frac{1}{273+T}\right)\right]} \tag{5.42}$$

λ is computed by:

$$\lambda = \begin{cases} 14a, & anode \\ 12.6 + 1.4a, & cathode \end{cases} \tag{5.43}$$

where a corresponds to the water activity given by:

$$a = \frac{C_{H_2O}^{CL/PEM}RT}{P_{sat}} \tag{5.44}$$

Both expressions for obtaining λ in Equation **(5.43)** are based in the measurements conducted by Springer *et al.* [89]. However, in order to simplify the calculations, the anode expression used in this work is a linear approximation [232] of the original correlation. Equation **(5.43)** also implies that α is between 0 and 1 in the anode, and between 1 and 3 in the cathode, which is often the case in PEM fuel cells normal operation.

The water vapor molar concentrations in both sides of the membrane, needed to obtain the corresponding values of α, are calculated by:

$$C_{H_2O}^{CL_a/PEM} = C_{H_2O(v)}^{GC_a\,inlet} - \alpha \frac{I}{2F}\left(\frac{\delta^{CL_a}}{D_{H_2O}^{CL_a}} + \frac{\delta^{GDL_a}}{D_{H_2O}^{GDL_a}} + \frac{A^{GC_a/GDL_a}}{Q_{H_2}}\right) \tag{5.45}$$

$$C_{H_2O}^{CL_c/PEM} = C_{H_2O}^{GDL_c/CL_c} + (1+\alpha)\frac{I}{2F}\frac{\delta^{CL_c}}{D_{H_2O}^{CL_c}} \tag{5.46}$$

where $C_{H_2O(v)}^{GC_a\,inlet}$ refers to the water vapor molar concentration in anode GCs inlet, A^{GC_a/GDL_a} to the total area of the anode GCs facing the GDL, and Q_{H_2} to the hydrogen volumetric gas flow rate. Equation **(5.45)** considers the mass transfer resistance of water vapor in the porous CL and GDL, and the anode GCs are considered as a continuously stirred tank reactor (CSTR). Equation **(5.46)** is analogue to Equation **(5.37)** and $C_{H_2O(v)}^{GDL_c/CL_c}$ is obtained using $Y_{H_2O}^{GDL_c/CL_c}$, which corresponds to $Y_{H_2O}^{*}$ provided by the 3D domain.

5.1.5. Numerical implementation

The present model is implemented in the CFD commercial code ANSYS Fluent, version 15.0. The 1D domain is incorporated into the 3D domain through UDFs written in C programming language. At each iteration, $Y_{O_2}^{*}$, $Y_{H_2O}^{*}$, and s^{*} in every computational cell adjacent to the GDL bottom wall are provided by the 3D computation. These values, together with the anode operating conditions and kinetic and cell design parameters, are used in the 1D domain to calculate I and α. These values are then applied to adjust the GDL bottom wall species boundary condition in the 3D domain.

In the 1D domain calculations, D_{PEM} is considered as a constant when integrating Equation **(5.41)**, so an analytical solution can be obtained. Such simplification lies in the fact that D_{PEM} does not vary significantly in the range of $4 < \lambda < 20$, and in PEM fuel cells operation λ is usually between those values. After substituting Equations **(5.42)**-

(5.46) into Equation **(5.41)** (after integration), and performing some algebraic manipulations, α can be obtained as a function of I. The α expression is then inserted into Equations **(5.45)** and **(5.46)** and, using Equations **(5.42)-(5.44)**, σ_{PEM} (Equation **(5.40)**) can also be obtained as a function of I. Placing the expression of σ_{PEM} in Equation **(5.41)** and then Equations **(5.36)-(5.38)** in Equation **(5.35)** results into an analytic equation having I as the unique unknown. This equation is numerically solved using the Newton-Raphson method. After convergence, the calculated values of I and α are used in Equations **(5.28)** and **(5.29)**, which are inserted in Equations **(5.25)-(5.27)** to obtain the new values of Y_{O_2}, Y_{H_2O}, and s to be returned to the 3D domain.

Regarding the 3D domain solution methods, pressure-based segregated solver is adopted for the incompressible flow, and the explicit VOF formulation is applied to track the interface between fluids. The gaseous species equations in the gas-phase are solved using the built-in species transport model. For liquid water saturation, the conservation equation of a User Defined Scalar (UDS) within the gas-phase is solved, being the flux and unsteady functions, as well as the diffusion term, defined through UDFs. Semi-Implicit Method for Pressure Linked Equations (SIMPLE) scheme is used for pressure-velocity coupling. Least squares cell based method is adopted for gradient spatial discretization, whereas Pressure Staggering Option (PRESTO!) scheme is employed for pressure discretization. Momentum discretization is achieved through the second order upwind methodology. The geometric reconstruction scheme is used to represent the interface between fluids using the PLIC approach from the work of Youngs [138]. First order upwind scheme is employed for spatial discretization of gaseous species and liquid water saturation equations. The varying time-step method is used applying a maximum global courant number of 2, with minimum and maximum time-steps of 10^{-10} s and 10^{-5} s, respectively. During the major part of the simulations, the time-step was close to 10^{-6}. It approaches the maximum time-step in the beginning of the simulation, when the amount of water in the channel is lower. The time-step approaches the minimum value during the occurrence of specific events, such as the coalescence of two droplets, which require more numerical stability to be resolved.

5.1.6. Calculation procedure

The first step of the calculation procedure is to obtain a steady-state solution. In this initial stage, the VOF method is not activated (by setting the liquid water velocity in each pore equal to 0). The results of this solution comprise species (including water saturation in the GDL), current density, pressure and velocity distributions. The results of this steady-state solution are then used as the initial values for the two-phase flow transient calculation. In the beginning of the transient calculation, because liquid water generation rate ($N_{H_2O}(l)$) is already available in all the domain, water velocity can be obtained for all the pores designed at the GDL surface (Equation **(5.33)**). Such procedure decreases considerably the overall simulation time. It is also in accordance with the real operation of a PEM fuel cell, because the distribution of gaseous species along the cell occurs much more rapidly than the liquid water distribution.

5.1.7. Computational geometry and mesh

An unstructured mesh with 1,259,416 tetrahedral elements with minimum and maximum size of 7.0×10^{-5} m and 2.5×10^{-4} m, respectively, was employed for the simulations of this chapter, for a 25 cm^2 PEM fuel cell with the same features of the cells used in the experimental tests (see Chapter **3)**. ANSYS Meshing was used for mesh generation. The mesh size was selected considering the results of mesh size tests (**Appendix C**). It was observed that, although the selected mesh presents a loss in the interface definition (**Figure C.1**) and lower water content (**Figure C.3**) in the GC in comparison to those obtained when employing more refined meshes, it can reasonable capture the general two-phase flow patterns (**Figure C.1** and **Figure C.4**). For the water emergence, two pores with 200 μm of diameter are designed in each straight section of the serpentine channel. The diameter considered for each pore was chosen in order to represent the largest pores found in the GDL, from which liquid water tends to move. This is a value within the range employed in other VOF numerical studies [131, 173] and has the same order of magnitude of the GDL larger pores, as reported in studies addressing the structural features of such materials [127, 129]. **Figure 5.3** displays the computational geometry and mesh applied in the simulations conducted in this chapter.

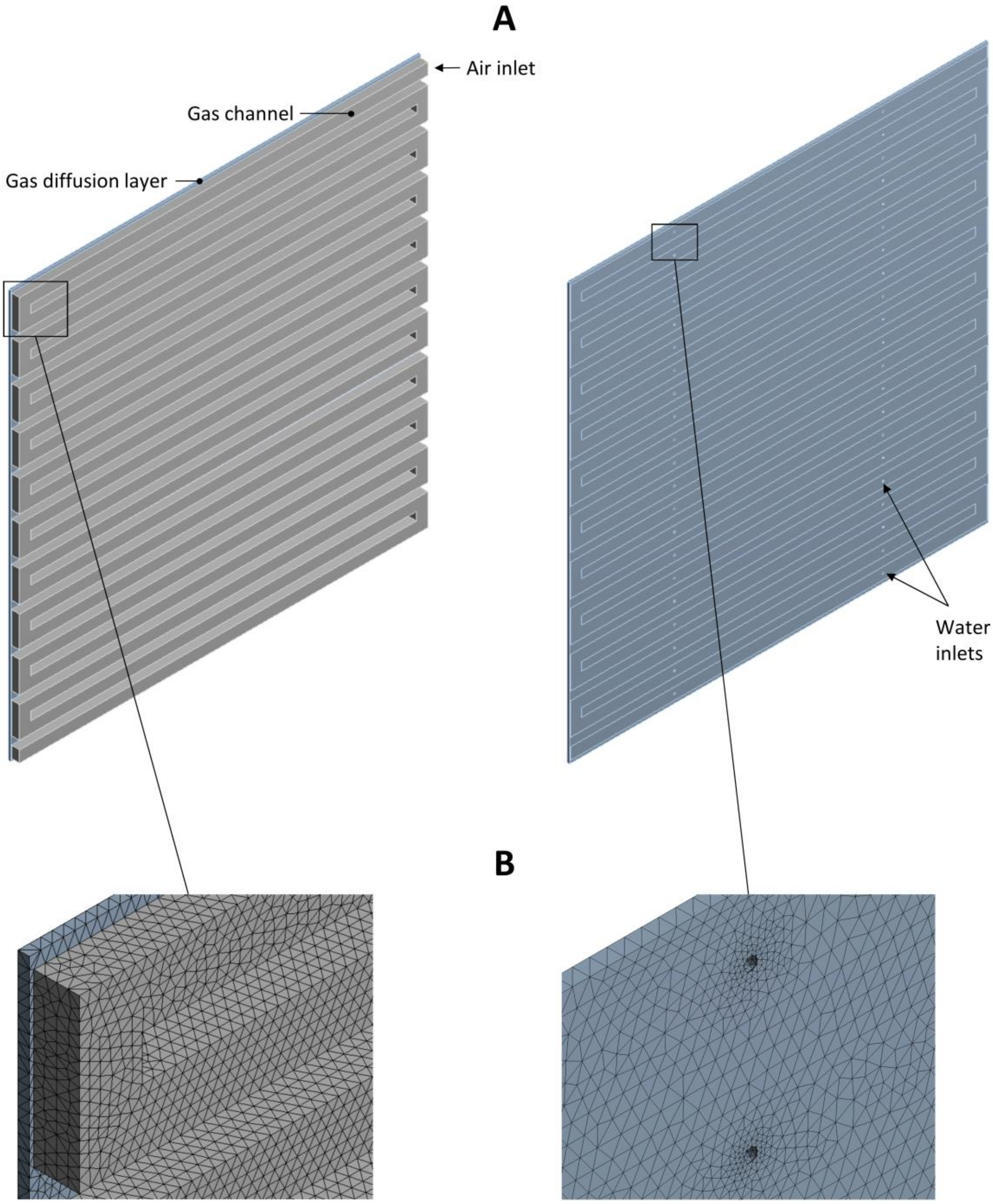

Figure 5.3. Images of the computational (A) geometry and (B) mesh applied in the model.

5.2. Experimental validation

The cell performance is depicted in **Figure 5.4,** in terms of polarization (**Figure 5.4** A) and power density (**Figure 5.4** B) curves simulated by the model and that obtained experimentally. Here, the experimental results were corrected taking into account the internal electrical resistance (iR) of the cell, which was found to be exceptionally high for the hardware employed, about 0.16 Ω cm^2, accounting for more than 2/3 of the cell total resistance. Such high value of iR was found to be caused by poor electrical contacts between the cell components, namely between the graphite plates and the GDLs. From the analysis of **Figure 5.4**, a good agreement between the model predictions and the cell experimental performance can be observed. At high current densities, it can be seen that the model slightly overpredicts the experimental results. At 0.70 A cm^{-2}, the voltage is about 15 % higher than the experimental value. This is probably due to the usage of the Leverett J-function to calculate the liquid water saturation, which may be inappropriate for the GDLs of PEM fuel cells, as already discussed in Section **5.1.4.1**. The level of liquid water saturation might be underpredicted by this correlation, similarly to that reported by Ramos-Alvarado *et al.* [226], causing the model to overpredict the cell performance at high currents, where the effects of flooding are more significant.

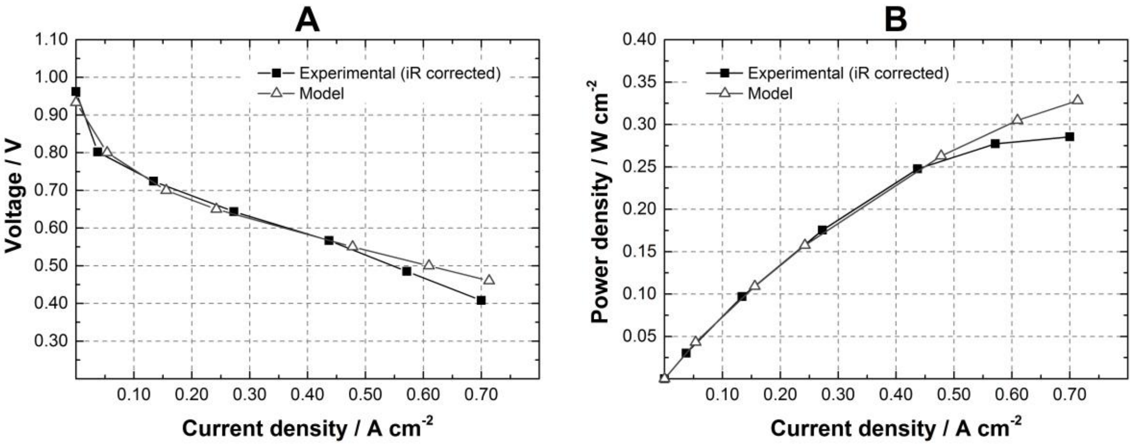

Figure 5.4. Fuel cell performance obtained experimentally and calculated by the present model. A – Polarization curve; B – Power density curve.

The individual voltage losses are displayed in **Figure 5.5**, including the cathode overpotential (**Figure 5.5** A) and the ohmic losses (**Figure 5.5** B), obtained experimentally through EIS measurements and calculated by the model. It can be seen that the model is able to correctly separate the different contributions that affect the cell operation. The voltage decrease with increasing current density is mainly dominated by the cathode overpotential, which includes losses from the activation of the electrochemical reactions, and mass transfer resistance due to flooding occurring at high currents.

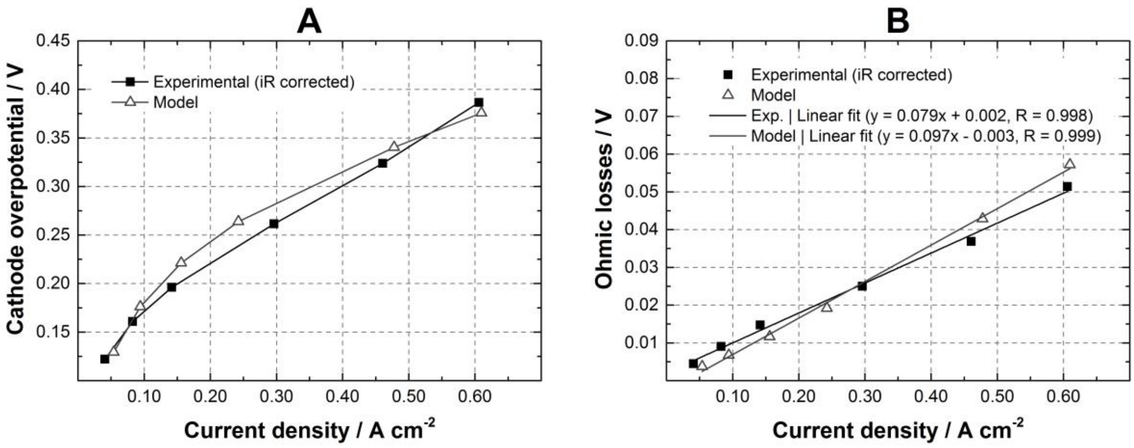

Figure 5.5. Individual voltages losses obtained experimentally and calculated by the present model. A – Cathode overpotential; B – Ohmic losses.

The model input parameters giving rise to the results presented in this chapter are shown in **Table 5.1**. Parameters related with the fuel cell design and operating conditions were set equal to those employed in the experiments. Moreover, important kinetic parameters, namely the OCV, the cathode transfer coefficient, α_c, and reference exchange current density, I_0^{ref}, were obtained experimentally. In Section **3.3.3** is explained how I_0^{ref} and α_c were obtained through EIS measurements. This eliminates the need to arbitrarily assume such values, therefore increasing the accuracy of the model predictions. A recent study [233] stressed out the importance of gathering reliable and robust input data, with focus on the kinetics of the electrochemical reactions, in order to assure an adequate predictive capability of PEM fuel cells models.

Table 5.1. Model input parameters.

Parameter	**Value**
Active area, A_{active}	25×10^{-4} m^2
GCs width	1.4×10^{-3} m
GCs height	1.0×10^{-3} m
Anode CL thickness, δ^{CL_a}	60×10^{-6} m (assumed)
Anode GDL thickness, δ^{GDL_a}	250×10^{-6} m [a]
Anode CL porosity, ε^{CL_a}	0.4 (assumed)
Anode GDL porosity, ε^{GDL_a}	0.5 (assumed)
Cathode CL thickness, δ^{CL_c}	60×10^{-6} m (assumed)
Cathode GDL thickness, δ^{GDL_c}	250×10^{-6} m [a]
Cathode CL porosity, ε^{CL_c}	0.4 (assumed)
Cathode GDL porosity, ε^{GDL_c}	0.5 (assumed)
GDL permeability for air, K_{air}	10^{-12} m^2 [4, 165, 167, 219]
GDL permeability for liquid water, K_w (VOF method)	10^{-15} m^2 (assumed, see Section **5.1.4.1**)
GDL permeability for liquid water, K_w (saturation model)	2.55×10^{-13} m^2 [103]
Channel walls contact angle, θ^{GCs}	50.3 ° (measured, see Section **3.2**)
GDL contact angle, θ^{GDL}	138.1 ° (measured, see Section **3.2**)
Electro-osmotic drag coefficient, n_{drag}^{sat}	2.7 [89]
Membrane molecular weight, M_{PEM}	1.1 kg mol^{-1} (assumed)
Membrane dry density, ρ_{PEM}	1970 kg m^{-3} [9]
Membrane thickness, δ^{PEM}	50.8×10^{-6} m [9]
Cathode transfer coefficient, α_c	0.343 (measured, see Section **3.3.3**)
Reference exchange current density, I_0^{ref}	0.011 A cm^{-2} (measured, see Section **3.3.3**)
Reference oxygen concentration, $C_{O_2}^{ref}$	7.641 mol m^{-3} (C_{O_2}at the inlet)
Open circuit voltage, OCV	0.933 V (measured, see Section **3.3.3**)
Temperature, T	40 ºC
Absolute pressure, P	1 atm
Hydrogen stoichiometry, λ_{H_2}	1.1
Air stoichiometry, λ_{air}	2.2
Relative humidity of hydrogen, RH_{H_2}	50 %
Relative humidity at air, RH_{air}	90 %
Operating voltage, V	0.3 to 0.8 V

[a] Internal thickness at 0.025 MPa. Information provided by the MEAs supplier.

Figure 5.6 contains images of the liquid water distribution in the serpentine channel of the transparent fuel cell (**Figure 5.6** A) (operated at 0.10 A cm^{-2} and λ_{air} = 2.2) and that simulated by the present model (**Figure 5.6** B) (V = 0.40 V). The images shown were obtained after a relatively stable operation was achieved, in which the general flow patterns did not change considerably over time. The temporal analysis of the processes of water emergence, accumulation and movement before reaching such state are analyzed in detail in the next section, using the model simulations. From the analysis of **Figure 5.6**, it can be seen that the present model can capture some of the main liquid water flow patterns observed experimentally. In both situations, it can be observed a general trend for water to be accumulated at the elbows of the channel (**Figure 5.6** A (1) and **Figure 5.6** B (1)). This occurs due to the low air velocity verified in corners of the elbows. Moreover, the formation of long water films attached to the side walls of the channel can also be visualized in the experimental (**Figure 5.6** A (2)) and simulation results (**Figure 5.6** B (2)). It is important to remark that such comparison consists on a qualitative one. In the experiments, the exact location of water emergence was not controllable. Moreover, as already explained, water generation rate in the simulations had to be increased to achieve practical simulation times. Several *ex-situ* experiments [170, 181, 205] have been conducted, where the liquid water flow is visualized in micro-channels especially designed to simulate those of a PEM fuel cell, using a syringe pump to precisely control water emergence location and velocity. The conditions of such tests could be replicated in numerical simulations employing the VOF method, and the results (liquid water distribution [170, 181, 205], droplets departure time [205] and two-phase flow pressure drop [170]) were almost identical to those obtained experimentally, clearly asserting the suitability of the VOF method to simulate the two-phase flow in conditions similar to PEM fuel cells.

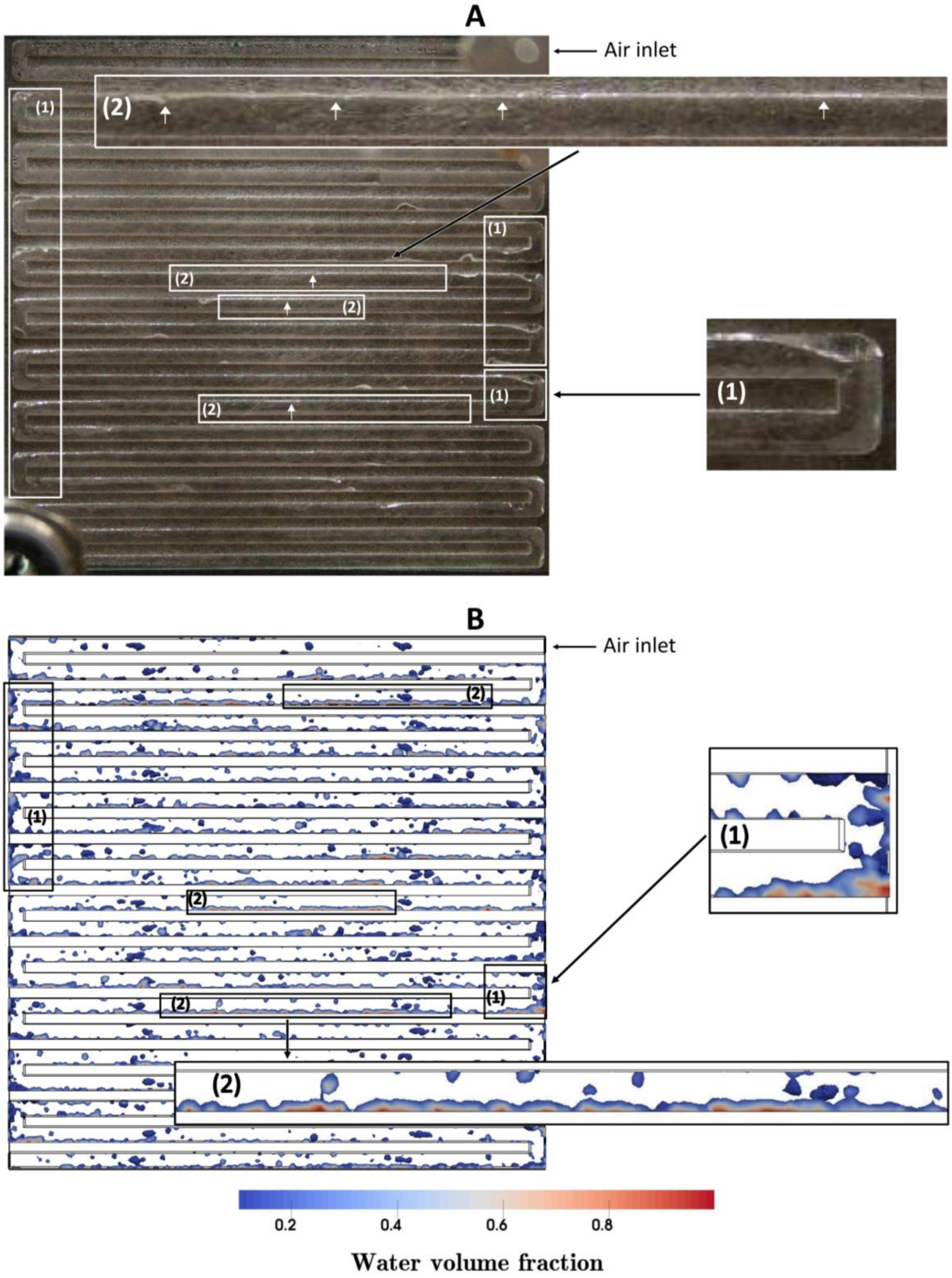

Figure 5.6. Images of liquid water distribution inside the serpentine channel of a 25 cm^2 PEM fuel cell. A – Cathode of the transparent fuel cell; B – Simulation results from the present model. (1) Water accumulation at the elbows; (2) Water films attached to the side walls of the channel.

5.3. Results and discussion

5.3.1. Water dynamics in the serpentine channel

Figure 5.7 shows liquid water volume fraction in the serpentine channel at different time instants for two different operating voltages: 0.60 V and 0.40 V. Simulations for 0.70 V, 0.50 V and 0.30 V were also conducted. However, since the analysis of the results for 0.60 V and 0.40 V is sufficient to capture the effects of operating voltage in liquid water distribution, they are not shown here with the purpose of brevity.

For 0.60 V, at 5.76 ms, it can be seen liquid water emerging into the channel through the pores designed at the GDL surface, representing the main pathways for water transport, and the formation of droplets that grow in size with time. It can also be observed that these droplets do not suffer much deformation and are still attached to the GDL surface. For 0.40 V and at 5.34 ms, the droplets are generally larger, several are considerably deformed, and some already detached from the GDL surface, starting to move downstream. It can also be visualized some smaller droplets being ripped out from larger droplets due to the influence of the air flow. At 0.40 V, current density is higher (**Figure 5.4** and **Figure 5.8**), more water is generated (**Figure 5.9**), and thus water velocity in each pore is higher (**Figure 5.10**). Results shown in **Figure 5.8, Figure 5.9** and **Figure 5.10** are discussed in detail in the next section. Because more water is entering through each pore, droplets grow into a larger size and interact more significantly with the air flow, and considerable deformation occurs. At 0.60 V and 11.16 ms, several droplets already detached from the GDL surface and start to move along the channel. It can be observed that some of these droplets move freely suspended in the channel, and others interact with the top (opposite to the GDL) and side walls of it. Moreover, as captured at 38.87 ms for 0.60 V, two droplets can interact with each other coalescing into a larger droplet. At 10.70 ms, for the case of 0.40 V, some of the droplets already reached and spread into the elbows of the serpentine channel. For 20.88 ms, at the same voltage, it can already be observed the tendency of water accumulation at the elbows of the channel and, at 32.38 ms, the first water films become visible. For the case at 0.60 V, water accumulation at the elbows of the channel only starts to be verified at 31.33 ms, and the first (small) water films are first visualized at 48.38 ms. From **Figure 5.7**, it is also clear that, at any time, more water is present in the channel for the case of lower voltage. Moreover, after a certain time, liquid water flow patterns do not change considerably. This is more clearly observed for the case of 0.40 V, in which similar liquid water distribution patterns are observed from 32.38 to 70.04 ms. The most significant change during such interval is only on the amount of water present in the channel.

An important remark about the time scale of the results shown in this work should here be made. As explained in Section **5.1.4.1**, the velocity of water in each pore needs to be amplified in order to speed-up water accumulation in the channel and reduce the computational times. That makes the characteristic time of the numerical results here presented to be the millisecond (ms). However, in real PEM fuel cells, the processes of water emergence and accumulation in the GCs has a higher characteristic time, from a few seconds to many minutes [57, 60, 62, 216, 234].

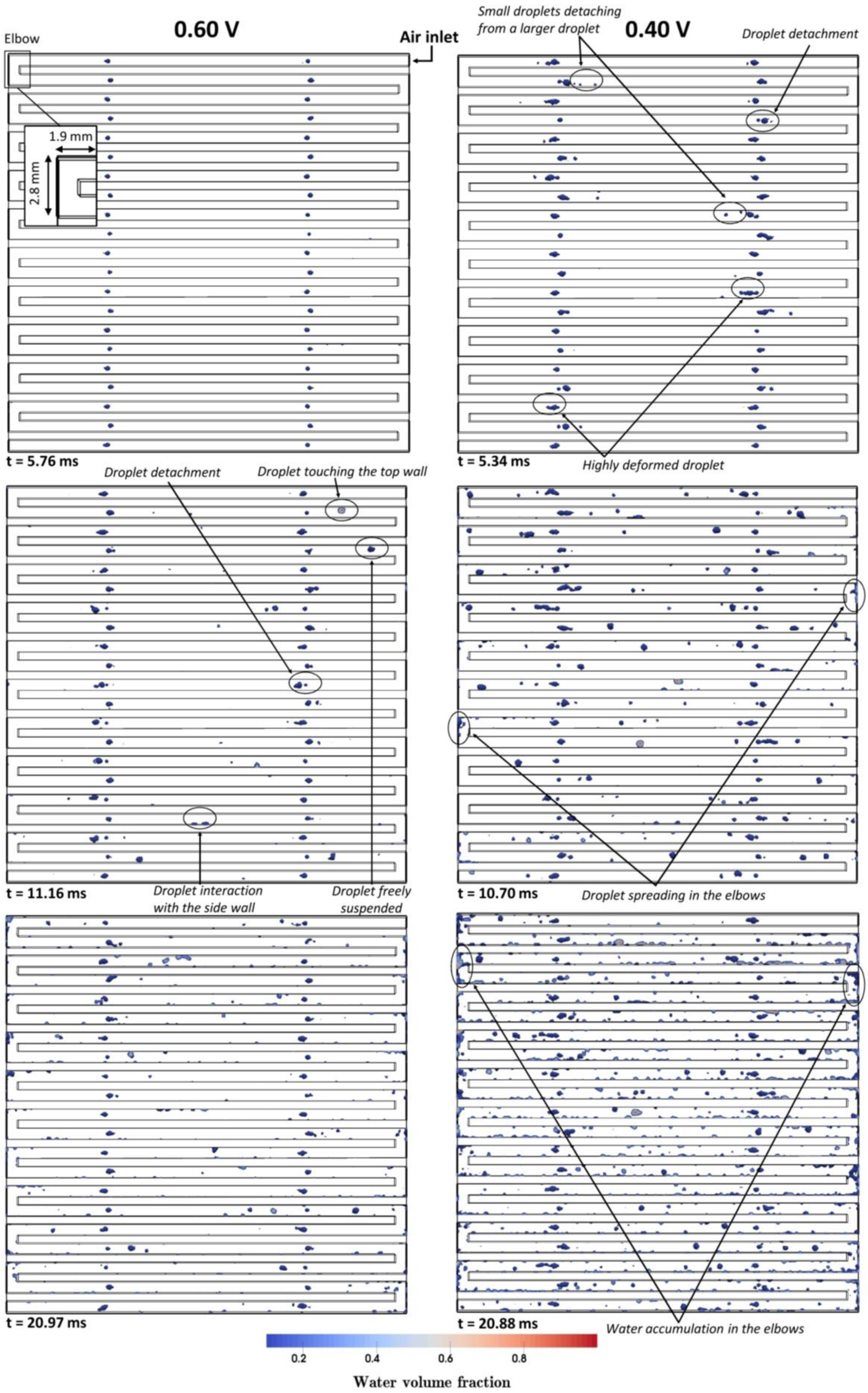

Figure 5.7. Water dynamics in the serpentine channel for two different operating voltages.

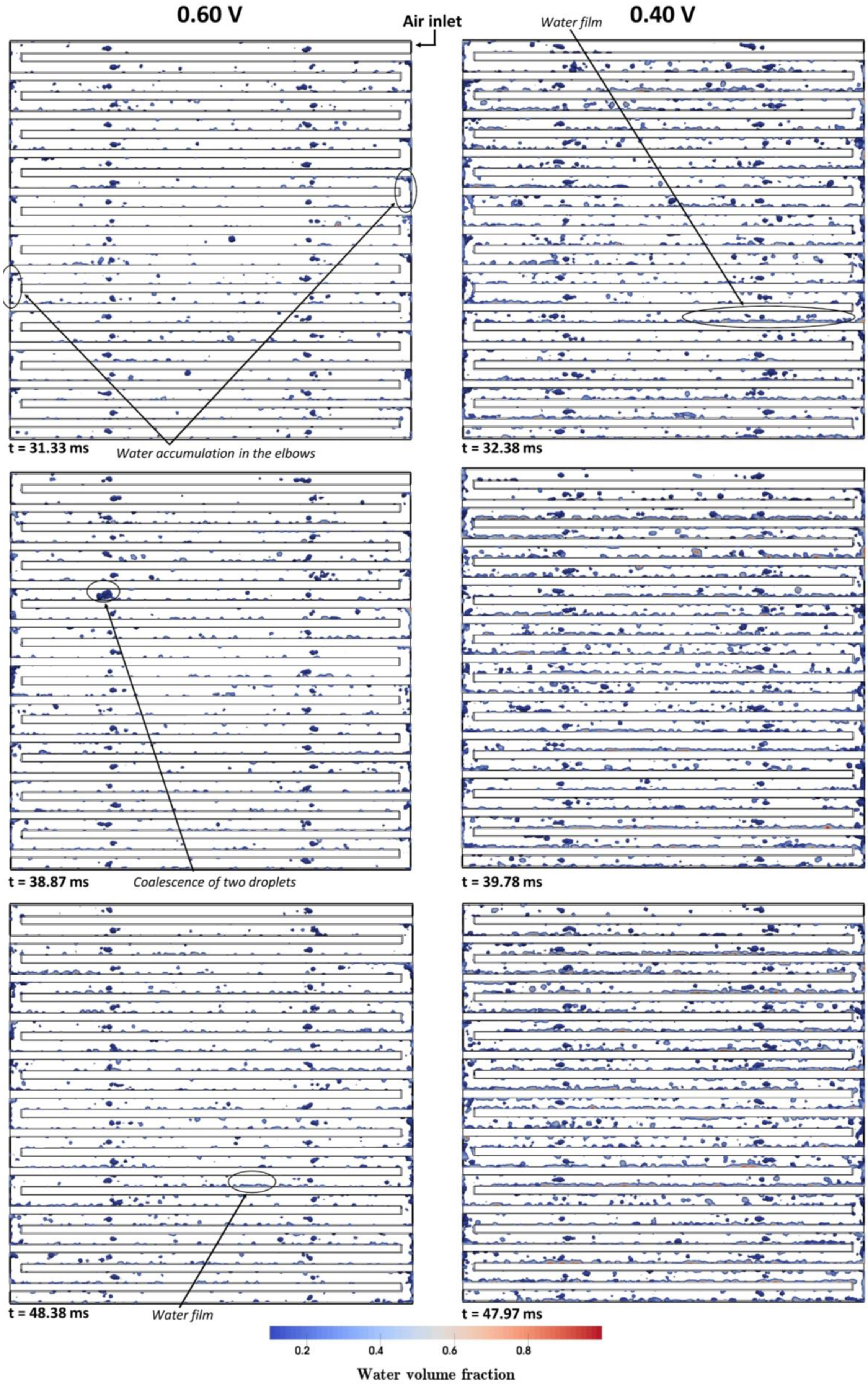

Figure 5.7 (Continued)

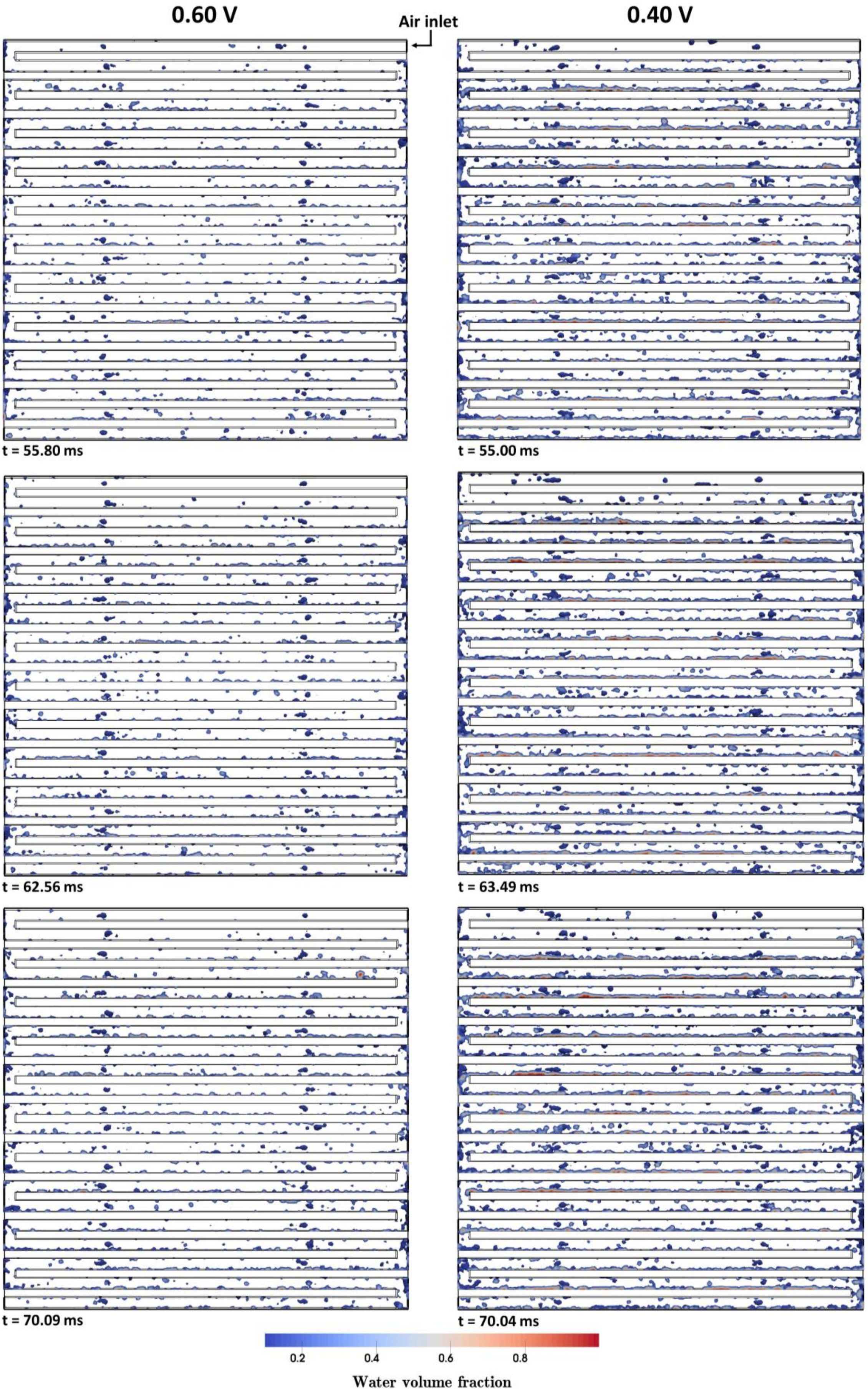

Figure 5.7 (Continued)

5.3.2. Current density and liquid water generation rate distributions and water velocity in each pore

Figure 5.8 contains the current density spatial distribution for different operating voltages. The results obtained at 0.50 V are not shown in **Figure 5.8** for the sake of simplicity, as they agree with those from 0.40 V and 0.30 V. The same procedure is applied to **Figure 5.9** and **Figure 5.15**. As expected, and as shown in **Figure 5.4**, higher current densities are obtained for lower voltages. For all voltages, the current density is higher in the areas adjacent to serpentine channel, because in this region the convective flow of air is stronger and oxygen reaches the reactive sites more rapidly. It can also be observed that current density decreases along the channel length in all cases, from the inlet to the outlet, because oxygen is being consumed along the channel and its mass fraction decreases. Moreover, the decrease of current along the channel is more significant for lower voltages, because oxygen consumption rate is higher in such conditions.

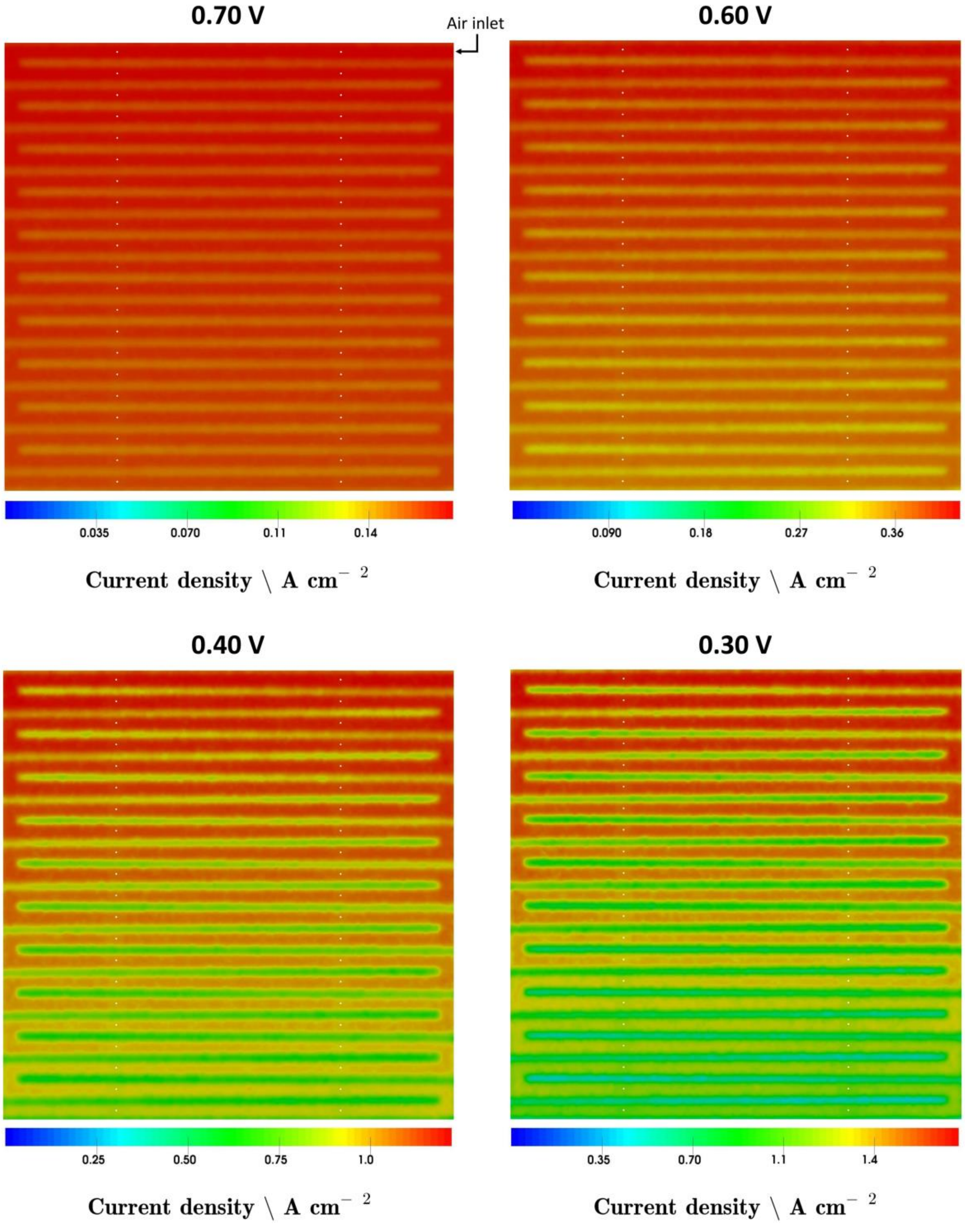

Figure 5.8. Current density distribution for different operating voltages.

Contrarily to current density, liquid water generation rate distribution along the cell active area varies when changing the operating voltage, as shown in **Figure 5.9**. For 0.70 V, liquid water generation rate generally increases along the channel length, until it stabilizes close to the outlet. At such voltage, the water production rate (directly proportional to current density) is low. In the area close to the inlet, the water vapor being produced is generally insufficient to saturate the air stream, and therefore liquid water generation rate is very low. However, as air continues to move along the channel, it continues to uptake water vapor, until it becomes saturated. This results into more significant amounts of liquid water being generated. As shown in **Figure 5.8**, current density does not decrease considerably along the channel, so does the water production rate. Therefore, liquid water generation rate tends to stabilize at the region close to outlet. For 0.40 V and 0.30 V, the water production rate is high, and the air stream becomes saturated right after entering the cell. In such cases, the current density, and thus the water production rate, decreases significantly along the channel. Because all the water produced condensates, liquid water generation rate also decreases along the channel. An intermediate case between those just described occurs at 0.60 V. Close to the channel inlet, liquid water generation rate is lower, and then increases in the middle region. However, because the decrease of current density and water production along the channel is higher than that verified at 0.70 V, the liquid water generation rate tends to decrease in the region closer to the outlet. This is also the case with more uniform liquid water generation rate.

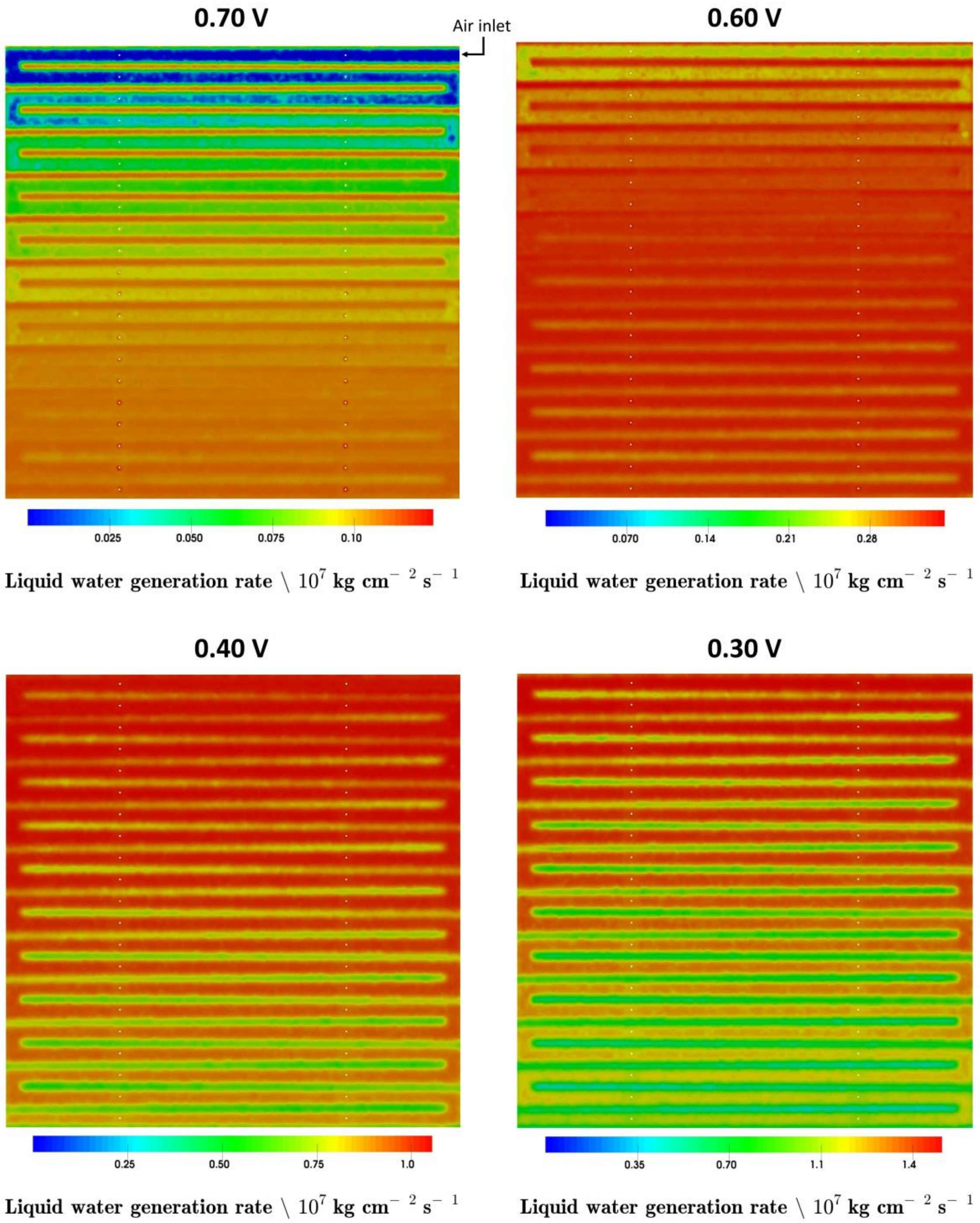

Figure 5.9. Liquid water generation rate distribution for different operating voltages.

The water velocity in each pore, for different operating voltages, is depicted in **Figure 5.10.** Pore 1 is the pore closest to the air inlet and pore 42 is the one closest to the outlet. It can be seen that: at 0.70 V, the water velocity generally increases along the channel length and stabilizes close to the outlet; at 0.60 V the water velocity is approximately uniform; and at 0.50 V, 0.40 V and 0.30 V the water velocity tends to decrease along the channel. Such profiles generally agree with the local liquid water generation rate discussed above. The fluctuations of water velocity in the pores observed in **Figure 5.10** are due to differences in the area of the pores and the corresponding GDL bottom wall sections, used to compute the water velocity. These deviations arise during mesh generation, and the subsequent discrete division of the GDL bottom wall into several zones.

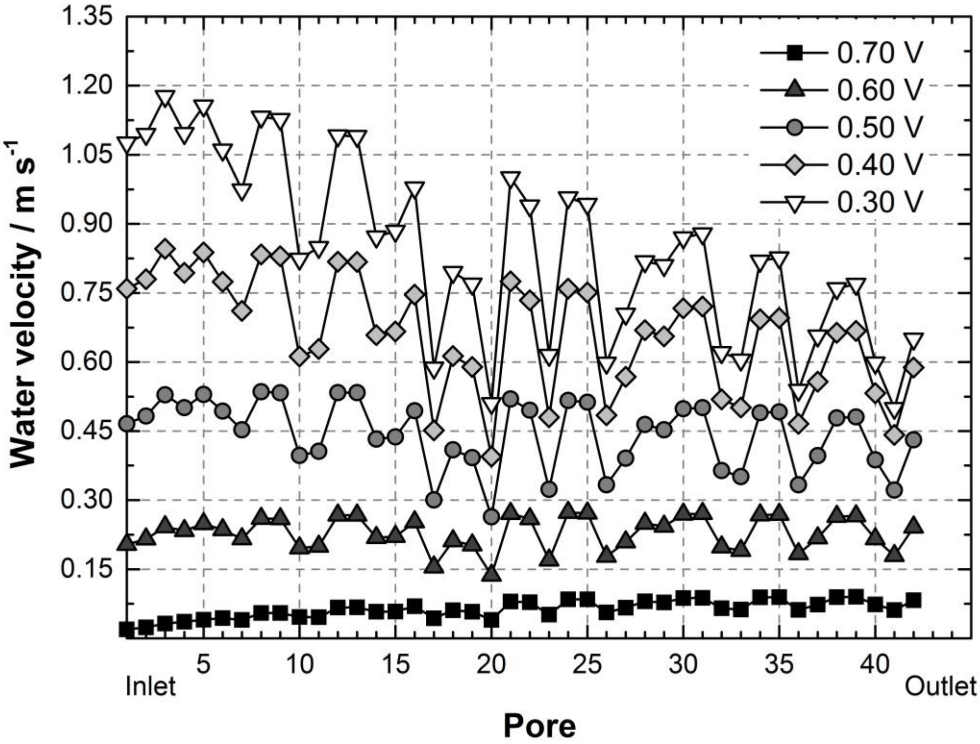

Figure 5.10. Water velocity in each pore designed at the GDL surface.

5.3.3. Two-phase flow pressure drop

The temporal evolution of two-phase flow pressure drop for different operating voltages is depicted in **Figure 5.11**. First, it can be seen that pressure drop increases when the operating voltage decreases. This occurs because, as shown in **Figure 5.9**, liquid water generation rate is higher for lower voltages, and higher water content in the channel raises flow resistance. Second, an increase in pressure drop with respect to time is observed, due to water being continuously entering and accumulating in the channel. At some point, the liquid water flow rate at the outlet is expected to match its emergence rate, and the water content and consequently the two-phase flow pressure drop will stabilize.

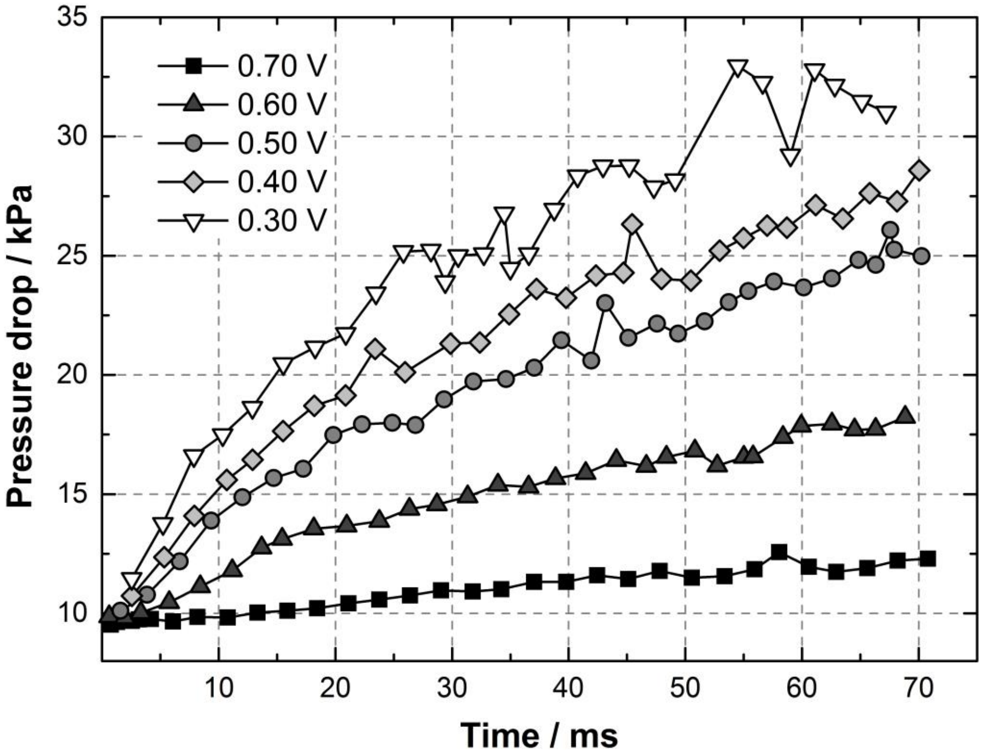

Figure 5.11. Two-phase flow pressure drop at various operating voltages.

5.3.4. Quantification of water content local distribution

One important drawback of experimental techniques applied in the field of the two-phase flow in PEM fuel cells is the difficulty in getting precise quantitative information of water content location, although interesting progress has been achieved with image processing from optical visualization of liquid water inside transparent fuel cells [57, 59, 235]. Therefore, this section is dedicated to the quantification of water content at different locations of the serpentine channel. Such information complements the qualitative analysis of water dynamics presented in Section **5.3.1**.

Figure 5.12 shows the volume-weighted water content (volume of liquid water divided by the total volume) in the entire serpentine channel, in its straight sections and at its elbows, over time and for different operating voltages. In **Figure 5.7** is shown the region considered to calculate the water content in an elbow. For all cases, it can be seen that the volume-weighted water content at the elbows is considerably higher than that of the complete serpentine and its straight sections, except in the initial period when all droplets are still attached to the GDL surface (located in the straight sections). Such results were already expected taking into account the liquid water distribution in the GCs depicted in **Figure 5.6** and **Figure 5.7**. They also agree with that reported from the direct visualization of liquid water distribution inside a transparent fuel cell with image processing [57].

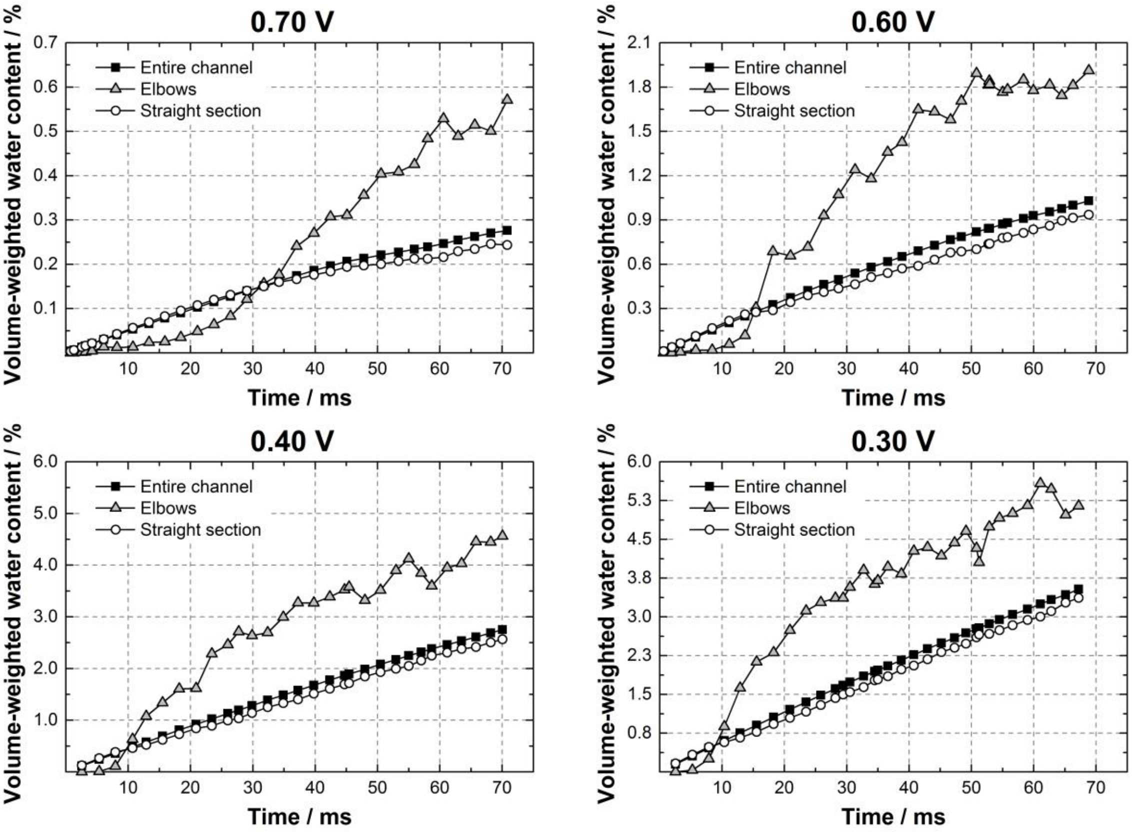

Figure 5.12. Volume-weighted water content in the serpentine channel, in its straight sections and at its elbows at various operating voltages.

The time-averaged volume-weighted water content in different sections of the serpentine channel is depicted in **Figure 5.13** for several voltages**,** after dividing the channel into 21 approximately equal sections, from the inlet to the outlet. Section 1 is that closest to the inlet and section 21 is the one closest to the channel outlet. A graphical representation of the volume-weighted water content in each section over time would result into 21 lines for each voltage, and its interpretation would be very challenging. After a first analysis of the results, it was verified that the trend of volume-weighted water content *vs* channel section remains generally constant over time. Therefore, the time-averaged volume-weighted water content for each channel is here shown for clarity. From the analysis of **Figure 5.13**, it can be seen that the water content along the channel length generally agrees with the water velocity in each pore shown in **Figure 5.10**, except for the case of the two first channel portions, which water content is lower than that of the following sections. This occurs because, contrarily to the other sections which are continuously being fed by water coming from upstream sections, section 1 does not have any section upstream and section 2 has just section 1.

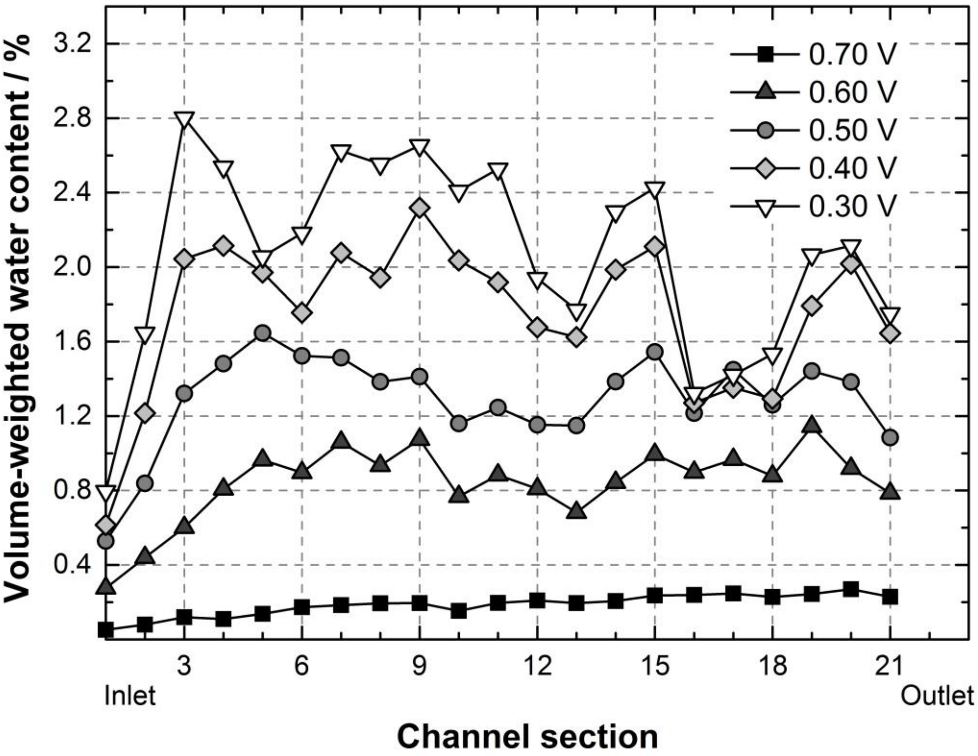

Figure 5.13. Time-averaged volume-weighted water content in different sections of the serpentine channel at various operating voltages, after dividing the channel into 21 approximately equal sections, from the inlet to the outlet.

Figure 5.14 shows the water coverage ratio (area covered by liquid water divided by the total surface area) of the top and side walls of the serpentine channel, as well as that of the GDL surface, over time and for various operating voltages. Except for 0.70 V, in which very little liquid water accumulates in the GC, it can be seen that the water coverage ratio of the top and side walls is considerably higher than that of the GDL surface. This is a desired scenario, because water accumulation in the GDL surface should be avoided, otherwise it would hamper the air flow through the GDL and the oxygen supply to the CL. The reason for higher water accumulation in the top and side walls is due to their hydrophilic nature that causes water to adhere into them, explaining the appearance of the water films visualized in **Figure 5.6** and **Figure 5.7.** The results from **Figure 5.14** generally agree (qualitatively) with those from other numerical studies that consider similar channel walls wettability and a hydrophobic GDL [131, 202]. Moreover, they confirm that the approach adopted in the present model to account for the hydrophobicity of the GDL surface (see Section **5.1.4.1**) is appropriate.

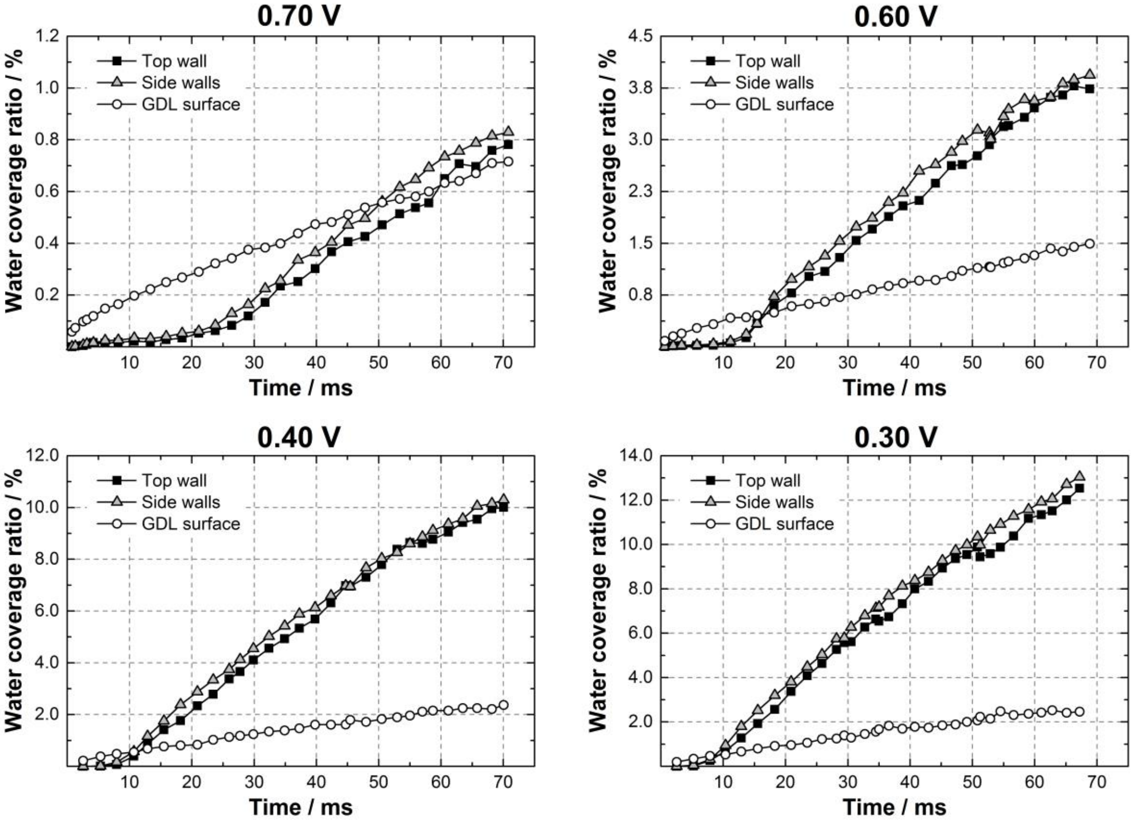

Figure 5.14. Water coverage ratio at different operating voltages in the top and side walls of the serpentine channel, and in the GDL surface.

5.3.5. Liquid water saturation in the GDL and its effects on the cell performance

Figure 5.15 shows liquid water saturation in the GDL bottom wall at various operating voltages. In general, liquid water saturation distribution along the channel length follows the same trend as liquid water generation rate, shown in **Figure 5.9** and discussed above. It can also be seen that more water is accumulated under the land region (the area not adjacent to the serpentine channel), because the convective flow is weaker than that in the region adjacent to the channel. Therefore, water is removed with greater difficulty from this location.

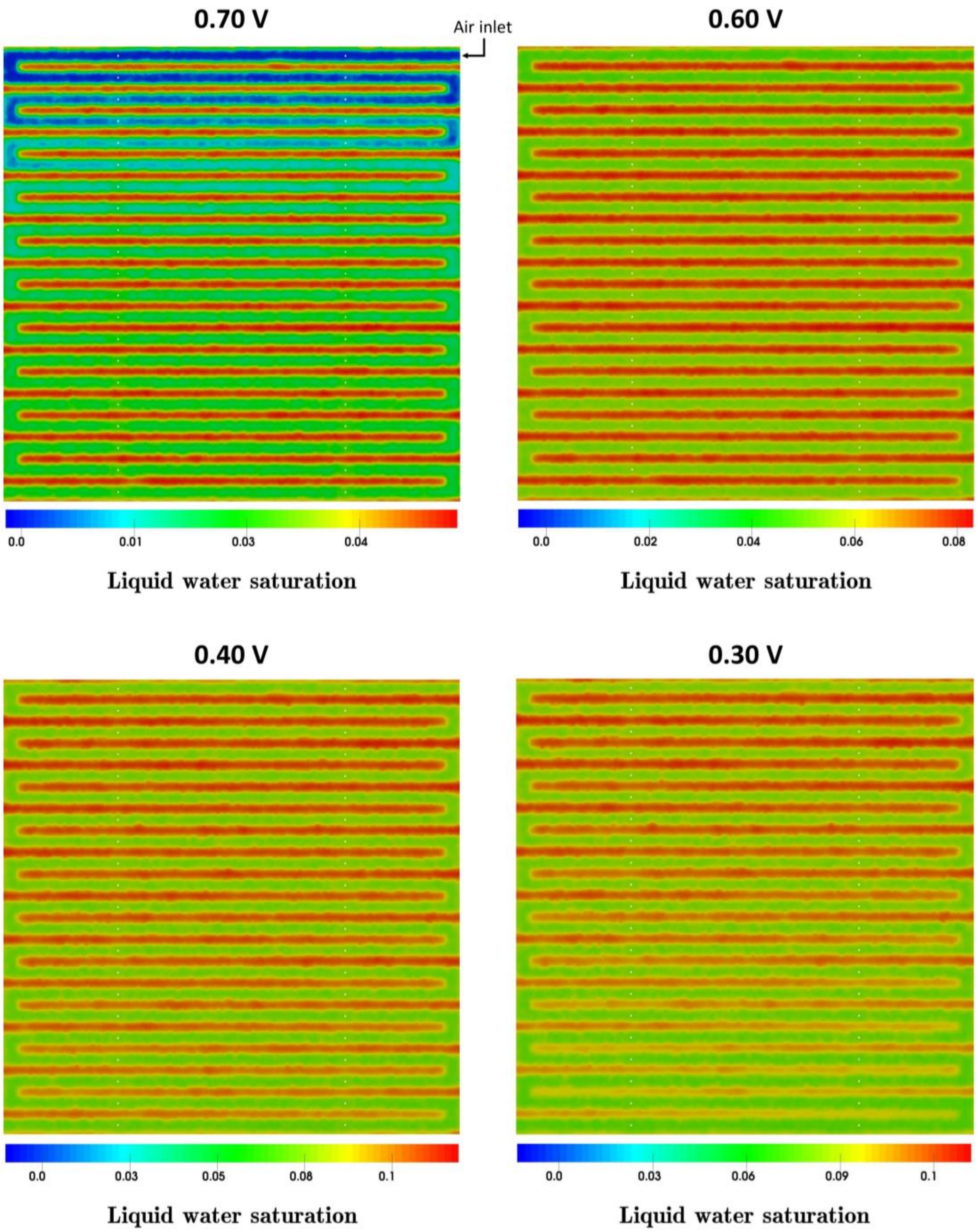

Figure 5.15. Liquid water saturation distribution at the GDL bottom wall for different operating voltages.

Figure 5.16 contains single-phase and two-phase flow predictions of the cell performance, in terms of polarization curve, calculated by the present model. In single-phase flow calculations, liquid water saturation is set equal to 0 for all voltages, and in two-phase flow calculations the liquid water saturation shown in **Figure 5.15** (area-weighted average values) is used in Equations **(5.11)** and **(5.35)** to compute the effects of liquid water flooding: the decrease in the effective diffusion coefficient; and the coverage of the active sites of the CL, respectively. It can be seen that the present two-phase flow model estimates lower performances at high currents, where mass transfer limitations are dominant. Such results show that the model can effectively account for the influence of flooding in the cell operation.

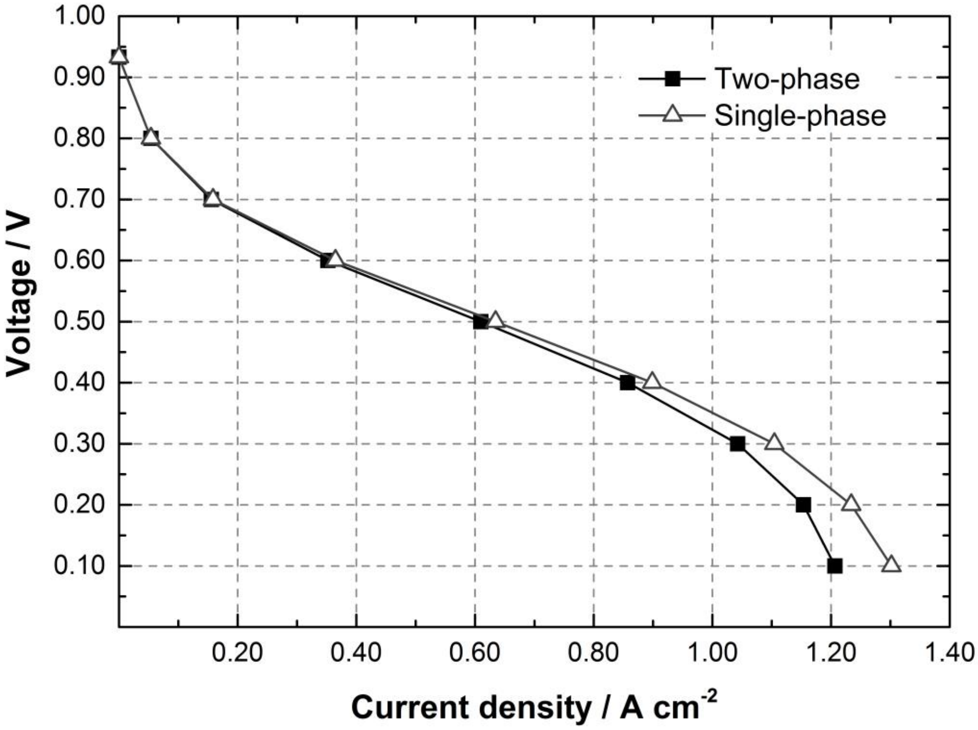

Figure 5.16. Single and two-phase flow model predictions of a fuel cell polarization curve.

5.4. Summary

In this chapter, the 1D + 3D numerical model of a PEM fuel cell developed during this work was described. The model couples the VOF method to simulate the two-phase flow in the cathode GCs with the electrochemical reactions and the water balance in the membrane. Additionally, the multi-fluid saturation model was implemented in order to obtain liquid water saturation in the GDL.

The model was successfully validated against an experimental polarization curve, and it can effectively separate the different voltage losses that affect the cell output. Moreover, it was shown that the model is capable of capturing relevant two-phase flow patterns observed experimentally: the water accumulation at the elbows of the serpentine channel and the formation of long water films attached to the side walls.

The water dynamics inside the serpentine channel for different voltages was analyzed. Water droplets emergence, detachment and interaction with the channel walls and other droplets were shown. At a lower voltage, droplets grew larger and suffered more deformation, and the amount of water accumulated in the channel was higher. Such fact was also observed when looking to the two-phase flow pressure drop, that increased when the voltage decreased. It was also observed that, after a certain time, the liquid water distribution in the channel did not change considerably over time.

The water velocity in each pore designed at the GDL surface for water emergence in the GCs was correlated with liquid water generation rate and current density distributions. It was observed that, for a higher voltage, water velocity of the pores increased along the channel length, whereas at lower voltages it tended to decrease along the channel.

The water content in different locations of the serpentine was quantified and the results showed that, as expected from the analysis of liquid water distribution, the volume-weighted water content was higher at the elbows of the serpentine channel. When dividing the serpentine into equal sections, from inlet to outlet, it was seen that the water content along the channel length generally followed the same trend as the water velocity in the pores. Furthermore, the water coverage ratio was significantly higher in the hydrophilic top and side walls of the channel in comparison with that of the GDL hydrophobic surface.

Single-phase and two-phase flow simulations were performed and it was observed that lower performances were predicted at high currents when the two-phase flow was considered, showing that the model can compute the effects of water flooding on the cell operation.

6. NUMERICAL SIMULATIONS

In this chapter, results of numerical simulations performed with the model described in the previous chapter are presented. The focus is on the two-phase flow in the serpentine channel of a PEM fuel cell cathode. The first part contains a study on the effects of the channel walls wettability. Different contact angles are set to the serpentine walls, and the resulting two-phase flow patterns are analyzed under different operating voltages and air stoichiometries. Moreover, the influence of considering local variations of the channel surfaces wettability is investigated. In the second part, the two-phase flow in a cell with a multi-serpentine flow field design is analyzed and the results are compared to those obtained with a single-serpentine one.

6.1. Effect of the channel walls wettability

Table 6.1 displays the operating voltage, air stoichiometry and walls contact angle applied in the numerical simulations conducted to investigate the effects of the walls wettability of a single-serpentine channel. It also shows the air inlet velocity and the corresponding Reynolds (Re), Weber (We) and Capillary (Ca) numbers. The model inputs were the same as those displayed in **Table 5.1**, except for the cell active area and the channel width, which were changed to 2.4 cm^2 and 1.0×10^{-3} m, respectively. The multiplicative factor for the liquid water velocity (X in Equation **(5.33)**) was also changed to 2000, in order to keep water inlet velocity close to that obtained in the simulations conducted in the previous chapter. Moreover, a more refined mesh was employed (Mesh 2 in **Appendix C**). It can be seen in **Table 6.1** that the air stoichiometries employed are higher than those usually applied in a typical PEM fuel cell (see Section **1.3.4.3**). Such values were selected in order to obtain air inlet velocities that are close to those verified in PEM fuel cells with larger active areas, which are commonly applied in automotive applications and operated with forced air flow. Fuel cells with small active area such as that employed in the present chapter are usually employed in portable applications, which generally rely on natural convection for the air supply (air breathing fuel cells). A small active area is here used with forced air flow as it results into a smaller mesh with more reasonable simulation times than those obtained with the mesh applied in the previous chapter, which exceeded two months when lower voltages were applied (in a computer having a Intel Core i7-2600 K @ 3.40 GHz CPU (all 8 processes used) and 8 GB RAM).

In the present chapter, the focus is on analyzing the cathode two-phase flow mostly from the fluid dynamics perspective. However, it is important to mention that the model developed in this work can also be used to predict the cell electrochemical performance under various operating conditions and cell designs. To illustrate that, **Appendix D** contains I-V curves calculated by the model (steady-state solutions, see Section **5.1.6**) predicting the effect of temperature, pressure, air stoichiometry and flow field design.

Table 6.1. Operating voltage, air stoichiometry (with the corresponding air velocity, Reynolds (Re), Weber (We) and Capillary (Ca) numbers) and walls static contact angle employed in the numerical simulations conducted to study the effects of the serpentine channel walls wettability.

Simulation nº	Voltage	Air stoichiometry	Air velocity	Re	We	Ca	Contact angle
1	0.60 V	10	7.60 m s^{-1}	436	0.93	0.07	40 °
2							60 °
3							90 °
4							120 °
5							140 °
6		15	11.4 m s^{-1}	653	2.09	0.11	40 °
7							60 °
8							90 °
9							120 °
10							140 °
11		23	17.5 m s^{-1}	1000	4.93	0.16	40 °
12							60 °
13							90 °
14							120 °
15							140 °
16	0.50 V	10	7.60 m s^{-1}	436	0.93	0.07	40 °
17							60 °
18							90 °
19							120 °
20							140 °
21		15	11.4 m s^{-1}	653	2.09	0.11	40 °
22							60 °
23							90 °
24							120 °
25							140 °
26		23	17.5 m s^{-1}	1000	4.93	0.16	40 °
27							60 °
28							90 °
29							120 °
30							140 °

6.1.1. Water dynamics in the serpentine channel with different walls wettability

Figure 6.1 depicts liquid water distribution in the serpentine channel with different walls wettability. The results displayed were obtained at an operating voltage of 0.50 V and an air stoichiometry of 10. Because water dynamics with respect to time was already discussed in the previous chapter (Section **5.3.1**), the focus here is mainly on the resulting two-phase flow patterns. It can be seen in **Figure 6.1** that the wettability of the channel walls has a significant influence on water dynamics. When hydrophilic (wettable) channel walls are considered (**Figure 6.1** A and **Figure 6.1** B), the water spreads into the walls and there is the formation of long water films that attach to the upper corners of the channel. Moreover, such films are longer when the walls contact angle is lower, because decreasing the contact angle leads to higher wall adhesion forces. When the channel walls are considered to be hydrophobic (non-wettable) (**Figure 6.1** D and **Figure 6.1** E), the low adhesion forces prevent water from spreading into the walls. Therefore, water moves along the channel mainly in the form of droplets. It can also be observed that more and smaller droplets are found when the walls hydrophobicity is higher (**Figure 6.1** E). In such case, the weak adhesion forces cause the droplets to detach more easily from the walls, preventing the formation of larger droplets. The case where a contact angle of 90 ° is applied (**Figure 6.1** C) represents an intermediate scenario between those just described. Water is also observed to move along the channels as films in the upper corners, but such films are shorter than those observed when the walls are considered to be hydrophilic. In addition, some droplets can be found attached to the channel surfaces.

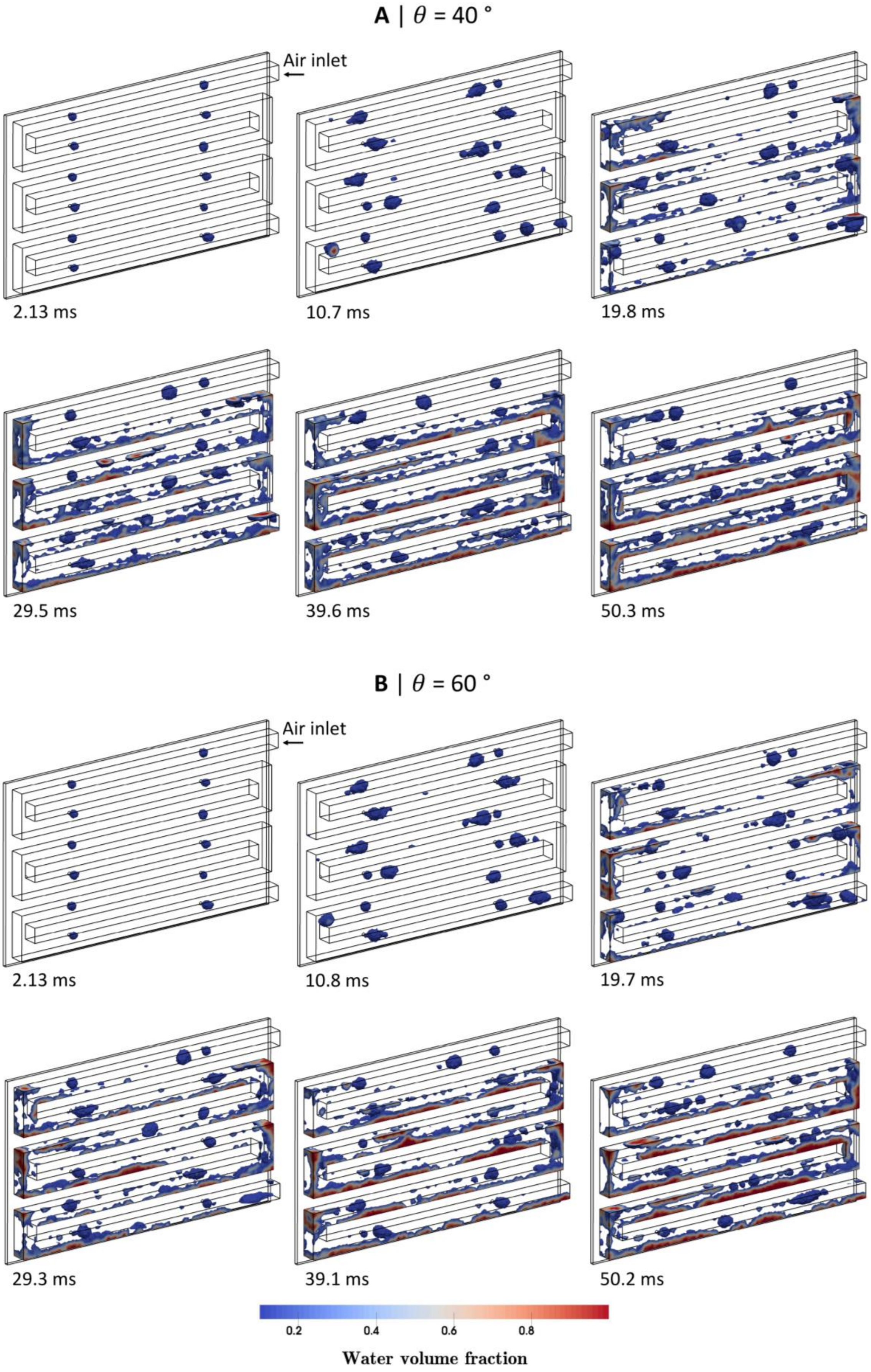

Figure 6.1. Water dynamics in a serpentine channel with different walls contact angle (θ).

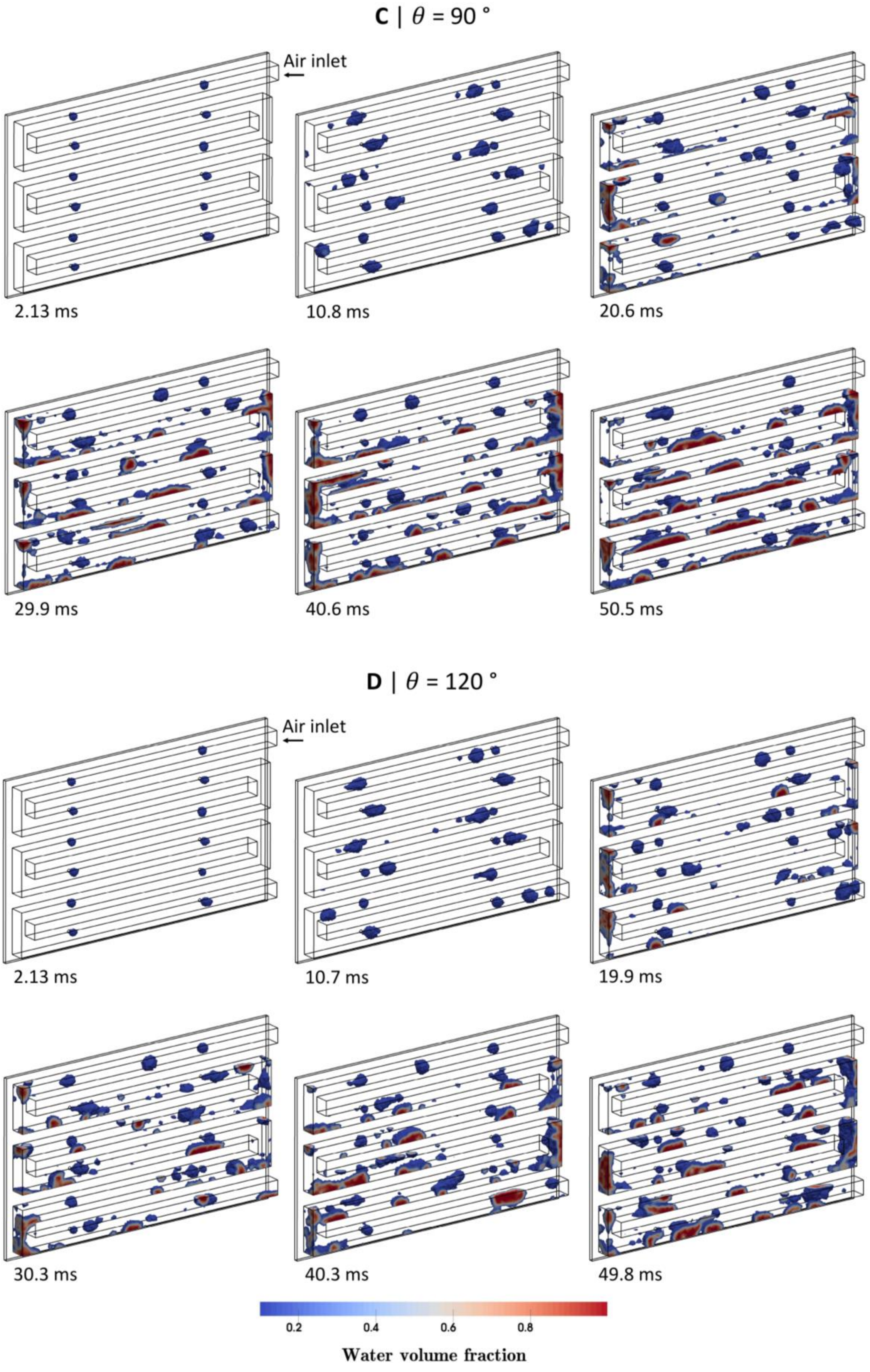

Figure 6.1 (Continued)

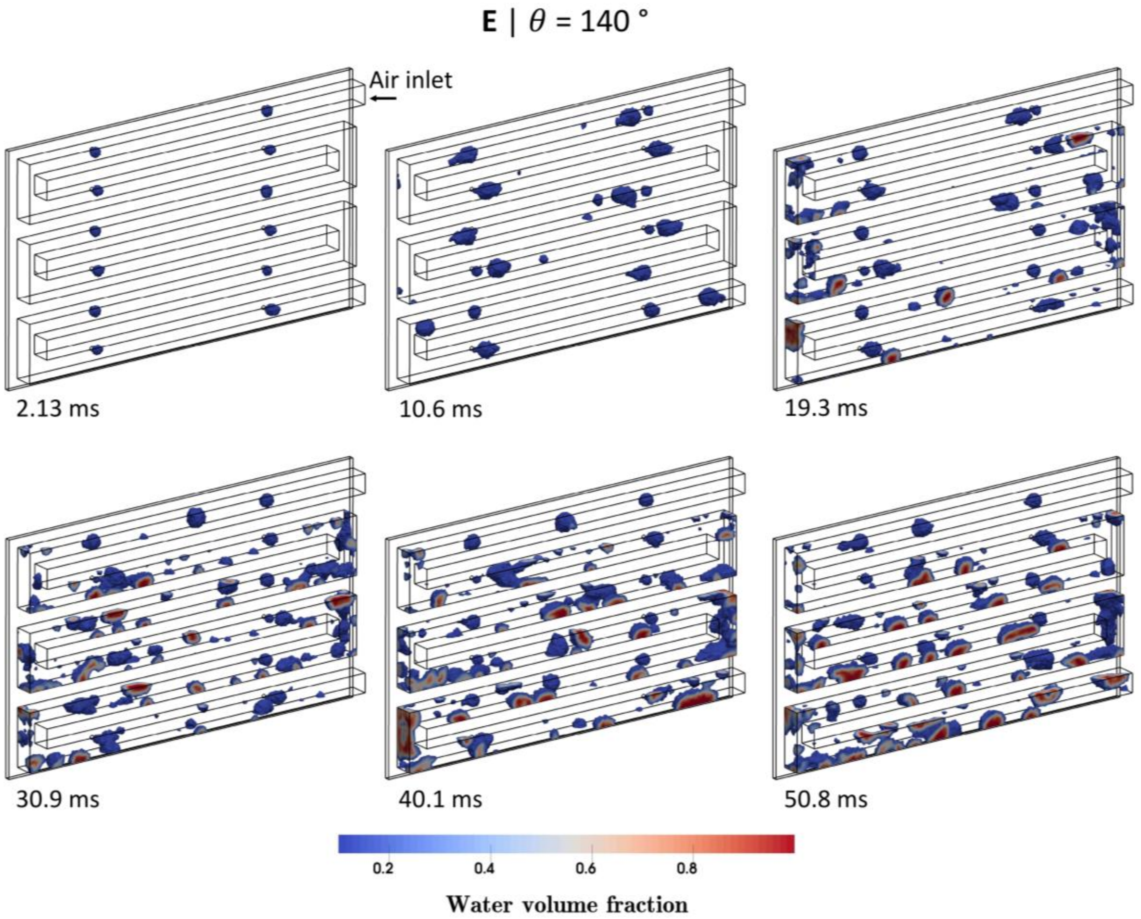

Figure 6.1 (Continued).

Figure 6.2 displays the two-phase flow pressure drop with respect to time for different values of the channel walls wettability. It can be seen that pressure drop reaches higher values when the walls are considered hydrophobic. In such case, water movement as droplets occupies a larger portion of the channel cross-section area than that filled by the films formed when hydrophilic surfaces are employed, increasing the flow resistance. Moreover, larger pressure fluctuations are observed when considering hydrophobic walls. Because there is a great number of droplets in the channel, there is a higher chance for these droplets to interact with each other, forming very large droplets that lead to a sudden increase in the pressure drop. When a blower or a compressor is used to supply air, as in transportation applications, higher pressure drops should be avoided because they increase the power consumption of these devices, leading to a decrease in the overall system efficiency.

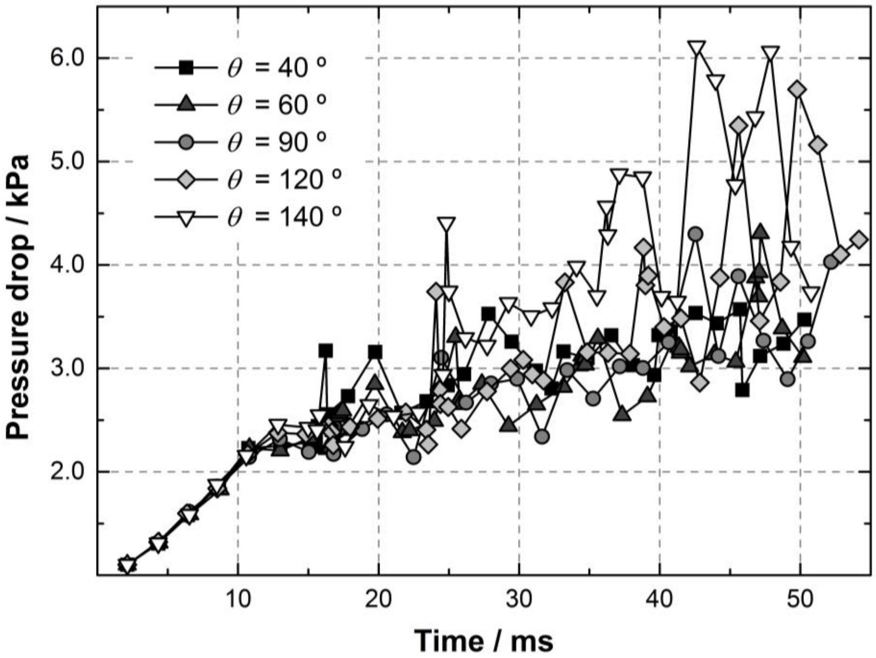

Figure 6.2. Two-phase flow pressure drop in the serpentine channel with different channel walls contact angle (θ).

The time-averaged volume-weighted water content in the entire serpentine channel, at its elbows and in its straight sections, as a function of the walls contact angle, is shown in **Figure 6.3**. The temporal profile of such values is very similar to that depicted in **Figure 5.12**. Therefore, the time-averaged values are here shown as they allow a more straightforward analysis. Such as verified in the previous chapter for a 25 cm^2 fuel cell (Section **5.3.4**), the volume-weighted water content is higher at the elbows of the serpentine channel. In addition, it can be seen that the elbows water content is lower when applying the lowest (40 °) and the highest (140 °) walls contact angle. In the most hydrophilic case, water spreads more easily forming longer films that extend out of the elbows. In the more hydrophobic case, the weak adhesion forces prevent the droplets, which have also lower volume than those in the less hydrophobic case (120 °), to accumulate at the elbows.

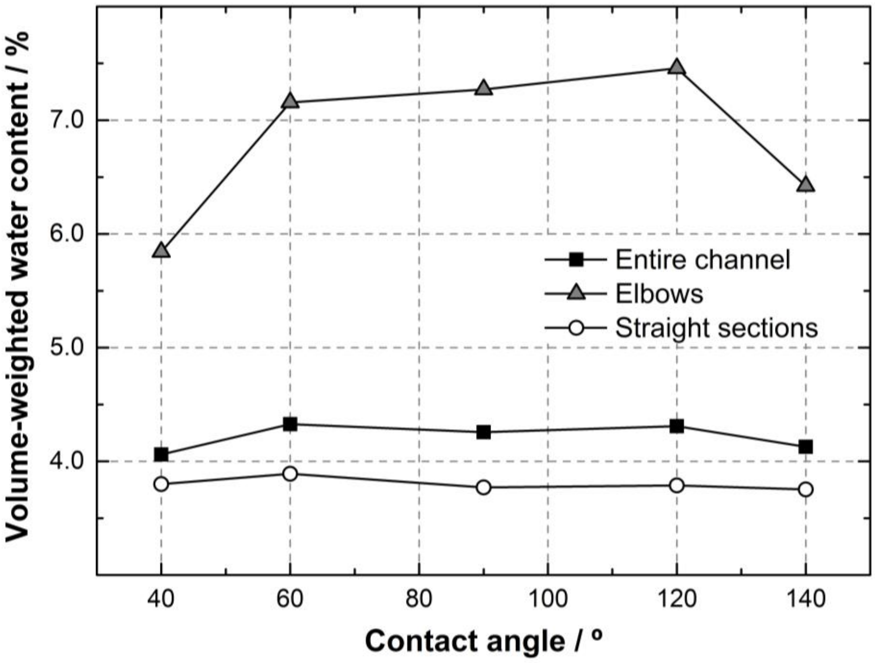

Figure 6.3. Time-averaged volume-weighted water content in the serpentine channel, at its elbows and in its straight sections, as a function of the channel walls contact angle.

Figure 6.4 displays the time-averaged water coverage ratio in the top and side walls of the serpentine channel and in the GDL surface, as a function of the walls contact angle. Like the volume-weighted water content, the temporal profile of water coverage ratio is close to that shown in the previous chapter (**Figure 5.14**). It can be seen that the water coverage ratio is higher in the top and side walls of the channel. However, the coverage of these walls by liquid water decreases considerably as the contact angle is increased. Such results are in accordance with the two-phase flow patterns shown in **Figure 6.1**: when the channel walls are hydrophilic water spreads in their surfaces, whereas when they are hydrophobic water flows in the form of droplets with less interaction with the walls. Moreover, **Figure 6.4** shows that the GDL surface water coverage ratio does not change considerably for all the values of the channel walls wettability considered. Therefore, the access of oxygen to the CL was not significantly changed. In accordance, the cell electrochemical performance was not affected: the current density produced was about 0.73 A cm^{-2} for all the cases addressed in this section. In fact, the cell performance was not affected by the channel walls wettability in any of the simulations conducted in this work.

Taking into account all the results presented in this section, hydrophilic walls can be considered the most appropriate option concerning the serpentine channel walls wettability. Although they do not result into a direct improvement in the cell electrochemical performance, they reduced the two-phase flow pressure drop that would lead to higher efficiencies of PEM fuel cell systems when blowers or compressors are used to control the air flow rate.

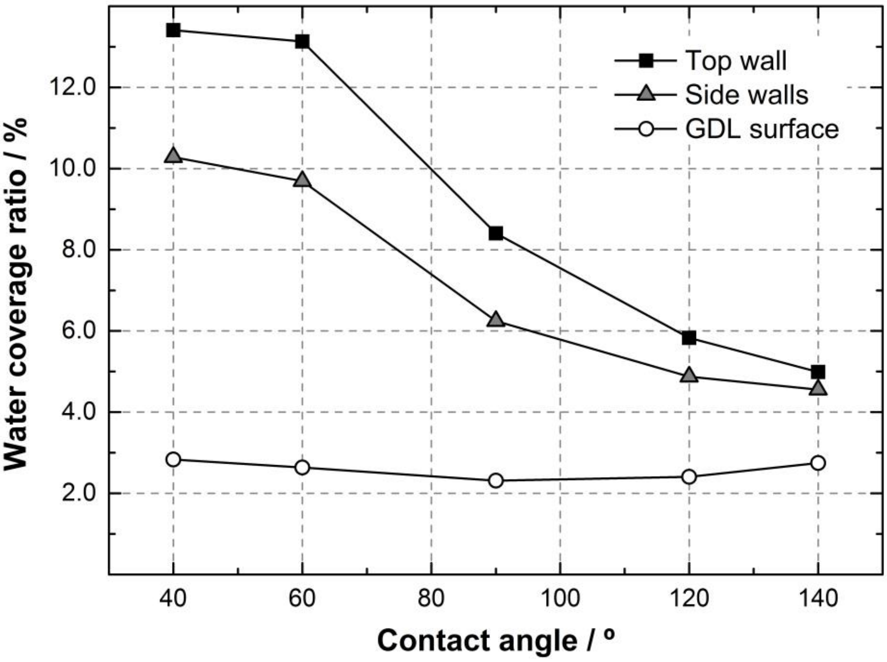

Figure 6.4. Time-averaged water coverage ratio in the top and side walls of the serpentine channel and in the GDL surface, as a function of the channel walls contact angle.

6.1.2. Effect of air stoichiometry

In this section, the impact of the air stoichiometry on the two-phase flow patterns in the serpentine channel is investigated. **Figure 6.5** shows the liquid water distribution at about 40 ms for different air stoichiometries and channel walls wettability. These results were obtained at 0.50 V. It can be seen that similar two-phase patterns are observed when considering air stoichiometries of 10 and 15, although the influence of wettability becomes less evident in the latter case, especially when comparing cases with closer contact angles (**Figure 6.7** A *vs* **Figure 6.7** B and **Figure 6.7** D *vs* **Figure 6.7** E). When the air stoichiometry is set to 23, however, the two-phase flow patterns change considerably, and they are no longer influenced by the walls wettability. Increasing the air stoichiometry leads to higher air velocities in the channel, which increases the shear force of the air flow. Therefore, for a given wettability, raising the air stoichiometry increases the importance of the shear force over the wall adhesion forces. When the shear force is high enough, such as the case of a stoichiometry of 23, the wall adhesion effects become irrelevant, and the water flow is dominated by shear force.

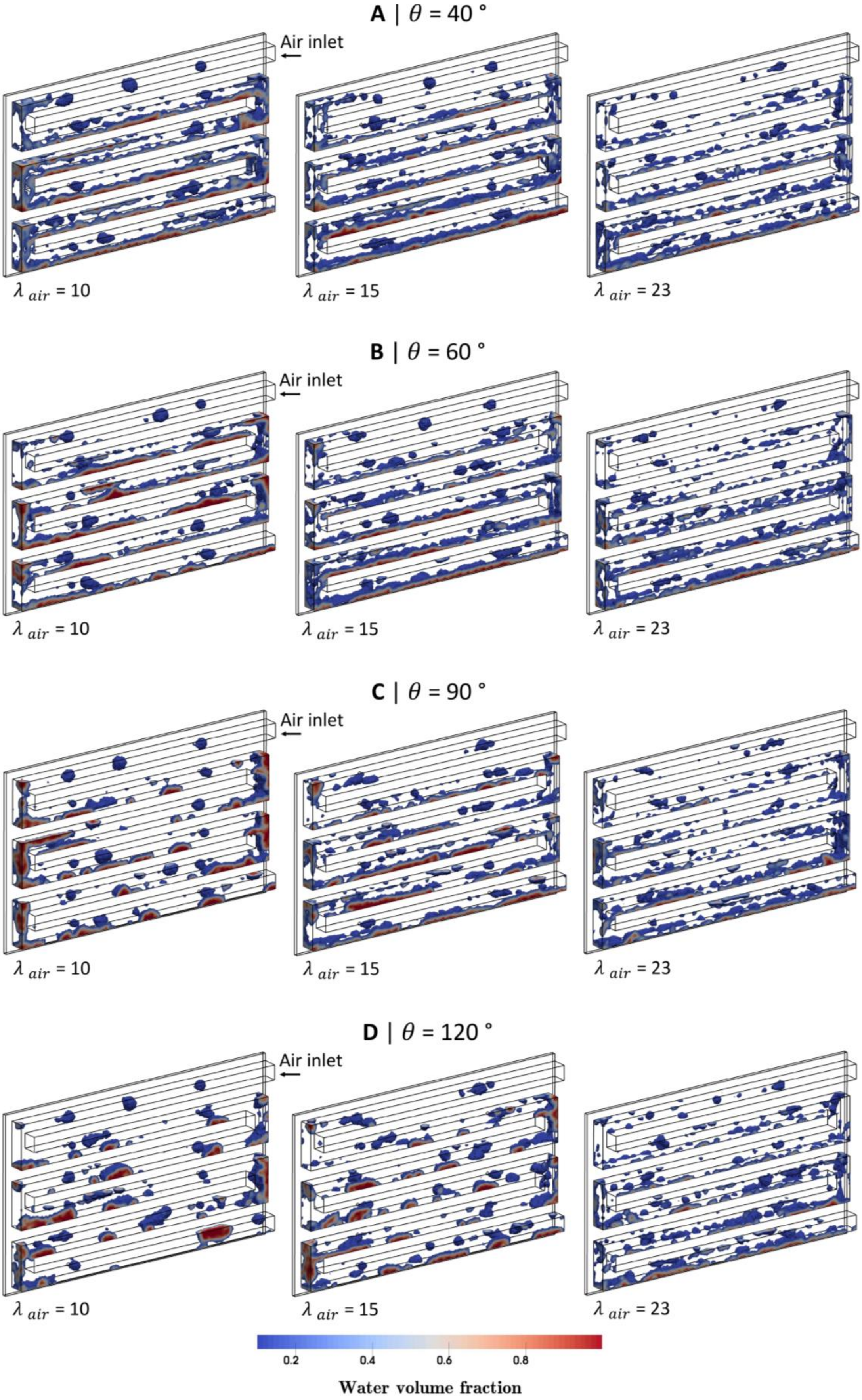

Figure 6.5. Water distribution in the serpentine channel at about 40 ms for several air stoichiometries (λ_{air}) and channel walls contact angle (θ).

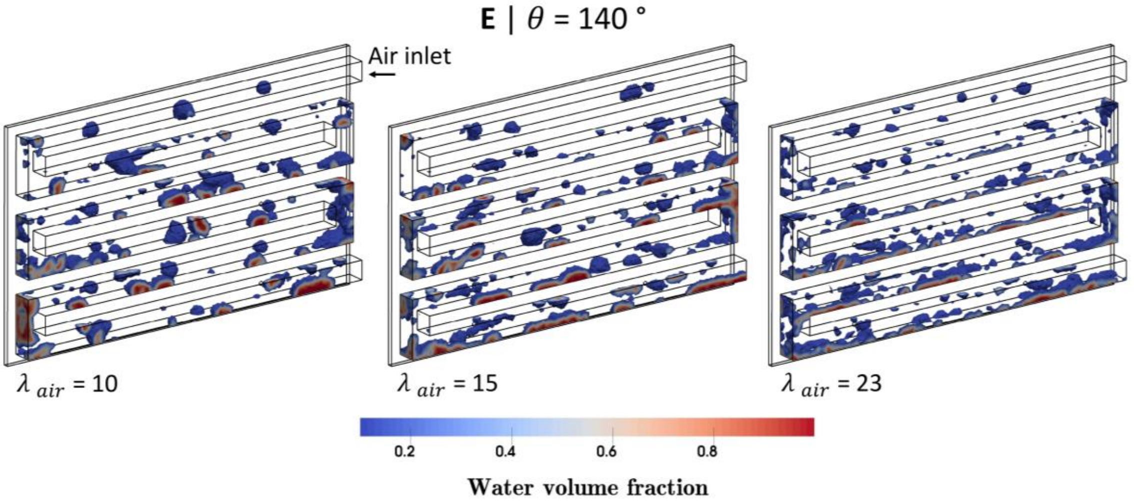

Figure 6.5 (Continued)

Figure 6.6 shows the two-phase flow pressure drop for various air stoichiometries and channel walls wettability. Because pressure losses are proportional to the gas velocity (in laminar regime), the two-phase flow pressure drop increases as the air stoichiometry increases. It can also be seen that the walls wettability only significantly affects pressure drop for the lowest air stoichiometry tested, which is in accordance with that discussed when analyzing the liquid water distribution (**Figure 6.5**). Moreover, the pressure drop increases over time for an air stoichiometry of 10 and 15, whereas for the highest value of air stoichiometry it remains approximately constant after about 20 ms. This occurs because at higher air velocities liquid water is removed more rapidly, not only leading into a lower water content (**Figure 6.7**) but also into a faster stabilization of the amount of water present in the channel.

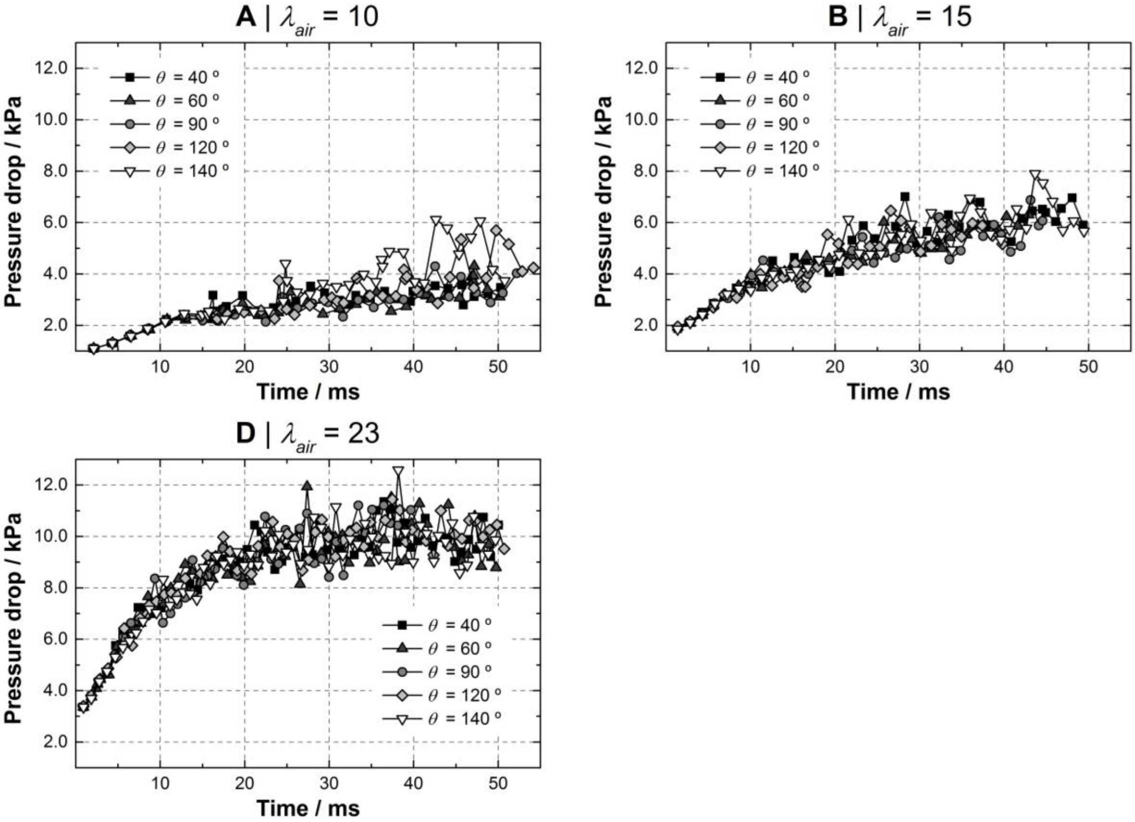

Figure 6.6. Two-phase flow pressure drop in the serpentine channel for different values of air stoichiometries (λ_{air}) and channel walls contact angle (θ).

The values of the time-averaged volume-weighted water content in the entire serpentine channel, at its elbows and in its straight sections, for different air stoichiometries and as a function of the channel walls wettability are depicted in **Figure 6.7**. The results for the walls water coverage ratio are shown in **Figure 6.8**. Both **Figure 6.7** and **Figure 6.8** support what was discussed above, *i.e.*, increasing air stoichiometry decreases the amount of water present in the channel and reduces the influence of the walls wettability.

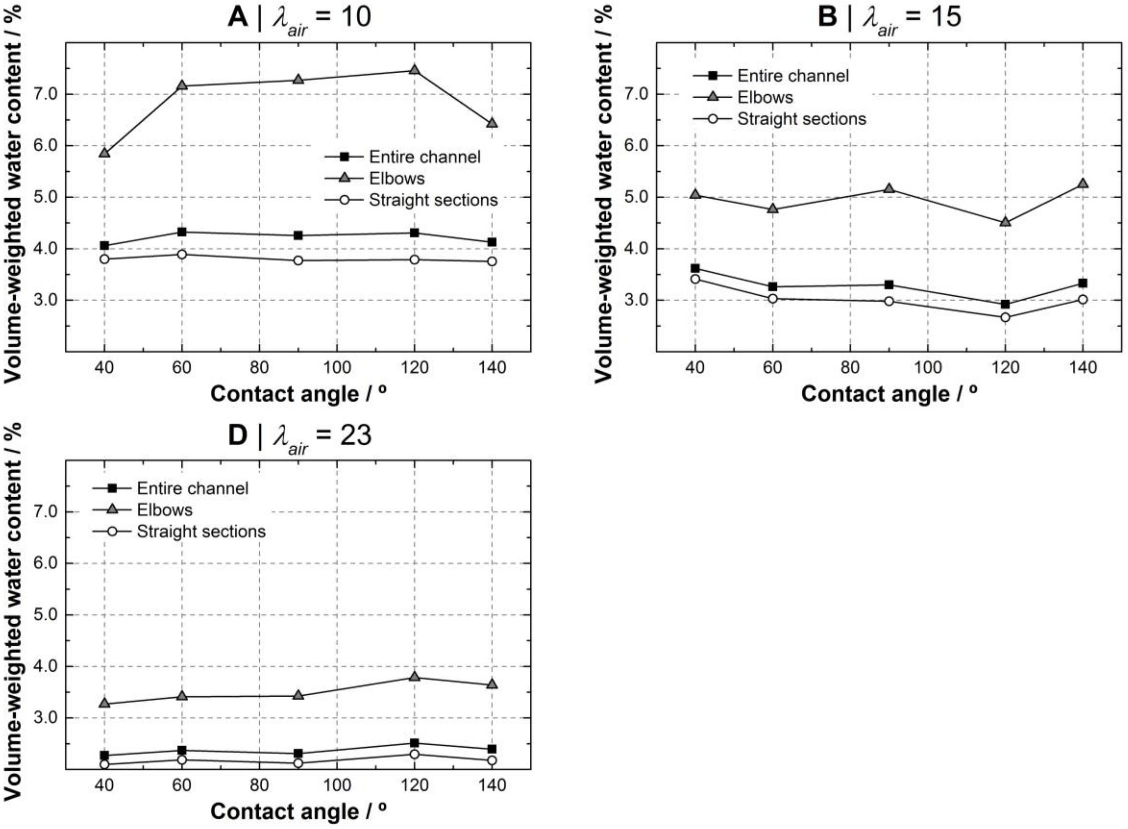

Figure 6.7. Time-averaged volume-weighted water content in the serpentine channel, at its elbows and in its straight sections, for several air stoichiometries (λ_{air}) and channel walls contact angle.

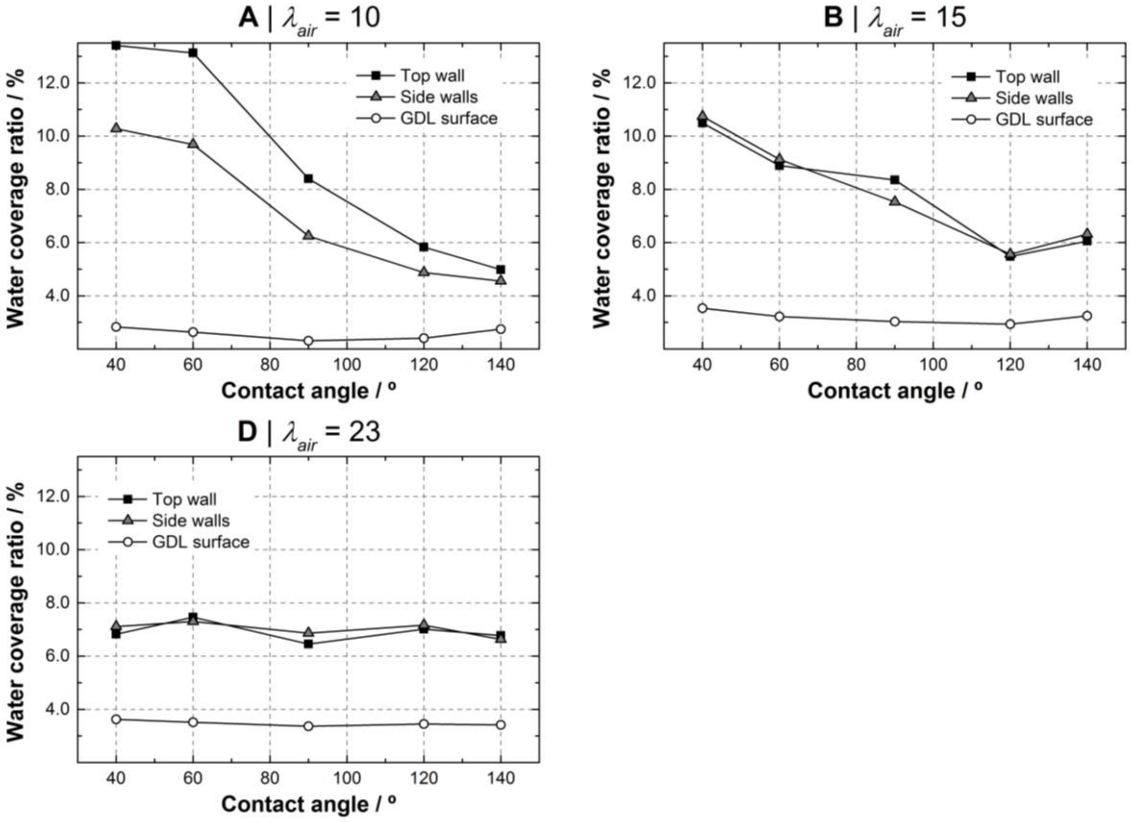

Figure 6.8. Time-averaged water coverage ratio in the top and side walls of the serpentine channel and in the GDL surface, for several stoichiometries (λ_{air}) and channel walls contact angle.

The results of the present section show that the two-phase flow patterns are only affected by the GCs walls wettability when the air stoichiometry is not too high. Regarding the cell electrochemical performance, it improves when the air stoichiometry increases (see **Appendix D**). However, pressure drop also increases significantly when the air stoichiometry is higher (**Figure 6.6**). That is why air stoichiometry is referred as a system design variable [4], because the gain in fuel cell power output caused by increasing the air stoichiometry must be weighted considering the increase in energy consumption of the blower to ensure such stoichiometry.

6.1.3. Effect of operating voltage

The effects of operating voltage on the two-phase in a serpentine channel was already discussed in detail in the previous chapter (Section **5.3**). Here the focus is on investigating if the channel walls wettability affects the two-phase flow in the same way for two different operating voltages. In the simulations conducted in this chapter, increasing the voltage from 0.60 V to 0.50 V results into a 100 % increase of the water inlet velocity in each pore (from about 0.40 m s^{-1} to 0.80 m s^{-1}). The results of the present section (for an air stoichiometry of 10) clearly show that altering the operating voltage does not change how the walls wettability affect the two-phase flow. Similar water distributions are observed (**Figure 6.9**) and the two-phase flow pressure drop (**Figure 6.10**) follows the same temporal profile for both voltages considered. Moreover, the time-averaged volume-weighted water content (**Figure 6.11**) and walls water coverage ratio (**Figure 6.12**) dependence on the GCs walls wettability is kept when the operating voltage is changed. The only significant differences are the higher values of pressure drop, water content and walls water coverage ratio, for any given wettability, obtained when the operating voltage is decreased. The reasons for such outcome were already discussed in the previous chapter (see Sections **5.3.3** and **5.3.4**).

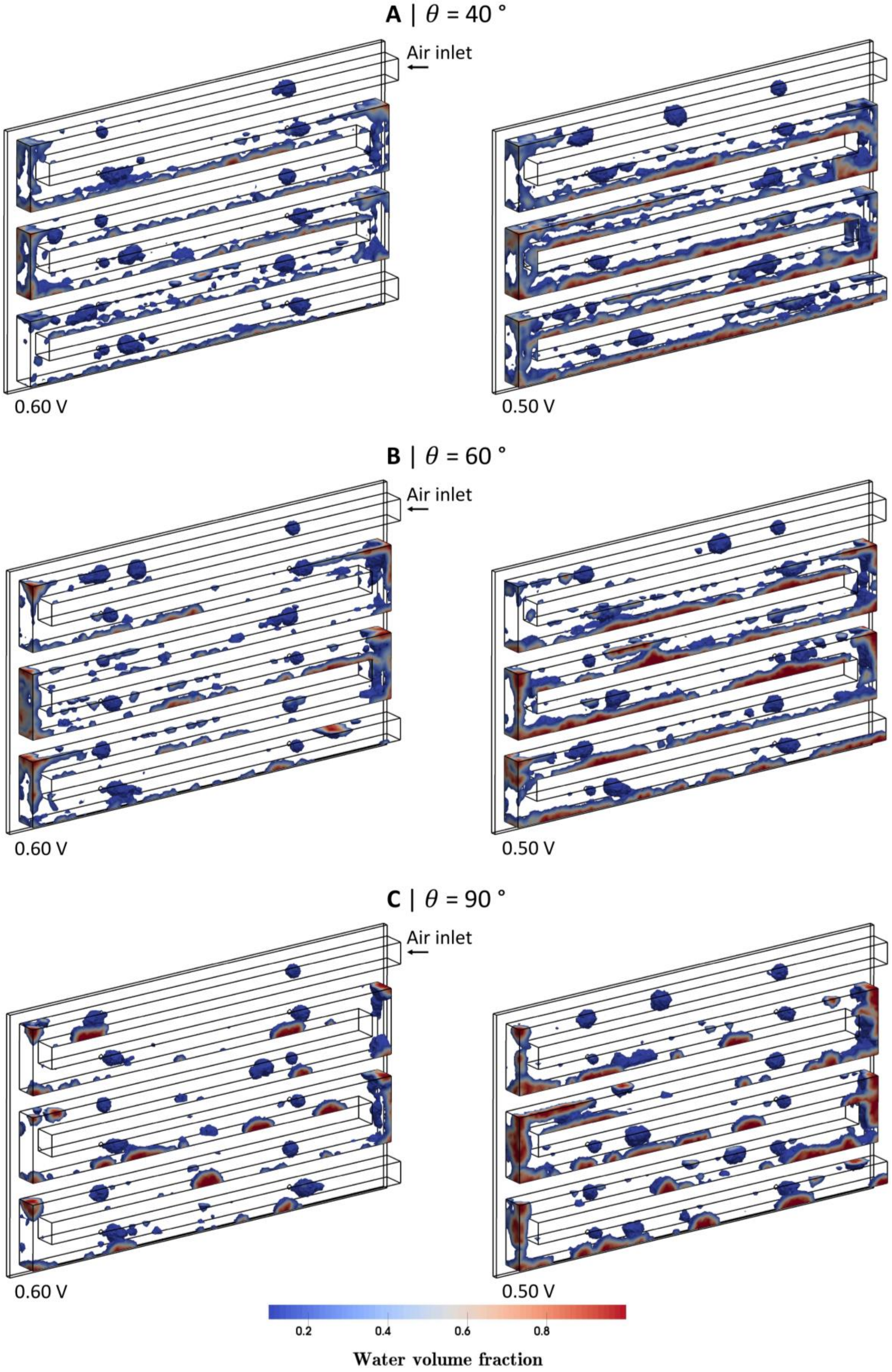

Figure 6.9. Water distribution in the serpentine channel at about 40 ms for two different operating voltages and several channel walls contact angle (θ).

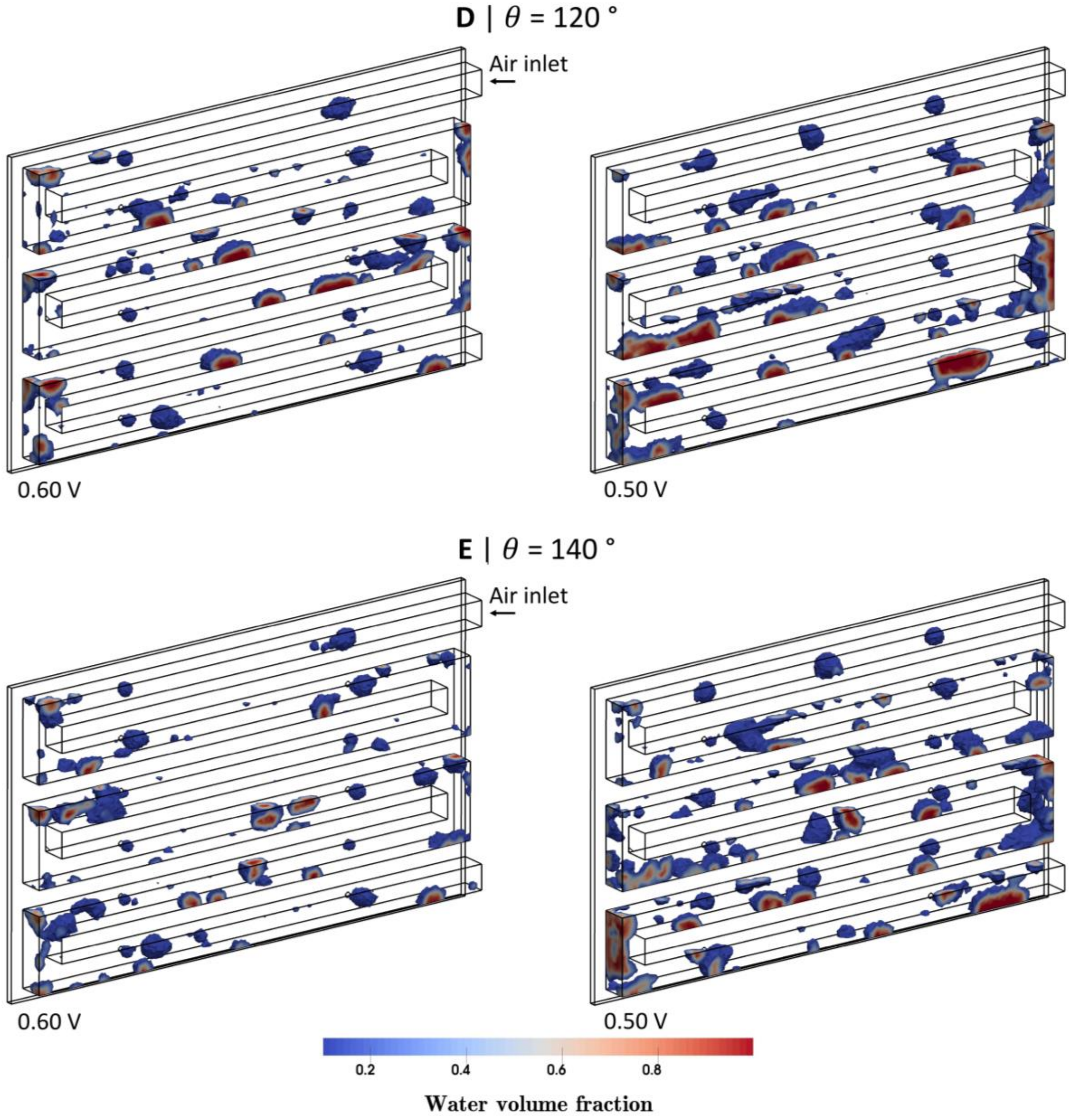

Figure 6.9 (Continued).

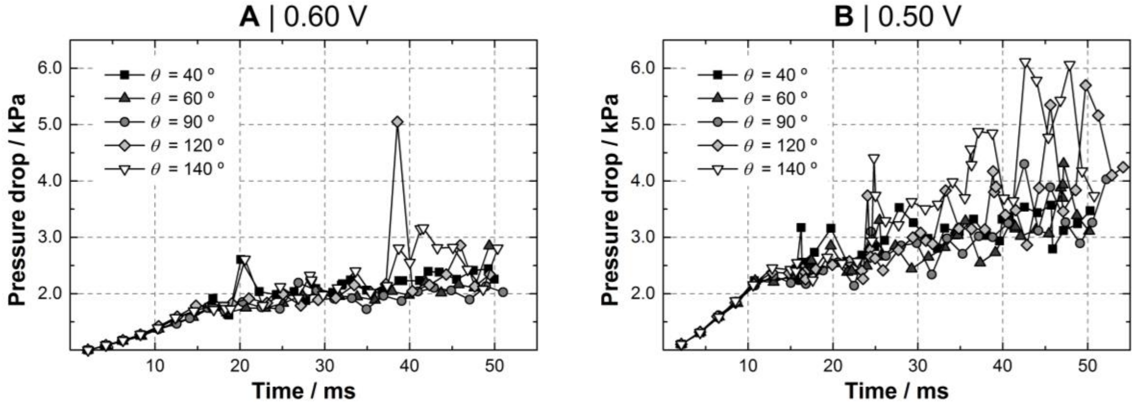

Figure 6.10. Two-phase flow pressure drop in serpentine channel for two different operating voltages and several channel walls contact angle (θ).

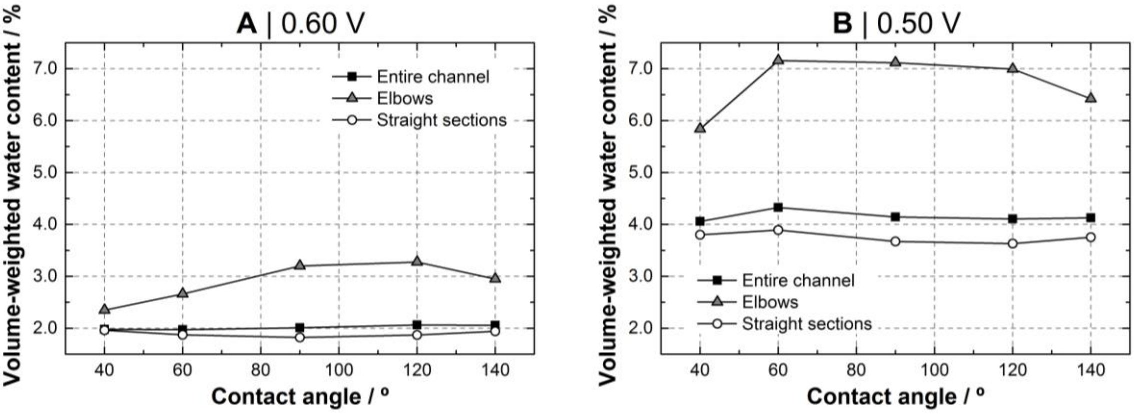

Figure 6.11. Time-averaged volume-weighted water content in the serpentine channel, at its elbows and in its straight sections, for two different operating voltages and several channel walls contact angle.

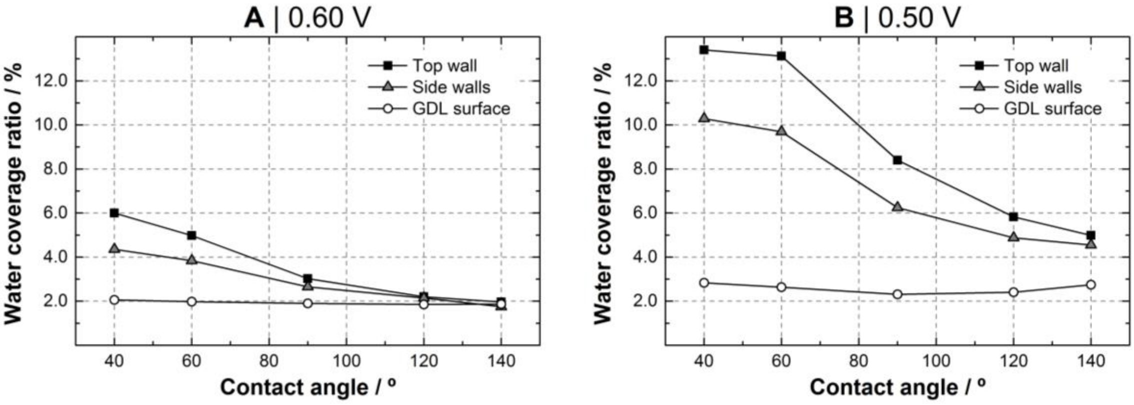

Figure 6.12. Time-averaged water coverage ratio in the top and side walls of the serpentine channel and in the GDL surface, for two different operating voltages and several channel walls contact angle.

6.1.4. Different wettability at the elbows of the serpentine channel

For all cases presented in the previous sections, the results show that the amount of water accumulated at the elbows of the serpentine channel is significantly higher than that in the straight sections. Song *et al.* [198] employed the VOF method to investigate the effects of setting the turning part (elbow) of a U-shaped channel hydrophobic while keeping the straight sections hydrophilic, and the results revealed that this configuration results into beneficial two-phase flow patterns (low water content in the channel and reduced GDL water coverage ratio). In this section, the model developed in this work is applied to investigate how the variation of the elbows wettability affects the two-phase flow in a complete serpentine channel.

Figure 6.13 displays the water dynamics in a serpentine channel having walls entirely hydrophilic (**Figure 6.13** A) or hydrophobic (**Figure 6.13** C), having hydrophobic walls at the elbows and hydrophilic walls in the straight sections (**Figure 6.13** B), and having hydrophilic walls at the elbows and hydrophobic walls in the straight sections (**Figure 6.13** D). Such patterns were obtained at an operating voltage of 0.60 V and air stoichiometry of 10. Analyzing the water distribution in cases A and B, it is visible that setting the elbow walls to hydrophobic (**Figure 6.13** B) prevents the water accumulation at the elbows which is verified when the entire channel is hydrophilic (**Figure 6.13** B). This is confirmed in **Figure 6.14**, where it can be seen that the volume-weighted water content at the elbows is generally lower when they are hydrophobic. There is a pick value in the water content at the elbows between 40 and 50 ms for the case with hydrophobic elbows (**Figure 6.14** B) that, after a carefully analysis, was found be caused by a unique event of two large droplets reaching the elbows at the same time. When analyzing the water distribution in cases C and D, the effect of considering hydrophilic elbow walls (D) is also evident, since water spreading can be observed at the elbows which does not occur when the channel walls are considered homogeneously hydrophobic (**Figure 6.13** C). However, in this case the volume-weighted water content (**Figure 6.14** C and D) was not substantially affected. As for two-phase flow pressure drop (**Figure 6.15**), it was not significantly affected by varying the elbows wettability. When analyzing the walls water coverage ratio (**Figure 6.16**), contrarily to that reported by Song *et al.* [198], considering the elbow walls as hydrophobic and the remaining walls as hydrophilic (**Figure 6.16** B) did not result into lower GDL water coverage ratio in comparison with the cases having homogenously hydrophilic (**Figure 6.16** A) or hydrophobic (**Figure 6.16** C) walls. In fact, the two hybrid cases tested in this study led to higher GDL water coverage ratio (**Figure 6.16** B and D) than that obtained considering entirely hydrophilic or hydrophobic channel walls. (**Figure 6.16** A and C).

The reason for the results of the present study being different from those in Ref. [198] might be related with the different domains used. Song *et al.* [198] considered a 11.2 mm long U-shaped channel having an elbow with a length of 3.1 mm. This means that the wettability of more than 27 % of the channel was changed. In the present work, a 121 mm long complete serpentine was used having 5 elbows that occupy less than 17 % of total channel length. This may explain why changing the wettability of the elbow in the work of Song *et al.* [198] presented more significant differences than those observed here.

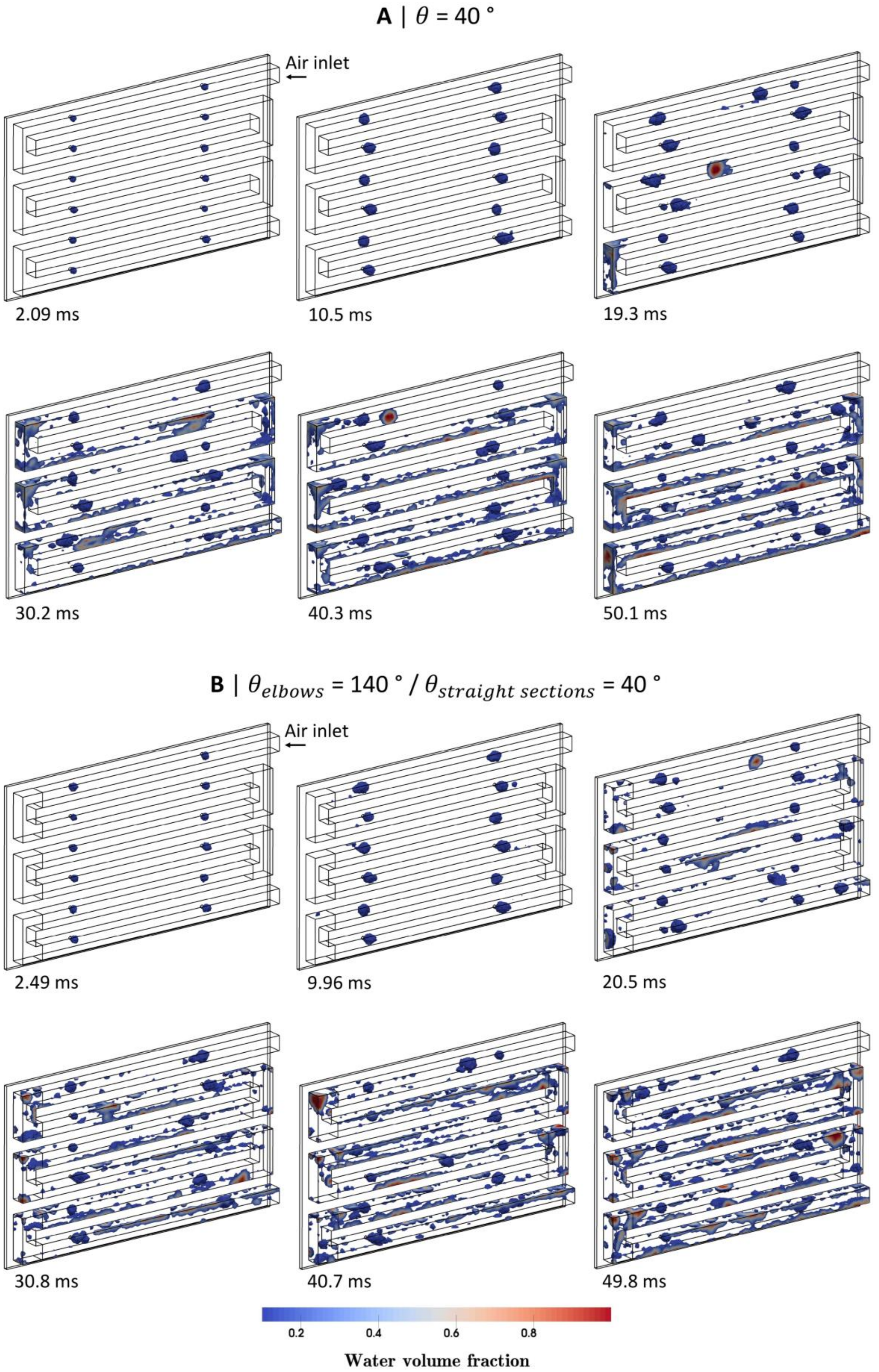

Figure 6.13. Water dynamics in a serpentine channel considering different contact angles (θ) at the elbow walls.

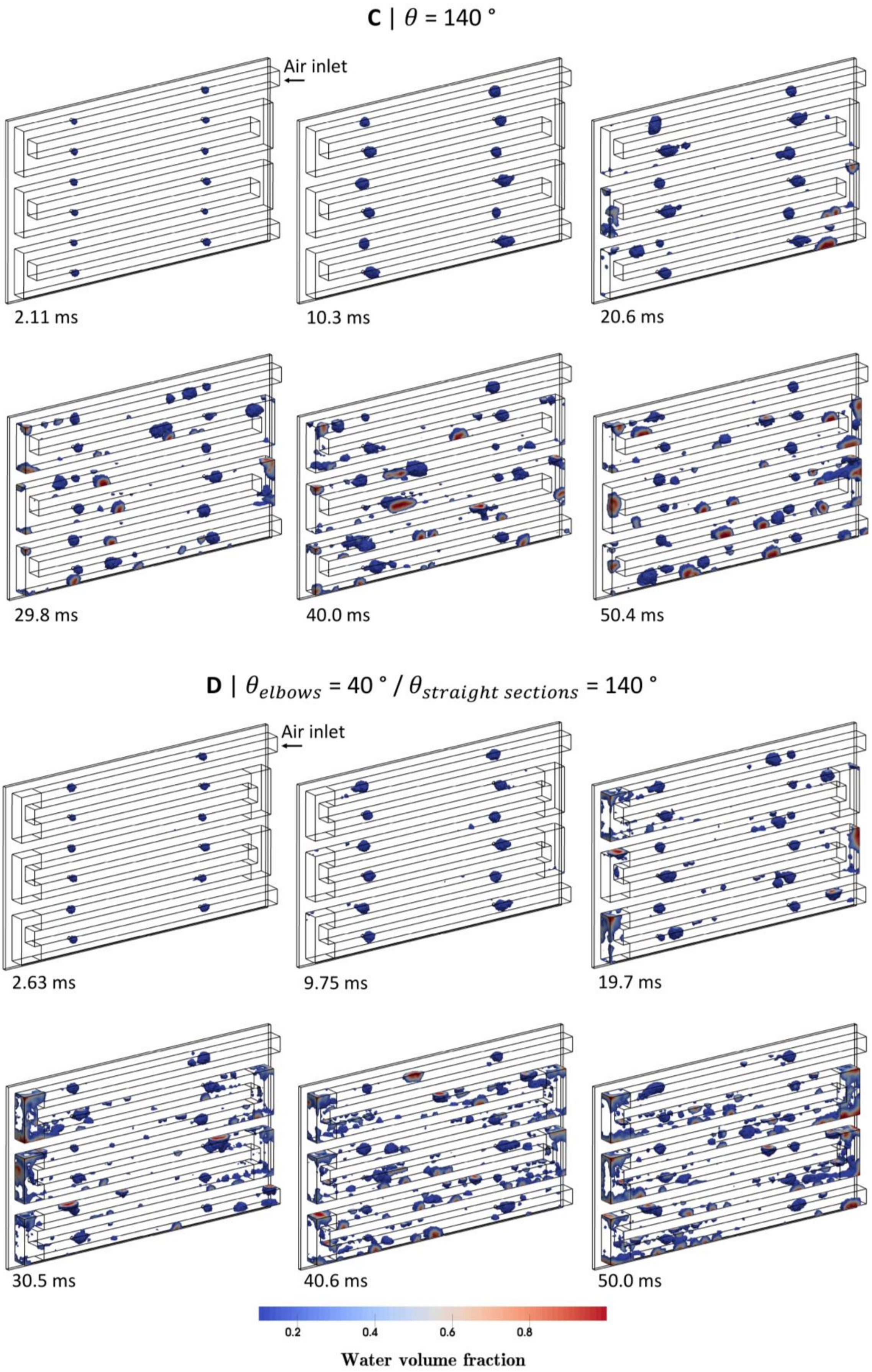

Figure 6.13 (Continued)

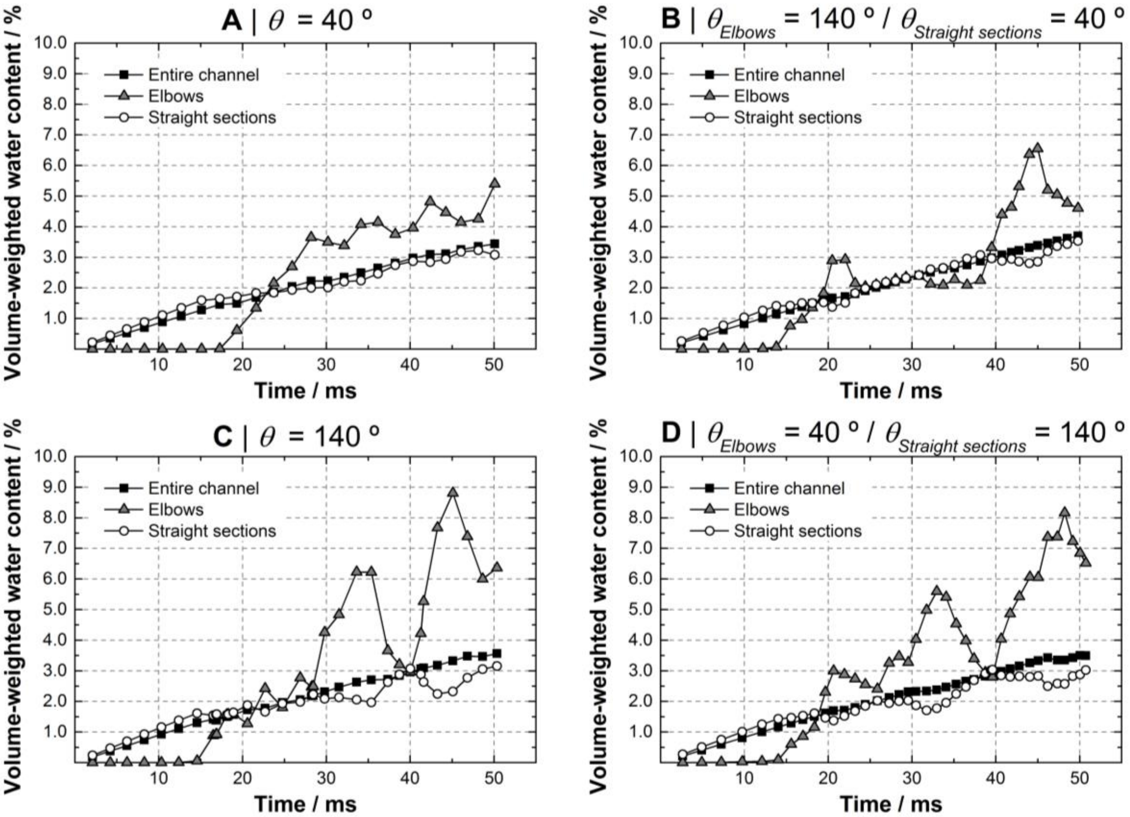

Figure 6.14. Volume-weighted water content in the serpentine channel, at its elbows and in its straight sections considering different contact angles (θ) at the elbow walls.

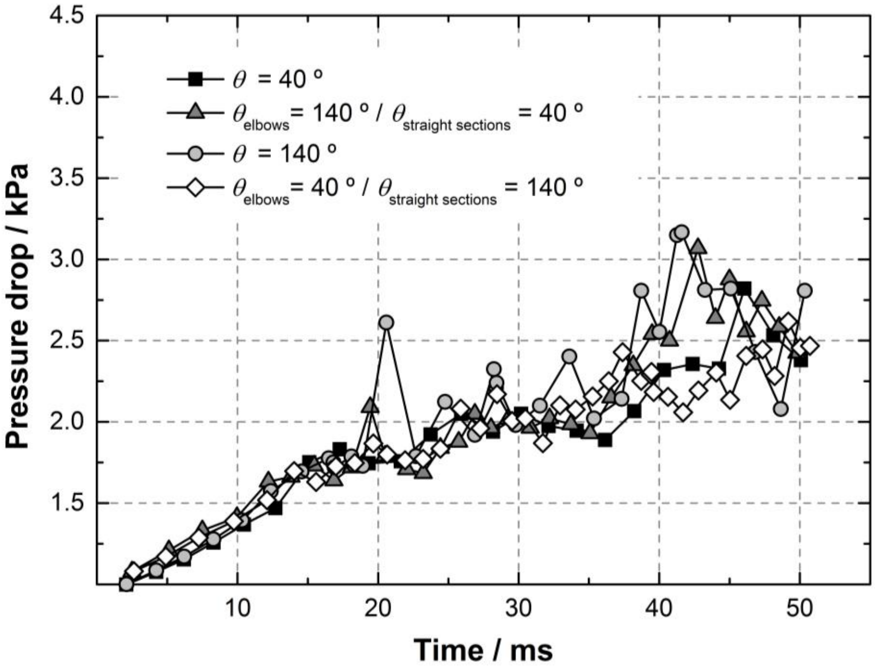

Figure 6.15. Two-phase flow pressure drop in the serpentine channel considering different contact angles (θ) at the elbow walls.

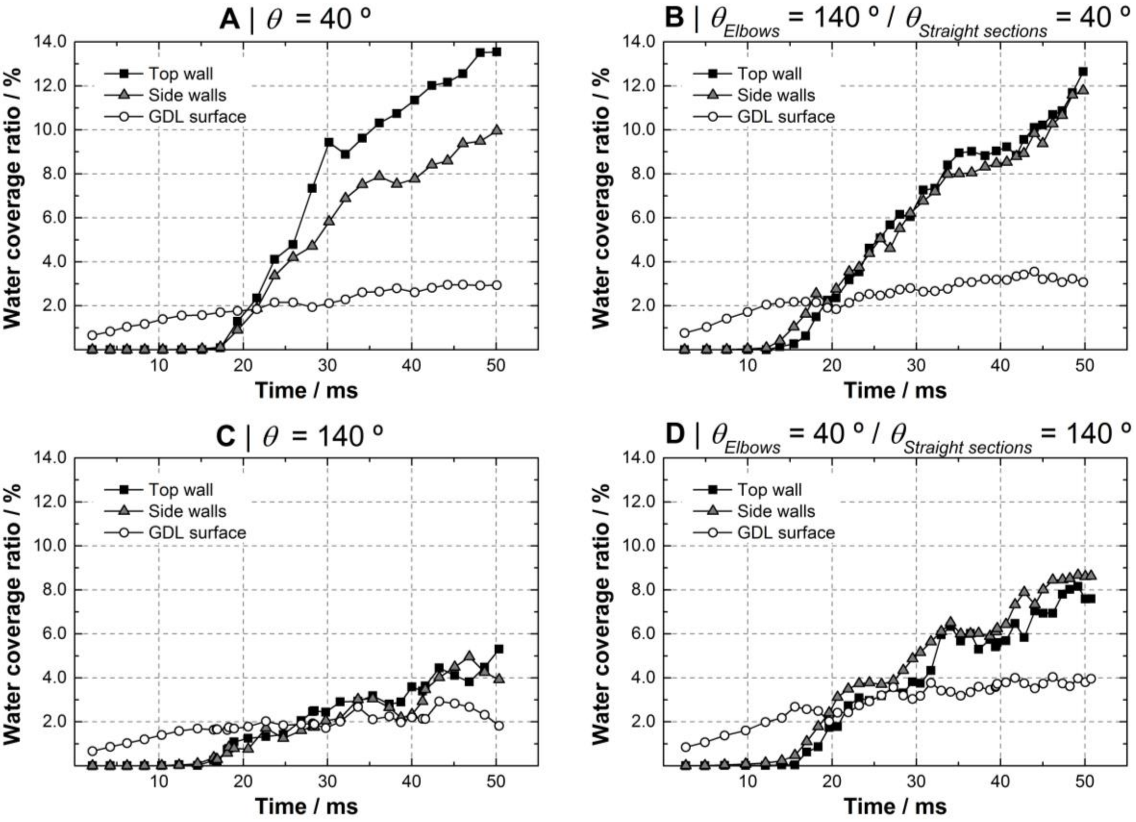

Figure 6.16. Water coverage ratio in the top and side walls of the serpentine channel and at the GDL surface considering different contact angle (θ) at the elbow walls.

6.1.5. Different wettability in the top and side walls

In this section, the influence of applying different wettability values in the top and side walls of the serpentine channel is analyzed. **Figure 6.17** shows water distribution in a channel with hydrophilic top walls and hydrophobic side walls (**Figure 6.17** A), and in a channel with hydrophobic top walls and hydrophilic side walls (**Figure 6.17** B). The results shown here were also obtained at an operating voltage of 0.60 V and air stoichiometry of 10. As expected, setting the top walls hydrophilic and the side ones hydrophobic leads to water accumulation in the top walls, whereas considering the top walls hydrophobic and the side ones hydrophilic forces water to move along the side walls. That also becomes evident when analyzing the top and side walls water coverage ratio depicted in **Figure 6.18**. Moreover, it can be seen that the hybrid case with hydrophilic top walls presents the lowest GDL water coverage ratio whereas the hybrid case with hydrophobic top walls presents the highest. When the top walls are hydrophilic and the side ones are hydrophobic, water is trapped in the top of the channel, and therefore is kept far from the GDL. When the top walls are set hydrophobic and the side walls hydrophilic, water spreads in the side walls reaching lower corners of the channel and thus touching the GDL surface. Analyzing the two-phase flow pressure drop, displayed in **Figure 6.19**, it can be seen that both hybrid cases result into pressure drop profiles that are closer to that obtained when all the channel walls are set hydrophilic, and therefore into lower pressure drop values than those verified when all the walls are set hydrophobic. Having part of the channel walls hydrophilic in the hybrid cases reduces the accumulation of large droplets, verified when all the channel walls are hydrophobic, thus leading to a lower flow resistance. As for the volume-weighted water content, depicted in **Figure 6.20**, it can be seen that the hybrid case with hydrophilic top walls presents the lowest water content at the elbows. The hybrid case with hydrophilic top walls exhibits higher elbows water content than that obtained when all the walls are considered hydrophilic, and similar time-averaged values than those obtained when all the walls are set hydrophobic, but with smaller fluctuations.

Considering the results obtained in this section, the case in which the top walls of the serpentine channel are set hydrophobic and the side ones hydrophilic might be a better alternative than having all the walls hydrophilic or hydrophobic. This hybrid configuration creates a desirable two-phase pattern, in which water is kept in the top of the channel and thus the GDL surface water coverage ratio is reduced, without generating an increase in pressure drop.

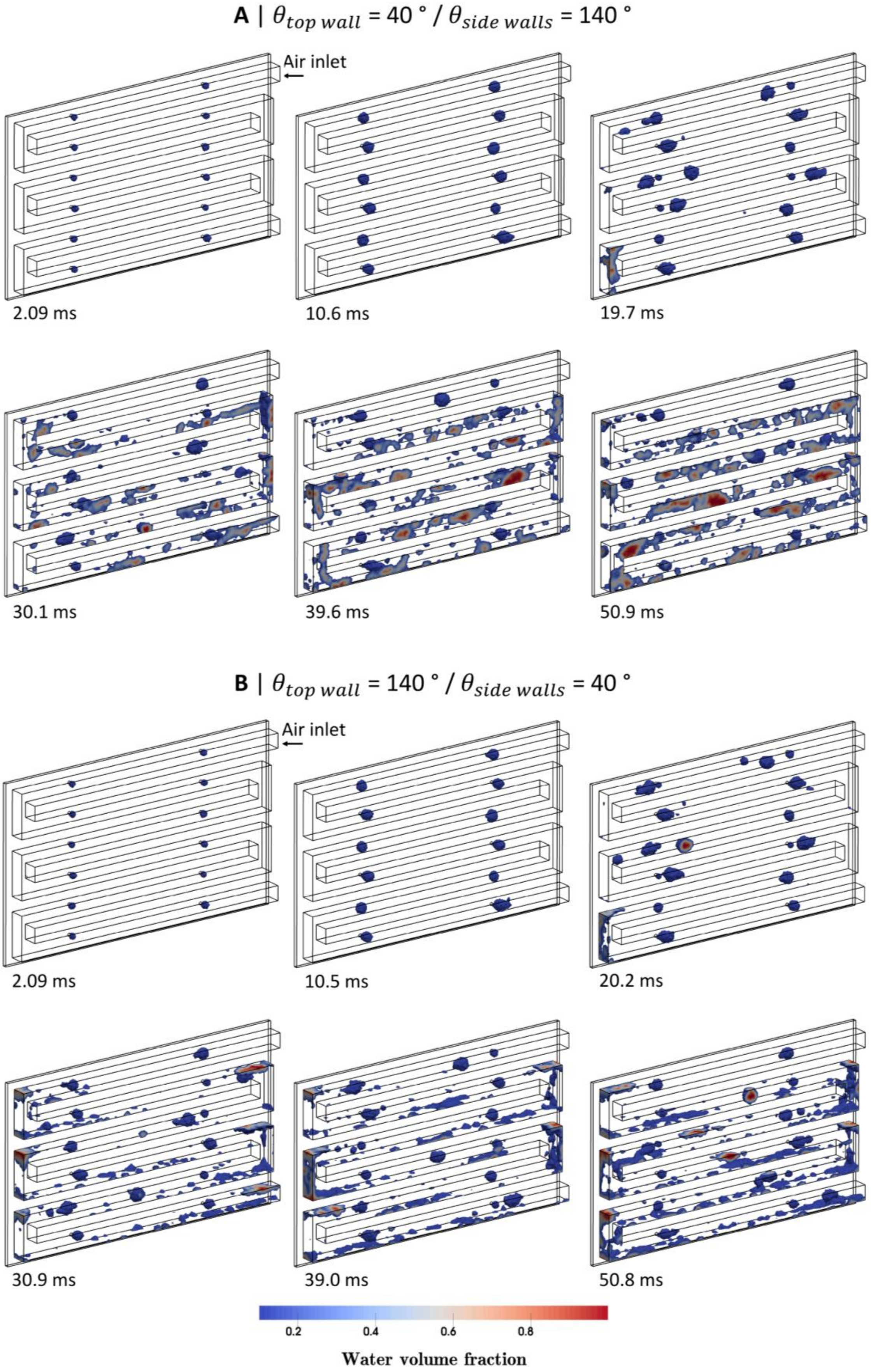

Figure 6.17. Water dynamics in a serpentine channel considering different contact angle (θ) in the top and side walls.

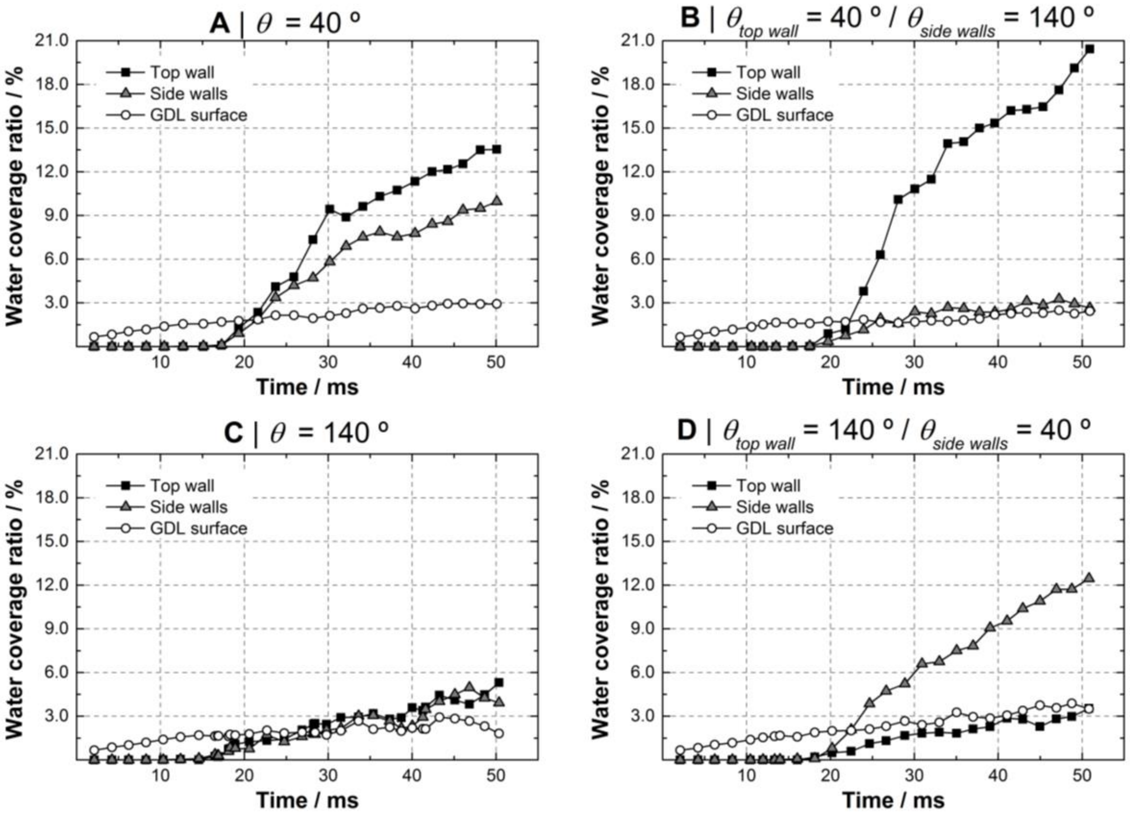

Figure 6.18. Water coverage ratio in the top and side walls of the serpentine channel and at the GDL surface considering different contact angle in the top and side walls.

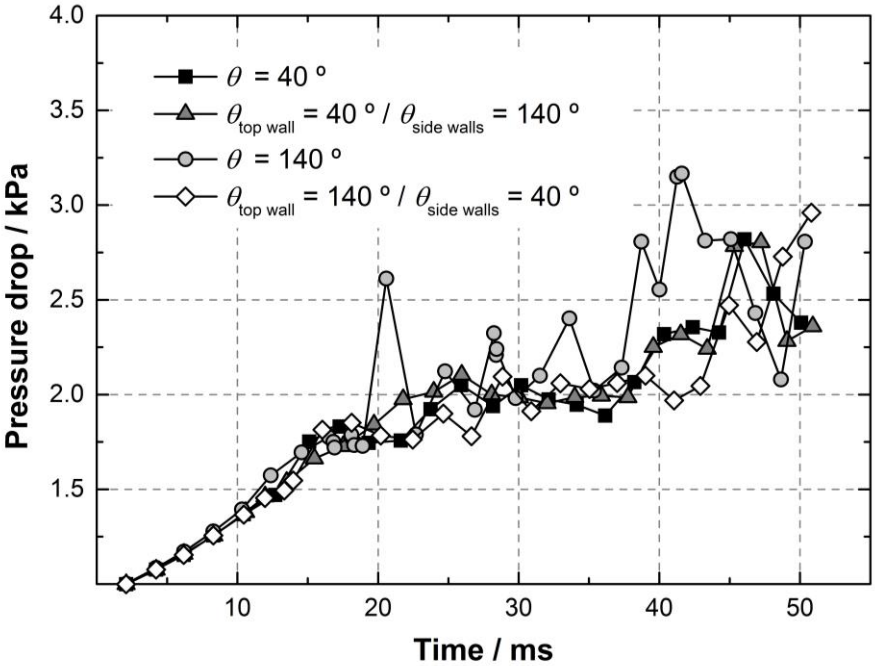

Figure 6.19. Two-phase flow pressure drop in the serpentine channel considering different contact angle (θ) in the top and side walls.

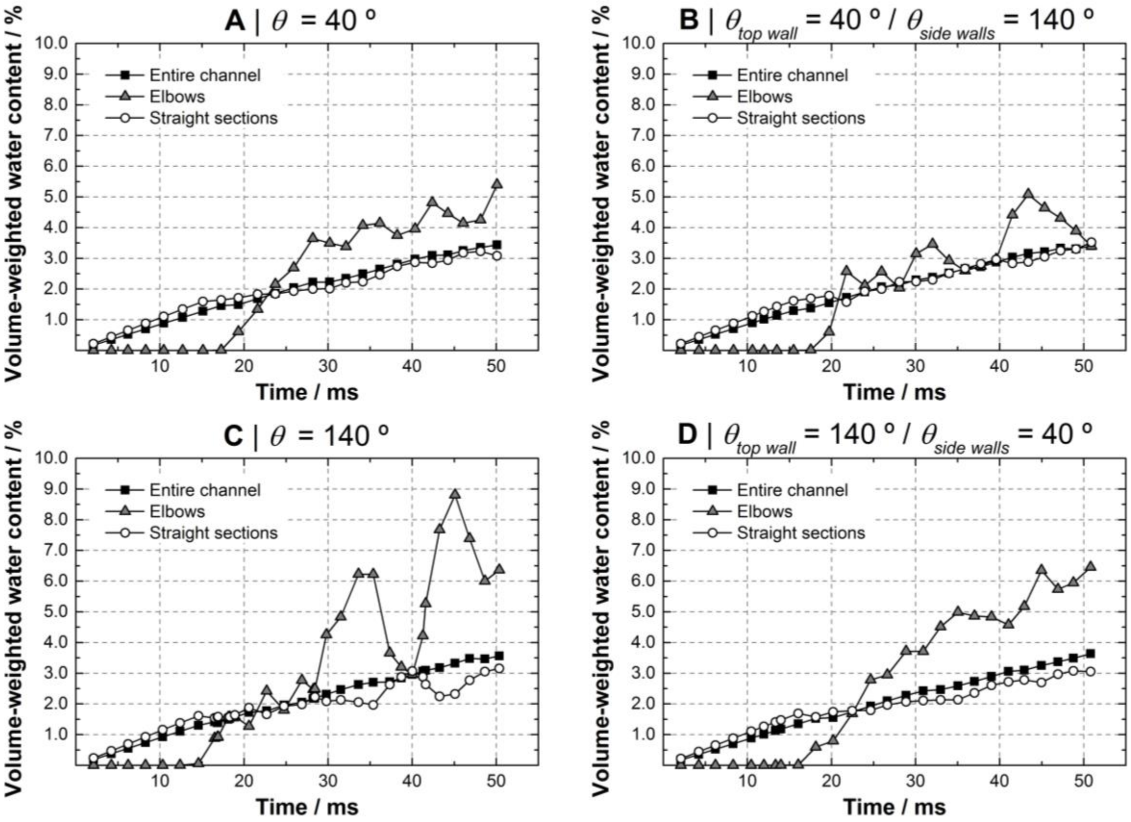

Figure 6.20. Volume-weighted water content in the serpentine channel, at its elbows and in its straight sections considering different contact angle (θ) in the top and side walls.

6.2. Single *vs* multi-serpentine flow field design

Figure 6.21 displays liquid water distribution with respect to time in single and multi-serpentine channels with hydrophilic (**Figure 6.21** A and B) and hydrophobic walls (**Figure 6.21** C and D), at an operating voltage of 0.60 V and air stoichiometry of 10. It can be seen that the effect of the walls wettability is the same for both flow field designs. When the walls are hydrophilic, water spreads in the channel surfaces leading to the formation of long water films, whereas when the walls are set hydrophobic water is transported in the form of droplets. The reasons for the formation of such flow patterns were already discussed in Section **6.1.1**. Comparing the results from both flow field designs, it can be seen that water droplets emerging from the GDL surface are considerably larger when employing the multi-serpentine channel. Because this configuration divides the flow into two segments, each one has lower air velocity and thus reduced shear force. That is also the reason why in the multi-serpentine channel with hydrophilic walls there are more and wider water films, and in the multi-serpentine channel with hydrophobic walls there are less and larger droplets. This can be confirmed analyzing **Figure 6.22**. When the walls are set hydrophilic (**Figure 6.22** A and C), the top and side walls water coverage ratio is higher in multi-serpentine channel. When the walls are set hydrophobic (**Figure 6.22** B and D), the top and side walls water coverage ratio decreases when the multi-serpentine channel is employed. The two-phase flow pressure drop for both flow field designs tested is shown in **Figure 6.23**. As expected, it can be seen that the pressure drop is considerably higher when employing the single-serpentine design, due to the higher air velocity in the channel. As for the influence of the walls wettability, it affects the pressure drop in the same way for both designs, *i.e.*, higher values are reached when the walls are hydrophobic. Why this occurs was already explained in Section **6.1.1**. Regarding the volume-weighted water content, it can be seen that, contrarily to that observed in the single-serpentine channel, the water content at the elbows of the multi-serpentine channel is not consistently higher than that of the straight sections.

Single-serpentine channel is the most frequently used flow field for small active areas [4]. However, when it comes to fuel cells with large active areas, the excessive pressure drops associated with this configuration is often impeditive, as it generates significant parasitic energy losses. In such situations, the multi-serpentine flow field design is often more adequate, as it produces comparable electrical output to that obtained with a single-serpentine (**Appendix D)** with a much lower pressure drop (**Figure 6.23**).

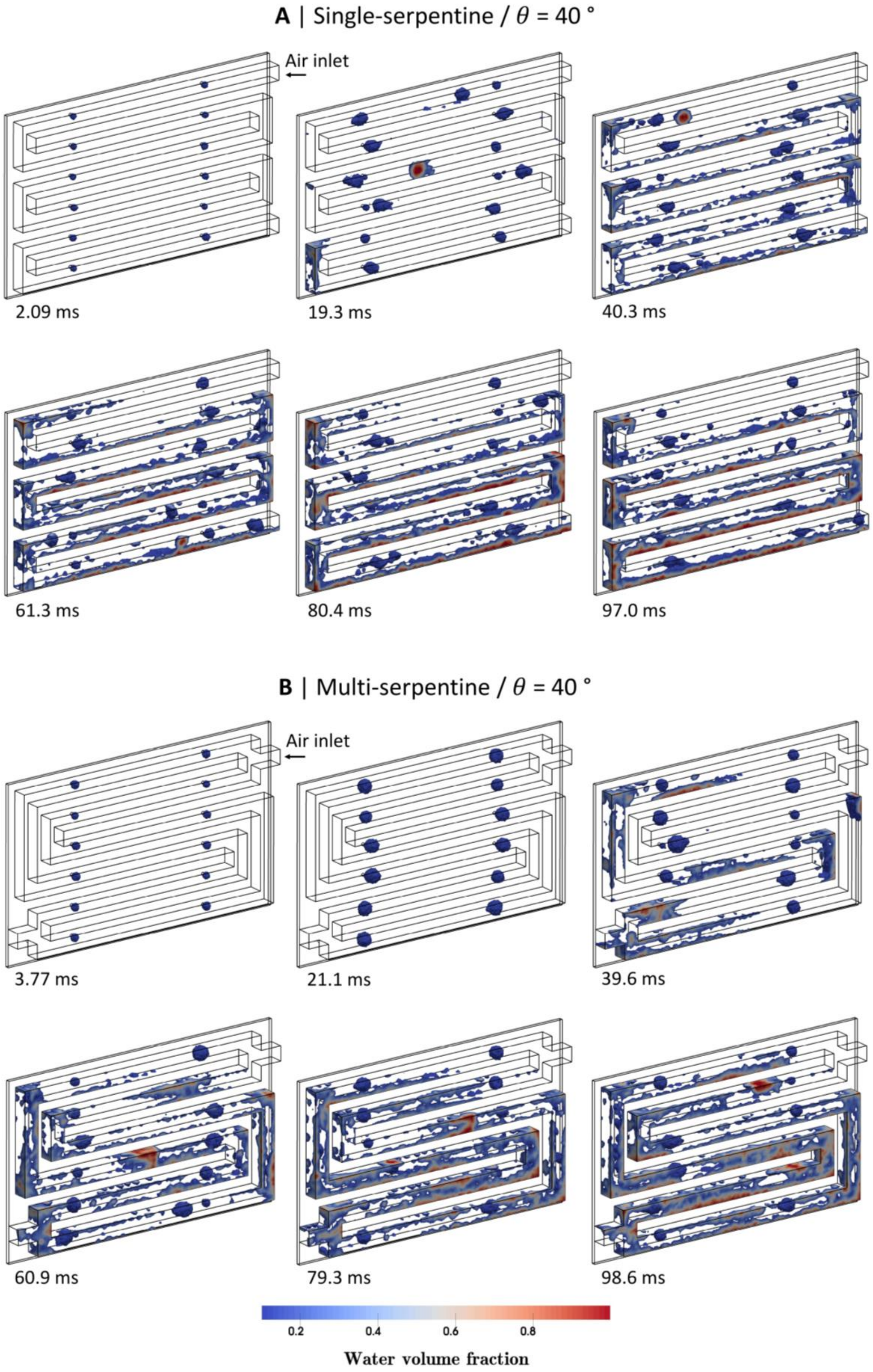

Figure 6.21. Water dynamics in single and multi-serpentine channels with different walls contact angle (θ).

C | Single-serpentine / θ = 140 °

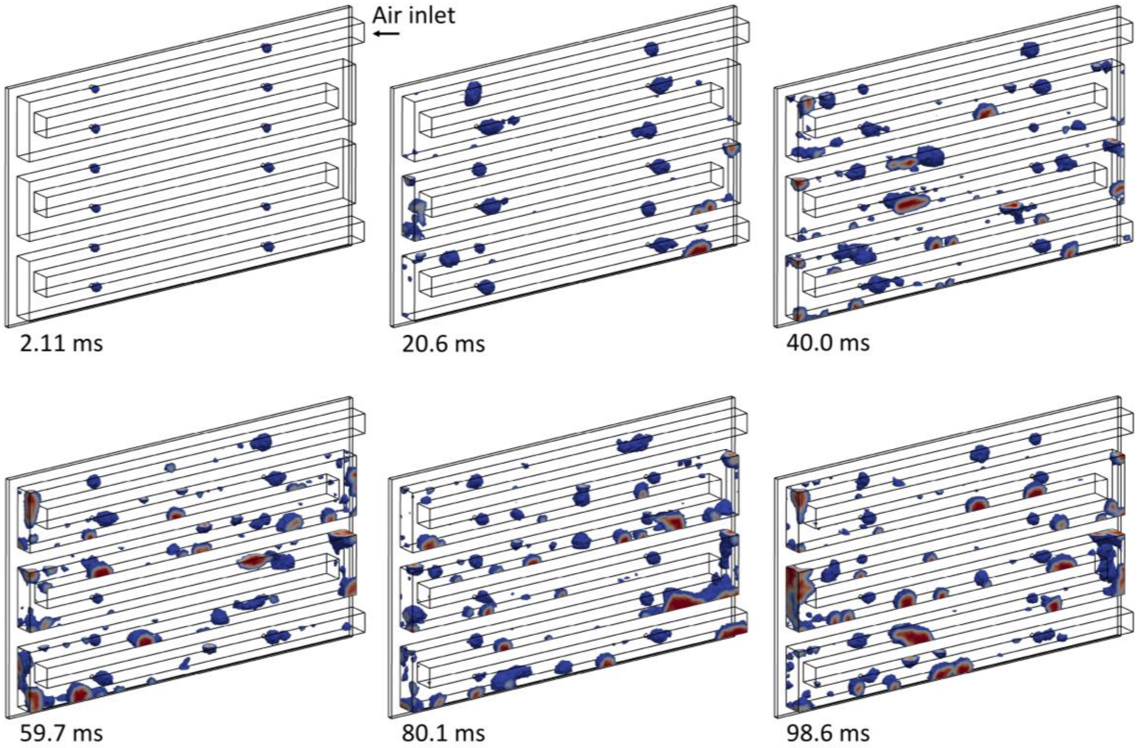

D | Multi-serpentine / θ = 140 °

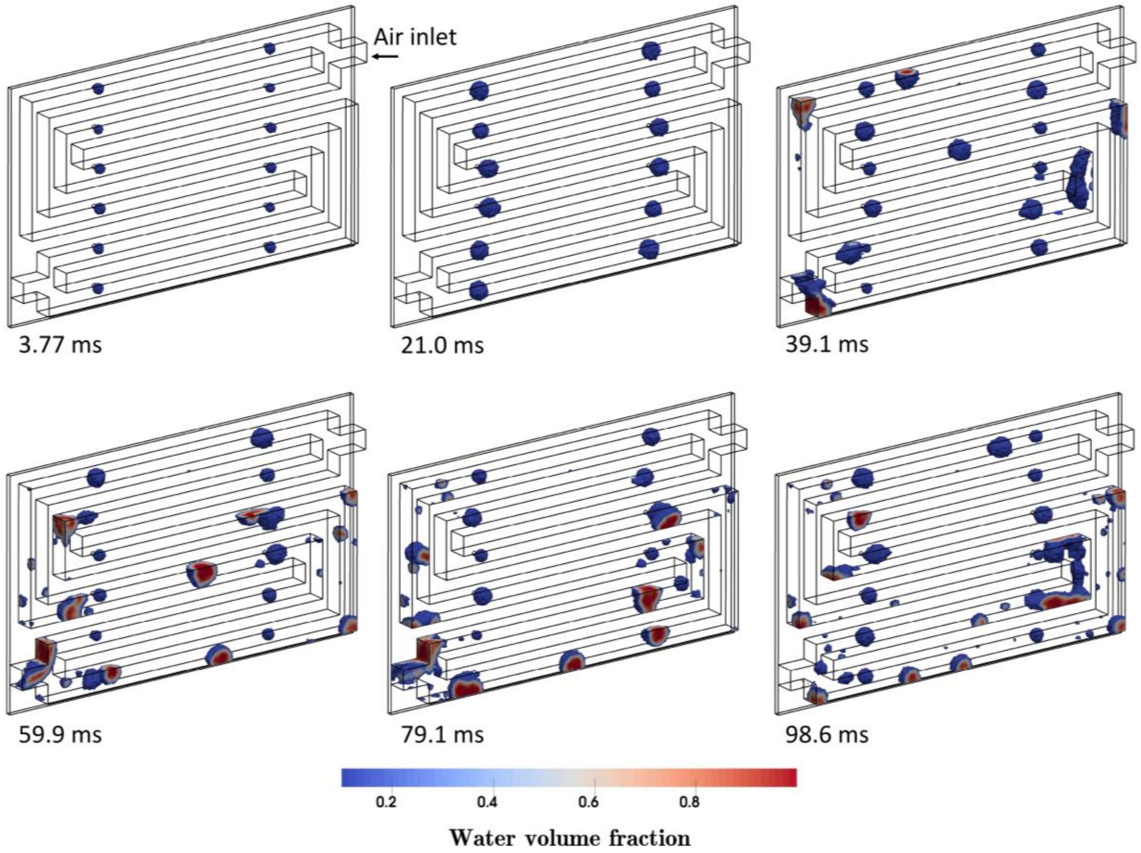

Figure 6.21. (Continued)

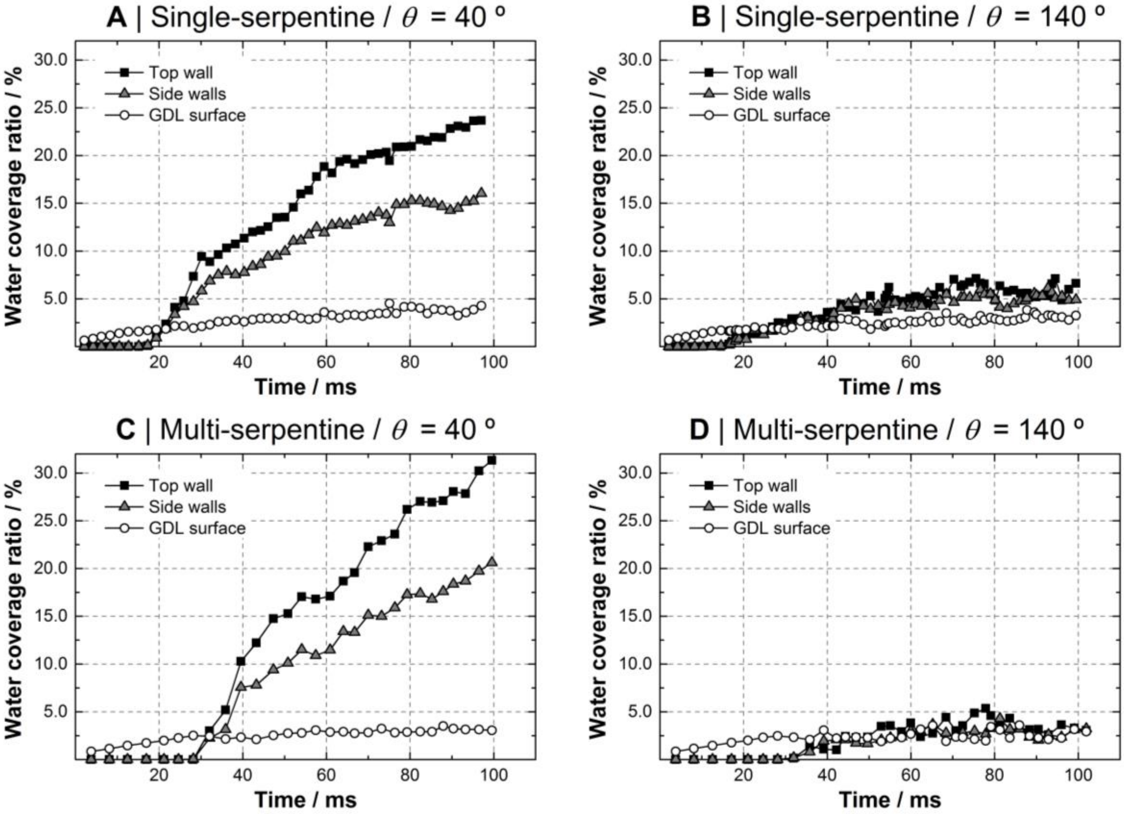

Figure 6.22. Water coverage ratio in the top and side walls of single and multi-serpentine channels with different walls contact angle (θ) and in the GDL surface.

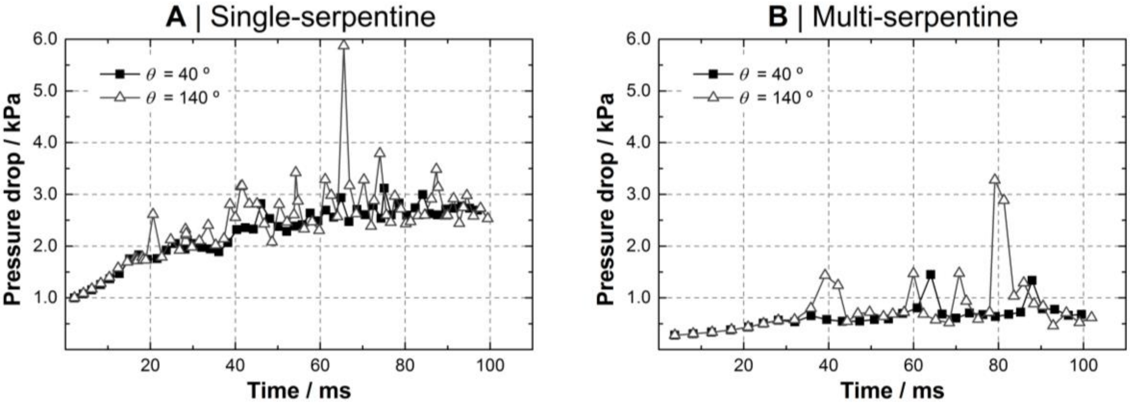

Figure 6.23. Two-phase flow pressure drop in single and multi-serpentine channels with different walls contact angle (θ).

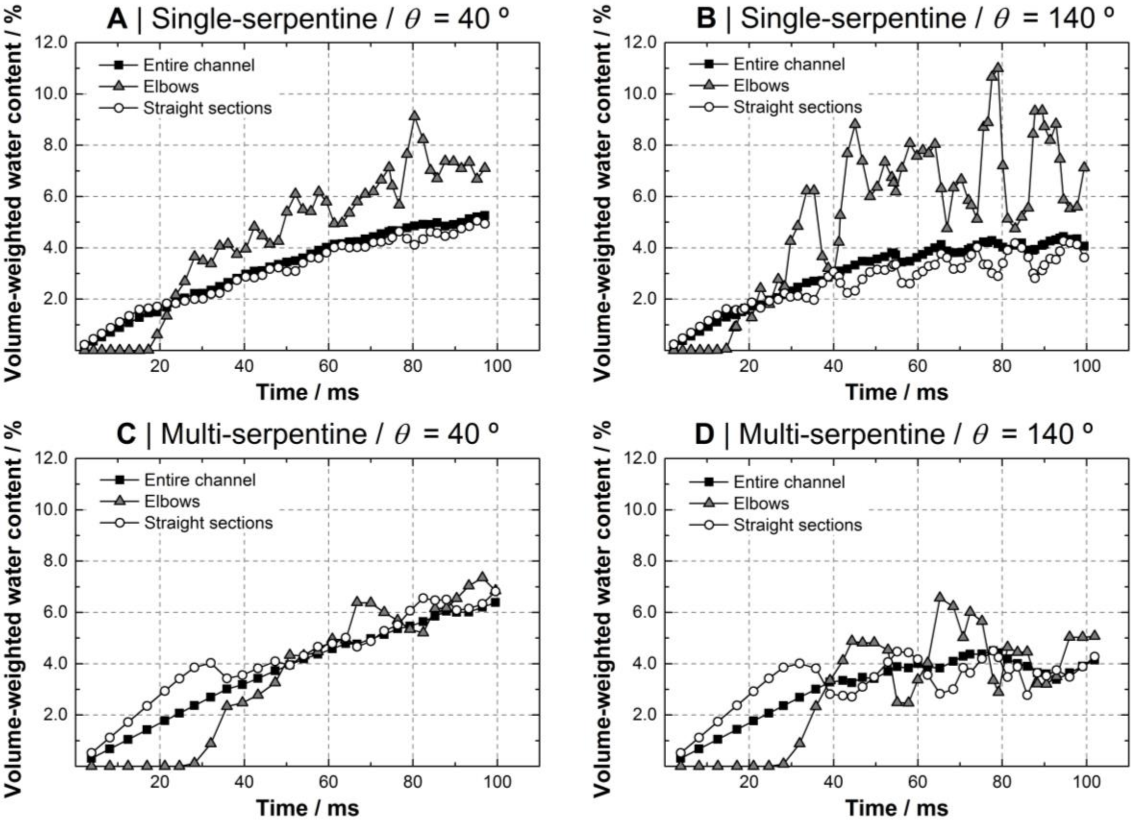

Figure 6.24. Volume-weighted water content in the entire single or multi-serpentine channel, in their straight sections and at their elbows, for different channel walls contact angle (θ).

6.3. Summary

Results of numerical simulations conducted with the model developed in this work were presented throughout this chapter. The effects of walls wettability on the two-phase flow in a single-serpentine channel were analyzed under different air stoichiometries and operating voltages. The two-phase flow in a multi-serpentine channel was also analyzed.

Setting the channel walls hydrophilic led water to spread in the walls, forming films attached to the channel upper corners. Water moved along the channel in the form of droplets when the walls were set hydrophobic. Higher two-phase flow pressure drops were obtained when considering the channel walls hydrophobic. Increasing the air stoichiometry decreased the effects of the channel walls wettability and led to an increase in pressure drop. The walls wettability affected the two-phase flow in the same way for two different operating voltages. Nevertheless, increasing the voltage decreased the amount of water in the channel and reduced the pressure drop.

Different values for the walls wettability was applied at the elbows of the serpentine channel. Although the water distribution at the elbows was affected by changing their wettability, it did not result in more favorable two-phase flow patterns. On the contrary, setting the top walls of the channel hydrophilic while keeping the side ones hydrophobic appeared to be more beneficial than having all the walls hydrophobic or hydrophilic, as it leads to lower GDL water coverage ratio without affecting the pressure drop.

Similar water distributions were found in single and multi-serpentine channels, in terms of the effects of the walls wettability. Nevertheless, wider water films (for the hydrophilic walls case) and larger water droplets (for the hydrophobic walls case) were found in the multi-serpentine channel, due to the lower air velocity in each segment of the channel. Accordingly, the pressure drop in the multi-serpentine channel was considerably lower than that obtained in the single-serpentine.

7. CONCLUSIONS AND FUTURE WORK

7.1. Conclusions

In this work, a 1D + 3D numerical model of a PEM fuel cell was developed. The VOF method was considered to track the air-water two-phase flow in the cathode GCs, along with electrochemical reactions and membrane water transport. The multi-fluid saturation model was also implemented to obtain the water distribution in the GDL and to compute its effects on the cell performance.

The model was validated in terms of its ability to predict the cell electrochemical performance and the two-phase flow in the cathode GCs. Calculated polarization curves were compared with experimental ones and a good agreement was observed. Two-phase flow model predictions were compared with the water distribution inside a transparent fuel cell and similar flow patterns could be found, namely the water accumulation at the elbows of a serpentine channel and the formation of long water films.

The water dynamics in a serpentine channel for different voltages was numerically analyzed. At a lower voltage, droplets grew larger and suffered more deformation, and more water was accumulated in the channel. In accordance, the two-phase flow pressure drop increased when the voltage decreased. Current density and liquid water generation spatial distributions were displayed and their relation with the water velocity in each pore designed at the GDL surface was shown. For a higher voltage, the water velocity in the pores increased along the channel length, whereas at lower voltages it tended to decrease. The water content in different locations of the serpentine was quantified. It was confirmed that more water accumulates at the elbows, and water content along the channel length (from inlet to outlet) was found to follow the same trend as the water velocity in the pores. Furthermore, top and side walls (hydrophilic) water coverage ratio was found to be considerably higher than that obtained on the hydrophobic GDL surface.

The test station and fuel cells developed to obtain the results for model validation were also used to conduct an experimental study on the MEA design, investigating the effects of the MPL, membrane thickness and GDL hydrophobic treatment. The results showed that the MPL improves the cell performance at low to medium current densities, due to a better hydration of the membrane. However, it reduced the cell output at high currents, probably due to liquid water flooding in the anode. Applying a thinner membrane significantly improved the cell performance due to lower ohmic losses. The GDL hydrophobic treatment also resulted into higher performances. Treated GDLs not only facilitated water removal, but also appear to have contributed to a better overall humidification of the cell.

Further numerical simulations were conducted to investigate the effect of the walls wettability in the two-phase flow in a single-serpentine channel, under different air stoichiometries and voltages. Water spread into the walls when they were hydrophilic, forming long films that accumulated in the upper corners of the channel. When hydrophobic walls were employed, water moved along the channel mostly in the form of droplets. The two-phase flow pressure drop was higher when the channel walls were hydrophobic. Increasing the air stoichiometry decreased the influence of the walls wettability. In fact, when the air stoichiometry was too high, the walls wettability no longer affected the two-phase flow patterns. Decreasing the operating voltage increased the amount of water in the channel, but the effect of the walls wettability remained the same. Changing the wettability of the elbows of the serpentine channel did not result into more beneficial two-phase flow patterns. However, results of setting the top walls hydrophilic while keeping the side walls hydrophobic suggested that it might be a better alternative than setting all the walls hydrophilic or hydrophobic. This configuration kept water way from the GDL surface decreasing its water coverage ratio, without affecting the pressure drop. The two-phase flow patterns in a multi-serpentine channel was also studied. Because the air velocity in each channel was lower, water droplets grew larger before detaching from the GDL surface, in comparison to what occurred in the single-serpentine configuration. Nevertheless, similar flow patterns were observed for both designs at different values of the walls wettability. However, the two-phase flow pressure drop was much lower in the multi-serpentine flow field.

7.2. Future work

In the model developed in this work, some important aspects on PEM fuel cells numerical simulation using the VOF method were addressed. However, like all mathematical models, it has limitations. Although the model considers the water transport in the membrane, it does not capture the significant decrease of the cell experimental performance when the RH of air is decreased, as can be seen in Chapter **4** (Section **4.1**) when comparing the results obtained at air RHs of 50 % and 90 %. The model does predict an increase in the ohmic losses when the air RH is decreased, but such increase is very small to affect the cell performance. The reason for such outcome is probably related with the fact that heat transfer is not considered in the present model. Temperature at the cathode CL is considerably higher than that in the other cell components, because it is where the exothermic ORR takes place. This would lead to water losses by evaporation that are not accounted for in the present model. Such water losses would be higher for lower air RHs because air can uptake more water vapor. Therefore, the inclusion of heat transfer effects is here recommended. The implementation of the cathode GDL/GCs interface could also be improved. Although the procedure here applied (see Section **5.1.4.1**) allows to simulate the hydrophobic nature of the GDL surface in a simple way, it imposes some limitations. For example, different levels for the GDL hydrophobicity cannot be tested and this layer cannot be set hydrophilic. Scheme programming in ANSYS Fluent might provide a way to set a phase-dependent boundary condition for the GDL/GCs interface that would eliminate this issue. For the gas-phase (air) an interior boundary condition should be used, and a wall boundary condition should be considered for the liquid-phase (water).

Further numerical and experimental investigations on the potential benefits of local variations of the gas channel walls wettability are also advised. However, at the same time, the feasibility of the coating processes used to change the walls wettability should be carefully evaluated, especially concerning the coating durability in the PEM fuel cell environment and its impact on the bipolar plates cost.

REFERENCES

[1] International Energy Agency. Key World Energy Statistics 2016.

[2] IPCC 2014. Climate Change 2014: Synthesis Report. Contribution of Working Groups I, II and III to the Fifth Assessment Report of the Intergovernmental Panel on Climate Change [Core Writing Team, R.K. Pachauri and L.A. Meyer (eds.)]. IPCC, Geneva, Switzerland, 151 pp.

[3] W. R. Grove. XXIV. On voltaic series and the combination of gases by platinum. Philosophical Magazine Series 3. 1839;14:127-30.

[4] F. Barbir. PEM Fuel Cells: Theory and Practice. second ed: Academic Press; 2013.

[5] C. Spiegel. PEM fuel cell modeling and simulation using MATLAB: Academic Press; 2008.

[6] J. Andrews, B. Shabani. The role of hydrogen in a global sustainable energy strategy. Wiley Interdisciplinary Reviews: Energy and Environment. 2014;3:474-89.

[7] T. Morgan. The hydrogen economy - A non-technical review. 2006.

[8] S. Mekhilef, R. Saidur, A. Safari. Comparative study of different fuel cell technologies. Renew Sust Energ Rev. 2012;16:981-9.

[9] DuPont. DuPont™ Nafion® PFSA Membranes - NR 211 and NR 212. 2009.

[10] K. S. Ngai, S. Ramesh, K. Ramesh, J. C. Juan. A review of polymer electrolytes: fundamental, approaches and applications. Ionics. 2016;22:1-21.

[11] C. M. Branco, S. Sharma, M. M. de Camargo Forte, R. Steinberger-Wilckens. New approaches towards novel composite and multilayer membranes for intermediate temperature-polymer electrolyte fuel cells and direct methanol fuel cells. J Power Sources. 2016;316:139-59.

[12] R. Wycisk, P. N. Pintauro, J. W. Park. New developments in proton conducting membranes for fuel cells. Curr Opin Chem Eng. 2014;4:71-8.

[13] S. J. Peighambardoust, S. Rowshanzamir, M. Amjadi. Review of the proton exchange membranes for fuel cell applications. Int J Hydrogen Energy. 2010;35:9349-84.

[14] G. Lin, T. Van Nguyen. Effect of thickness and hydrophobic polymer content of the gas diffusion layer on electrode flooding level in a PEMFC. J Electrochem Soc. 2005;152:A1942-A8.

[15] S. Park, J. Lee, B. N. Popov. Effect of PTFE content in microporous layer on water management in PEM fuel cells. J Power Sources. 2008;177:457-63.

[16] S. Park, B. N. Popov. Effect of cathode GDL characteristics on mass transport in PEM fuel cells. Fuel. 2009;88:2068-73.

[17] S. Shimpalee, U. Beuscher, J. W. Van Zee. Analysis of GDL flooding effects on PEMFC performance. Electrochim Acta. 2007;52:6748-54.

[18] C. Lim, C. Y. Wang. Effects of hydrophobic polymer content in GDL on power performance of a PEM fuel cell. Electrochim Acta. 2004;49:4149-56.

[19] L. Cindrella, A. Kannan, J. Lin, K. Saminathan, Y. Ho, C. Lin, et al. Gas diffusion layer for proton exchange membrane fuel cells—A review. J Power Sources. 2009;194:146-60.

[20] A. Jayakumar, S. Sethu, M. Ramos, J. Robertson, A. Al-Jumaily. A technical review on gas diffusion, mechanism and medium of PEM fuel cell. Ionics. 2014;21:1-18.

[21] J. Park, H. Oh, T. Ha, Y. I. Lee, K. Min. A review of the gas diffusion layer in proton exchange membrane fuel cells: Durability and degradation. Appl Energy. 2015;155:866-80.

[22] S. Park, J. Lee, B. N. Popov. A review of gas diffusion layer in PEM fuel cells: Materials and designs. Int J Hydrogen Energy. 2012;37:5850-65.

[23] D. Spernjak, A. K. Prasad, S. G. Advani. Experimental investigation of liquid water formation and transport in a transparent single-serpentine PEM fuel cell. J Power Sources. 2007;170:334-44.

[24] S. G. Kandlikar, E. J. See, M. Koz, P. Gopalan, R. Banerjee. Two-phase flow in GDL and reactant channels of a proton exchange membrane fuel cell. Int J Hydrogen Energy. 2014;39:6620-36.

[25] Y. Tabe, Y. Aoyama, K. Kadowaki, K. Suzuki, T. Chikahisa. Impact of micro-porous layer on liquid water distribution at the catalyst layer interface and cell performance in a polymer electrolyte membrane fuel cell. J Power Sources. 2015;287:422-30.

[26] A. Z. Weber, J. Newman. Effects of Microporous Layers in Polymer Electrolyte Fuel Cells. J Electrochem Soc. 2005;152:A677-A88.

[27] Z. Lu, M. M. Daino, C. Rath, S. G. Kandlikar. Water management studies in PEM fuel cells, part III: Dynamic breakthrough and intermittent drainage characteristics from GDLs with and without MPLs. Int J Hydrogen Energy. 2010;35:4222-33.

[28] A. Jayakumar, S. P. Sethu, M. Ramos, J. Robertson, A. Al-Jumaily. A technical review on gas diffusion, mechanism and medium of PEM fuel cell. Ionics. 2015;21:1-18.

[29] H. Kahraman, M. F. Orhan. Flow field bipolar plates in a proton exchange membrane fuel cell: Analysis & modeling. Energ Convers Manage. 2017;133:363-84.

[30] A. P. Manso, F. F. Marzo, J. Barranco, X. Garikano, M. Garmendia Mujika. Influence of geometric parameters of the flow fields on the performance of a PEM fuel cell. A review. Int J Hydrogen Energy. 2012;37:15256-87.

[31] W. J. Wruck, R. M. Machado, T. W. Chapman. Current Interruption—Instrumentation and Applications. J Electrochem Soc. 1987;134:539-46.

[32] F. N. Büchi, A. Marek, G. G. Scherer. In Situ Membrane Resistance Measurements in Polymer Electrolyte Fuel Cells by Fast Auxiliary Current Pulses. J Electrochem Soc. 1995;142:1895-901.

[33] K. R. Cooper, M. Smith. Electrical test methods for on-line fuel cell ohmic resistance measurement. J Power Sources. 2006;160:1088-95.

[34] E. A. Ticianelli, C. R. Derouin, S. Srinivasan. Localization of platinum in low catalyst loading electrodes to to attain high power densities in SPE fuel cells. J Electroanal Chem Interfacial Electrochem. 1988;251:275-95.

[35] X. Wang, I. M. Hsing, P. L. Yue. Electrochemical characterization of binary carbon supported electrode in polymer electrolyte fuel cells. J Power Sources. 2001;96:282-7.

[36] U. Koponen, H. Kumpulainen, M. Bergelin, J. Keskinen, T. Peltonen, M. Valkiainen, et al. Characterization of Pt-based catalyst materials by voltammetric techniques. J Power Sources. 2003;118:325-33.

[37] J. Yu, T. Matsuura, Y. Yoshikawa, M. N. Islam, M. Hori In Situ Analysis of Performance Degradation of a PEMFC under Nonsaturated Humidification. Electrochem Solid-State Lett. 2005;8:A156-A8.

[38] S. S. Kocha, J. Deliang Yang, J. S. Yi. Characterization of gas crossover and its implications in PEM fuel cells. AIChE J. 2006;52:1916-25.

[39] X. Yuan, H. Wang, J. Colin Sun, J. Zhang. AC impedance technique in PEM fuel cell diagnosis—A review. Int J Hydrogen Energy. 2007;32:4365-80.

[40] J. Wu, X. Z. Yuan, H. Wang, M. Blanco, J. J. Martin, J. Zhang. Diagnostic tools in PEM fuel cell research: Part I Electrochemical techniques. Int J Hydrogen Energy. 2008;33:1735-46.

[41] S. M. Rezaei Niya, M. Hoorfar. Study of proton exchange membrane fuel cells using electrochemical impedance spectroscopy technique–A review. J Power Sources. 2013;240:281-93.

[42] X. Yuan, C. Song, H. Wang, J. Zhang. Electrochemical impedance spectroscopy in PEM fuel cells: fundamentals and applications: Springer Science & Business Media; 2009.

[43] K. Cooper, M. Smith. Electrical test methods for on-line fuel cell ohmic resistance measurement. J Power Sources. 2006;160:1088-95.

[44] J. Wu, X. Zi Yuan, H. Wang, M. Blanco, J. J. Martin, J. Zhang. Diagnostic tools in PEM fuel cell research: Part II: Physical/chemical methods. Int J Hydrogen Energy. 2008;33:1747-57.

[45] B. H. Lim, E. H. Majlan, W. R. W. Daud, T. Husaini, M. I. Rosli. Effects of flow field design on water management and reactant distribution in PEMFC: a review. Ionics. 2016;22:301-16.

[46] P. Pei, Y. Li, H. Xu, Z. Wu. A review on water fault diagnosis of PEMFC associated with the pressure drop. Appl Energy. 2016;173:366-85.

[47] J. Kätzel, H. Markötter, T. Arlt, M. Klages, J. Haußmann, M. Messerschmidt, et al. Effect of ageing of gas diffusion layers on the water distribution in flow field channels of polymer electrolyte membrane fuel cells. J Power Sources. 2016;301:386-91.

[48] A. Iranzo, P. Boillat, J. Biesdorf, A. Salva. Investigation of the liquid water distributions in a 50 cm2 PEM fuel cell: Effects of reactants relative humidity, current density, and cathode stoichiometry. Energy. 2015;82:914–21.

[49] T. Kim, C. Sim, M. Kim. Research on water discharge characteristics of PEM fuel cells by using neutron imaging technology at the NRF, HANARO. Appl Radiat Isot. 2008;66:593-605.

[50] N. Pekula, K. Heller, P. A. Chuang, A. Turhan, M. M. Mench, J. S. Brenizer, et al. Study of water distribution and transport in a polymer electrolyte fuel cell using neutron imaging. Nucl Instrum Meth A. 2005;542:134-41.

[51] R. Satija, D. L. Jacobson, M. Arif, S. Werner. In situ neutron imaging technique for evaluation of water management systems in operating PEM fuel cells. J Power Sources. 2004;129:238-45.

[52] Z. Dunbar, R. I. Masel. Quantitative MRI study of water distribution during operation of a PEM fuel cell using Teflon® flow fields. J Power Sources. 2007;171:678-87.

[53] K. W. Feindel, L. P. A. LaRocque, D. Starke, S. H. Bergens, R. E. Wasylishen. In Situ Observations of Water Production and Distribution in an Operating H2/O2

PEM Fuel Cell Assembly Using 1H NMR Microscopy. J Am Chem Soc. 2004;126:11436-7.

[54] P. Antonacci, S. Chevalier, J. Lee, R. Yip, N. Ge, A. Bazylak. Feasibility of combining electrochemical impedance spectroscopy and synchrotron X-ray radiography for determining the influence of liquid water on polymer electrolyte membrane fuel cell performance. Int J Hydrogen Energy. 2015;40:16494–502.

[55] T. Mukaide, S. Mogi, J. Yamamoto, A. Morita, S. Koji, K. Takada, et al. In situ observation of water distribution and behaviour in a polymer electrolyte fuel cell by synchrotron X-ray imaging. J Synchrotron Radiat. 2008;15:329-34.

[56] I. Manke, C. Hartnig, M. Grünerbel, W. Lehnert, N. Kardjilov, A. Haibel, et al. Investigation of water evolution and transport in fuel cells with high resolution synchrotron x-ray radiography. Appl Phys Lett. 2007;90:174105-1-3.

[57] A. Bozorgnezhad, M. Shams, H. Kanani, M. Hasheminasab, G. Ahmadi. The experimental study of water management in the cathode channel of single-serpentine transparent proton exchange membrane fuel cell by direct visualization. Int J Hydrogen Energy. 2015;40:2808–32.

[58] D. Lee, J. Bae. Visualization of flooding in a single cell and stacks by using a newly-designed transparent PEMFC. Int J Hydrogen Energy. 2012;37:422-35.

[59] J. M. Sergi, S. G. Kandlikar. Quantification and characterization of water coverage in PEMFC gas channels using simultaneous anode and cathode visualization and image processing. Int J Hydrogen Energy. 2011;36:12381-92.

[60] I. S. Hussaini, C. Y. Wang. Visualization and quantification of cathode channel flooding in PEM fuel cells. J Power Sources. 2009;187:444-51.

[61] S. Ge, C. Y. Wang. Liquid water formation and transport in the PEFC anode. J Electrochem Soc. 2007;154:B998-B1005.

[62] K. Tüber, D. Pócza, C. Hebling. Visualization of water buildup in the cathode of a transparent PEM fuel cell. J Power Sources. 2003;124:403-14.

[63] S. Sailler, S. Rosini, M. A. Chaib, J. Y. Voyant, Y. Bultel, F. Druart, et al. Electrical and thermal investigation of a self-breathing fuel cell. J Appl Electrochem. 2007;37:161-71.

[64] A. Hakenjos, H. Muenter, U. Wittstadt, C. Hebling. A PEM fuel cell for combined measurement of current and temperature distribution, and flow field flooding. J Power Sources. 2004;131:213-6.

[65] H. Kim, K. Min. An experimental investigation of temperature distribution and flooding phenomena of cathode flow fields in a proton exchange membrane (PEM) fuel cell. J Mech Sci Technol. 2014;28:3837-43.

[66] K. Jiao, I. E. Alaefour, G. Karimi, X. Li. Simultaneous measurement of current and temperature distributions in a proton exchange membrane fuel cell during cold start processes. Electrochim Acta. 2011;56:2967-82.

[67] M. Wilkinson, M. Blanco, E. Gu, J. J. Martin, D. P. Wilkinson, J. J. Zhang, et al. In Situ Experimental Technique for Measurement of Temperature and Current Distribution in Proton Exchange Membrane Fuel Cells. Electrochem Solid-State Lett. 2006;9:A507-A11.

[68] L. C. Pérez, L. Brandão, J. M. Sousa, A. Mendes. Segmented polymer electrolyte membrane fuel cells—A review. Renew Sust Energ Rev. 2011;15:169-85.

[69] J. Stumper, S. A. Campbell, D. P. Wilkinson, M. C. Johnson, M. Davis. In-situ methods for the determination of current distributions in PEM fuel cells. Electrochim Acta. 1998;43:3773-83.

[70] myFC. myFC PowerTrekk 2.0. Available at: http://www.myfcpower.com/pages/powertrekk-about-the-charger (Accessed 19 May 2017).

[71] Horizon. MiniPak – hand held fuel cell charger (USB). Available at: http://www.horizonfuelcellshop.com/europe/product/minipak/ (Accessed 19 May 2017).

[72] Kiyoshi Ota / Bloomberg. Toho Gas units for an "ene-farm" household fuel cell system sit outside a smart home developed by Toyota in Toyota City, Japan, on Oct. 17, 2014. Available at: https://www.bloomberg.com/news/articles/2015-01-15/fuel-cells-for-homes-japanese-companies-pitch-clean-energy (Accessed 19 May 2017).

[73] HyLIFT-EUROPE: Powering The Future. Industry Europe. 2016;26:5.

[74] Toyota. Toyota Mirai – Novo Automóvel a Hidrogénio. 2016. Available at: https://www.toyota.pt/world-of-toyota/articles-news-events/2014/o-toyota-mirai.json (Accessed 19 May 2017).

[75] Michael Wittwer / Alstom. Alstom unveils its zero-emission train Coradia iLint at InnoTrans. 2016. Available at: http://www.alstom.com/press-centre/2016/9/alstom-unveils-its-zero-emission-train-coradia-ilint-at-innotrans/ (Accessed 19 May 2017).

[76] H. Li, Y. Tang, Z. Wang, Z. Shi, S. Wu, D. Song, et al. A review of water flooding issues in the proton exchange membrane fuel cell. J Power Sources. 2008;178:103-17.

[77] W. Dai, H. Wang, X. Yuan, J. J. Martin, D. Yang, J. Qiao, et al. A review on water balance in the membrane electrode assembly of proton exchange membrane fuel cells. Int J Hydrogen Energy. 2009;34:9461-78.

[78] M. Ji, Z. Wei. A review of water management in polymer electrolyte membrane fuel cells. Energies. 2009;2:1057-106.

[79] S. G. Kandlikar, M. L. Garofalo, Z. Lu. Water management in a PEMFC: Water transport mechanism and material degradation in gas diffusion layers. Fuel Cells. 2011;11:814-23.

[80] T. Ous, C. Arcoumanis. Degradation aspects of water formation and transport in Proton Exchange Membrane Fuel Cell: A review. J Power Sources. 2013;240:558-82.

[81] T. Jahnke, G. Futter, A. Latz, T. Malkow, G. Papakonstantinou, G. Tsotridis, et al. Performance and degradation of Proton Exchange Membrane Fuel Cells: State of the art in modeling from atomistic to system scale. J Power Sources. 2016;304:207-33.

[82] C. Siegel. Review of computational heat and mass transfer modeling in polymer-electrolyte-membrane (PEM) fuel cells. Energy. 2008;33:1331-52.

[83] D. Cheddie, N. Munroe. Review and comparison of approaches to proton exchange membrane fuel cell modeling. J Power Sources. 2005;147:72-84.

[84] A. Bıyıkoğlu. Review of proton exchange membrane fuel cell models. Int J Hydrogen Energy. 2005;30:1181-212.

[85] H. Wu. A review of recent development: Transport and performance modeling of PEM fuel cells. Appl Energy. 2016;165:81-106.

[86] G. Song, H. Meng. Numerical modeling and simulation of PEM fuel cells: Progress and perspective. AcMSn. 2013;29:318-34.

[87] M. Andersson, S. B. Beale, M. Espinoza, Z. Wu, W. Lehnert. A review of cell-scale multiphase flow modeling, including water management, in polymer electrolyte fuel cells. Appl Energy. 2016;180:757-78.

[88] J. Kone, X. Zhang, Y. Yan, G. Hu, G. Ahmadi. Three-dimensional multiphase flow computational fluid dynamics models for proton exchange membrane fuel cell: A

theoretical development. The Journal of Computational Multiphase Flows. 2017;0:1-23.

[89] T. E. Springer, T. Zawodzinski, S. Gottesfeld. Polymer electrolyte fuel cell model. J Electrochem Soc. 1991;138:2334-42.

[90] D. M. Bernardi, M. W. Verbrugge. A Mathematical Model of the Solid-Polymer-Electrolyte Fuel Cell. J Electrochem Soc. 1992;139:2477-91.

[91] D. M. Bernardi, M. W. Verbrugge. Mathematical model of a gas diffusion electrode bonded to a polymer electrolyte. AIChE J. 1991;37:1151-63.

[92] V. Gurau, H. Liu, S. Kakaç. Two-dimensional model for proton exchange membrane fuel cells. AIChE J. 1998;44:2410-22.

[93] S. Um, C. Y. Wang, K. Chen. Computational fluid dynamics modeling of proton exchange membrane fuel cells. J Electrochem Soc. 2000;147:4485-93.

[94] U. Pasaogullari, C. Y. Wang. Two-Phase Modeling and Flooding Prediction of Polymer Electrolyte Fuel Cells. J Electrochem Soc. 2005;152:A380-A90.

[95] S. Mazumder, J. V. Cole. Rigorous 3-D mathematical modeling of PEM fuel cells II. Model predictions with liquid water transport. J Electrochem Soc. 2003;150:A1510-A7.

[96] L. You, H. Liu. A two-phase flow and transport model for the cathode of PEM fuel cells. Int J Heat Mass Tran. 2002;45:2277-87.

[97] Z. Wang, C. Y. Wang, K. Chen. Two-phase flow and transport in the air cathode of proton exchange membrane fuel cells. J Power Sources. 2001;94:40-50.

[98] T. Berning. A three-dimensional, two-fluid model of PEM fuel cell cathodes. ECS Trans. 2008;16:23-34.

[99] G. He, P. Ming, Z. Zhao, A. Abudula, Y. Xiao. A two-fluid model for two-phase flow in PEMFCs. J Power Sources. 2007;163:864-73.

[100] T. Berning, N. Djilali. A 3D, Multiphase, Multicomponent Model of the Cathode and Anode of a PEM Fuel Cell. J Electrochem Soc. 2003;150:A1589-A98.

[101] V. Gurau, T. A. Zawodzinski Jr, J. A. Mann Jr. Two-phase transport in PEM fuel cell cathodes. J Fuel Cell Sci Technol. 2008;5:021009.

[102] Q. Ye, T. Van Nguyen. Three-dimensional simulation of liquid water distribution in a PEMFC with experimentally measured capillary functions. J Electrochem Soc. 2007;154:B1242-B51.

[103] J. H. Nam, M. Kaviany. Effective diffusivity and water-saturation distribution in single-and two-layer PEMFC diffusion medium. Int J Heat Mass Tran. 2003;46:4595-611.

[104] U. Pasaogullari, C. Wang. Liquid water transport in gas diffusion layer of polymer electrolyte fuel cells. J Electrochem Soc. 2004;151:A399-A406.

[105] C. Yin, J. Gao, X. Wen, G. Xie, C. Yang, H. Fang, et al. In situ investigation of proton exchange membrane fuel cell performance with novel segmented cell design and a two-phase flow model. Energy. 2016;113:1071-89.

[106] N. W. Lee, Y. S. Kim, M. Kim, M. S. Kim. Numerical analysis on the effect of voltage change on removing condensed water inside the GDL of a PEM fuel cell. J Mech Sci Technol. 2016;30:4383-90.

[107] C. Z. Qin, S. M. Hassanizadeh. A new approach to modelling water flooding in a polymer electrolyte fuel cell. Int J Hydrogen Energy. 2015;40:3348–58.

[108] S. Kang. Quasi-three dimensional dynamic modeling of a proton exchange membrane fuel cell with consideration of two-phase water transport through a gas diffusion layer. Energy. 2015;90:1388–400.

[109] L. Xing, X. Liu, T. Alaje, R. Kumar, M. Mamlouk, K. Scott. A two-phase flow and non-isothermal agglomerate model for a proton exchange membrane (PEM) fuel cell. Energy. 2014;73:618–34.

[110] H. Y. Wang, W. J. Yang, D. W. Lee, Y. B. Kim. Development of a Micro Temperature Sensor and 3D Temperature Analysis for a Proton Exchange Membrane Fuel Cell. Fuel Cells. 2014;14:626–34.

[111] T. Cao, H. Lin, L. Chen, Y. He, W. Tao. Numerical investigation of the coupled water and thermal management in PEM fuel cell. Appl Energy. 2013;112:1115–25.

[112] S. P. Jung, C. I. Lee, C. C. Chen. An efficient method for numerical predictions of the performance characteristics of fuel cells. I. Model development and validation. J Power Sources. 2012;199:179-94.

[113] X. Liu, G. Lou, Z. Wen. Three-dimensional two-phase flow model of proton exchange membrane fuel cell with parallel gas distributors. J Power Sources. 2010;195:2764-73.

[114] A. Esposito, C. Pianese, Y. G. Guezennec. Coupled modeling of water transport and air–droplet interaction in the electrode of a proton exchange membrane fuel cell. J Power Sources. 2010;195:4149-59.

[115] R. B. Ferreira, D. S. Falcão, V. B. Oliveira, A. M. F. R. Pinto. A one-dimensional and two-phase flow model of a proton exchange membrane fuel cell. J Chem Technol Biotechnol. 2015;90:1547-51.

[116] ANSYS Inc. ANSYS Fluent Fuel Cell Modules Manual - Release 15.0. 2013.

[117] G. R. Molaeimanesh, M. H. Akbari. Role of wettability and water droplet size during water removal from a PEMFC GDL by lattice Boltzmann method. Int J Hydrogen Energy. 2016;41:14872-84.

[118] D. H. Jeon, H. Kim. Effect of compression on water transport in gas diffusion layer of polymer electrolyte membrane fuel cell using lattice Boltzmann method. J Power Sources. 2015;294:393-405.

[119] B. Han, M. Ni, H. Meng. Three-Dimensional Lattice Boltzmann Simulation of Liquid Water Transport in Porous Layer of PEMFC. Entropy. 2015;18:17.

[120] G. R. Molaeimanesh, M. H. Akbari. A three-dimensional pore-scale model of the cathode electrode in polymer-electrolyte membrane fuel cell by lattice Boltzmann method. J Power Sources. 2014;258:89-97.

[121] X. Niu, T. Munekata, S. Hyodo, K. Suga. An investigation of water-gas transport processes in the gas-diffusion-layer of a PEM fuel cell by a multiphase multiple-relaxation-time lattice Boltzmann model. J Power Sources. 2007;172:542-52.

[122] B. Straubhaar, J. Pauchet, M. Prat. Pore network modelling of condensation in gas diffusion layers of proton exchange membrane fuel cells. Int J Heat Mass Tran. 2016;102:891-901.

[123] C. Z. Qin, S. Hassanizadeh, L. Van Oosterhout. Pore-Network Modeling of Water and Vapor Transport in the Micro Porous Layer and Gas Diffusion Layer of a Polymer Electrolyte Fuel Cell. Computation. 2016;4:21.

[124] M. Fazeli, J. Hinebaugh, A. Bazylak. Incorporating Embedded Microporous Layers into Topologically Equivalent Pore Network Models for Oxygen Diffusivity Calculations in Polymer Electrolyte Membrane Fuel Cell Gas Diffusion Layers. Electrochim Acta. 2016;216:364-75.

[125] B. Straubhaar, J. Pauchet, M. Prat. Water transport in gas diffusion layer of a polymer electrolyte fuel cell in the presence of a temperature gradient. Phase change effect. Int J Hydrogen Energy. 2015;40:11668–75.

[126] B. Markicevic, N. Djilali. Analysis of liquid water transport in fuel cell gas diffusion media using two-mobile phase pore network simulations. J Power Sources. 2011;196:2725-34.

[127] G. Luo, Y. Ji, C. Wang, P. K. Sinha. Modeling liquid water transport in gas diffusion layers by topologically equivalent pore network. Electrochim Acta. 2010;55:5332-41.

[128] M. Rebai, M. Prat. Scale effect and two-phase flow in a thin hydrophobic porous layer. Application to water transport in gas diffusion layers of proton exchange membrane fuel cells. J Power Sources. 2009;192:534-43.

[129] P. K. Sinha, C. Wang. Pore-network modeling of liquid water transport in gas diffusion layer of a polymer electrolyte fuel cell. Electrochim Acta. 2007;52:7936-45.

[130] R. B. Ferreira, D. S. Falcão, V. B. Oliveira, A. M. F. R. Pinto. Numerical simulations of two-phase flow in proton exchange membrane fuel cells using the volume of fluid method – A review. J Power Sources. 2015;277:329-42.

[131] Y. Ding, X. Bi, D. P. Wilkinson. 3D simulations of the impact of two-phase flow on PEM fuel cell performance. Chem Eng Sci. 2013;100:445-55.

[132] L. Chen, T. Cao, Z. Li, Y. He, W. Tao. Numerical investigation of liquid water distribution in the cathode side of proton exchange membrane fuel cell and its effects on cell performance. Int J Hydrogen Energy. 2012;37:9155-70.

[133] A. D. Le, B. Zhou. A general model of proton exchange membrane fuel cell. J Power Sources. 2008;182:197-222.

[134] J. E. Welch, F. H. Harlow, J. P. Shannon, B. J. Daly. The MAC method. A computing technique for solving viscous, incompressible, transient fluid-flow problems involving free surfaces1966.

[135] W. F. Noh, P. Woodward. SLIC (simple line Interface Calculation). In: A. I. van Dooren, Baines MJ, editors. Lect Notes Phys. New York: Springer; 1982. p. 273-85.

[136] C. W. Hirt, B. D. Nichols. Volume of fluid (VOF) method for the dynamics of free boundaries. J Comput Phys. 1981;39:201-25.

[137] D. Gerlach, G. Tomar, G. Biswas, F. Durst. Comparison of volume-of-fluid methods for surface tension-dominant two-phase flows. Int J Heat Mass Tran. 2006;49:740-54.

[138] D. L. Youngs. Time-dependent multi-material flow with large fluid distortion. In: Morton KW, Baines MJ, editors. Numerical methods for fluid dynamics. New York: Academic Press; 1982. p. 273-85.

[139] M. D. Torrey, L. D. Cloutman, R. C. Mjolsness, C. Hirt. NASA-VOF2D: a computer program for incompressible flows with free surfaces. STIN. 1985;86:30116.

[140] M. D. Torrey, R. C. Mjolsness, L. R. Stein. NASA-VOF3D: A three-dimensional computer program for incompressible flows with free surfaces. STIN. 1987;88:10288.

[141] ANSYS Inc. ANSYS Fluent Theory Guide - Release 15.0. 2013.

[142] J. Brackbill, D. B. Kothe, C. Zemach. A continuum method for modeling surface tension. J Comput Phys. 1992;100:335-54.

[143] P. Quan, B. Zhou, A. Sobiesiak, Z. Liu. Water behavior in serpentine micro-channel for proton exchange membrane fuel cell cathode. J Power Sources. 2005;152:131-45.

[144] A. Golpaygan, N. Ashgriz. Effects of oxidant fluid properties on the mobility of water droplets in the channels of PEM fuel cell. Int J Energ Res. 2005;29:1027-40.

[145] Y. H. Cai, J. Hu, H. P. Ma, B. L. Yi, H. M. Zhang. Effects of hydrophilic/hydrophobic properties on the water behavior in the micro-channels of a proton exchange membrane fuel cell. J Power Sources. 2006;161:843-8.

[146] K. Jiao, B. Zhou, P. Quan. Liquid water transport in parallel serpentine channels with manifolds on cathode side of a PEM fuel cell stack. J Power Sources. 2006;154:124-37.

[147] K. Jiao, B. Zhou, P. Quan. Liquid water transport in straight micro-parallel-channels with manifolds for PEM fuel cell cathode. J Power Sources. 2006;157:226-43.

[148] A. Theodorakakos, T. Ous, M. Gavaises, J. Nouri, N. Nikolopoulos, H. Yanagihara. Dynamics of water droplets detached from porous surfaces of relevance to PEM fuel cells. J Colloid Interface Sci. 2006;300:673-87.

[149] Z. Zhan, J. Xiao, M. Pan, R. Yuan. Characteristics of droplet and film water motion in the flow channels of polymer electrolyte membrane fuel cells. J Power Sources. 2006;160:1-9.

[150] K. Jiao, B. Zhou. Innovative gas diffusion layers and their water removal characteristics in PEM fuel cell cathode. J Power Sources. 2007;169:296-314.

[151] P. Quan, M. Lai. Numerical study of water management in the air flow channel of a PEM fuel cell cathode. J Power Sources. 2007;164:222-37.

[152] X. Zhu, P. Sui, N. Djilali. Numerical simulation of emergence of a water droplet from a pore into a microchannel gas stream. Microfluid Nanofluid. 2007;4:543-55.

[153] X. Zhu, P. Sui, N. Djilali. Dynamic behaviour of liquid water emerging from a GDL pore into a PEMFC gas flow channel. J Power Sources. 2007;172:287-95.

[154] K. Jiao, B. Zhou. Accelerated numerical test of liquid behavior across gas diffusion layer in proton exchange membrane fuel cell cathode. J Fuel Cell Sci Technol. 2008;5:041011

[155] A. Bazylak, D. Sinton, N. Djilali. Dynamic water transport and droplet emergence in PEMFC gas diffusion layers. J Power Sources. 2008;176:240-6.

[156] C. Fang, C. Hidrovo, F. Wang, J. Eaton, K. Goodson. 3-D numerical simulation of contact angle hysteresis for microscale two phase flow. Int J Multiphase Flow. 2008;34:690-705.

[157] A. Golpaygan, N. Ashgriz. Multiphase flow model to study channel flow dynamics of PEM fuel cells: deformation and detachment of water droplets. Int J Comput Fluid D. 2008;22:85-95.

[158] K. Jiao, B. Zhou. Effects of electrode wettabilities on liquid water behaviours in PEM fuel cell cathode. J Power Sources. 2008;175:106-19.

[159] E. Shirani, S. Masoomi. Deformation of a Droplet in a Channel Flow. J Fuel Cell Sci Technol. 2008;5:041008.

[160] X. Zhu, P. Sui, N. Djilali. Three-dimensional numerical simulations of water droplet dynamics in a PEMFC gas channel. J Power Sources. 2008;181:101-15.

[161] A. D. Le, B. Zhou. A generalized numerical model for liquid water in a proton exchange membrane fuel cell with interdigitated design. J Power Sources. 2009;193:665-83.

[162] A. D. Le, B. Zhou. Fundamental understanding of liquid water effects on the performance of a PEMFC with serpentine-parallel channels. Electrochim Acta. 2009;54:2137-54.

[163] A. D. Le, B. Zhou. A numerical investigation on multi-phase transport phenomena in a proton exchange membrane fuel cell stack. J Power Sources. 2010;195:5278-91.

[164] Y. Ding, H. Bi, D. Wilkinson. Three-dimensional numerical simulation of water droplet emerging from a gas diffusion layer surface in micro-channels. J Power Sources. 2010;195:7278-88.

[165] P. Quan, M. C. Lai. Numerical simulation of two-phase water behavior in the cathode of an interdigitated proton exchange membrane fuel cell. J Fuel Cell Sci Technol. 2010;7:011017.

[166] W. Du, L. Zhang, X. T. Bi, D. P. Wilkinson, J. Stumper, H. Wang. Gas - Liquid two-phase flow in minichannels with liquid side introduction. Ind Eng Chem Res. 2010;49:6709-21.

[167] G. He, Y. Yamazaki, A. Abudula. The effect of wall roughness on the liquid removal in micro-channels related to a proton exchange membrane fuel cell(PEMFC). J Power Sources. 2010;195:1561-8.

[168] P. V. Suresh, S. Jayanti. Effect of air flow on liquid water transport through a hydrophobic gas diffusion layer of a polymer electrolyte membrane fuel cell. Int J Hydrogen Energy. 2010;35:6872-86.

[169] J. W. Park, K. Jiao, X. Li. Numerical investigations on liquid water removal from the porous gas diffusion layer by reactant flow. Appl Energy. 2010;87:2180-6.

[170] A. D. Le, B. Zhou, H. Shiu, C. Lee, W. Chang. Numerical simulation and experimental validation of liquid water behaviors in a proton exchange membrane fuel cell cathode with serpentine channels. J Power Sources. 2010;195:7302-15.

[171] H. i. Kim, J. H. Nam, D. Shin, T. Y. Chung, Y. G. Kim. A numerical study on liquid water exhaust capabilities of flow channels in polymer electrolyte membrane fuel cells. CAP. 2010;10:S91-S6.

[172] X. Zhu, Q. Liao, P. C. Sui, N. Djilali. Numerical investigation of water droplet dynamics in a low-temperature fuel cell microchannel: Effect of channel geometry. J Power Sources. 2010;195:801-12.

[173] Y. Ding, H. Bi, D. P. Wilkinson. Three dimensional numerical simulation of gas–liquid two-phase flow patterns in a polymer–electrolyte membrane fuel cells gas flow channel. J Power Sources. 2011;196:6284-92.

[174] S. Kang, B. Zhou, C. H. Cheng, H. R. Shiu, C. I. Lee. Liquid water flooding in a proton exchange membrane fuel cell cathode with an interdigitated design. Int J Energ Res. 2011;35:1292-311.

[175] X. Wang, B. Zhou. Liquid water flooding process in proton exchange membrane fuel cell cathode with straight parallel channels and porous layer. J Power Sources. 2011;196:1776-94.

[176] B. Mondal, K. Jiao, X. Li. Three-dimensional simulation of water droplet movement in PEM fuel cell flow channels with hydrophilic surfaces. Int J Energ Res. 2011;35:1200-12.

[177] K. A. Raman, B. Mondal, X. Li. Water Droplet Transport in Single Gas Flow Channel of PEM Fuel Cell. Int J Adv Therm Sci Eng. 2011;2:27-33.

[178] A. Golpaygan, A. Sarchami, N. Ashgriz. Three-dimensional multiphase flow model to study channel flow dynamics of PEM fuel cells. Int J Energ Res. 2011;35:1188-99.

[179] X. Zhu, P. C. Sui, N. Djilali, Q. Liao. Dynamics of emerging water droplet subjected to sidewall with different wettabilities in a fuel cell cathode channel. Fuel Cells. 2011;11:404-12.

[180] Y. Cai, T. Chen, T. Yang, J. Xiao. Mechanism of water transport in serpentine cathode channels of proton exchange membrane fuel cells. J Power Sources. 2012;209:90-104.

[181] J. G. Carton, V. Lawlor, A. G. Olabi, C. Hochenauer, G. Zauner. Water droplet accumulation and motion in PEM (Proton Exchange Membrane) fuel cell mini-channels. Energy. 2012;39:63-73.

[182] L. Chen, H. Luan, Y. He, W. Tao. Effects of Roughness of Gas Diffusion Layer Surface on Liquid Water Transport in Micro Gas Channels of a Proton Exchange Membrane Fuel Cell. Numer Heat tr A-Appl. 2012;62:295-318.

[183] S. C. Cho, Y. Wang, K. S. Chen. Droplet dynamics in a polymer electrolyte fuel cell gas flow channel: Forces, Deformation and detachment. II: Comparisons of analytical solution with numerical and experimental results. J Power Sources. 2012;210:191-7.

[184] C. Qin, D. Rensink, S. M. Hassanizadeh, S. Fell. Direct simulation of liquid water dynamics in the gas channel of a polymer electrolyte fuel cell. J Electrochem Soc. 2012;159:B434-B43.

[185] Z. Y. Ahmad, S. Didari, J. Moon, T. A. Harris. Computational Fluid Dynamics of Water Droplet Formation and Detachment from Gas Diffusion Layer. ECS Trans. 2013;45:89-100.

[186] L. Chen, Y. He, W. Tao. Effects of surface microstructures of gas diffusion layer on water droplet dynamic behaviors in a micro gas channel of proton exchange membrane fuel cells. Int J Heat Mass Tran. 2013;60:252-62.

[187] Y. Ding, R. Anderson, L. Zhang, X. Bi, D. P. Wilkinson. Simulations of two-phase flow distribution in communicating parallel channels for a PEM fuel cell. Int J Multiphase Flow. 2013;52:35-45.

[188] Y. Ding, H. Bi, D. Wilkinson. 3D Simulations of the Impact of Two-phase Flow on PEM Fuel Cell Performance. Chem Eng Sci. 2012;100:445–55.

[189] Y. Ding, X. T. Bi, D. P. Wilkinson. Numerical investigation of the impact of two-phase flow maldistribution on PEM fuel cell performance. Int J Hydrogen Energy. 2013;39:469–80.

[190] É. Fontana, E. Mancusi, A. A. Ulson de Souza, S. M. A. Guelli Ulson de Souza. Flow regimes for liquid water transport in a tapered flow channel of proton exchange membrane fuel cells (PEMFCs). J Power Sources. 2013;234:260-71.

[191] E. Mancusi, É. Fontana, A. A. Ulson de Souza, S. M. A. Guelli Ulson de Souza. Numerical study of two-phase flow patterns in the gas channel of PEM fuel cells with tapered flow field design. Int J Hydrogen Energy. 2013;39:2261–73.

[192] M. Hossain, S. Z. Islam, A. Colley-Davies, E. Adom. Water dynamics inside a cathode channel of a polymer electrolyte membrane fuel cell. Renew Energ. 2013;50:763-79.

[193] H. Kim, S. Jeon, M. Song, K. Kim. Numerical simulations of water droplet dynamics in hydrogen fuel cell gas channel. J Power Sources. 2013;246:679-95.

[194] Y. Qin, Q. Du, Y. Yin, K. Jiao, X. Li. Numerical investigation of water dynamics in a novel proton exchange membrane fuel cell flow channel. J Power Sources. 2013;222:150-60.

[195] Y. Qin, X. Li, Q. Du, Y. Yin, K. Jiao. Effect of wettability on water removal from the gas diffusion layer surface in a novel proton exchange membrane fuel cell flow channel. Int J Hydrogen Energy. 2013;38:12879–85.

[196] Y. Qin, X. Li, K. Jiao, Q. Du, Y. Yin. Effective removal and transport of water in a PEM fuel cell flow channel having a hydrophilic plate. Appl Energy. 2014;113:116-26.

[197] N. Bao, Y. Zhou, K. Jiao, Y. Yin, Q. Du, J. Chen. Effect of gas diffusion layer deformation on liquid water transport in proton exchange membrane fuel cell. Eng Appl Comp Fluid. 2014;8:26-43.

[198] M. Song, H. Kim, K. Kim. Effects of hydrophilic/hydrophobic properties of gas flow channels on liquid water transport in a serpentine polymer electrolyte membrane fuel cell. Int J Hydrogen Energy. 2014;39:19714–21.

[199] M. Ashrafi, M. Shams. Effects of heterogeneous surface of gas diffusion layers on droplet transport in microchannels of PEM fuel cells. Int J Hydrogen Energy. 2015;41:1974–89.

[200] R. B. Ferreira, D. S. Falcão, V. B. Oliveira, A. M. F. R. Pinto. Numerical simulations of two-phase flow in an anode gas channel of a proton exchange membrane fuel cell. Energy. 2015;82:619-28.

[201] S. M. A. Guelli Ulson de Souza, E. Mancusi, É. Fontana, A. A. Ulson de Souza. CFD Simulation of Two-Phase Flow Patterns in the Gas Channel of a Proton Exchange Membrane Fuel Cell. Chem Eng Technol. 2015;38:1229–34.

[202] J. H. Jo, W. T. Kim. Numerical simulation of water droplet dynamics in a right angle gas channel of a polymer electrolyte membrane fuel cell. Int J Hydrogen Energy. 2015;40: 8368–83.

[203] D. Lorenzini-Gutierrez, S. G. Kandlikar, A. Hernandez-Guerrero, F. Elizalde-Blancas. Residence time of water film and slug flow features in fuel cell gas channels and their effect on instantaneous area coverage ratio. J Power Sources. 2015;279:567-80.

[204] Z. Niu, K. Jiao, F. Zhang, Q. Du, Y. Yin. Direct numerical simulation of two-phase turbulent flow in fuel cell flow channel. Int J Hydrogen Energy. 2015;41:3147–52.

[205] M. Ashrafi, M. Shams, A. Bozorgnezhad, G. Ahmadi. Simulation and experimental validation of droplet dynamics in microchannels of PEM fuel cells. Heat Mass Transfer. 2016;52:2671–86.

[206] Y. Cai, T. Yang, P.-C. Sui, J. Xiao. A numerical investigation on the effects of water inlet location and channel surface properties on water transport in PEMFC cathode channels. Int J Hydrogen Energy. 2016;41:16220–9.

[207] Y. Hou, G. Zhang, Y. Qin, Q. Du, K. Jiao. Numerical simulation of gas liquid two-phase flow in anode channel of low-temperature fuel cells. Int J Hydrogen Energy. 2016. DOI: 10.1016/j.ijhydene.2016.09.219.

[208] F. Zhang, X. Yang, C. Wang. Liquid water removal from a polymer electrolyte fuel cell. J Electrochem Soc. 2006;153:A225-A32.

[209] S. C. Cho, Y. Wang, K. S. Chen. Droplet dynamics in a polymer electrolyte fuel cell gas flow channel: Forces, deformation, and detachment. I: Theoretical and numerical analyses. J Power Sources. 2012;206:119-28.

[210] X.-Z. Yuan, S. Zhang, J. C. Sun, H. Wang. A review of accelerated conditioning for a polymer electrolyte membrane fuel cell. J Power Sources. 2011;196:9097-106.

[211] USFCC Single Cell Testing Task Force. Single Cell Test Protocol. 2006;05-014B.2.

[212] R. B. Ferreira, D. S. Falcão, V. B. Oliveira, A. M. F. R. Pinto. Experimental study on the membrane electrode assembly of a proton exchange membrane fuel cell: effects of microporous layer, membrane thickness and gas diffusion layer hydrophobic treatment. Electrochim Acta. 2017;224:337-45.

[213] M. Ciureanu, R. Roberge. Electrochemical impedance study of PEM fuel cells. Experimental diagnostics and modeling of air cathodes. J Phys Chem B. 2001;105:3531-9.

[214] M. I. Rosli, D. J. Borman, D. B. Ingham, M. S. Ismail, L. Ma, M. Pourkashanian. Transparent PEM fuel cells for direct visualization experiments. J Fuel Cell Sci Technol. 2010;7:061015.

[215] M. Mathias, J. Roth, J. Fleming, W. Lehnert. Diffusion media materials and characterisation. In: Vielstich W, Lamm A, Gasteiger H, editors. Handbook of Fuel Cells: Fundamentals, Technology and Applications. New York: John Wiley & Sons; 2003. p. 517-37.

[216] X. Yang, F. Zhang, A. Lubawy, C. Wang. Visualization of liquid water transport in a PEFC. Electrochem Solid-State Lett. 2004;7:A408-A11.

[217] X. Liu, H. Guo, C. Ma. Water flooding and two-phase flow in cathode channels of proton exchange membrane fuel cells. J Power Sources. 2006;156:267-80.

[218] M. Vera. A single-phase model for liquid-feed DMFCs with non-Tafel kinetics. J Power Sources. 2007;171:763-77.

[219] J. T. Gostick, M. W. Fowler, M. A. Ioannidis, M. D. Pritzker, Y. M. Volfkovich, A. Sakars. Capillary pressure and hydrophilic porosity in gas diffusion layers for polymer electrolyte fuel cells. J Power Sources. 2006;156:375-87.

[220] E. N. Fuller, P. D. Schettler, J. C. Giddings. New method for prediction of binary gas-phase diffusion coefficients. Industrial & Engineering Chemistry. 1966;58:18-27.

[221] S. Wang, Y. Wang. Investigation of the through-plane effective oxygen diffusivity in the porous media of PEM fuel cells: Effects of the pore size distribution and water saturation distribution. Int J Heat Mass Tran. 2016;98:541-9.

[222] Y. Wang, S. Wang. Evaluation and modeling of PEM fuel cells with the Bruggeman correlation under various tortuosity factors. Int J Heat Mass Tran. 2017;105:18-23.

[223] M. Leverett. Capillary behavior in porous solids. Transactions of the AIME. 1941;142:152-69.

[224] K. S. Udell. Heat transfer in porous media considering phase change and capillarity—the heat pipe effect. Int J Heat Mass Tran. 1985;28:485-95.

[225] X. Wang, Y. Wang, Y. Chen, C. Si, A. Su, D. G. Lee. Proton exchange membrane fuel cell modeling with diffusion layer-based and sands-based capillary pressure correlations: Comparative study. J Taiwan Inst Chem Eng. 2014;45:1532–41.

[226] B. Ramos-Alvarado, A. Hernandez-Guerrero, M. W. Ellis. Non-equilibrium two-phase model of the air-cathode of a PEM fuel cell based on GDL experimental water transport characteristics. J Power Sources. 2013;232:376-88.

[227] E. C. Kumbur, K. V. Sharp, M. M. Mench. On the effectiveness of Leverett approach for describing the water transport in fuel cell diffusion media. J Power Sources. 2007;168:356-68.

[228] E. C. Kumbur, K. V. Sharp, M. M. Mench. Validated Leverett Approach for Multiphase Flow in PEFC Diffusion Media: II. Compression Effect. J Electrochem Soc. 2007;154:B1305-B14.

[229] E. C. Kumbur, K. V. Sharp, M. M. Mench. Validated Leverett Approach for Multiphase Flow in PEFC Diffusion Media: I. Hydrophobicity Effect. J Electrochem Soc. 2007;154:B1295-B304.

[230] E. C. Kumbur, K. V. Sharp, M. M. Mench. Validated Leverett Approach for Multiphase Flow in PEFC Diffusion Media: III. Temperature Effect and Unified Approach. J Electrochem Soc. 2007;154:B1315-B24.

[231] Q. Ye, T. V. Nguyen. Three-Dimensional Simulation of Liquid Water Distribution in a PEMFC with Experimentally Measured Capillary Functions. J Electrochem Soc. 2007;154:B1242-B51.

[232] R. O'Hayre, S. Cha, W. Colella, F. B. Prinz. Fuel Cell Fundamentals. 1st ed. USA: John Wiley & Sons, Inc.; 2006.

[233] T. Bednarek, G. Tsotridis. Issues associated with modelling of proton exchange membrane fuel cell by computational fluid dynamics. J Power Sources. 2017;343:550-63.

[234] F. B. Weng, A. Su, C. Y. Hsu, C. Y. Lee. Study of water-flooding behaviour in cathode channel of a transparent proton-exchange membrane fuel cell. J Power Sources. 2006;157:674-80.

[235] A. Bozorgnezhad, M. Shams, H. Kanani, M. Hasheminasab, G. Ahmadi. Two-phase flow and droplet behavior in microchannels of PEM fuel cell. Int J Hydrogen Energy. 2016;41:19164–81.

Appendix A. Hydrophobicity of the GDL/CG interface: increasing water permeability in the GDL *vs* setting the GDL/CG interface as a hydrophobic wall

In this appendix, results of simulations where the liquid water permeability in the GDL was increased to simulate the hydrophobicity of the GDL/GC interface are compared with those when this interface was set as an actual hydrophobic wall (wall boundary condition) (θ = 138.1 º). Because in the latter case air does not penetrate into the GDL, and therefore no electrical current and water is produced, the velocity of liquid water was manually set as 0.40 m s^{-1} in both cases, so its dynamics could be analyzed. The results shown are for a fuel cell with a serpentine channel and 2.4 cm^2 of active area (more details in Section **6.1**). **Figure A.1** displays water distribution in the channel, **Figure A.2** depicts the two-phase flow pressure drop, **Figure A.3** shows the volume-weighted water content in the channel, and **Figure A.4** contains the water coverage ratio in the channel top and side walls and in the GDL surface. The only difference worth mentioning is on the GDL surface water coverage ratio, which was higher when setting the GDL/GC interface as a hydrophobic wall. However, the value obtained was also very small, and considerably lower than that on the top and side walls of the channel. Therefore, the same two-phase flow patterns were achieved.

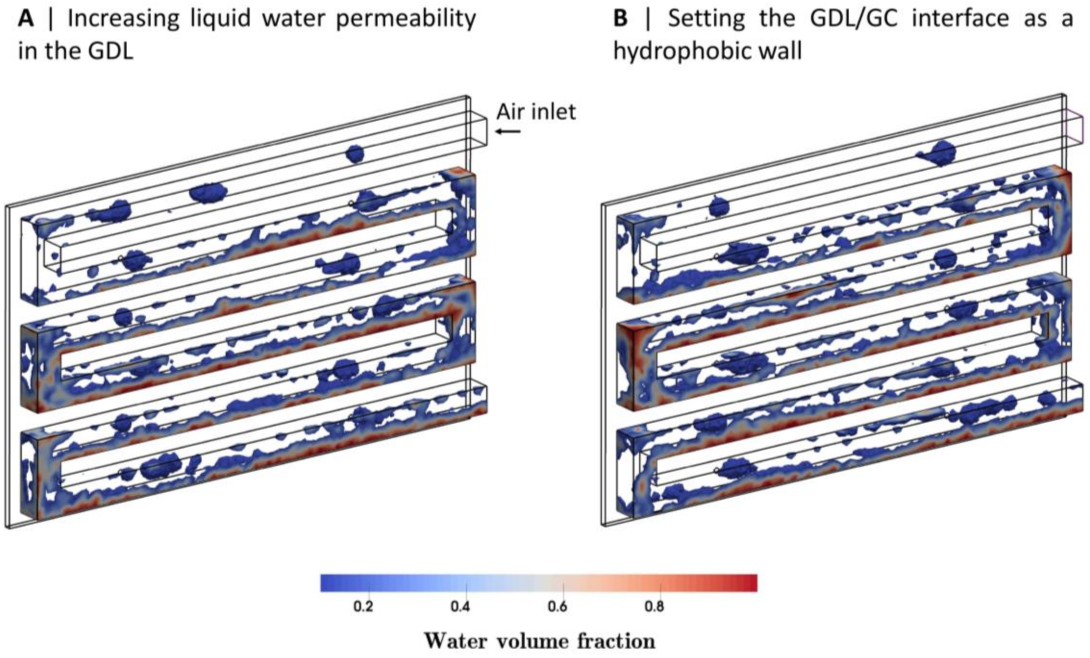

Figure A.1. Water distribution in a serpentine channel when the hydrophobicity of the GDL/CG interface was considered by (A) increasing liquid water permeability in the GDL or (B) setting the GDL/CG interface as an actual hydrophobic wall.

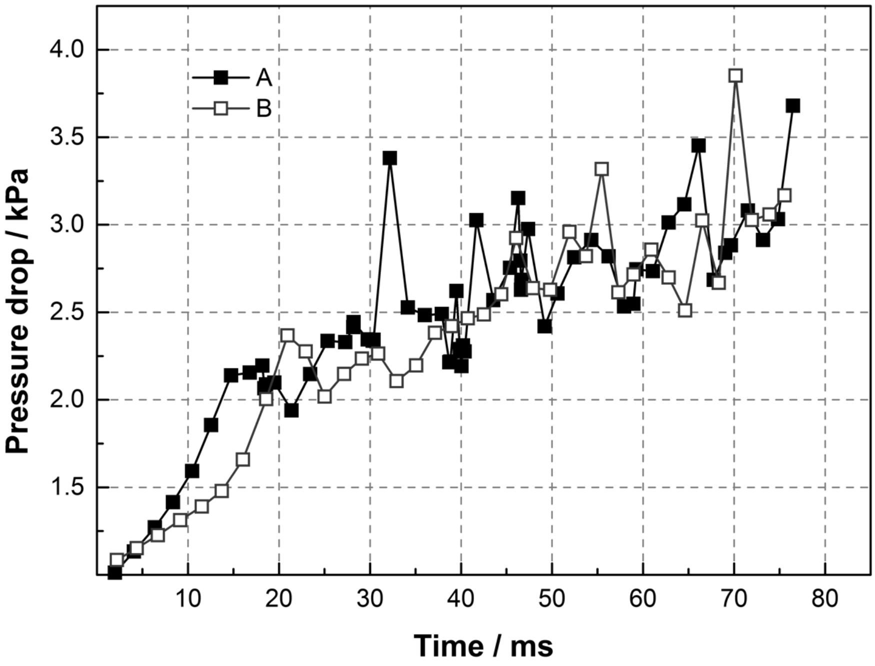

Figure A.2. Two-phase flow pressure drop when the hydrophobicity of the GDL/CG interface was considered by (A) increasing liquid water permeability in the GDL or (B) setting the GDL/CG interface as an actual hydrophobic wall.

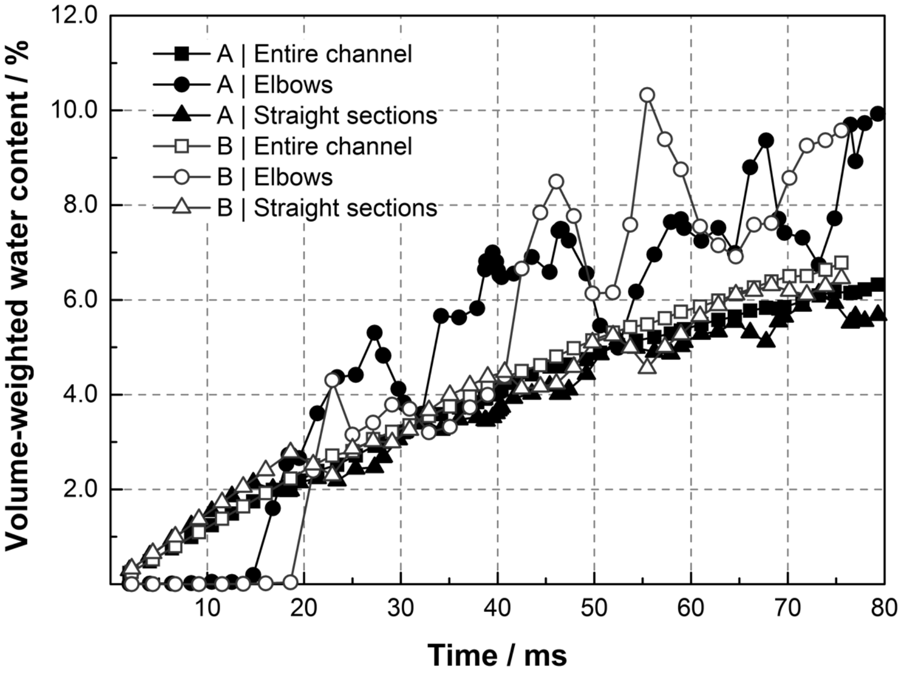

Figure A.3. Volume-weighted water content when the hydrophobicity of the GDL/CG interface was considered by (A) increasing liquid water permeability in the GDL or (B) setting the GDL/CG interface as an actual hydrophobic wall.

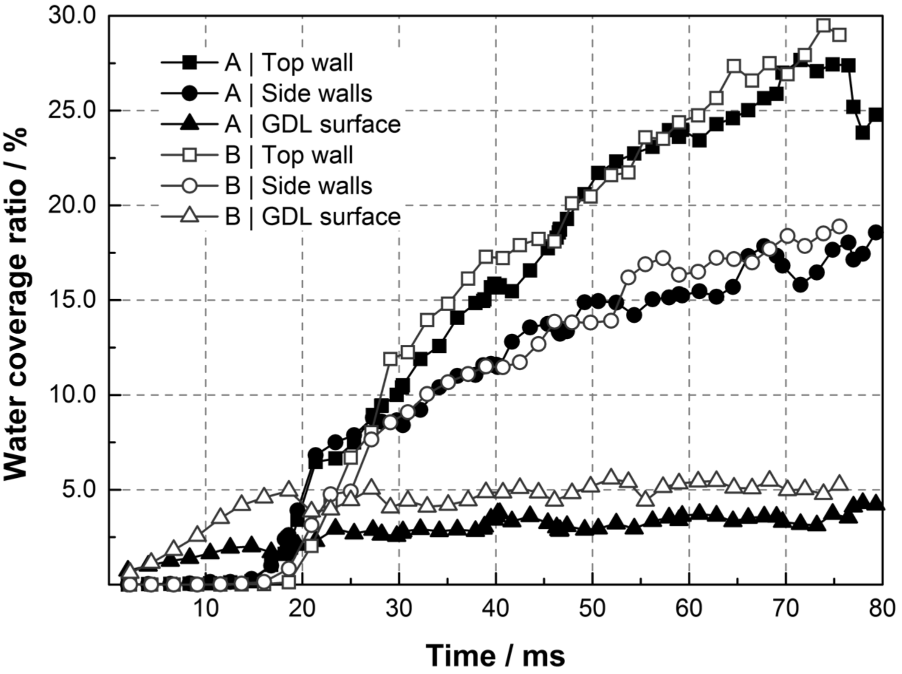

Figure A.4. Water coverage ratio in the top and side walls of the channel and in the GDL surface, when the hydrophobicity of the GDL/CG interface was considered by (A) increasing liquid water permeability in the GDL or (B) setting the GDL/CG interface as an actual hydrophobic wall.

Appendix B. Effect of considering source terms for water condensation in the GDL

Figure B.1 displays liquid water saturation distribution in the GDL/CL interface when source terms for water condensation were not considered (**Figure B.1** A), and when such source terms were included (**Figure B.1** B). The results shown are for a fuel cell with a serpentine channel and 2.4 cm^2 of active area (more details in Section **6.1**). It can be seen that similar profiles were obtained applying both approaches. Nevertheless, the area-weighted average of the water saturation in the case without source terms (around 0.072) was slightly higher than that calculated when considering the source terms (about 0.065).

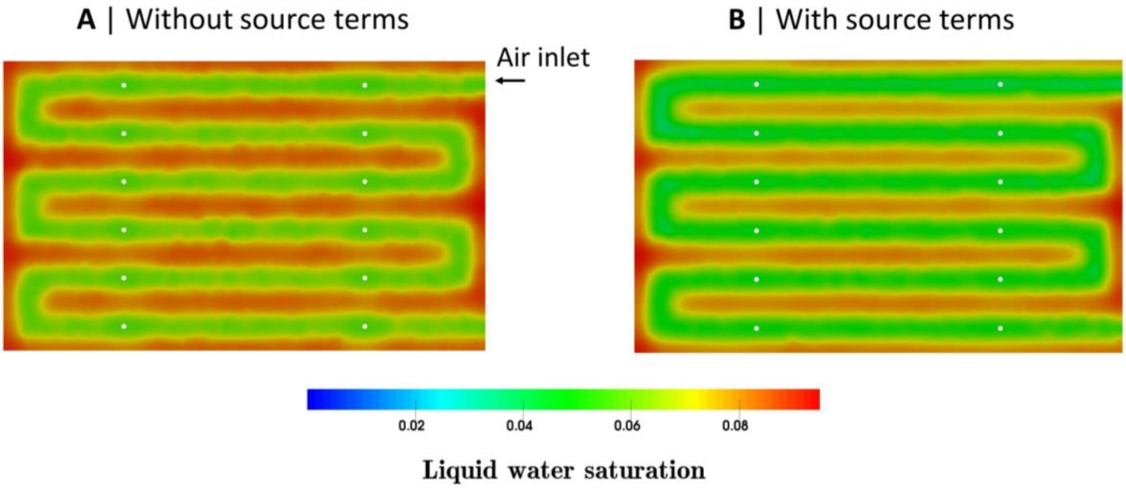

Figure B.1. Liquid water saturation distribution in the GDL/CL interface without considering source terms for water condensation (A) and when such source terms were included (B).

Appendix C. Mesh size test

The effects of changing the mesh size are shown in this appendix. A small cell with a 14.2 mm U-shaped channel was used in order to be able to employ very refined meshes. Apart from meshes having tetrahedral elements, a very refined mesh with hexahedral elements was also tested. **Table C.1** shows the main features of the meshes considered. **Figure C.1** depicts the distribution of water in the channel, **Figure C.2** shows the two-phase flow pressure drop, **Figure C.3** displays the volume-weighted water content and **Figure C.4** contains the water coverage ratio in the top and side walls of the channel and in the GDL surface. It can be seen that Mesh 1 and 2 (especially Mesh 1) predicted lower values of water content in the channel (**Figure C.3**). However, the same general two-phase flow patterns were maintained, *i.e.*, water movement along the channel in the top corners of the channel (**Figure C.1** and **Figure C.4**). Moreover, the droplet shape (**Figure C.1**) is very similar for all meshes. To avoid unpractical simulations times, Mesh 1 was used in the simulations of Chapter **5** (25 cm^2 cell). For the simulations conducted in Chapter **6** (2.4 cm^2 cell), Mesh 2 was employed.

Table C.1. Features of the meshes employed to investigate the effect of the mesh size.

Mesh	Min. size (m)	Max. size (m)	Elements number and type	Nodes number
1	7.0×10^{-5}	2.5×10^{-4}	36,237 (tetrahedral)	7,582
2	5.0×10^{-5}	2.0×10^{-4}	101,652 (tetrahedral)	20,170
3	2.0×10^{-5}	7.0×10^{-5}	355,374 (tetrahedral)	68,543
4	4.0×10^{-5}		342,941 (hexahedral)	1,452,514

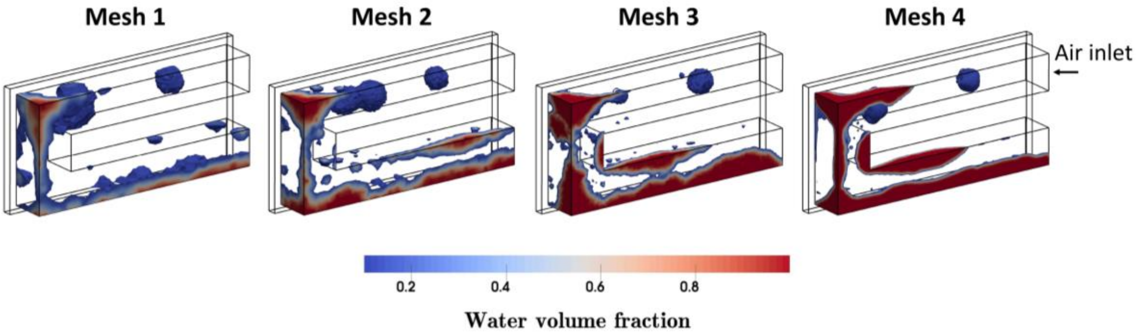

Figure C.1. Water distribution after 30 ms in a U-shaped channel with different meshes.

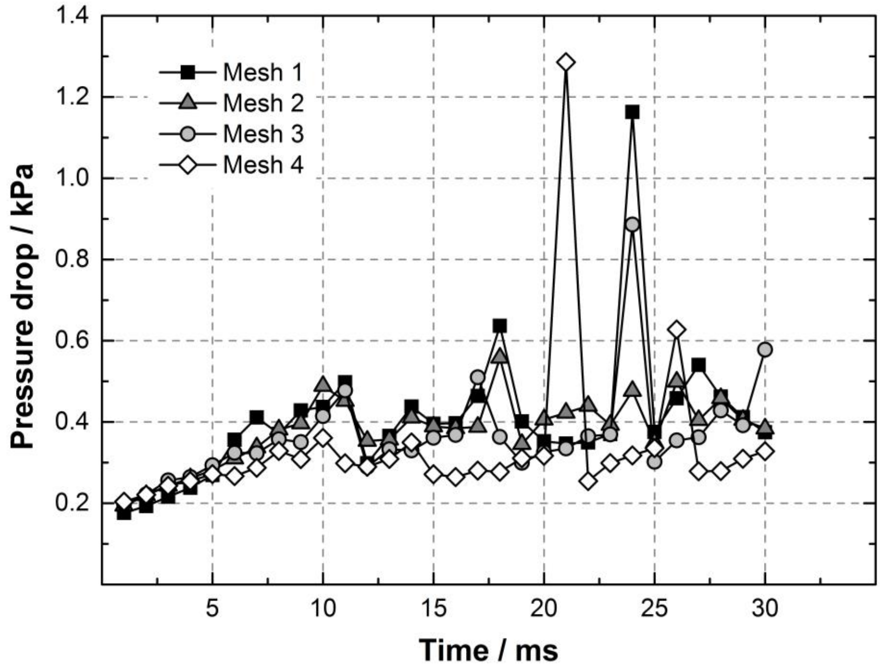

Figure C.2. Two-phase flow pressure drop for different meshes.

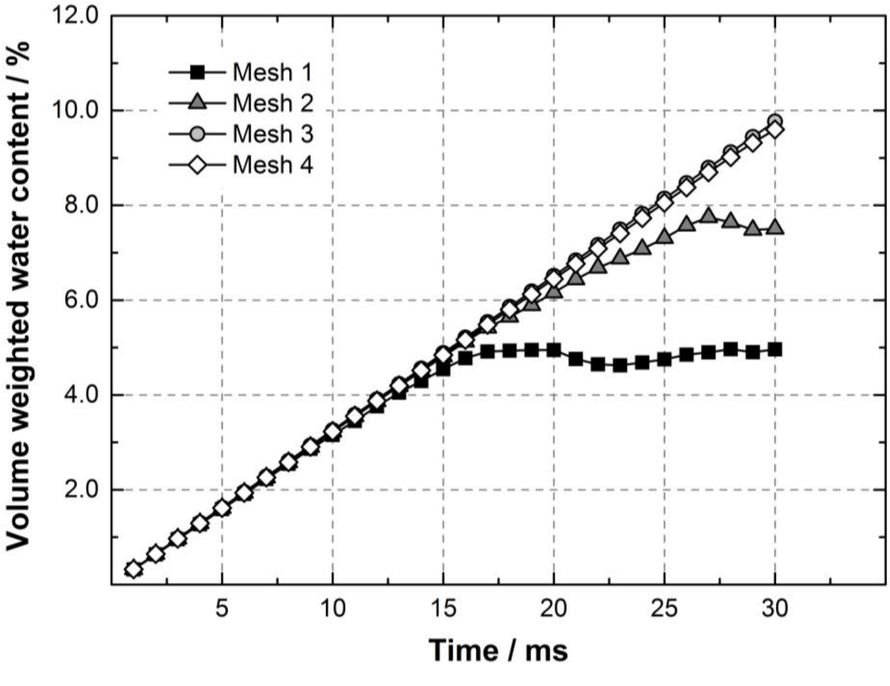

Figure C.3. Volume-weighted water content in a U-shaped channel with different meshes.

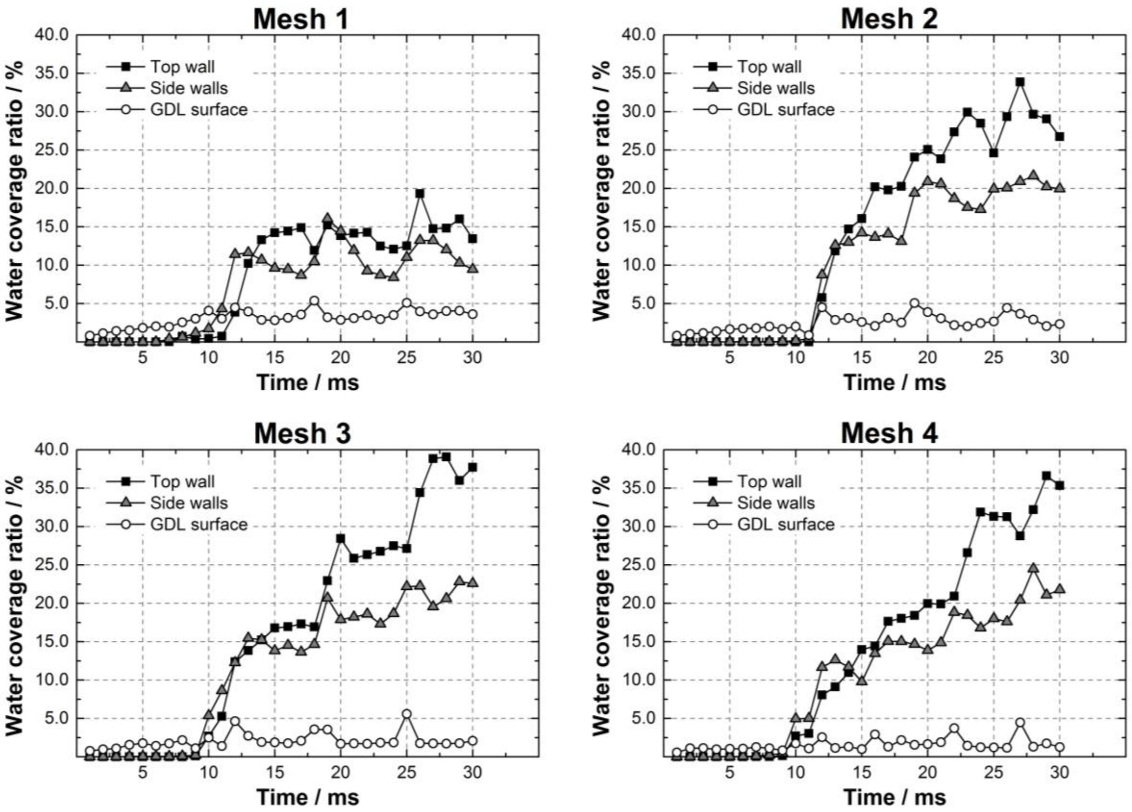

Figure C.4. Water coverage ratio in the top and side walls of the channel and in the GDL surface, for a U-shaped channel with different meshes.

Appendix D. Additional simulation results: effect of operating conditions and flow field design on the cell performance

Figure D.1 displays polarization curves obtained at different operating temperatures, pressures and air stoichiometries, as well as using different flow field designs. The results shown were obtained with a fuel cell having 2.4 cm^2 of active area (more details in Section **6.1**). Moreover, they correspond to steady-state solutions (see Section **5.1.6**).

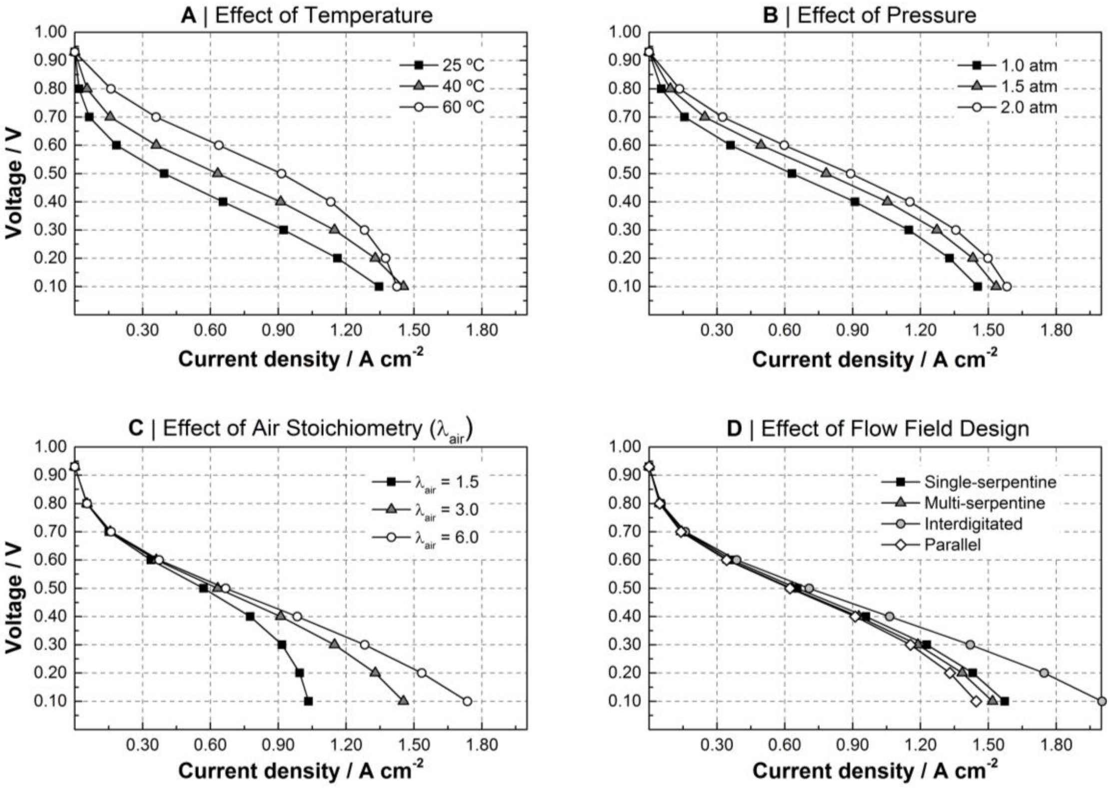

Figure D.1. Polarization curves at different (A) temperatures, (B) pressures and (C) air stoichiometries, and using different (D) flow field designs.